

Topological band crossings in metals, magnets, and non-Hermitian systems

Von der Fakultät Mathematik und Physik der Universität Stuttgart
zur Erlangung der Würde eines Doktors der Naturwissenschaften
(Dr. rer. nat.) genehmigte Abhandlung

vorgelegt von

Moritz M. Hirschmann

aus Böblingen, Deutschland

Hauptberichter:	Prof. Dr. Walter Metzner
Mitberichter:	Dr. Andreas P. Schnyder
	Prof. Dr. Hans Peter Büchler
	Prof. Dr. Shinsei Ryu
Prüfungsvorsitzender:	Prof. Dr. Martin Dressel
Tag der mündlichen Prüfung:	8. September 2021

Max-Planck-Institut für Festkörperforschung
Universität Stuttgart

2021

Contents

List of Abbreviations	iv
Abstract/Kurzzusammenfassung	v
1. Introduction	1
1.1. Topological semimetals	1
1.1.1. Bulk properties of topological semimetals	6
1.1.2. The surface of topological semimetals	8
1.1.3. Material realizations	9
1.2. Symmetry	10
1.2.1. Continuous symmetries and conservation laws	12
1.2.2. Quantum anomalies of topological semimetals	13
1.2.3. Bloch theorem and eigenbases	17
1.2.4. Groups and their representations in solids	19
1.3. Topological phases	24
1.3.1. Homotopy	24
1.3.2. Topological systems and the Altland-Zirnbauer classification	26
1.3.3. Bulk-boundary correspondence	30
1.3.4. Phases with and without topology	31
1.3.5. Other facets of condensed matter topology	32
1.4. Topological invariants, models, and surface states	34
1.4.1. Berry connection	35
1.4.2. Berry curvature	40
1.4.3. Anomalous Hall conductivity	47
1.4.4. Weyl semimetal: surface states and chirality	49
1.4.5. Constructing tight-binding models	51
1.4.6. Determination of surface states	52
1.4.7. Topological versus trivial surface states	54

2. Topological band crossings	57
2.1. Preliminaries	57
2.1.1. Enforced and accidental features	58
2.1.2. Kramers theorem	58
2.1.3. Topological charges	61
2.2. Conditions for nodal features	63
2.2.1. Nodal points	64
2.2.2. Nodal lines	78
2.2.3. Nodal planes	82
3. Band crossings in solids	89
3.1. Topological crossings in trigonal space groups	90
3.1.1. Accordion-like band structure	91
3.1.2. Hourglass nodal lines	95
3.2. Topological crossings in tetragonal space groups	97
3.2.1. The flavors of chiral point crossings	99
3.2.2. Weyl nodal lines	105
3.2.3. Trivial fourfold crossings and their proximity to Weyl semimetals	108
3.2.4. Enforced \mathbb{Z}_2 topology	110
3.3. Topological nodal planes in ferromagnetic MnSi	113
3.3.1. Identifying nodal planes by de Haas-van Alphen spectroscopy	114
3.3.2. Symmetry eigenvalues	118
3.3.3. Surface States	121
3.3.4. Berry curvature	124
3.4. The magnetic antiperovskite Eu_3PbO	126
3.4.1. Antiperovskites: structure, materials, topology	126
3.4.2. Magnetic order in Eu_3PbO	127
3.4.3. Band topology	130
3.4.4. Surface states	134
3.4.5. Anomalous Hall conductivity in the ferromagnetic order	136
3.5. Topology in different magnetic phases of SmB_6	138
4. Semimetals with higher-order topology	141
4.1. Higher-order topology	141
4.2. Higher-order Weyl superconductor	143

5. Exceptional topology	149
5.1. Non-Hermitian quantum mechanics	149
5.1.1. \mathcal{PT} -symmetric quantum mechanics	150
5.1.2. Biorthogonal quantum mechanics	151
5.1.3. Topology in non-Hermitian systems	153
5.2. Non-Hermitian Kitaev chain	155
5.2.1. Pfaffian invariant	156
5.2.2. Localized zero mode	158
5.3. Non-Hermitian semimetals	160
5.3.1. Non-Hermitian Weyl semimetal	160
5.3.2. Termination dependent topology	161
Summary and outlook	167
Appendix	171
A. Symmetries in tight-binding models	171
B. Berry curvature with arbitrary crystalline symmetries	174
C. Tight-binding model for SG 19.27	177
D. Tight-binding model for SG 4.9	178
E. Tight-binding model for Eu_3PbO	179
Bibliography	215
Deutsche Zusammenfassung	217
List of publications	223
Acknowledgments	225

List of Abbreviations

BZ	Brillouin zone
DFT	Density functional theory
dHvA	De Haas-van Alphen
HOTI	Higher-order topological insulator
HOWSC	Higher-order Weyl superconductor
SDOS	Surface density of states
SG	Space group
SOC	Spin-orbit coupling
TRIM	Time-reversal invariant momentum
TRS	Time-reversal symmetry
0D, 1D, 2D, 3D	Zero-, one-, two-, three-dimensional

Abstract

Topological band crossings in the energy spectra of systems with a discrete translation symmetry have proven to be a promising field of study. Their presence is connected to the emergence of prominent effects, like the negative linear magnetoresistance, the anomalous Hall effect, the chiral anomaly, and arc-like surface states, which exhibit open Fermi surfaces on the boundary of the system. The latter can be understood in terms of the bulk topology, where the band crossings correspond to a phase transition between different topological phases that extend over subsets of the parameter space.

In this work we give symmetry-based criteria to infer the existence of various point, line, and plane crossings. After a general introduction to topological semimetals, quantum anomalies, topology and its use for the classification of quantum mechanical systems, as well as the modern theory of polarization in chapter 1, we collect in chapter 2 symmetry arguments for the different types of topological band crossings that we will use in the course of this thesis [1, 2]. This includes also a comprehensive study on enforced nodal planes [3].

With the foundation of our main study laid out, we discuss in chapter 3 various enforced band crossings in all trigonal [1] and tetragonal [2] space groups (SGs). We present the first direct measurement of nodal planes, by considering the ferromagnetic phase of MnSi, and give a detailed analysis of the topological charges associated to nodal planes and Weyl points in this system [3]. In a recent work, this is extended to CoSi, where we refine the previous discussions of the topological charges by our insights into the existence of enforced topological nodal planes [4]. We conclude the chapter with on-going work regarding two additional magnetic systems, the antiferromagnetic, ferrimagnetic and ferromagnetic phases of Eu_3PbO [5] as well as the heavy-fermion compound SmB_6 with applied pressure [6].

In the last two chapters we consider band crossings in a broader context. Chapter 4 is concerned with a centrosymmetric higher-order topology in Weyl superconductors. We introduce a model with Weyl points for a two-dimensional superconductor in an electric field [7]. This model exhibits surface states only for certain terminations, which, unlike previous proposals, is not a consequence of a higher moment of the electric polarization in the bulk. Chapter 5 presents a treatise on the topology in non-Hermitian systems, which commonly exhibit exceptional points as crossings in their band structure. We discuss the Kitaev chain with gain and loss in the presence of different non-Hermitian perturbations. Hereby, we investigate under which conditions the Hermitian topological invariant is still well-defined [8]. If Dirac and Weyl semimetals are subject to non-Hermitian perturbations, we find that conventional topological invariants do not accurately describe the emergence of surface states [9]. We discuss a method to obtain the topological invariants in accordance with the topological surface states.

Inhaltsangabe

Topologische Bandkreuzungen in den Energiespektren translationsinvarianter Systeme stellen ein viel versprechendes Forschungsgebiet dar. Die Existenz solcher Bandkreuzungen steht in Verbindung mit dem Auftreten physikalischer Effekte, wie einem negativen Magnetwiderstand, dem anomalen Hall Effekt, der chiralen Anomalie und bogenförmigen Oberflächenzuständen, sogenannten Fermi-Bögen, die als offene Fermiflächen in Erscheinung treten. Die letzteren leiten sich von der Topologie im Inneren des Materials ab, wobei dort die Bandkreuzungen als Übergänge zwischen Untersystemen unterschiedlicher Topologie auftreten.

In dieser Arbeit stellen wir auf der Basis der kristallinen Symmetrien Kriterien auf, um die Existenz verschiedener Punkt-, Linien- und Flächenkreuzungen vorherzusagen. Nach einer allgemeinen Einleitung zu topologischen Halbmetallen, Quantenanomalien, Topologie und ihrer Verwendung zur Klassifizierung quantenmechanischer Systeme, sowie einer Einführung in die moderne Theorie der Polarisierung in Kapitel 1, sammeln wir in Kapitel 2 hinreichende Symmetrieargumente für unterschiedliche Typen topologischer Bandkreuzungen. Letztere werden im Rahmen dieser Dissertation angewendet [1, 2], wobei ein Schwerpunkt auf einer umfassenden Untersuchung von Systemen mit entarteten Ebenen liegt [3].

Aufbauend auf diesen Grundlagen werden in Kapitel 3 die erzwungenen Bandkreuzungen in trigonalen [1] und tetragonalen [2] Raumgruppen behandelt. Als Anwendungsbeispiel unserer Klassifizierung entarteter Ebenen in ferromagnetischem MnSi, berichten wir über die erste direkte Messung dieses Kreuzungstyps. Hierbei analysieren wir außerdem die tatsächlichen topologischen Ladungen im realen Material für die Weyl-Punkte und die entarteten Ebenen [3]. Mit diesem Ansatz lässt sich außerdem die Diskussion der Topologie in paramagnetischem CoSi erweitern [4]. Wir schließen Kapitel 3 mit einem Ausblick auf zwei weitere magnetische Systeme. Zum einen untersuchen wir die antiferromagnetische, ferrimagnetische und ferromagnetische Phase von Eu_3PbO bezüglich den topologischen Bandkreuzungen und dem anomalen Hall-Effekt [5] und zum anderen wenden wir die Symmetrieanalyse auf das Schwerfermionenmetall SmB_6 unter dem Einfluss eines äußeren Drucks an [6].

In den letzten beiden Kapiteln beleuchten wir topologische Bandkreuzungen in einem breiteren Kontext. Kapitel 4 widmet sich der Topologie höherer Ordnung in Weyl-Halbmetallen, wobei wir ein Modell mit Weyl-Punkten für einen zweidimensionalen, inversionssymmetrischen Supraleiter in einem externen elektrischen Feld vorschlagen. Dieses Modell zeigt topologische Oberflächenzustände, die sich, anders als für bereits bekannte Modelle, nicht auf ein höheres Moment der Polarisierung zurückführen lassen [7]. In Kapitel 5 stellen wir Konzepte zur Beschreibung der Topologie nichthermitescher Systeme vor, deren exzeptionelle Punkte ebenfalls eine Art der Bandkreuzung darstellen. Um festzustellen ob sich die bisherige Analyse

hermitescher Systeme auf den nichthermiteschen Fall übertragen lässt, betrachten wir eine Kitaev Kette für die mit verschiedenen nichthermiteschen Potentialen der Gewinn und Verlust von Teilchen modelliert wird. Wir untersuchen die möglichen Bedingungen unter denen die topologische Invariante der hermiteschen Systeme auch für dieses System wohldefiniert bleibt [8]. Im Kontrast dazu steht der letzte Abschnitt dieses Kapitels zu Dirac- und Weyl-Halbmatalen, die ebenfalls nichthermiteschen Störungen ausgesetzt werden. Die konventionelle Invariante ist in diesen Systemen nicht im Einklang mit den topologischen Oberflächenzuständen [9]. Wir führen eine Methode ein, die es ermöglicht dennoch topologische Invarianten konsistent zu definieren.

1. Introduction

In the following chapter we introduce the diverse field of topological semimetals and review the basic principles underlying the present work. First we highlight why the study of topological semimetals is a worthwhile endeavor before we take a step back to lay the foundations of the ensuing discussion. The understanding of physics, from cosmology over classical mechanics down to the study of elementary particles, is guided and simplified by the symmetries of the universe. In this respect quantum mechanics and in extension also the present work are no exception. For quantum mechanics all physics is in principle encapsulated in a many-body Schrödinger equation, a partial differential equation for which a direct solution is rarely feasible. Yet, symmetries allow us to extract predictions, to simplify calculations and to reach general statements. After reviewing the basics of symmetry considerations we move to the closely related but ultimately different topic of topology. The mathematical field of topology classifies abstract as well as concrete objects by their behavior under smooth transformations. Such a classification can also be applied to the field of condensed matter physics. Both symmetry and topology are not just mere means to bring order into the plethora of physical phenomena, but they also characterize and predict measurable properties.

1.1. Topological semimetals

A semimetal has no gap in the energy spectrum of its electrons, nevertheless it exhibits a vanishing density of states in the vicinity of the Fermi energy. For these two properties to occur at once, the band structure must contain a degeneracy of its energy levels at a point or a line. This is different to semiconductors or insulators that exhibit no density of states, due to an indirect gap in their energy spectrum, as well as to cases without a band gap, where the Fermi energy lies within a band and hence there is a non-zero density of states.

If we consider a semimetal as a condensed matter system with a discrete translation invariance, then the spectrum can be understood as a function $E_n(\mathbf{k})$. Hereby, the crystal momentum \mathbf{k} is the quantum number that corresponds to the translation symmetry and it is given by vectors within the three-dimensional (3D) Brillouin zone (BZ) $\mathbf{k} \in [-\pi, \pi]^3$, cf. Sec. 1.2.3. A

degeneracy between energy levels n and $n + 1$ in the electronic spectrum, as it must occur for some n in any semimetal, corresponds to $E_n(\mathbf{k}_0) = E_{n+1}(\mathbf{k}_0)$ for at least one $\mathbf{k}_0 \in [-\pi, \pi]^3$. In other words, as a function of \mathbf{k} the bands $E_n(\mathbf{k})$ cross or at least touch. For a semimetal the points \mathbf{k}_0 lie on a 0D or 1D submanifold of the BZ, such that the density of states vanishes although there is no gap in the spectrum.

Since a crossing is the exception in a generally nondegenerate band structure, a systematic analysis of band crossings has already been proposed in 1937 [10, 11]. Zero- and one-dimensional perturbatively stable crossings of energy levels were found on the basis of the Hartree and Fock approximations. Even predating the works on topology, it was noticed that the multiplicity of point-like crossings at a generic position \mathbf{k}_0 in the BZ of an electronic system must be at least four in the presence of time-reversal symmetry (TRS). Time reversal relates a band crossing at \mathbf{k}_0 to $-\mathbf{k}_0$, hence it is surprising that four crossings must occur, instead of just two. At the time the presence of four point crossings could not be explained completely, see Sec. 2.1.3 for more details. Without other symmetries besides translation it has been found that in the vicinity of such point crossings the dispersion fulfills $E_n(\mathbf{k}_0) - E_n(\mathbf{k}_0 + \boldsymbol{\kappa}) \propto |\boldsymbol{\kappa}|$ for small vectors $\boldsymbol{\kappa}$ [10].

Today such point crossings, also referred to as nodal points or point nodes, in condensed matter systems are seen as an emergent realization of the Dirac equation. The Dirac equation for the electron is a partial differential equation with respect to time and space. It was conceived to replace the Schrödinger equation for the electron to obtain a theory that is consistent with Lorentz covariance demanded by special relativity. In its derivation the spinor structure of spin-1/2 fermions, like the electron, is introduced [12]. If one uses a plane-wave basis and chooses appropriate 4D matrices, the equation for the Dirac spinors ψ of a free, massive particle takes the form

$$\begin{pmatrix} \mathbf{k} \cdot \boldsymbol{\sigma} & m\sigma_0 \\ m\sigma_0 & -\mathbf{k} \cdot \boldsymbol{\sigma} \end{pmatrix} \psi = E(\mathbf{k})\psi, \quad (1.1.1)$$

where \mathbf{k} is proportional to the real momentum, $\boldsymbol{\sigma} = (\sigma_x, \sigma_y, \sigma_z)$ denotes the Pauli matrices and σ_0 is the 2×2 identity matrix. The Dirac equation in the form of Eq. 1.1.1 may emerge in the low-energy expansion of a band structure in a solid state system, albeit with a smaller energy scale [13], see Fig. 1.1a.

While the spin of the electron requires a two-component spinor, the Dirac equation uses four components, whereby half of the states correspond to oppositely charged particles [12]. Within the modern interpretation, the additional two components of ψ are considered to describe the antiparticle of the electron, the positron. Yet, before the positron had been measured for the first time [14], Hermann Weyl set the mass to $m = 0$ to study a two-component spinor equation

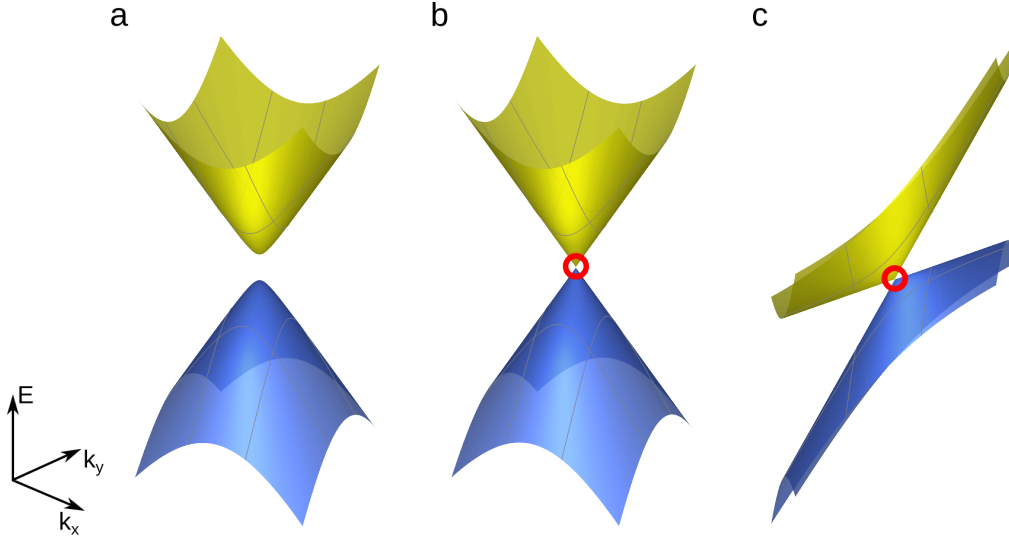


Figure 1.1.: Schematic illustration of the band structure as function of k_x and k_y near a massive type-I Dirac point (a), a type-I Weyl point (b), and a type-II Weyl point (c). Band touching points are marked with a red circle.

without the seemingly superfluous components [15]. No so-called Weyl fermions, obeying this equation, have been found in particle physics, e.g., known fermions like electrons and neutrinos are massive particles [16, 17]. Nevertheless, as we have discussed above, there are linear dispersing band crossings in periodic systems, which bear a surprising similarity to the Weyl fermions [10]. Indeed, like Dirac fermions also the Weyl fermions can be found as the effective low-energy description of condensed matter systems, e.g., pyrochlore iridates were predicted to host point-like crossings obeying the Weyl equation [18]. The low-energy physics near a single Weyl point at \mathbf{k}_0 of a solid state system is described by the Hamiltonian [13]

$$H_{\text{Weyl}} = v_i k_i + (k_i - k_{0i}) A_{ij} \sigma_j, \quad (1.1.2)$$

where $A_{ij} \in \mathbb{R}$ is a system specific constant matrix, the vector v_i encodes the tilt of the band structure, and we use the convention that every repeated index is summed over, with $i, j \in \{x, y, z\}$. Note that the tilt in the energy spectrum for non-zero v_i breaks the Lorentz invariance in the low-energy model Eq. 1.1.2. In other words, the solid-state realization is more diverse than the high-energy proposal. If there exists a direction $\tilde{\mathbf{k}}$ for which the sign of the slope in the dispersion is determined by the term $v_i \tilde{k}_i$, then the Weyl point is considered to be of type-II, see Fig. 1.1c, distinguishing it from the original case, i.e., type-I, see Fig. 1.1b [19, 20]. A type-II Weyl point exhibits extended Fermi surfaces, and thus cannot occur as a semimetal. Yet, from the topological perspective the following discussion of Weyl points applies to both types.

The chirality of a Weyl point is defined by $\nu = \text{sgn}(\det(A))$. For a periodic lattice, as an approximation to the bulk of some system, the Nielsen-Ninomiya theorem states that the number of left-handed fermions equals the number of right-handed fermions [21]. Thus, in the context of a Weyl (semi)metal, for each band the sum of all chiralities vanishes or there must be more gapless manifolds, besides the Weyl points, with an associated chirality. To account for this theorem regarding Weyl fermions on a lattice, we consider a second low-energy model, which incorporates two Weyl fermions, one for each handedness [22]:

$$H_{\text{Weyl}} = \tau_z \boldsymbol{\sigma} \cdot \mathbf{k} + \boldsymbol{\sigma} \cdot \mathbf{b} + \tau_z b_0, \quad (1.1.3)$$

where a second set of Pauli matrices τ_i is introduced to distinguish the valleys around the two Weyl points. The vector \mathbf{b} corresponds to half of the separation in momentum space, and the number b_0 represents half of the energy difference between the two Weyl points. For simplicity Eq. 1.1.3 contains neither tilt nor velocities different from unity. The quantities \mathbf{b} and b_0 will be shown to quantify the electrical response for a Weyl semimetal at half filling. In this work we will refer to a Weyl point as “half-filled”, if the Fermi energy is situated at the band touching point. For the Weyl points in Eqs. 1.1.2 and 1.1.3 this corresponds to a Fermi energy E_F with $E_F = 0$. If both bands of a Weyl point are completely filled, their topological contribution to the electronic response cancels, cf. Sec. 3.4.5.

The above representation of two Weyl points, Eq. 1.1.3, illustrates the connection between Weyl and Dirac points. In the limit of $\mathbf{b} \rightarrow \mathbf{0}$ and $b_0 \rightarrow 0$, these two Weyl points of opposite chirality merge into one fourfold degeneracy, a massless Dirac point. Alternatively, one may obtain Weyl points by starting from a Dirac point in the sense of Eq. 1.1.1, which exhibits away from the crossing twofold degenerate bands that are protected by inversion and time-reversal symmetry, see the discussion of Kramers theorem in Sec. 2.1.2. Time-reversal symmetry is broken in the low-energy model of the Weyl semimetal in Eq. 1.1.3. An inversion symmetry represented by τ_x relates the two Weyl points for $b_0 = 0$. Breaking the TRS to obtain Weyl points from a Dirac point is the basic idea behind our work on the antiperovskite material Eu_3PbO , see Sec. 3.4.

A clarification regarding naming conventions is needed, because both Dirac and Weyl points are used to label gapless crossings in band structures. Here, we refer to Weyl points if a 0D band crossing occurs in odd dimensions and carries a chirality as topological charge. The term Dirac points is used more broadly for the remaining cases of point-like crossings. We use it for fourfold band crossings that can be thought of as two overlapping Weyl points of opposite chirality. Unlike Weyl points, a Dirac point does not need to be gapless, i.e., $m \neq 0$ is possible in Eq. 1.1.1, see Fig. 1.1a. In other words, the common features of all conventional Dirac crossings is a linear dispersion over a reasonable energy range, which in the presence of a gap

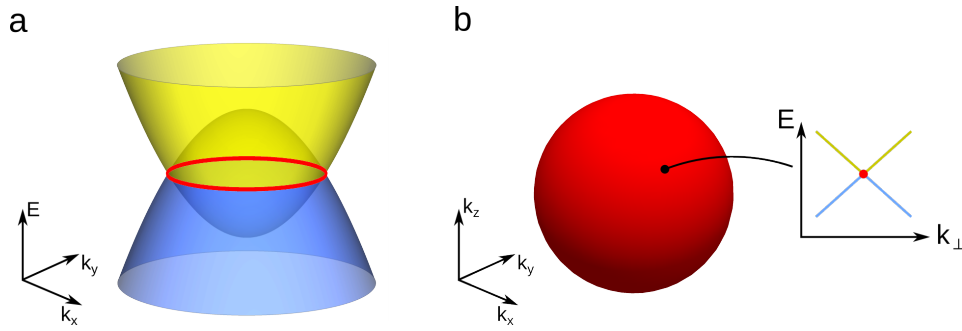


Figure 1.2.: Schematic illustration of a nodal line and a nodal surface. **a** Band structure in the vicinity of a circular nodal line (red) as function of k_x and k_y . **b** Manifold of nodal points of a spherical nodal surface (red) in three-dimensional reciprocal space. The band structure along the direction k_\perp normal to the nodal surface is shown in the inset.

will occur only in some distance to the avoided crossing.

Twofold or fourfold degenerate lines are referred to as Weyl [23, 24] or Dirac nodal lines [25, 26], respectively, see Fig. 1.2a. Such line degeneracies look like Weyl or Dirac points, when restricted to a plane perpendicular to the tangent vector of the line. Their presence generally requires different symmetries and they obey a different topological classification. Without the protecting symmetry a nodal line by itself is unstable. In the context of crystalline systems they can be commonly found in mirror planes or along high-symmetry lines if several symmetries are involved in their protection. Notably, such nodal lines must form closed curves within the BZ.

We have discussed so far 0D nodal points and 1D lines embedded in three dimensions. Furthermore, a 2D nodal feature is also a possible gapless submanifold of 3D k space. Since these band features are unstable [10], crystalline symmetries or topological invariants are indispensable to protect them [27–30]. Regarding the nomenclature, both the terms “nodal surface” or “nodal plane” are used to describe a gapless 2D manifold in the BZ. While the first expression is more general, see Fig. 1.2b, the second term implies that the gap closing occurs on a plane within the BZ. One should note that a system with nodal surfaces or planes cannot be a semimetal, because its density of states does not vanish. The study of nodal surfaces in the context of topological band crossings is a recent and ongoing endeavor. We devote the sections 2.2.3 and 3.3 to nodal planes, where we will also give a more comprehensive discussion of the literature.

1.1.1. Bulk properties of topological semimetals

In this section we will review several features of 3D semimetals. It has been shown that the 0D or 1D nodal manifolds are not just a curiosity, but lead to various effects and signatures in macroscopic quantities [31]. Electrons, since they are fermions, require empty states into which they can be excited by thermal fluctuations or by external perturbations. In this context one must consider the density of states $D(E)$, which for a regular 3D metal with a parabolic band is given by $D(E) \propto \sqrt{E}$ [32]. Away from the band edge this density of states is non-zero and slowly varies with energy. This is different to a semimetal, e.g., with a linear dispersion around a point crossing at $E = 0$, where a brief calculation shows that $D(E) \propto E^2$. This vanishing density of states with a slow increase as function of E leads, at small temperatures, to an insulating behavior, e.g., as it is seen in $\text{Y}_2\text{Ir}_2\text{O}_7$ [18].

To study the conventional resistance in Weyl and Dirac semimetals in more detail, processes of current relaxation must be considered. Besides the scattering at phonons, which diminishes with temperature, in normal metals only impurities remain relevant at low temperatures. For Weyl and Dirac semimetals at half-filling electron and hole currents play an equal role, which can be relaxed by Coulomb scattering, leading to a divergence of the resistivity at low temperatures [13, 33, 34]. For Weyl semimetals the resistance ρ was theoretically determined to be $\rho \propto 1/T$ at low temperatures [34, 35] and has been measured, for example, in Bi-doped $\text{Eu}_2\text{Ir}_2\text{O}_7$ [36]. A similar behavior was found, for example, in the Dirac semimetal Cd_3As_2 , albeit at the lowest probed temperatures the increase of resistivity saturates and even reduces slightly [37, 38].

Note, a nodal manifold is generally, even in the presence of crystalline symmetries, not fixed to the Fermi energy [39]. For a semimetal the Fermi energy needs to be at the nodal crossing, which is only the case for a specific electron count per unit cell. Also a sublattice symmetry, which leads to a symmetric spectrum with respect to $E = 0$, may stabilize the semimetallic phase, cf. Sec. 1.3.2.

Many-body effects correlate with the density of states, thus point crossings are generally stable in the presence of interactions [40], see also Sec. 1.3.5. Especially, a single Weyl point is stable against perturbations that preserve the translation symmetry, which follows from the low-energy description in Eq. 1.1.2. To see this, let us consider a perturbation, which has the form $p_i\sigma_i$. If it is added to the Hamiltonian, one obtains

$$H_{\text{Weyl}} = v_i k_i + (k_i + p_n(A^{-1})_{ni} - k_{0i})A_{ij}\sigma_j, \quad (1.1.4)$$

with the energy eigenvalues $E_{\pm}(\mathbf{k}) = v_i k_i \pm \sqrt{\sum_j (k_i + p_n(A^{-1})_{ni} - k_{0i})^2 A_{ij}^2}$. Hereby, the perturbation p_i does not remove the degeneracy of energy levels, but it changes the position of the

crossing to $\tilde{k}_{0i} = k_{0i} - p_n(A^{-1})_{ni}$. Although something like this had been noticed early on, see Ref. [10], it became only evident with the no-go theorem that Weyl points can only be removed by bringing two of them together [21].

A characteristic bulk phenomenon in particular of Weyl semimetals is the chiral anomaly. This feature has measurable consequences in the quantum limit, for which $\omega_c\tau \gg 1$ holds with the transport scattering life time τ and the cyclotron frequency $\omega_c \propto \frac{1}{m_c}$. The cyclotron mass m_c vanishes if the Fermi energy in a semimetal lies at the band crossing, i.e., the quantum limit is reached even for small magnetic fields [41]. In this limit, an applied magnetic field generates a linearly dispersing zeroth Landau level. With an electric field applied parallel to the magnetic field a charge imbalance between Weyl points of opposite chirality develops. This accumulation of chiral charges is predicted to diffuse through a Weyl semimetal and to induce a voltage difference somewhere else. The charge carriers move away from the original leads through which the charge imbalance has been created, a process referred to as “nonlocal transport” [42]. Quantum anomalies, like the chiral anomaly, will be discussed in more detail in Sec. 1.2.2. In the presence of Landau levels a relaxation process, which counteracts this accumulation of electric charge at Weyl points of a given chirality, can only occur due to scattering between Weyl cones [43]. This suppression of current relaxation leads to a negative longitudinal magnetoresistance. The difference to the case without the external magnetic field is that hereby an electric field would just slightly modify the electron distribution within a Weyl cone, and thus without the anomaly scattering processes exist within each Weyl cone.

We have discussed so far the quantum limit, but it is also possible to obtain the chiral anomaly in the semiclassical limit, i.e., for $\omega_c\tau \ll 1$. Using the Boltzmann kinetic equation one may derive a non-zero charge transport between different Weyl cones [44]. If the energies of two Weyl points relative to the Fermi level are different, then a current occurs even without an external electric field, see our discussion on the chiral magnetic effect in Sec. 1.2.2.

The chiral anomaly depends on the relative orientation of electric and magnetic fields, and thus the conductivity is angular dependent. Nevertheless, for an experimental observation one must consider other causes of angular dependence. An asymmetry of the Weyl points may lead to an angular dependence of the dispersion that occurs in the lowest Landau level [45]. It has been also pointed out that the emergence of Landau levels in the quantum limit suppresses the transport perpendicular to the magnetic field independently of the chiral anomaly [39]. In a magnetic field the current distribution may become inhomogeneous depending on the geometry of the sample and its electric contacts, which may result in current jetting, which also yields a negative longitudinal magnetoresistance [46].

The Berry curvature, see Sec. 1.4.2, exhibits a nontrivial texture in the vicinity of point degeneracies, which leads to an anomalous Hall effect, i.e., a Hall effect that does not require

an external magnetic field [47–49], see Secs. 1.2.2 and 1.4.3. Note that for the anomalous Hall effect TRS must still be broken, like for the regular Hall effect. An anomalous Hall-like current can also be found in nodal-line semimetals [50]. Furthermore, by using that the curvature modifies the semiclassical equations of motion, one finds an anomalous Nernst effect, i.e., a current perpendicular to a temperature gradient [51].

If a Weyl semimetal is subjected to circularly polarized light, a current emerges perpendicular to the direction of the vector of the electric field, because of the photogalvanic effect. For weakly tilted Weyl points also linearly polarized light is sufficient to induce a current [52].

To underscore the variety of effects in topological semimetals, we briefly mention also plasmons, i.e., the quantized excitations of charge-density waves. There are proposals of an unusual damping of plasmons in two dimensional Dirac semimetals [53] and a topological frequency shift that may distinguish hole and electron doping of a Weyl semimetal [54]. Charge carriers of different bands may contribute to the measurable effects [55].

1.1.2. The surface of topological semimetals

So far we have focused on the interior or bulk of semimetallic systems, i.e., effectively infinite systems. As we will discuss in section 1.3.3 there is a close relation between the topological properties of the bulk system, which is well described with periodic boundary conditions, and its surface, where a finite lattice of the same system ends. The effect of topology is in many cases the emergence of quantum mechanical states localized at the surfaces, edges or corners of a finite size system. Topological semimetals are no exception. This can be understood by considering a topological invariant in a subspace of the bulk BZ. In Weyl semimetals open Fermi surfaces, i.e., Fermi arcs, occur in the spectra of finite systems and connect the points in reciprocal space, where the bulk gaps close [18], see Sec. 1.4.4. Hereby, the non-zero Chern number between the Weyl points leads to surface states, which can be measured, for example, by angular resolved photoemission spectroscopy [56]. Such surface states exhibit a chiral dispersion, i.e., all surface states disperse in the same direction [57].

Different surface states can be found between Dirac points, which have been measured, e.g., in graphene [58, 59], by scanning tunneling microscopy [60]. This is related to a non-zero π -Berry phase, see Sec. 1.4.1, which can be found when encircling the Dirac points [47]. Similarly, nodal-line semimetals exhibit a π -Berry phase on a path around the nodal line, and thus surface states within the projection of the nodal line, commonly called drumhead surface states [61–64].

Quantum oscillations can be understood by semiclassical electron orbits that form a closed loop on the Fermi surface. But as Fermi arcs correspond to open Fermi surfaces the expected

orbits have been proposed to travel, at least partially, through the bulk to connect different Fermi arcs, i.e., possibly even opposite surfaces in a slab geometry [65].

To probe the surface of topological semimetals, one may take advantage of the coupling between electric charge and electromagnetic fields that leads to plasmon-polaritons. Inherited from the Fermi arc, the surface plasmon exhibits a chiral dispersion and anisotropic propagation [66]. Whether the collective excitation of electrons may travel through the bulk of a Weyl semimetal or whether it stays as plasmon-polariton at the surface, is predicted to be tunable by mechanical strain [67, 68].

1.1.3. Material realizations

The linear dispersion in the vicinity of a nodal point in the band structure may promise faster electronic devices, and the chiral surface states reduce the dissipation of surface currents [69]. To explore and measure such properties of semimetals, it is necessary to identify new material realizations. Motivated by the possible applications we shall give a brief overview of topological semimetals and their features of interest.

The most renowned realization of 2D massless Dirac points, which corresponds to $m = 0$ and $\mathbf{k} \in \mathbb{R}^2$ in Eq. 1.1.1, is graphene, a single layer of graphite [41, 58, 60, 70]. Weyl points and twofold degenerate nodal lines can be found in other carbon allotropes. These include three dimensional systems that comprise graphene-like sheets that exhibit bonds between the carbon layers, yielding a three dimensional structure [71].

Three dimensional Dirac semimetals have been identified among centrosymmetric, i.e., inversion symmetric, compounds, e.g., Na_3Bi [72] and Cd_3As_2 [37]. The compound ZrSiS is a centrosymmetric semimetal with fourfold nodal lines and exhibits only weak spin-orbit coupling (SOC) [73]. Dirac nodal lines have been proposed to occur in the absence of SOC in fcc Ca, Sr, and Yb. However, in the presence of SOC, which is particularly large in Yb, the nodal lines in these elements are gapped [25]. The compound Ca_3P_2 is an example of a nodal-line semimetal with negligible SOC, with nodal lines in the mirror plane [61]. While in the previous two examples SOC removes the nodal band feature, the converse is predicted to occur for Ta_3SiTe_6 and Nb_3SiTe_6 , where the Dirac points and nodal lines only occur once SOC is taken into account [26]. Hereby, crystalline symmetries and time reversal enforce the existence of nodal features, an approach that we will pursue in Sec. 2 and 3. Dirac crossings are not limited to inorganic systems, for example, the triclinic organic compound $\alpha\text{-(BEDT-TTF)}_2\text{I}_3$ exhibits two massless, tilted Dirac cones [53].

In a Weyl semimetal inversion or time-reversal symmetry must be broken. Among the noncentrosymmetric compounds there are, for example, a family of transition metal compounds

including TaAs, TaP, NbAs, and NbP [46, 56, 74], as well as WTe₂, which has been predicted as a type-II Weyl semimetal [19]. To obtain a large time-reversal symmetry breaking one may consider magnetic compounds. The magnetic pyrochlore iridates A₂Ir₂O₇, with A = Y, Eu, Nd, Sm, or Pr, are semimetals with a non-collinear magnetic order. For Y₂Ir₂O₇ there are 24 symmetry-related Weyl points in the vicinity of the Fermi energy, the same number as in TaAs, TaP, NbAs, and NbP [18, 36, 45, 75]. There is evidence for twofold degenerate nodal lines and their drumhead surface states in TlTaSe₂ [63] and SrAs₃ [64], where a mirror symmetry is necessary to protect the line crossing.

Many more materials have been considered so far, and it is beyond the scope of this work to give a comprehensive discussion of all possible material candidates for topological semimetals, see the reviews Ref. [57], on Weyl and Dirac semimetals, and Ref. [76], on nodal line semimetals, for more examples. To make the various different semimetals and their realizations accessible, we shall look to the underlying symmetries as a unifying principle. In the course of this work, we will show that the existence of band crossings, their number, and their topology are in many cases deducible from the crystalline symmetries.

1.2. Symmetry

Symmetries are a powerful organizing and simplifying principle in physical systems and their mathematical descriptions. The terminology is used broadly, but all symmetries have in common that they restrict the system in question by giving a relation that maps one of its parts to another. Thus, one may make statements about systems, for which only the symmetry is specified. To exemplify the idea, consider an arbitrary real function $f(x)$ fulfilling

$$f(x) = -f(-x). \tag{1.2.1}$$

Such a relation can be considered as a symmetry. One notices not only that the function $f(x < 0)$ is defined by its values $f(x > 0)$ but also that the quantitative statement $f(0) = 0$ follows. In the study of topological semimetals, conclusions of the latter type will not occur as plainly as here, but such exact statements are nevertheless possible.

Symmetries come in many different varieties and types, for example, continuous or discrete, as global or local, as well as external or internal and as unitary or antiunitary symmetries [77]. We will give examples to explain and motivate these distinctions.

Continuous symmetries are characterized by the application of operations that are defined by a continuous variable. Consider the isotropy of space itself as an example for such a symmetry. The associated operations are the rotations in 3D space and depend continuously on their angle

variables. In other words, a symmetry, like “isotropy”, has symmetry operations represented as elements of a group, which correspond to the transformations under which the theory must be invariant for the symmetry to be fulfilled. Other continuous symmetries are the translations in space and time in an empty universe. For a discrete symmetry the variables may only take discrete values but possibly still countably infinite many. A fourfold rotation symmetry, a discrete symmetry, can be found in a square lattice, where the set of symmetry operations corresponds to a group with only four elements. Inversion, time reversal, and the symmetry displayed in Eq. 1.2.1 are discrete symmetries as well.

Global symmetries are represented by operators that do not depend on the spatial coordinate. For example, the global $U(1)$ symmetry of the quantum mechanical wave function is understood as the freedom to multiply any wave function $\tilde{\psi}(\mathbf{r}) = \exp(i\phi)\psi(\mathbf{r})$ with a constant complex phase ϕ without changing its physical content. Local symmetries are represented with spatially dependent operations and play a central role in quantum field theory and the descriptions of gauge bosons. By demanding that the particle field, corresponding to the wave function in the first quantized picture, does not only fulfill the global, but the local $U(1)$ symmetry leads to the introduction of a gauge field. Both fields together fulfill the local symmetry, and the thereby introduced gauge field corresponds to the electromagnetic field.

An external symmetry is a property of the arrangement of objects in space. As would be the case for a screw rotation within a lattice or for the isotropy of empty space. In the context of the present work we refer to external symmetries as “crystalline” symmetries, and assume that the isotropy of space will be always broken by some lattice. An internal symmetry, on the other hand, describes properties of a building block of the theory. On the level of fundamental physics a possible operation for an inner symmetry is the charge conjugation C , which switches a particle with its antiparticle. A corresponding symmetry is found in combination with parity \mathcal{P} , synonymous to spatial inversion, and time reversal \mathcal{T} . Any relativistic quantum field theory exhibits the $C\mathcal{P}\mathcal{T}$ -symmetry, a statement known as the $C\mathcal{P}\mathcal{T}$ -theorem [78].

One may finally distinguish between symmetry operations that are unitary, like spatial operations, and those that are antiunitary, like charge conjugation and time reversal, according to their representation. This distinction is meaningful due the qualitatively different conclusions that can be drawn from either symmetry. For our purpose to identify topological semimetals, the main task is to relate the eigenvalues and eigenstates of the Hamiltonian operator of a time-independent Schrödinger equation. The presence of a unitary symmetry allows us to simplify the Hamiltonian into a block diagonal structure. For antiunitary symmetries this is not possible, but they nevertheless give information about the eigensystem, for example by the Kramers theorem as in Sec. 2.1.2.

In the following section, Sec. 1.2.1, we discuss conservation laws as a consequence of

continuous symmetries, which is the preparation to the field theoretical derivation of the chiral anomaly. Finally we will turn towards discrete symmetries, which will play an important role in the remainder of this work.

1.2.1. Continuous symmetries and conservation laws

To broaden the exposition of symmetries in physics and to introduce the Lagrangian formalism, commonly used to describe various anomalies in semimetallic systems, cf. Sec. 1.2.2, we discuss the Noether theorem [79]. The Noether theorem states in its modern formulation that each continuous symmetry of a classical system implies the existence of a conserved quantity. A quantity is conserved if its total time-derivative vanishes. Such quantities are, for example in classical mechanics, energy, momentum, and angular momentum, which can be traced back to the symmetries of Euclidean space [80]. The corresponding continuous symmetries are described by the transformations represented in the Galilean group, comprising translations in time and space, and rotations. While the conserved quantities are already found in the Newtonian description, the Noether theorem is a constructive approach to determine a conserved quantity from infinitesimal transformations, which leave the Lagrangian invariant.

In the context of semimetals one may first formulate Noethers theorem in the language of Lagrangian densities, a description of classical continuum dynamics. Hereby, conservation laws will be rephrased as continuity equations. For the quantum mechanical description of semimetals the classical Lagrangian can then be quantized within the path integral formulation, which will give rise to deviations from Noethers theorem. These deviations are the quantum anomalies prevalent in topological semimetals, cf. Sec. 1.2.2. Following the notation of Ref. [81] the action functional $S[\phi]$ is denoted as

$$S[\phi] = \int_M d^m x \mathcal{L}(\phi^i, \partial_\mu \phi^i), \quad (1.2.2)$$

where the Lagrangian density \mathcal{L} is integrated over an m -dimensional manifold M described by the coordinates $\{x^\mu\}$ and is itself a function of the fields $\phi^i(x) = \phi^i(\{x^\mu\})$, $i = 1, \dots, n$ and their derivatives. Under the assumption that the fields ϕ^i obey an extremal principle, i.e., the physical fields make the action functional stationary, $DS[\phi] = 0$, one obtains the Euler-Lagrange equations

$$\forall x, i : \partial_\mu \frac{\partial \mathcal{L}}{\partial(\partial_\mu \phi^i)} - \frac{\partial \mathcal{L}}{\partial \phi^i} = 0. \quad (1.2.3)$$

The solution of the above differential equations combined with a set of initial conditions determine the dynamic of the fields ϕ^i . To apply the Noether theorem one needs a symmetry

transformation acting on the coordinates x_μ and the fields ϕ^i by

$$x_\mu \longrightarrow x'_\mu = x_\mu + \left. \frac{\partial x_\mu}{\partial \omega_a} \right|_{\omega=0} \omega_a(x), \quad (1.2.4)$$

$$\phi^i(x) \longrightarrow \phi'^i(x') = \phi^i(x) + \omega_a(x) F_a^i[\phi], \quad (1.2.5)$$

where the parameters $\{\omega_a\}$ parameterize the infinitesimal transformation, while the functionals $\{F_a^i[\phi]\}$ capture the change of the fields. Hereby, a summation over repeated indices is used. The Noether current is defined as

$$j_\mu^a = \left(\frac{\partial \mathcal{L}}{\partial(\partial_\mu \phi^i)} \partial_\nu \phi^i - \mathcal{L} \delta_{\mu\nu} \right) \left. \frac{\partial x_\nu}{\partial \omega_a} \right|_{\omega=0} - \frac{\partial \mathcal{L}}{\partial(\partial_\mu \phi^i)} F_a^i. \quad (1.2.6)$$

Consider a theory with a continuous symmetry, i.e., its action is invariant under the transformation given in Eqs. 1.2.4 and 1.2.5, and the fields fulfill the equation of motion Eq. 1.2.3. The theorem then states that the Noether current is conserved $\partial_\mu j_\mu^a = 0$ or, in other words, the current fulfills a continuity equation. If we take the manifold M to be the $(d + 1)$ -dimensional Euclidean space including a time dimension, an integration of $\partial_\mu j_\mu^a = 0$ over the d spatial dimensions can be simplified with Stokes theorem to $\partial_0 Q^a = 0$ by introducing a conserved charge

$$Q^a = \int d^d x j_0^a, \quad (1.2.7)$$

where it has been assumed that all spatial current components decay towards infinity. Thus, the continuous symmetry leads to conserved quantities Q^a . In the next section we will apply this basic result to the chiral current in a Weyl semimetal and discuss how it is modified in the quantum theory.

1.2.2. Quantum anomalies of topological semimetals

To understand the quantum anomalies of a Weyl semimetal, we discuss its symmetries with the aid of the low-energy model in Eq. 1.1.3. Hereby, we introduce the conservation law of chiral charge, before pointing towards the quantum anomaly that modifies this result. To obtain a unified description we begin this discussion by introducing the path integral quantization of quantum field theory.

One rewrites the partition function \mathcal{Z} , which captures the physics of the system, using resolutions of identity in terms of fermionic coherent states. These coherent states are chosen along a path, which is in the following parameterized by the variable τ , which acts in place of

time in the path integral. It can be expressed as [81]

$$\mathcal{Z} = \int D(\bar{\psi}, \psi) \exp(-S[\bar{\psi}, \psi]), \quad \text{with} \quad (1.2.8)$$

$$S[\bar{\psi}, \psi] = \int_0^\beta d\tau (\bar{\psi} \partial_\tau \psi + H(\bar{\psi}, \psi) - \mu N(\bar{\psi}, \psi)), \quad (1.2.9)$$

where ψ and $\bar{\psi}$ are independent Grassman spinor fields, the chemical potential is given by μ and particle number by $N(\bar{\psi}, \psi)$. In the derivation of Eq. 1.2.8, the factor $\beta = 1/T$, with temperature T , in the quantum partition function $\mathcal{Z} = \text{tr} \exp(-\beta(H - \mu N))$ has been split into intervals, which define a subdivision of the path. In the limit of infinitely small steps this yields the path integral measure $D(\bar{\psi}, \psi) = \lim_{N \rightarrow \infty} \prod_{n=1}^N d(\bar{\psi}^n, \psi^n)$. To respect the anticommutation property of Grassman variables the fields fulfill the boundary condition $\bar{\psi}(0) = -\bar{\psi}(\beta)$ and $\psi(0) = -\psi(\beta)$. For simplicity we use units with $\hbar = c = 1$.

The action $S[\bar{\psi}, \psi]$ defined in Eq. 1.2.8 can be interpreted as the canonical form of the Hamiltonian action [81]. With this in mind one may take the Hamiltonian describing two Weyl points, Eq. 1.1.3, $H_{\text{Weyl}} = \tau_z \boldsymbol{\sigma} \cdot \mathbf{k} + \boldsymbol{\sigma} \cdot \mathbf{b} + \tau_z b_0$ and replace \mathbf{k} by the momentum operator in the position basis to obtain the action [22]

$$S = \int d\tau d^3r \bar{\psi} (\partial_\tau + b_0 \tau_z + \tau_z \boldsymbol{\sigma} \cdot (-i\nabla + \tau_z \mathbf{b})) \psi \quad (1.2.10)$$

at half-filling by setting $\mu = 0$. The chiral symmetry of this action is represented by a transformation of field operators

$$\psi \rightarrow \exp(i\tau_z \omega) \psi \approx (1 + i\omega \tau_z) \psi, \quad \bar{\psi} \rightarrow \exp(-i\tau_z \omega) \bar{\psi} \approx (1 - i\omega \tau_z) \bar{\psi}, \quad (1.2.11)$$

where the second step is the approximation for infinitesimal ω . A Noether current for this chiral symmetry can be defined with Eq. 1.2.6 as

$$j_\mu^{\text{ch}} = -\frac{\partial \mathcal{L}}{\partial(\partial_\mu \psi^j)} i(\tau_z \psi)^j, \quad (1.2.12)$$

$$j_0^{\text{ch}} = -i\bar{\psi} \tau_z \psi, \quad \mathbf{j}^{\text{ch}} = -\bar{\psi} \boldsymbol{\sigma} \psi, \quad (1.2.13)$$

where j_0 corresponds to the τ coordinate, whereas the vector \mathbf{j} represents the spatial component of the current. To bring this Noether current into a more compact form we introduce matrices γ_μ with $\mu \in \{1, 2, 3, 4\}$

$$\gamma_4 = -i\tau_x, \quad \gamma_n = i\tau_y \sigma_n, \quad \text{for } n \in \{1, 2, 3\}, \quad \text{and} \quad \gamma_5 = \tau_z. \quad (1.2.14)$$

The Hamiltonian and γ_5 commute, and thus the eigenstates of the Hamiltonian can be labeled by their γ_5 eigenvalues $\nu = \pm 1$, i.e., the chirality. This quantity will reappear in our discussions

of lattice models for Weyl materials, due to its importance to surface states and electrical response functions. If one defines $\psi^\dagger = \bar{\psi}\tau_x$, the classically conserved chiral particle current, i.e., $\partial_\mu j^{\text{ch},\mu} \stackrel{\text{class.}}{=} 0$, takes the form [82]

$$j_\mu^{\text{ch}} = \psi^\dagger \gamma_\mu \gamma_5 \psi. \quad (1.2.15)$$

With this classical result the significance of the chiral anomaly can be understood, because as stated before the chiral current j_μ^{ch} is not conserved in the quantum theory. This non-conservation can be identified in several ways. In a magnetic field a Weyl point exhibits a linearly dispersing lowest Landau level. Once an electric field is applied more electrons occupy this level, i.e., the number of electrons with one chirality increases, cf. Sec. 1.1.1 [43]. One can also describe the Weyl semimetal as a surface theory of a four-dimensional quantum Hall system [82], which yields the modified continuity equation

$$\partial_\mu j^{\text{ch},\mu} = -\frac{e^3}{2\pi^2} \mathbf{E} \cdot \mathbf{B}. \quad (1.2.16)$$

While the chiral current is not conserved, the regular charge current still is, $\partial_\mu j^\mu = 0$, because Weyl points always occur in pairs of opposite chirality [83]. To convey more insight into the chiral anomaly and its connection to the path integral measure, we consider the current j^μ in the presence of the electromagnetic vector potential. First, we summarize the Fujikawa method, see Ref. [22], using the action in Eq. 1.2.10 modified by a minimal coupling $(\partial_\tau, -i\nabla) \rightarrow (\partial_\tau + ieA_0, -i\nabla + e\mathbf{A})$, where the electromagnetic vector potential $A_\mu = (A_0, \mathbf{A})$ is added. To motivate the gauge field introduced in the minimal coupling, the global U(1) symmetry is extended to a local symmetry, which is similar to the first step of the Fujikawa method, where the transformation in Eq. 1.2.11 is changed to a local operation parametrized by the function $\theta(\mathbf{r}, \tau)$. Unlike for the minimal coupling procedure, one does not demand a local symmetry to introduce a new gauge field, but instead maps the Hamiltonian to a Dirac Hamiltonian with

$$\psi \rightarrow \exp(-i\tau_z \theta(\mathbf{r}, \tau)/2) \psi, \quad \bar{\psi} \rightarrow \bar{\psi} \exp(i\tau_z \theta(\mathbf{r}, \tau)/2), \quad (1.2.17)$$

where one finds that the path integral measure $D(\bar{\psi}, \psi)$ is not invariant under the transformation. After a heat kernel regularization the additional term S_θ appears within the action: [22]

$$S_\theta = \frac{e^2}{4\pi^2} \int d^4x \theta(\mathbf{r}, t) \mathbf{E} \cdot \mathbf{B} = -\frac{e^2}{8\pi^2} \int dt d^3r \partial_\mu \theta \epsilon^{\mu\nu\rho\lambda} A_\nu \partial_\rho A_\lambda. \quad (1.2.18)$$

The first expression in Eq. 1.2.18 contains the characteristic $\mathbf{E} \cdot \mathbf{B}$ term known from the context of axion electrodynamics, an originally purely hypothetical extension to the Maxwell equations [84]. Note that the remaining action has lost in this process the terms including b_0 and \mathbf{b} and taken the anomaly-free Dirac form $S = \int d\tau d^3r \bar{\psi} i\gamma^\mu (\partial_\mu + ieA_\mu) \psi$. For the second

equality in Eq. 1.2.18 the fields are expressed with the electromagnetic vector potential and the time coordinate is Wick rotated to describe real time, which changes the space of the integration from Euclidean to the Minkowski space. In our description the electromagnetic fields are not quantized and thus we can directly obtain the current by a variation with respect to the electromagnetic potential.

$$j_\nu = \frac{e^2}{4\pi^2} \partial_\mu \theta \epsilon^{\mu\nu\rho\lambda} \partial_\rho A_\lambda, \quad (1.2.19)$$

where $\theta = 2\mathbf{b} \cdot \mathbf{r} - 2b_0 t$. The resulting current

$$\mathbf{j} = \frac{e^2}{2\pi^2} \mathbf{b} \times \mathbf{E} + \frac{e^2}{2\pi^2} b_0 \mathbf{B}, \quad (1.2.20)$$

and the density

$$\rho = \frac{e^2}{2\pi^2} \mathbf{b} \cdot \mathbf{B} \quad (1.2.21)$$

describe an anomalous Hall effect and the chiral magnetic effect by their first and second term, respectively [82, 85]. In other words, a Weyl metal exhibits an anomalous Hall effect proportional to the separation \mathbf{b} of the Weyl points in reciprocal space and a chiral magnetic effect proportional to their difference in energy b_0 .

The emergence of a current $\propto b_0 \mathbf{B}$, even in the absence of an electric field, because of the chiral magnetic effect is unusual and deserves more discussion. It has been shown that the ground state of a many-body system comprising electrons described by a kinetic term and subject to a lattice potential as well as electron-electron interactions cannot exhibit a non-zero current expectation value [86]. Accordingly, the chiral magnetic effect does not occur for Weyl fermions regularized on a lattice [85]. Nevertheless, one may understand the chiral magnetic effect as a property of a nonequilibrium system, where a charge imbalance between Weyl nodes, i.e., an effective non-zero b_0 is created by an external current [44, 57].

If the chiral magnetic effect is no equilibrium property, one should also scrutinize the first term in Eq. 1.2.20, which corresponds to the anomalous Hall effect. To find the adequate interpretation for this term, note that an equilibrium current due to the chiral magnetic effect is an artifact, because only the states in the vicinity of the Weyl points up to a momentum cutoff are considered [85]. This cutoff procedure makes the lattice model equivalent to the low-energy description that leads to Eq. 1.2.20. For the anomalous Hall effect no cutoff is needed, because the contribution of the Weyl points is dominated by the Berry curvature in the vicinity of the crossings. The concept of Berry curvature will be introduced in more detail in Sec. 1.4.2. Hence, the low-energy and the lattice description of a Weyl semimetal qualitatively match for the anomalous Hall effect even in equilibrium [85].

As we have seen above, the chiral symmetry of the action is broken by the path integral quantization. The same may also happen for inversion symmetry in 2D theories, leading to the parity anomaly of Dirac nodal line semimetals [50]. After this brief treatise of continuous symmetries, we turn towards the inherent symmetries of crystalline lattices. The ensuing discussion will focus on discrete internal and external symmetries and their relevance to topological semimetals.

1.2.3. Bloch theorem and eigenbases

In the previous section we have considered topological semimetals with a continuous translation symmetry, but for electrons in a periodic crystal this symmetry is broken due to the Coulomb potential of the atoms. Nevertheless, the Hamiltonian operator H retains a discrete translation symmetry $T_{\mathbf{R}}$ for any lattice vector \mathbf{R} . While we have considered infinitesimal symmetry transformations in Secs. 1.2.1 and 1.2.2, we must now consider finite translations and rotations for lattice models. Mathematically, the symmetry is implemented by the vanishing commutation relation, $[H, T_{\mathbf{R}}] = 0$, which enables us to choose a common eigenbasis $\psi(\mathbf{r})$ of H and $T_{\mathbf{R}}$, with

$$H\psi(\mathbf{r}) = E\psi(\mathbf{r}), \quad \text{and} \quad T_{\mathbf{R}}\psi(\mathbf{r}) = c(\mathbf{R})\psi(\mathbf{r}). \quad (1.2.22)$$

Here, the eigenvalue $c(\mathbf{R})$ of the translation can be determined from the group structure of translations and the normalization of states to have the form $c(\mathbf{R}) = \exp(i\mathbf{k} \cdot \mathbf{R})$, where \mathbf{k} is a vector in reciprocal space [32]. Suppose the lattice is subject to periodic boundary conditions, i.e., it holds that $\psi(\mathbf{r}) = \psi(\mathbf{r} + N_{\alpha}\mathbf{R})$ with N_{α} lattice points in the $\alpha \in \{x, y, z\}$ direction. Then, the number of different values of \mathbf{k} is finite and can be given by

$$\mathbf{k} = \sum_{\alpha \in \{x, y, z\}} \frac{n_{\alpha}}{N_{\alpha}} \mathbf{b}_{\alpha} \quad \text{with} \quad \mathbf{b}_{\alpha} \cdot \mathbf{a}_{\beta} = 2\pi\delta_{\alpha\beta}, \quad (1.2.23)$$

where the integer $n_{\alpha} \in \{-\frac{N_{\alpha}}{2}, \dots, \frac{N_{\alpha}}{2}\}$ parametrizes all \mathbf{k} in the first BZ for a given basis of vectors \mathbf{a}_{α} and \mathbf{b}_{α} , which describe the real and reciprocal lattices, respectively. An overview of the BZs corresponding to different lattice symmetries can be found in Refs. [87] and [88]. The action of the translation $T_{\mathbf{R}}$ onto a vector in space is $\mathbf{r} \rightarrow \mathbf{r} + \mathbf{R}$ and thus one obtains that

$$T_{\mathbf{R}}\psi_{\mathbf{k}}(\mathbf{r}) = \psi_{\mathbf{k}}(\mathbf{r} + \mathbf{R}) = e^{i\mathbf{k} \cdot \mathbf{R}}\psi_{\mathbf{k}}(\mathbf{r}), \quad (1.2.24)$$

where we indicate the translation eigenvalue of $\psi_{\mathbf{k}}$ with the subscript \mathbf{k} . The function

$$u_{\mathbf{k}}(\mathbf{r}) = e^{-i\mathbf{k} \cdot \mathbf{r}}\psi_{\mathbf{k}}(\mathbf{r}) \quad (1.2.25)$$

is then invariant under any translation with a lattice vector \mathbf{R} , which is found using the expression of \mathbf{k} given in Eq. 1.2.23. If the definition of $u_{\mathbf{k}}(\mathbf{r})$ is reformulated as

$$\psi_{\mathbf{k}}(\mathbf{r}) = e^{i\mathbf{k}\cdot\mathbf{r}} u_{\mathbf{k}}(\mathbf{r}) \quad (1.2.26)$$

one obtains the Bloch theorem that states that any eigenfunction $\psi_{\mathbf{k}}(\mathbf{r})$ of the Hamiltonian H can be written as the product of an eigenfunction of the translation operator, $e^{i\mathbf{k}\cdot\mathbf{r}}$, and a lattice periodic function $u_{\mathbf{k}}(\mathbf{r})$ that remains to be determined by the Schrödinger equation [32]. In this way one achieves, by choosing a suitable symmetry consistent basis, that the Schrödinger equation does only need to be solved for \mathbf{r} within a single unit cell instead of the full lattice. If the Schrödinger equation is expressed as a matrix eigenvalue problem, the Bloch theorem corresponds to a block diagonalization of the full Hamiltonian.

In the following chapter we will often use the tight-binding approximation, where a basis of localized orbitals $\phi_n(\mathbf{r} - \mathbf{R})$, at the position \mathbf{R} and with quantum number n , is used to express the functions $\psi_{\mathbf{k}}(\mathbf{r})$. The matrix elements of the Hamiltonian H with respect to the basis functions, form a finite dimensional matrix representation $H(\mathbf{k})$ of the Hamiltonian operator. Generally, the localized atomic orbitals, $\phi_n(\mathbf{r} - \mathbf{R}_1)$ and $\phi_n(\mathbf{r} - \mathbf{R}_2)$ at $\mathbf{R}_1 \neq \mathbf{R}_2$, are not orthogonal, which can be remedied by introducing the orthonormal Wannier states $w_n(\mathbf{r} - \mathbf{R})$. Formally, they are defined by the exact solutions $\psi_{n\mathbf{k}}(\mathbf{r})$

$$w_n(\mathbf{r} - \mathbf{R}) = \frac{1}{\sqrt{N}} \sum_{\mathbf{k}} e^{-i\mathbf{k}\cdot\mathbf{R}} \psi_{n\mathbf{k}}(\mathbf{r}). \quad (1.2.27)$$

In practical calculations one may try to use approaches like linear combinations of local atomic orbitals to obtain both orthogonal and localized eigenfunctions [89] or a suitable choice of phase conventions in the Bloch functions such that the Wannier functions become maximally localized [90].

The choice of common eigenstates of translations and the Hamiltonian, splits the problem into independent subspaces defined by the eigenvalue $e^{i\mathbf{k}\cdot\mathbf{R}}$ of the translation symmetry. We will see that choosing a common eigenbasis with the crystalline symmetries does not only simplify the representation, it also implies statements about the presence or absence of band crossings, and gives thereby an indication for the presence of semimetals. Without symmetries (or topology) a band crossing leading to a topological semimetal occurs at a given point in the BZ only with a vanishing probability [10]. To be specific, if we consider the Hamiltonian in a given basis as a finite dimensional matrix, and we choose a common eigenbasis with a symmetry operator, a crossing of bands of different eigenvalues corresponds to bands originating from different subspaces. Due to the block diagonal form no coupling terms between the crossing energy levels may coexist with the given symmetry. To be able to describe other symmetries

than translation, we extend in the next section the use of common eigenbases and introduce some aspects of group theory.

1.2.4. Groups and their representations in solids

In many systems several crystalline symmetries must be considered together. Generally, the consecutive application of two symmetry operations corresponds to a third symmetry, i.e, the symmetries form a group. For periodic lattices there can be symmetries corresponding to 2-, 3-, 4-, and 6-fold rotations, different mirror planes, and inversion, besides the set of all translations that leave the lattice invariant [77]. Taking all possible combinations of a given set of symmetry operations yields a group structure, which includes the inverse operations and the identity e . If all symmetry groups that are in agreement with a suitable lattice of points are considered, one obtains the 32 crystallographic point groups. Hereby, a point group contains only symmetries that have at least one common fixed point. In total there are 14 Bravais lattices, which correspond to the qualitatively different types of 3D lattices. A real crystal is not only a lattice of points, but a regular arrangement of unit cells that may contain more than one atom each. The symmetry groups of such crystals do not only include the crystallographic point groups, but also group elements with symmetries that have no fixed point. If one considers groups that contain all possible symmetries of a crystal, one finds the 230 space groups. Each SG can be labeled for example by its number or its Hermann-Mauguin symbol, e.g., SG 16 with three twofold rotations can be also denoted by $P222$, where P indicates the underlying primitive orthorhombic Bravais lattice, see the references [88,91] for a complete list of SGs. In two dimensions there are only 17 different SGs, also known as wallpaper groups, which are relevant to 2D systems as well as the study of surface states [92].

For many applications it is useful to consider a representation of the symmetry group \mathcal{G} , $D : \mathcal{G} \rightarrow GL(\mathcal{V})$, which is a mapping from \mathcal{G} into the set of matrices, which act on the vector space \mathcal{V} . The representation D respects the group structure, i.e.,

$$D(g_1)D(g_2) = D(g_1 \circ g_2), \quad (1.2.28)$$

where $g_1, g_2 \in \mathcal{G}$ and \circ is the multiplication of group elements. If the function D fulfills the above equation it is a homomorphism, but as we will discuss below there are other types of representations. An intuitive representation is the d dimensional representation in space, using orthogonal matrices $D(g) \in O(d)$, which represent the action on d -dimensional vectors \mathbf{r} . To describe rotations and translations, one may use the Seitz notation $\{D(g), \mathbf{t}_g\}$, where the second entry represents a translation by the vector \mathbf{t}_g [93], see Fig. 1.3 for the example of a twofold screw rotation symmetry. Note that the vector \mathbf{r} , unlike \mathbf{R} , does not need to be a

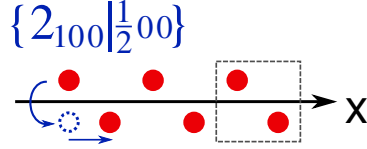


Figure 1.3.: Schematic representation of a twofold screw rotation acting on a chain of atoms (red).

lattice vector. The product of two operations $\{D(g_1), \mathbf{t}_1\}$ and $\{D(g_2), \mathbf{t}_2\}$ can be computed as $\{D(g_1), \mathbf{t}_1\}\{D(g_2), \mathbf{t}_2\} = \{D(g_1)D(g_2), D(g_1)\mathbf{t}_2 + \mathbf{t}_1\}$.

Above, space groups were introduced as the symmetry groups of crystals, which comprise unit cells with one or more atoms. The possible locations of atomic sites within a unit cell are classified by the Wyckoff positions. Each Wyckoff position $\mathbf{r}_{\text{Wyckoff}}$ refers to a set of vectors that is obtained as the intersection between one unit cell and the set $\{D(g)\mathbf{r}_{\text{Wyckoff}} + \mathbf{t}_g \mid g \in \mathcal{G}\}$. In other words, $\mathbf{r}_{\text{Wyckoff}}$ stands in place for all equivalent vectors of the Wyckoff position. Each space group may have several Wyckoff positions, which differ by their number of elements. The number of elements varies because there may be fixed points \mathbf{r} for some $g \in \mathcal{G}$ such that $D(g)\mathbf{r} + \mathbf{t}_g = \mathbf{r} + \mathbf{R}$ holds up to a full lattice translation \mathbf{R} .

As we have discussed in Sec. 1.2.3, making use of the translation symmetry reduces the eigenvalue problem of a lattice with a macroscopic number N_α of unit cells to a single unit cell. Likewise the group of all translations represents an infinite subset of any SG \mathcal{G} . In the following we want to consider how the symmetries are modified by switching to a block $H(\mathbf{k})$ within the full Hamiltonian H . A generic position in the unit cell has generally a lower symmetry, i.e., the position is left invariant by less symmetry operations than a lattice site with the full symmetry of the crystal. The same is true for the reciprocal lattice and thus the symmetry group $\mathcal{G}_{\mathbf{k}}$ of $H(\mathbf{k})$ is generally smaller, i.e., the relevant symmetry group $\mathcal{G}_{\mathbf{k}}$, known as the “little group” depends on the position we choose in reciprocal space. $\mathcal{G}_{\mathbf{k}}$ contains all symmetries $g \in \mathcal{G}$ that fulfill $D(g)\mathbf{k} = \mathbf{k} + \mathbf{K}$ for a reciprocal lattice vector \mathbf{K} . If the Hamiltonian H has the symmetry $g \in \mathcal{G}$ represented by the unitary matrix $U(g)$, then one may conclude from $[U(g), H] = 0$ that the corresponding representation acts on $H(\mathbf{k})$ as

$$U_{\mathbf{k}}^\dagger H(\mathbf{k}) U_{\mathbf{k}} = H(D_U \mathbf{k}), \quad (1.2.29)$$

where $U_{\mathbf{k}}$ is a unitary matrix representing the symmetry for a single unit cell, and the matrix D_U is the action of the symmetry on reciprocal space, which is given by $D_U = \tilde{D}_U^T$ with the action \tilde{D}_U on real space, see Appendix A for a derivation.

To learn more about the representations $U_{\mathbf{k}}$, let us represent translations by their eigenvalues, $\exp(i\mathbf{k} \cdot \mathbf{R})$, as in Eq. 1.2.24, which is suitable as a representation that acts on an eigenstate of

the Hamiltonian $H(\mathbf{k})$. Accordingly, we denote the group of all translations by $\mathcal{T}_{\mathbf{k}}$. The factor group $\mathcal{G}_{\mathbf{k}}/\mathcal{T}_{\mathbf{k}}$ is isomorphic to the group of the remaining symmetries of the Hamiltonian $H(\mathbf{k})$, i.e., its point group including only the rotations and mirror symmetries [77, 92]. If all occurring full translations in the elements of $\mathcal{G}_{\mathbf{k}}$ are expressed by their 1D representation in terms of rotation eigenvalues, the remaining symmetry operations can be represented by a multiplier group that is isomorphic to $\mathcal{G}_{\mathbf{k}}/\mathcal{T}_{\mathbf{k}}$. The multiplier algebra which can be expressed starting from the Seitz notation as

$$\begin{aligned} \{D(g_1), \mathbf{t}_1\}\{D(g_2), \mathbf{t}_2\} &= \{D(g_1)D(g_2), D(g_1)\mathbf{t}_2 + \mathbf{t}_1\} \\ &= \{D(g_1)D(g_2), \mathbf{t}_{12}\}\{D(e), D(g_1)\mathbf{t}_2 + \mathbf{t}_1 - \mathbf{t}_{12}\} \\ &= e^{-i\mathbf{k}\cdot(D(g_1)\mathbf{t}_2 + \mathbf{t}_1 - \mathbf{t}_{12})}\{D(g_1)D(g_2), \mathbf{t}_{12}\}, \end{aligned} \quad (1.2.30)$$

where $D(e)$ is the representation of the neutral element and \mathbf{t}_{12} is chosen as a vector within the unit cell, i.e., shorter than any of the basis vectors, such that the expression $D(g_1)\mathbf{t}_2 + \mathbf{t}_1 - \mathbf{t}_{12}$ is a real space lattice vector [92]. Suppose each energy band of the Hamiltonian $H(\mathbf{k})$ is labeled according to the representation of $\mathcal{G}_{\mathbf{k}}$. The energies and states at any \mathbf{k}' that is in the vicinity of \mathbf{k} are similar to the energies and states of the latter, likewise are the corresponding representations at \mathbf{k} and \mathbf{k}' connected by compatibility relations.

Note that the multiplier group representation in Eq. 1.2.30 is not a group in the conventional sense, because the set is not closed under multiplication because the translation $D(g_1)\mathbf{t}_2 + \mathbf{t}_1$ can be equal or larger than a real space lattice vector. If the little group $\mathcal{G}_{\mathbf{k}}$ is isomorphic to $\mathcal{G}_{\mathbf{k}}/\mathcal{T}_{\mathbf{k}}$ for all \mathbf{k} , the SG \mathcal{G} is called symmorphic, or if not nonsymmorphic. A symmetry element can also be called nonsymmorphic if it does not leave any point of space invariant, whereas symmorphic symmetries have at least one fixed point. The presence of a nonsymmorphic symmetry operation implies that a SG is nonsymmorphic, but the converse is not true. There are two counterexamples, i.e., SGs 24 and 199, which are nonsymmorphic body-centered SGs although none of their symmetries are nonsymmorphic by themselves [94, 95]. As we will discuss later, see Sec. 2.1.3, Weyl points may only exist at a point \mathbf{k}_{Weyl} if the little group $\mathcal{G}_{\mathbf{k}_{\text{Weyl}}}$ does not contain mirror or inversion symmetry. A group that only contains rotations is called a Sohncke space group. But since it is only the little group that must lack mirror or inversion symmetry to host a Weyl point and not the full space group, we use instead the term ‘‘chiral’’ group for such a $\mathcal{G}_{\mathbf{k}_{\text{Weyl}}}$. Hereby, we understand ‘‘chiral’’ as the absence of mirror and inversion symmetry at \mathbf{k}_{Weyl} . One should note that in the context of chemistry chiral groups already have a different meaning, where they denote groups with screw rotations of definite handedness [96].

We can now find representations for any space group element obeying the multiplier algebra of Eq. 1.2.30. What we have done corresponds to a basis choice for the Hamiltonian that

yields the translations in their irreducible representation, i.e., the 1D representation as the factors $\exp(i\mathbf{k} \cdot \mathbf{R})$ [77]. If $H(\mathbf{k})$ is a matrix of size larger than one, due to the presence of different sites or orbitals within a unit cell, we can use the symmetries of $\mathcal{G}_{\mathbf{k}}$ to further simplify the Hamiltonian by choosing a basis where the $U_{\mathbf{k}}$ in Eq. 1.2.29 are a sum of irreducible representations. Such irreducible representations of the little groups have been tabulated [88,97]. We proceed with a general analysis without specifying the considered crystal.

In real crystals the electrons contribute a spin degree of freedom to the Hamiltonian. Without SOC there is an internal, continuous $SU(2)$ symmetry corresponding to arbitrary rotations of spin. As we must generally expect a non-vanishing coupling between different spin orientations, we consider in the following how the point group symmetries act on a spin-1/2. A rotation $C_{\phi}^{\mathbf{v}}$ by an angle ϕ around an axis, which is indicated by the unit vector \mathbf{v} , rotates the spin by $\frac{\phi}{2}$ in spinor space. This can be represented by

$$D(C_{\phi}^{\mathbf{v}}) = e^{+i\frac{\phi}{2}\mathbf{v}\cdot\boldsymbol{\sigma}} = \cos\left(\frac{\phi}{2}\right)\sigma_0 + i\mathbf{v} \cdot \boldsymbol{\sigma} \sin\left(\frac{\phi}{2}\right), \quad (1.2.31)$$

where the Pauli matrices σ_i act on a two component spinor. For mirror symmetries the invariance of the expectation value of spin can be used to motivate their spin representation, $D(M) \propto \mathbf{m} \cdot \boldsymbol{\sigma}$, where \mathbf{m} denotes the normal vector of the mirror plane and the proportionality is up to a phase factor. We choose the proportionality constant to be i , such that the inversion operation expressed as the product $D(M^x)D(M^y)D(M^z) = 1$ it is trivial in spin space, fulfilling the axial vector property of spin. So far we have given specific representations, for the action of symmetries on spin. On more abstract grounds, one may introduce double groups by adding the element \bar{E} that commutes with all group elements and is understood as a rotation by 2π . Here, the 2π rotation is represented by $D(\bar{E}) = D(C_{2\pi}^{\mathbf{v}}) = -\sigma_0$.

To highlight that the considered symmetries act both in space and inner degrees of freedom, we introduce the following notation. We denote a rotation C around the rotation axis given by α and that is combined with a translation by (x, y, z) as

$$C_n^{\alpha}(x, y, z) = U_{\mathbf{k}}(C) \otimes D(C_{\frac{2\pi}{n}}^{\alpha}), \quad (1.2.32)$$

and for a mirror symmetry M with a normal vector α and simultaneous translation by (x, y, z) we write

$$M^{\alpha}(x, y, z) = U_{\mathbf{k}}(M) \otimes D(M^{\alpha}), \quad (1.2.33)$$

where $U_{\mathbf{k}}$ describes the action on orbitals within a unit cell and is also responsible for reproducing the exponentials of the multiplier group, see Eq. 1.2.30, due to the spatial action of $\{\tilde{D}_U, (x, y, z)^T\}$. Since one needs the action on real space to use Eq. 1.2.29, we use \tilde{D}_U as the

rotational part of a rotation $C_n^\alpha(x, y, z)$ or a mirror symmetry $M^\alpha(x, y, z)$. If we are discussing specifically a screw or glide rotation symmetry, we use $\tilde{C}_n^\alpha(x, y, z)$ or $\tilde{M}^\alpha(x, y, z)$ in place of $C_n^\alpha(x, y, z)$ or $M^\alpha(x, y, z)$, respectively. As will be discussed in Sec. 2.2.1, we will avoid to define a specific $U_{\mathbf{k}}(C)$ but instead use that the n th power of $C_n^\alpha(x, y, z)^n$ is proportional to a representation of the identity element of the little group $\mathcal{G}_{\mathbf{k}}$, which holds analogously for the second power of $U_{\mathbf{k}}(M)$. If there is a set of mutually commuting operators, we can choose a common eigenbasis and refer to the bands with their symmetry labels. In the course of this work we will make use of up to three mutually commuting symmetries at once, in addition to translations. Elements of the little group that are not part of the chosen set of mutually commuting operators will then relate the eigenvalues, which implies identical energies for the corresponding eigenstates, and may thus lead to an increased degeneracy. In other words, there cannot be matrix elements that couple bands of different symmetry eigenvalues in a symmetric Hamiltonian. The resulting degenerate eigenstates correspond then to a subset or even all of the possible irreducible representations of $\mathcal{G}_{\mathbf{k}}$.

So far we have discussed only unitary symmetries. However, there are antiunitary symmetries, for example, time-reversal \mathcal{T} , which acts on the Hamiltonian $H(\mathbf{k})$ as

$$U_{\mathcal{T}}^{-1} H^*(\mathbf{k}) U_{\mathcal{T}} = H(-\mathbf{k}), \quad (1.2.34)$$

where $U_{\mathcal{T}}$ is a unitary matrix, which can be represented by $U_{\mathcal{T}} = i\sigma_y$ acting on the spin degree of freedom. Kramers theorem, see Sec. 2.1.2, gives a condition for when TRS pairs states to each other, which can be understood as an increased dimension of the irreducible representation of the little group $\mathcal{G}_{\mathbf{k}}$. To determine when a group representation is enlarged due to time-reversal, one may consult the Herring criterion [88, 92, 98]. Depending on the characters of the squares of each group element, i.e., the traces of the corresponding matrices, the considered representations can be distinguished into real, complex, and pseudo-real representations. A pseudoreal representation D is equivalent to the representation D^* , where all elements are complex conjugated, and D contains complex entries. The addition of TRS pairs complex and pseudoreal representations, and thus doubles an irreducible representation, and thus leads to a degeneracy of bands. Note that due to the action of TRS on reciprocal space, i.e., $\mathbf{k} \rightarrow -\mathbf{k}$, the little group $\mathcal{G}_{\mathbf{k}}$ has to be considered for a time-reversal invariant momentum (TRIM).

If a magnetic field is applied or a spontaneous magnetization emerges, the symmetry is reduced, but generally not to a unitary subgroup, because the symmetries can also occur in combinations with time reversal. The (double-valued) space group co-representations capture the resulting magnetic space groups [88, 99]. There are two naming conventions OG (Opechowski-Guccione) and BNS (Belov-Neronova-Smirnova) that describe the SGs by the basis adjusted to the magnetic order and the original basis of the parent compound,

respectively [88, 100]. Overall the magnetic space groups can be classified into 230 Shubnikov groups, i.e., the SGs that do not contain TRS, 230 gray groups, which contain time reversal \mathcal{T} as a independent group element, and 1191 “black and white groups” adding up to a total of 1651 possible SGs to describe 3D materials [101]. Black and white groups \mathcal{G}_{BW} can be constructed from a subgroup \mathcal{F} of a space group \mathcal{G} by $\mathcal{G}_{\text{BW}} = \mathcal{F} + (\mathcal{G} - \mathcal{F})\mathcal{T}$. This construction can be understood by considering a crystal comprising black and white sites, which are only related to each other by symmetry operations that include \mathcal{T} , hence the name black and white groups.

Using the discussed concepts of group theory, it is possible to deduce the existence of enforced band crossings, which in some cases may be movable, for example, along a rotation axis, but cannot be removed [102]. The dimension of irreducible representations at high-symmetry points implies such band crossings [103, 104]. It has also been shown that topological band crossings can be enforced by considering compatibility relations between the representations on different rotation axis as well as the overall order of representations [105].

1.3. Topological phases

Topology studies the shape of mathematical objects, but unlike geometry all properties are considered only up to arbitrary continuous deformations [106]. A continuous deformation is called a homeomorphism if itself and its inverse are continuous. If there is a homeomorphism between two topological spaces, they are homeomorphic to each other. For example, any compact simply connected 3D manifold without a boundary is homeomorphic to a 3-sphere, a result, which is known as the Poincaré conjecture [107]. For our purposes the object of study is the space of all Hamiltonians and in the presence of symmetries each Hamiltonian can be assigned to one of several distinct topological phases, which are quantified by topological invariants. We will begin our discussion by a brief introduction to the concept of homotopy, its application to Hamiltonians leading to the Altland-Zirnbauer-classification, and the implications for the surfaces of topological materials. We conclude our introduction to topology with an overview beyond the paradigm of topological insulators and superconductors.

1.3.1. Homotopy

Suppose we have two closed paths in some topological space X , e.g., \mathbb{R}^2 , that are given by the functions $\alpha, \beta : I \rightarrow X$ with the interval $I = [0, 1]$. The paths α and β are homotopic if there is

a homotopy, i.e., a continuous map $F : I \times I \rightarrow X$ with [106]

$$F(s, 0) = \alpha(s), \quad F(s, 1) = \beta(s), \quad (1.3.1)$$

where $s \in [0, 1]$ is arbitrary. The mapping F can be used as an equivalence relation between all possible paths, α and β , and thus leads to equivalence classes that form the first homotopy group $\pi_1(X, x_0)$, where x_0 is one reference point that is shared among all paths, which can be omitted if X is arcwise connected. Elements of the homotopy group can be combined by connecting their starting and endpoints at $s = 0$ and $s = 1$, respectively, and rescaling the argument of the combined path. Higher homotopy groups π_n can be defined by replacing the interval I with the cube $I = [0, 1]^n$.

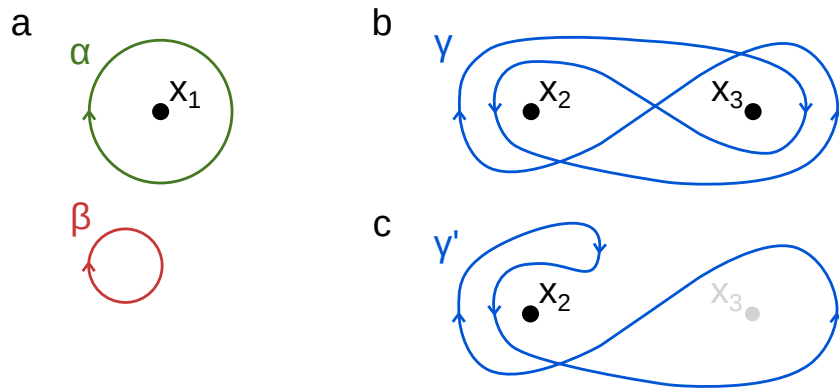


Figure 1.4.: Closed paths illustrating nontrivial homotopy groups. The points x_1, x_2, x_3 that are excluded from the plane \mathbb{R}^2 are given by black dots. **a** While the path α (green) encircles the point x_1 , the path β (red) does not. The paths α and β are not homotopic to each other. **b** Two points, x_2, x_3 are excluded from the plane. The path γ (blue) encircles both points twice and in opposite directions, but cannot be contracted. **c** The point x_3 is added to the plane and the path γ can be contracted to a point. This is indicated by γ' , which is a path homotopic to γ only if the paths can cross x_3 .

To illustrate a nontrivial first homotopy group, let us consider a 2D plane where the point x_1 is removed, $X = \mathbb{R}^2 \setminus \{x_1\}$, see Fig. 1.4a. The two closed paths α and β are inequivalent, i.e., they belong to different elements of the homotopy group $\pi_1(\mathbb{R}^2 \setminus \{x_1\})$, since only α encircles the point x_1 and a homotopy F cannot cross x_1 , as long as x_1 is excluded from the codomain of α . One may consider the deformation retract of $\mathbb{R}^2 \setminus \{x_1\}$, which is the circle S^1 around x_1 . For both, $\mathbb{R}^2 \setminus \{x_1\}$ and S^1 , the homotopy groups are isomorphic, denoted by \cong , and yield $\pi_1(\mathbb{R}^2 \setminus \{x_1\}) \cong \pi_1(S^1) \cong \mathbb{Z}$ [106]. In other words, closed paths can be distinguished by the number of times they encircle the point x_1 .

As a final example, let us consider the path γ shown in Fig. 1.4b, where two points x_2 and x_3 have been removed from the plane, $\mathbb{R}^2 \setminus \{x_2, x_3\}$, which is noteworthy due to its practical relevance, see Ref. [108]. While the path in Fig. 1.4b cannot be contracted to a constant path, i.e., a point, the same line can be contracted in Fig. 1.4c, where the point x_3 has been added to the set of destination. The reason for this is that the path γ encircles both x_2 and x_3 twice and each time in both directions, such that the total winding number adds up to zero. Note that the homotopy group $\pi_1(\mathbb{R}^2 \setminus \{x_2, x_3\})$ is non-Abelian, and thus different sequences in which x_2 and x_3 are encircled are generally not homotopic to each other even if they have the same total winding. Once one of the points x_2 or x_3 is added to the plane, the path γ and equivalently γ' become homotopic to the trivial path, see Fig. 1.4c.

1.3.2. Topological systems and the Altland-Zirnbauer classification

In the following we summarize the classification of gapped and gapless phases in terms of strong topology [109]. Hereby, weak topology refers to the presence of the strong topology, as described below, in a subset of the full system. The classification of topological insulators and superconductors depends on the presence or absence as well as the form of the three symmetries, time reversal \mathcal{T} , particle-hole symmetry \mathcal{C} , and their combination $\mathcal{S} = \mathcal{T}\mathcal{C}$, which is called chiral or sublattice symmetry. We have already encountered the time reversal \mathcal{T} in Sec. 1.2.4. Particle-hole symmetry is an intrinsic property of superconductors described by mean-field Hamiltonians expressed with Nambu spinors. Both symmetries, \mathcal{T} and \mathcal{C} , contain a complex conjugation, which imposes to some extent a reality constraint on the Hamiltonian, for example, for spinless particles with TRS, i.e., $\mathcal{T}^2 = +1$, one may choose real eigenstates [110]. Accordingly, the ten Altland-Zirnbauer symmetry classes are split into two complex classes and eight real classes, see Table 1.1 [111]. The symmetries are formally defined by

$$\mathcal{T}^{-1}H\mathcal{T} = H, \quad \mathcal{T} = U_{\mathcal{T}}K, \quad \mathcal{T}^2 = \pm 1, \quad (1.3.2)$$

$$\mathcal{C}^{-1}H\mathcal{C} = -H, \quad \mathcal{C} = U_{\mathcal{C}}K, \quad \mathcal{C}^2 = \pm 1, \quad (1.3.3)$$

$$\mathcal{S}^{-1}H\mathcal{S} = -H, \quad \mathcal{S} = U_{\mathcal{S}}, \quad \mathcal{S}^2 = 1, \quad (1.3.4)$$

where the signs in front of the identity operators, ± 1 , distinguish different types of time-reversal and particle-hole symmetries.

To classify the Hamiltonians depending on these three symmetries one may use homotopy groups [109, 112, 113]. Instead of paths in a plane, we now consider the Hamiltonian, as a mapping from the d -dimensional BZ to an N -dimensional Hilbert space. If we are considering gapped phases, one may consider the analog to the deformation retract for the target space $\mathbb{R} \setminus x_1$, which we considered in Sec. 1.3.1, and flatten the bands into two degenerate energy levels, one

above and one below the gap. The whole topology is then captured by the eigenstates of this new Hamiltonian. Note that for topological semimetals, i.e., gapless phases, the band crossings can be enclosed by a manifold, on which the bands are gapped, where then one may apply the classification of gapped topological phases.

It turns out that homotopy groups of flattened Hamiltonians are not sufficient, because it is possible that the addition of trivial bands changes the outcome [113]. The goal is thus to obtain a “stable equivalence”, where the addition of symmetry allowed terms does not change which Hamiltonians are equivalent. One may describe a Hamiltonian of the required symmetries by a Dirac model, see Eq. 1.1.1, and the addition of extra terms can then be described by extensions of Clifford algebras [109]. A complex Clifford algebra Cl_d is generated by a set of d mutually anticommuting matrices that square to $+1$. The generators of Cl_d can be used to form a gapless Dirac Hamiltonian in d dimensions, which can become gapped by adding a mass term using Cl_{d+1} . The set of possible mass terms forms a classifying space C_d and its connectivity, i.e., the 0th homotopy group $\pi_0(C_d)$, determines how many different mass terms and thus different topological phases exist. So far we did not use any symmetry, the result thus corresponds to the classification of class A in Table 1.1. The classifying spaces are restricted by the symmetries and yield various topological phases, whereby each entry of Table 1.1 corresponds to the different topological invariants, e.g., the entry \mathbb{Z} denotes that there can be topological phases that are distinguished by an invariant $\nu \in \mathbb{Z}$. The classifying spaces of complex Altland-Zirnbauer classes exhibit a so-called Bott periodicity of two, $C_d = C_{d+2}$, whereas for the classifying spaces \mathcal{R} of real classes have a eightfold periodicity $\mathcal{R}_d = \mathcal{R}_{d+8}$ [109]. The dimension can be generalized to $\delta = d - D$, which includes the spatial dimension d and the codimension $D + 1$ of a defect, with $D = 0$ for a gapped phase without defects [109]. Topological defects refer to discontinuities in a spatially varying system parameter, whereby the system is considered in a sufficient distance such that the bulk energy gap is not compromised by the defect. Such defects may occur due to dislocations in crystals or superconducting vortices around magnetic flux lines in superconductors. The dimension δ is used in Table 1.1 together with the symmetries, as discussed before, to identify the relevant topological classification [109].

In the present work we are less interested in topological insulators and superconductors but rather topological semimetals [109]. The classification presented in Table 1.1 can be applied to gapless systems by considering gapped subsystems of dimension d_{FS} that enclose the Fermi surface of the nodal point, line, or surface. One then defines the codimension $p = d - d_{\text{FS}}$ for a d dimensional semimetal. Furthermore, two types of semimetals must be distinguished. One denotes Fermi surfaces with “FS1” if they are mapped into themselves under the inversion of \mathbf{k} due to time-reversal symmetry \mathcal{T} or particle-hole symmetry C , e.g., a point crossing at a TRIM. The second type, “FS2”, is not left invariant and crossings at different points in the BZ are

mapped to each other. This distinction between “FS1” and “FS2” is denoted in Table 1.1 and leads to a shift relative to the dimension δ for topological insulators.

For example, class A without any symmetries in two dimensions, $\delta = 2$, corresponds to the Chern insulators, which are characterized by the value of their first Chern number, see Sec. 1.4.2 [114–117]. A Weyl semimetal, i.e., $d = 3$ with broken inversion but time-reversal symmetry belongs to class AII. Its point-like Fermi surfaces lead to the codimension $p = 3 - 0 = 3$. If we consider Weyl points that are away from the TRIMs, the Fermi surface is of the type “FS2” and one finds the symmetry class $\mathbb{Z}_2^{a,b}$ in Table 1.1, which does not protect the Fermi surfaces, i.e., the Weyl points. The superscript a indicates that in this case also the entry in class A must be consulted, which indicates a \mathbb{Z} invariant. This is the Chern number we expect from the previous discussions in the context of the Nielsen-Ninomiya theorem [83].

In the presence of crystalline symmetries the classification is modified and topological crystalline phases appear [61, 118]. For inversion symmetric systems it is possible to calculate \mathbb{Z}_2 invariants using the Wilson loop [119], see Sec. 1.4.1, or inversion eigenvalues [120]. So far we have given some insights into the topological classification, but a comprehensive discussion of topological insulators and superconductors is beyond the scope of this work, thus we refer to the following books and reviews [109, 121–123].

Class	\mathcal{T}	\mathcal{C}	\mathcal{S}	FS1 $p =$	7	8	1	2	3	4	5	6
				FS2 $p =$	1	2	3	4	5	6	7	8
				δ	0	1	2	3	4	5	6	7
A	0	0	0		\mathbb{Z}	0	\mathbb{Z}	0	\mathbb{Z}	0	\mathbb{Z}	0
AIII	0	0	1		0	\mathbb{Z}	0	\mathbb{Z}	0	\mathbb{Z}	0	\mathbb{Z}
AI	+	0	0		\mathbb{Z}	0	0^a	0	$2\mathbb{Z}$	0	$\mathbb{Z}_2^{a,b}$	\mathbb{Z}_2^b
BDI	+	+	1		\mathbb{Z}_2^b	\mathbb{Z}	0	0^a	0	$2\mathbb{Z}$	0	$\mathbb{Z}_2^{a,b}$
D	0	+	0		$\mathbb{Z}_2^{a,b}$	\mathbb{Z}_2^b	\mathbb{Z}	0	0^a	0	$2\mathbb{Z}$	0
DIII	-	+	1		0	$\mathbb{Z}_2^{a,b}$	\mathbb{Z}_2^b	\mathbb{Z}	0	0^a	0	$2\mathbb{Z}$
AII	-	0	0		$2\mathbb{Z}$	0	$\mathbb{Z}_2^{a,b}$	\mathbb{Z}_2^b	\mathbb{Z}	0	0^a	0
CII	-	-	1		0	$2\mathbb{Z}$	0	$\mathbb{Z}_2^{a,b}$	\mathbb{Z}_2^b	\mathbb{Z}	0	0^a
C	0	-	0		0^a	0	$2\mathbb{Z}$	0	$\mathbb{Z}_2^{a,b}$	\mathbb{Z}_2^b	\mathbb{Z}	0
CI	+	-	1		0	0^a	0	$2\mathbb{Z}$	0	$\mathbb{Z}_2^{a,b}$	\mathbb{Z}_2^b	\mathbb{Z}

Table 1.1.: Symmetry classes and the corresponding topological phases of semimetals, as well as insulators and superconductors with and without defects [109]. The first column denotes the label of the symmetry class, which is defined by the entries in the columns \mathcal{T} , \mathcal{C} , and \mathcal{S} . If a symmetry is present the sign of its square is indicated in the corresponding column, whereas chiral symmetry \mathcal{S} squares either to 1 or is absent, which is denoted by 0. δ and p denote the dimension and the codimension of the defect, respectively, for a considered system. The types of the topological invariants are denoted by \mathbb{Z}_2 , $2\mathbb{Z}$, \mathbb{Z} , and 0, where 0 means that there is only one (topologically trivial) phase. The superscript “a” denotes that a gapless phase can be protected also by class A or AIII, whereas the superscript “b” denotes that the Fermi surface of a gapless phase is not protected by the topological invariant \mathbb{Z}_2 .

1.3.3. Bulk-boundary correspondence

If one can describe a solid state system with a basis of sufficiently localized states, which in turn are only connected by finite range hopping terms, then one would expect that the eigenstates and energies of a system with periodic boundary conditions are reasonably close to the states corresponding to the interior of a finite system. This is the bulk-boundary correspondence in the sense that the existence of a boundary only leads to local modifications of a system. We will discuss in Sec. 5.3 that this property should not be taken for granted, at least in the context of non-Hermitian systems, even if all hopping terms are short-ranged.

The bulk-boundary correspondence is a central aspect of topology in condensed matter systems, because the topology identified for the bulk, e.g., according to Table 1.1, is tied to a symmetry protected gap. If a boundary to the vacuum is introduced to a topological system, the topology must change somewhere between the interior of the system and the vacuum that is by definition trivial. Since the energy gap of a topological insulator or superconductor has to close at the boundary to change the topology, there must be a gapless state localized at the surface.

Depending on the type of bulk topology and the dimension of surface states, different surface states emerge [109]. For example, a Chern insulator, class A with $\delta = 2$, exhibits chiral surface states, which means that the group velocity, i.e., the derivative of the dispersion for the surface bands, has only one definite sign on each termination. With time-reversal symmetry, e.g., class AII with $\delta = 3$, the surface states form Dirac cones at the TRIMs of the surface BZ, i.e., the BZ of the finite system [120]. Later we will give a more explicit example of the Fermi arcs, which exist due to the bulk-boundary correspondence in Weyl semimetals, see Sec. 1.4.4.

There are more rigorous approaches to relate the bulk topology to the emergence of topological surface states [120, 124, 125]. It has been shown that the ten Altland-Zirnbauer classes lead to the emergence of surface states by using a Green's function based representation of topological invariants, and its application to continuum models [124]. Different approaches, which are consistent with a lattice description, consider the electric polarization of the bulk states [126], or the time-reversal polarization for topological insulators [120]. Hereby, a change of polarization along a path on the surface has been related to a change in the number of the occupied states, which for a uniform chemical potential is only possible if a band crosses the energies of the bulk band gap. In other words, in this case a surface state occurs. An exact derivation is available, for example, for 2D topological insulators with time-reversal symmetry, where the number of surface states traversing the bulk gap is shown to coincide with the topological index of the bulk system [125].

A system with a well-defined atomic limit exhibits Anderson localization if disorder with a sufficient strength is introduced to the system. The surface states of topological insulators and

superconductors do not exhibit Anderson localization for symmetry preserving disorder and thus can exist only on the boundary of a topological bulk system [109]. The idea to consider topological systems as those without an atomic limit will be discussed later in the context of the study of elementary band representations and fragile topology, see Sec. 1.3.5.

1.3.4. Phases with and without topology

A phase of matter refers to a region in space defined by a homogeneous, characteristic property, an order parameter, like the density which distinguishes gaseous and liquid phases, or the vector of magnetization for the transition from paramagnetism to ferromagnetism [81]. For conventional phase transitions there is a local order parameter, which changes its value during the transition. An n th order transition is defined by a discontinuity in the n th derivative of the free energy, where in the case of $n \geq 2$ the phase transition is continuous.

For example, the transition from a paramagnetic into a ferromagnetic phase is a second order transition if the temperature is lowered in the absence of an external magnetic field. At the phase boundary to the magnetic order the magnetic susceptibility, i.e., the 2nd derivative of the free energy with respect to the external magnetic field, diverges and thus also the correlation length. Let us suppose we have a magnetic phase transition between two phases with the same arrangement of atoms. The magnetic space group \mathcal{G} of the ordered system is then a subgroup of the paramagnetic space group \mathcal{G}_0 , while the order parameter, the vector $\boldsymbol{\eta}$, belongs to the unit representation $D(g)$ with $D(g)\boldsymbol{\eta} = \boldsymbol{\eta}$ with $g \in \mathcal{G}$ [127]. We will discuss the implications of spatial symmetries on the electronic band structure for magnetic phases for two examples, see Secs. 3.4 and 3.5.

For topological phase transitions the order parameter remains mostly unknown. Note that the topological classification, as summarized in Sec. 1.3.2, uses the full Hamiltonian and thus a local order parameter, analogously to the magnetization for a conventional phase, is generally insufficient to describe a topological phase [109]. Nevertheless, one may define a quasi-local Chern marker that distinguishes the topological phases in real space and adds up to the regular Chern number for class A in two dimensions once it is integrated over the system, see Table 1.1 [128, 129].

In a renormalization scheme a diverging length scale is found close to the phase transition between a topologically trivial and a nontrivial topological insulator [130]. Instead of a susceptibility it is a curvature function, e.g., the Berry curvature, that diverges, while still preserving the quantization of the topological invariant.

1.3.5. Other facets of condensed matter topology

In this section we will briefly discuss some approaches to topology, which go beyond and are complementary to the tenfold way that we discussed in the previous sections.

Offside the tenfold way

The concept of higher-order topology generalizes the topological insulators, as discussed so far [131–134]. Hereby, it is not the surface but instead the boundary of the surface, which exhibits a nontrivial surface state. We will give a more detailed discussion in Sec. 4, where we also introduce a semimetallic counterpart to insulators with higher-order topology.

The classification in terms of the ten symmetry classes listed in Table 1.1 groups Hamiltonians into distinct sets, but makes a priori no statement in which systems a nontrivial invariant must occur. The study of irreducible representations of crystalline symmetries, cf. Sec. 1.2.4, reveals that due to the compatibility relations band crossings must occur. These may be moved within the BZ but not removed. Furthermore, by starting from localized Wannier orbitals, so-called “elementary band representations” can be calculated, which comprise energy bands as well as Bloch functions. A band representation is “elementary” if it corresponds to the smallest set of bands that are derived from a given atomic limit [102, 135, 136]. In some cases the number of necessarily connected bands can be smaller than the bands in an elementary band representation. If, in this case, the bands are not connected, one disconnected subset of bands within the elementary band representation is topologically nontrivial, which means it is by itself not connected to an atomic limit [137]. A topological insulator, e.g., in class AII in 3D with a band inversion fits into this scheme, because the modified orbital character at the band inversion cannot be understood by considering only the occupied bands. Recent works have used high-throughput density functional theory (DFT) calculations to identify topological materials using such arguments based on band representations [135, 137, 138].

The above approach to topology is not identical to the one in Sec. 1.3.2. One may consider models of bands that are topological, in the sense that they have no atomic limit, but become trivial once another trivial band is added, which is referred to as “fragile topology”. For a regular topological insulator the addition of trivial bands below the Fermi energy cannot affect the topology. One type of fragile order can be described by Euler classes, \mathbb{Z} invariants, which are defined analogously to Chern numbers as integral of a curvature function, but unlike the Chern number they are only defined for real eigenstates and the manifold of states must be orientable [139]. Eigenstates of a Hamiltonian can be chosen to be real in the presence of \mathcal{PT} -symmetry in 3D or with $C_2\mathcal{T}$ for 2D systems [139, 140]. For a nontrivial Euler class at least three bands and the presence of an even number of protected band crossings are required [140].

These crossings are similar to Weyl points in the sense that they are stable by themselves but can be annihilated in pairs. Due to the three involved bands, the possibility of non-Abelian braiding has been discussed [139–141].

A related approach is the use of symmetry indicators, whereby a set of occupied bands is represented by a tuple of the set $\mathbb{Z}^{d_{\text{BS}}} = \mathbb{Z} \times \mathbb{Z} \times \dots \times \mathbb{Z}$, which contains the multiplicities of symmetry representations for certain high-symmetry points in the BZ [142, 143]. After the set $\mathbb{Z}^{d_{\text{BS}}}$ is generalized to a group, only a subgroup corresponds to insulators with an atomic limit, which is used to determine a quotient group. The equivalence classes in the latter yield the topologically distinct insulators. This abstract classification has been related to the well known \mathbb{Z}_2 invariants [120] for 3D centrosymmetric, topological insulators in class AII and represents a generalization that also considers higher-order topology.

Stability of semimetals with interactions

For the study of topology in the context of interacting systems one may consider whether previously distinct topological phases become equivalent in the presence of interactions or whether new distinct topological phases emerge [109]. Hereby, commonly the term symmetry protected topology is used and one may distinguish short- and long-range entanglement. Since the present work comprises (effectively) non-interacting systems, we will discuss only briefly aspects of semimetals in the presence of interactions.

One possible approach to consider the stability of topological semimetals uses the Luttinger theorem. The Luttinger theorem [144], stating that the volume V_F enclosed by the Fermi surface is unchanged by interactions, can be understood, to some extent, on the grounds of a topological argument [145]. Hereby, in a gedankenexperiment a periodic system of d spatial dimensions is considered as a torus into which a magnetic flux is adiabatically inserted [146]. By relating the Hamiltonians with and without the flux to each other, a difference in the total momentum of the ground state can be found. Under the assumption that the system is a Fermi liquid the same change in momentum can be derived from the low-energy degrees of freedom. Together both results yield [145]

$$\frac{V_F}{(2\pi)^d} = q, \quad (1.3.5)$$

where $q \in \mathbb{Q}$ gives the number of occupied bands (including partial filling). Since Eq. 1.3.5 does not depend on the interaction strength, one obtains the Luttinger theorem. With the flux threading argument a notion of topology has been used, but because the volume of the Fermi surface V_F is continuous it does not directly relate to the topological invariants that we have discussed so far. Furthermore, the Luttinger theorem can be used to argue for the stability of

topological semimetals in the presence of interactions [147]. This result applies to spinless systems with nonsymmorphic symmetries and a well defined quasiparticle Fermi surface. The basic idea of this approach is to exchange the momentum in the previous argument with a nonsymmorphic symmetry eigenvalue, while arguing that after an insertion of a magnetic flux particles are moved from conduction to valence bands. A non-zero value of the topological invariant [147]

$$\tilde{\chi}_F = q \pmod{\mathcal{S}^*}, \quad (1.3.6)$$

indicates that with interactions, which do not break the considered spatial symmetries, a semimetal remains gapless. \mathcal{S}^* is the least common multiple of all ranks \mathcal{S}_g , which are defined for a symmetry element g by the conditions that $g^{\mathcal{S}_g}$ is symmorphic. For nonsymmorphic symmetries $\mathcal{S}_g > 1$, and thus $\mathcal{S}^* > 1$ is possible, which allows for semimetals even with integer filling q .

So far this section is concerned with generic semimetals. For the more specific case of Weyl points it has been found for a lattice model that the point nodes are stable under weak, short-ranged interactions [40]. This is expected because in the single particle picture Weyl points are protected by translation symmetry, which is not expected to be broken for a semimetal with weak, short-ranged interactions. But when considering a low-energy model for a Dirac or Weyl point, the limit of strong interactions leads to a Mott transition, which gaps out the topological band crossings even if the interactions do not break the crystalline symmetries [148, 149]. The difference between the last statement and the previous discussions in the context of the Luttinger theorem is the role of nonsymmorphic symmetries. The works in Refs. [148, 149] on the Mott transition in semimetals consider just low-energy models, for which any nonsymmorphic symmetry is reduced to a point group symmetry.

To summarize the results, topological semimetals are stable in the limit of weak, symmetry-preserving interactions or if there is a nonsymmorphic symmetry that protects the band crossing. When moving away from non-interacting topological semimetals subject to interactions one may consider recent results that nontrivial topology in interacting systems may also necessarily depend on a vanishing gap [150].

1.4. Topological invariants, models, and surface states

So far we have discussed the basic features of topological semimetals and outlined a range of general topics that should be kept in mind during the study of topology within condensed matter systems. In the following section we want to go more into detail and introduce the Berry

phase and Berry curvature, as well as their qualitative features in the presence of an underlying symmetry. These concepts combine homotopy and topological invariants with the electric polarization and electrical response in solids. The anomalous Hall conductivity, which we have encountered in the context of the chiral anomaly in Sec. 1.2.2, can be expressed in terms of the Berry curvature to describe a lattice system instead of a low-energy model. Furthermore, we summarize our computational methods to automatically generate tight-binding models with a given set of symmetries and illustrate the computation of topological charges and surface states for a Weyl semimetal. We conclude the present chapter by bringing the presence of topological surface states in the context of symmetry enforced as well as trivial surface states.

1.4.1. Berry connection

Besides the winding numbers classifying homotopies for the space of gapped Hamiltonians, the Berry connection and the Berry curvature can be employed in certain cases to obtain equivalent results by utilizing the eigenstates of the system. The Berry connection is related to concepts like the polarization, fractionally surface charges, as well as gauge freedom and topological obstructions to find continuous gauges. We begin by introducing the Berry vector potential, before discussing its relation to fiber bundles, where the same object is referred to as Berry connection.

The time-dependent Schrödinger equation,

$$i\hbar\partial_t |\psi(t)\rangle = H(t) |\psi(t)\rangle, \quad (1.4.1)$$

is invariant when the states are modified by an arbitrary, constant phase $|\psi\rangle \rightarrow \exp(i\varphi) |\psi\rangle$ with $\varphi \in [0, 2\pi)$, and also all expectation values of physical quantities remain unchanged by this transformation. If the Hamiltonian $H(\mathbf{R}(t))$ of a system is adiabatically changed due to a parameter $\mathbf{R}(t)$, where $t \in [0, T]$, such that the Hamiltonian returns to its initial form, $H(\mathbf{R}(0)) = H(\mathbf{R}(T))$, then one may find instantaneous eigenstates $|n(\mathbf{R})\rangle$ of the Hamiltonian for each parameter \mathbf{R} as the solutions of the stationary Schrödinger equation [121–123, 151]

$$E_n(\mathbf{R}) |n(\mathbf{R})\rangle = H(\mathbf{R}) |n(\mathbf{R})\rangle. \quad (1.4.2)$$

While one may change the phase at each time t for $|n(\mathbf{R})\rangle$, the solutions $|\psi(t)\rangle$ of the time-dependent problem Eq. 1.4.1 are continuous in t , and thus the gauge transformation defined by $\varphi(t)$ must become dependent on the time t as well. The choice of the gauge transformation is further restricted by $\varphi(0) = \varphi(T)$. This means that in a periodic time evolution the complex phase of a state $|\psi(t)\rangle$ can in general not be removed by a single valued transformation, instead a Berry phase γ is picked up [151]. The solutions to Eq. 1.4.1 for a slow, adiabatic time

evolution have to be given by the instantaneous eigenstate $|n(\mathbf{R})\rangle$ up to an unknown phase $\gamma_n(t)$. Additionally, the adiabatic theorem [152] states that there will be no transitions between nondegenerate energy levels. Thus one may write an ansatz by including the dynamical phase factor

$$|\psi(t)\rangle = \exp\left(-\frac{i}{\hbar} \int_0^t dt' E_n(\mathbf{R}(t'))\right) \exp(i\gamma_n(t)) |n(\mathbf{R})\rangle. \quad (1.4.3)$$

After substituting Eq. 1.4.3 into Eq. 1.4.1 results in

$$\partial_t \gamma_n(t) = i \langle n(\mathbf{R}(t)) | \nabla_{\mathbf{R}} n(\mathbf{R}(t)) \rangle \partial_t \mathbf{R} \quad (1.4.4)$$

$$\Rightarrow \gamma_n(t) = \int_0^t \mathcal{A}_n(\mathbf{R}) dR \quad \text{with} \quad \mathcal{A}_n(\mathbf{R}) = i \langle n(\mathbf{R}(t)) | \nabla_{\mathbf{R}} n(\mathbf{R}(t)) \rangle. \quad (1.4.5)$$

The phase $\gamma_n(t)$ and the introduced Berry vector potential $\mathcal{A}_n(\mathbf{R})$ are gauge dependent quantities [121],

$$|n(\mathbf{R})\rangle \rightarrow e^{i\chi(\mathbf{R})} |n(\mathbf{R})\rangle, \quad \mathcal{A}_n(\mathbf{R}) \rightarrow \mathcal{A}_n(\mathbf{R}) - \nabla_{\mathbf{R}} \chi, \quad (1.4.6)$$

$$\gamma_n(t) \rightarrow \gamma_n(t) + \chi(\mathbf{R}(0)) - \chi(\mathbf{R}(t)). \quad (1.4.7)$$

But if the parameter \mathbf{R} has returned at time $t = T$ to its original value, $\mathbf{R}(0) = \mathbf{R}(T)$, and since the phase of $|n(\mathbf{R})\rangle$ must be single valued, one finds that $\chi(\mathbf{R}(0)) - \chi(\mathbf{R}(t)) = 0 \pmod{2\pi}$. For a closed loop in parameter space the Berry phase γ_n of the n th band is gauge independent and tells us whether it is possible to choose an eigenstate that returns to its original value ($\gamma_n = 0$) or whether a phase is picked up in a periodic time evolution, $\gamma_n \neq 0$.

Berry phase in the Aharonov-Bohm effect

The discussion so far can be considered as a generalization of the Aharonov-Bohm effect, where a particle is moved around a magnetic flux line and its quantum mechanical state picks up a phase [151]. To see this, one may begin with a Hamiltonian $H(\mathbf{p}, \mathbf{r} - \mathbf{R})$, which confines a particle of charge q in the vicinity of \mathbf{R} , e.g., in a box, with instantaneous eigenfunctions $\phi_n(\mathbf{r} - \mathbf{R})$. The magnetic vector potential $\mathbf{A}(\mathbf{r})$ can be added by minimal coupling, which yields the Hamiltonian $H(\mathbf{p} - q\mathbf{A}(\mathbf{r}), \mathbf{r} - \mathbf{R})$ with the new eigenfunctions

$$\langle \mathbf{r} | n(\mathbf{R}) \rangle = \exp\left(\frac{iq}{\hbar} \int_{\mathbf{R}}^{\mathbf{r}} d\mathbf{r}' \cdot \mathbf{A}(\mathbf{r}')\right) \phi_n(\mathbf{r} - \mathbf{R}), \quad (1.4.8)$$

where the additional prefactor compensates for the additional term due to minimal coupling independently of the details of the Hamiltonian. The starting point of the line integral is in principle arbitrary, but if it is taken to be a fixed vector \mathbf{R}_0 , the path connecting \mathbf{R}_0 to \mathbf{r} would

become longer if the particle is moved away by changing \mathbf{R} in the Hamiltonian. Therefore, using any \mathbf{R}_0 in place of \mathbf{R} as the lower bound of the integral in Eq. 1.4.8 ultimately leads to an artificially multi-valued expression in Eq. 1.4.8, once the starting point is reached [153]. Yet, even if the previous remark is taken into account, a non-zero Berry phase occurs, which can be found by considering the Berry vector potential.

$$\mathcal{A}_n(\mathbf{R}) = i \langle n(\mathbf{R}) | \nabla_{\mathbf{R}} n(\mathbf{R}) \rangle = i \int d^3r \phi_n^*(\mathbf{r} - \mathbf{R}) \left(\frac{-iq}{\hbar} A(\mathbf{R}) + \nabla_{\mathbf{R}} \right) \phi_n(\mathbf{r} - \mathbf{R}) = \frac{q}{\hbar} A(\mathbf{R}), \quad (1.4.9)$$

$$\gamma_n(T) = \frac{q}{\hbar} \oint_{\mathcal{L}} d\mathbf{R} \cdot A(\mathbf{R}) = \frac{q\Phi}{\hbar}, \quad (1.4.10)$$

where the second term within the integration shown Eq. 1.4.9 is proportional to the expectation value of momentum $\langle p \rangle$, which vanishes for the considered trapped particle, $\langle p \rangle = 0$. As the Berry vector potential $\mathcal{A}(\mathbf{R})$ is proportional to the actual, electromagnetic vector potential $A(\mathbf{R})$, one can identify the contour integral along a loop \mathcal{L} around the magnetic flux, see Eq. 1.4.10 with the value of the enclosed magnetic flux Φ . The Aharonov-Bohm effect refers to a non-zero complex phase γ , which is accumulated even if the magnetic field is zero at the path covered by $\mathbf{R}(t)$ for $t = 0$ to $t = T$ [153]. Below in our discussion of the Berry curvature, we will show that the two vector potentials $\mathcal{A}(\mathbf{R})$ and $A(\mathbf{R})$ are conceptually related even beyond the Aharonov-Bohm effect

Berry phases in solids

In the following section we narrow the discussion down to condensed matter systems, for which we will discuss how the Berry vector potential relates to the electronic polarization and the related measurable quantities. J. Zak first noticed that in systems with translation invariance the parameter \mathbf{R} can be identified with the crystal momentum \mathbf{k} , which is naturally periodic within the BZ [154]. It was then found that the Berry phase is proportional to the band center q_n , a quantity specifying where a state corresponding to the band n is localized within the unit cell [155]. For a one-dimensional system with lattice constant a this relation is given by

$$\gamma_n = \frac{2\pi}{a} q_n, \quad q_n = \int_{-\infty}^{\infty} dx x |w_n(x)|^2, \quad (1.4.11)$$

where the Wannier function $w_n(x)$ of the n th band is used. The relation of the Berry phase and vector potential to the polarization and the Wannier functions can be generalized to three dimensions [156]

$$\mathbf{q}_n = \frac{V_{\text{cell}}}{(2\pi)^3} \int_{\text{BZ}} d^3k \mathcal{A}_n(\mathbf{k}) \quad (1.4.12)$$

where V_{cell} denotes the volume of the unit cell in real space. This result is reflected in the modern terminology, for which the expression ‘‘band center’’ is commonly replaced by ‘‘Wannier charge center’’. If inversion symmetry is present and we consider only one band that is well separated from the rest, the Wannier functions $w_n(x)$ must be either even or odd around the inversion centers and thus the charge center in one dimension is fixed to $q_n = 0$ or $\frac{a}{2}$, i.e, the Wyckoff positions, which is equivalent to a Berry phase quantized to $\gamma_n = 0$ or $\gamma_n = \pi$ [154]. When the Berry phase is quantized, it cannot change unless the gaps to other bands close, and thus it is a topological \mathbb{Z}_2 invariant.

In a real system more than one band will be occupied at a time and crossings are a common feature. To improve on these limitations the above results can be generalized [119] by replacing the Berry vector potential with the non-Abelian connection

$$\mathcal{A}_\mu^{mn} = \left\langle U_k^m \left| \frac{\partial}{\partial k_\mu} U_k^n \right. \right\rangle, \quad (1.4.13)$$

where m and n label the occupied bands and their corresponding periodic eigenfunctions $u_k^m(r)$ are represented in a tight-binding description as U_k^m . One can obtain the Wannier charge centers as eigenvalues from the Wilson loop, which is the matrix

$$\mathcal{W}(\mathcal{L}) = T \exp\left(- \int_{\mathcal{L}} dk_\mu \mathcal{A}_\mu(k)\right). \quad (1.4.14)$$

Here, T denotes that the exponential of the contour integral is understood as path-ordered and the loop \mathcal{L} must be chosen again as an incontractible path within the BZ, e.g., in one dimension $\mathcal{L} = [-\pi, \pi]$. Since the computational implementation of numerical derivatives of the eigenstates is unfavorable, a more practical approach is based on the discretization of the loop \mathcal{L} into a finite set of points $\{k^{(N)} = k^{(0)} + G, k^{(N-1)}, \dots, k^{(1)}, k^{(0)}\}$. A Wilson loop matrix can then be given for n_{occ} occupied bands as

$$\mathcal{W}^{mn} = \langle U_{k^{(0)}+G}^m | \prod_{\alpha=0}^{N-1} \sum_{j=1}^{n_{\text{occ}}} |U_{k^{(\alpha)}}^j \rangle \langle U_{k^{(\alpha)}}^j | U_{k^{(0)}}^n \rangle, \quad (1.4.15)$$

which yields the same eigenvalue spectrum as Eq. 1.4.14 if inversion symmetry is fulfilled [119]. Whereas the Berry phase γ_n distinguishes topologically distinct phases by whether they yield $\gamma_n = 0$ or $\gamma_n = \pi$, the corresponding invariant for the Wilson loop can be obtained from its eigenvalues $\exp(i\vartheta^n)$, where ϑ^n denotes the phase of the n th eigenvalue of \mathcal{W} . The corresponding topological invariant $N_{(-1)}$ is the multiplicity of eigenvalues with $\vartheta^n = \pi$ [119]. If the applicable topological classification allows only for a \mathbb{Z}_2 instead of a \mathbb{Z} invariant, one may consider whether $N_{(-1)}$ is odd or even to distinguish the phases.

So far the discussion did not consider that a Wilson loop can be dependent on its position in the BZ. This is relevant, for example, in a two-dimensional system, where positions in the BZ are given by (k_1, k_2) . Consider a Wilson loop $\mathcal{W}(\mathcal{L}_1)$, which is calculated on a straight path \mathcal{L}_1 along the k_1 direction. The matrix $\mathcal{W}(\mathcal{L}_1) = \mathcal{W}(\mathcal{L}_1(k_2))$ is a function of the second coordinate k_2 . A spectral flow of Wilson loop eigenvalues $\exp(i\theta_{k_2}^n)$ as function of k_2 contains the information required to define the first Chern number ν as [119]

$$\nu = \sum_{j=1}^{n_{\text{occ}}} \int dk_2 \frac{1}{2\pi} \frac{d\theta_{k_2}^j}{dk_2}, \quad (1.4.16)$$

which can be understood as the number of times the Wilson loop eigenvalues wind around the origin in the complex plane or, analogously, how many Wannier charge centers pass the full length of the unit cell in r_1 direction if k_2 is varied [119, 157]. An example for the winding of the Wilson loop eigenvalues in a system with only one occupied band is shown in Fig. 1.5c.

At several points we have made the connection to topological invariants, thus one should expect topological surface states for non-zero Berry phases. The equivalence between the Berry phase and the Wannier charge centers [154] can be related to the existence of surface charges and thus surface states. If the Wannier centers do not coincide with the positions of the positive charges, a bulk polarization is expected [156]. This happens in ferroelectric materials, where the characteristic signature of a nontrivial state would be a hysteresis of the current needed to switch the bulk polarization [158–160], cf. Sec. 1.4.2. The polarization P determines the charges at the surface, but the surface charge theorem [126] states that only the fractional part of the surface charge Q_{surf} can be obtained from the Wannier centers. Intuitively, the reason is the freedom to choose the crystalline unit cell that makes it possible to remove a part of the polarization calculated from the Berry vector potential. Nevertheless, the polarization $P = -e \sum_n^{n_{\text{occ}}} \mathbf{q}_n$ is obtained as the sum over the n_{occ} occupied Wannier centers \mathbf{q}_n , see Eq. 1.4.12, and can take multiples of a fractional electron charge e . Fractional surface charges have recently found renewed interest at the corner and hinges of HOTIs [161].

Geometric interpretation

Finally, we want to give a brief overview on how the Berry vector potential, or rather the Berry connection, is embedded into the framework of differential geometry [106]. Suppose the parameter vector \mathbf{R} is an element of a d -dimensional manifold, M , i.e., a topological space that locally looks like \mathbb{R}^d , which means that any small, open subset of the manifold is homeomorphic to \mathbb{R}^d . As the instantaneous eigenstate $|n(\mathbf{R})\rangle$ of the Hamiltonian $H(\mathbf{R})$ can be considered as a representative element of an equivalence class of states that differ only by a phase, we can think

of all possible states at \mathbf{R} as a $U(1)$ fiber of a fiber bundle. The combination of the manifold M and the $U(1)$ fiber is a principal bundle $P(M, U(1))$, which implies that the structure group acting on the fiber is identical to the fiber. When considering the states $|n(\mathbf{R})\rangle$ along a path \mathbf{R} on the manifold, we create a section, which maps from the manifold to the total space including both fiber and manifold. To move along the manifold one needs to consider a vector from the tangent space to encode the direction of the path. By introducing a connection one can define how the elements on the fiber change along the section. The connection one-form $\mathcal{A} = \mathcal{A}_\mu dR^\mu = \langle n(\mathbf{R}) | (d|n(\mathbf{R})\rangle)$ is an element of the cotangent space, which assigns a real number to vectors of the tangent space and encodes the change along the fiber, when moving over the manifold. With this exposition it is clear why the Berry phase can be understood as a geometric phase. If one uses the gauge freedom, i.e., the transformation in Eq. 1.4.6, the Berry connection can be canceled [162]:

$$\mathcal{A}^{\text{PT},n} = \mathcal{A}^n - \nabla\chi^{\text{PT}} = 0. \quad (1.4.17)$$

The above Berry connection $\mathcal{A}^{\text{PT},n}$ is given in the parallel transport gauge, where no complex phase is picked up. Parallel transport is understood more easily for a tangent vector that is transported along a closed path on a sphere, which due to the curvature of the sphere results in a final vector that is different from the starting vector. Analogously, if the eigenstate $|n(\mathbf{R})\rangle$ is parallel transported on a closed loop, its final complex phase will differ from the phase at the beginning of the loop. As one would expect from this picture, there is a curvature related to Berry phases that is analogous to the curvature of a sphere. In the following we will show the derivation of this Berry curvature from the Berry connection.

1.4.2. Berry curvature

The Berry curvature $\mathbf{\Omega}$ is closely related to the Berry connection. In this section we start from the relation of $\mathbf{\Omega}$ to measurable currents, based on the previous discussion of electrical polarization. Then, we expand the analogy between the Berry and the electromagnetic vector potentials, which has been discussed above for the Aharonov-Bohm effect. After a description of the numerical implementation to calculate the curvature, we close with a discussion on how crystalline symmetries restrict the Berry curvature, which is of importance for the anomalous Hall effect.

To measure an electric polarization due to a non-zero Berry phase, cf. Eqs. 1.4.11 and 1.4.12, one may consider the electric current that occurs once the lattice Hamiltonian is subjected to a change in an additional external parameter R . As a reminder, we have previously replaced the original, periodically tuned parameter R by the crystal momentum \mathbf{k} to capture the Berry phase

as a topological invariant of static systems. Now, we add to this an external parameter R . As the surface charge due to the bulk polarization is only given modulo integer charges [126], one may consider a pumping procedure in R to monotonously increase the polarization until its original value is reached by the periodicity of physically distinct polarizations [163]. The original Thouless pump of particles moved by a periodic potential, which leads to a quantized current, has been experimentally realized in a fermionic cold atom framework [164]. To understand the results of this pumping procedure, we will stay within the formalism of polarization [156].

The current \mathbf{J} connected to a change of polarization \mathbf{P} is given by

$$\mathbf{J} = \frac{d\mathbf{P}}{dt} = \frac{dR}{dt} \frac{d\mathbf{P}}{dR}, \quad (1.4.18)$$

where R specifies the external parameter of the Hamiltonian $H(R)$ with the eigenstates $|u_{n\mathbf{k}}\rangle$. Generally, to obtain the polarization \mathbf{P} the expectation value of the position operator must be considered, $\langle u_{m\mathbf{k}}|\mathbf{r}|u_{n\mathbf{k}}\rangle$. If this expression is reformulated in terms of eigenstate derivatives, a Berry curvature can be identified, which will lead to the conclusion that the change in polarization is quantized.

The Heisenberg equation of motion, $\mathbf{v} = -\frac{i}{\hbar}[\mathbf{r}, H]$, can be used to relate the position operator to the velocity. After a change to reciprocal space, the use of the stationary Schrödinger equation $H_{\mathbf{k}}|u_{n\mathbf{k}}\rangle = E_{n\mathbf{k}}|u_{n\mathbf{k}}\rangle$, and a projection onto the eigenbasis, $|u_{n\mathbf{k}}\rangle$, one obtains

$$\langle u_{m\mathbf{k}}|\mathbf{r}|u_{n\mathbf{k}}\rangle = i\hbar \frac{\langle u_{m\mathbf{k}}|\nabla_{\mathbf{k}}|u_{n\mathbf{k}}\rangle}{E_{n\mathbf{k}} - E_{m\mathbf{k}}}. \quad (1.4.19)$$

To apply Eq. 1.4.19 in the derivative of the expectation value of the position operator, a partition of unity must be introduced, which reduces in the first-order in R to a projector on the unoccupied bands at zero temperature. After some algebra one obtains for the derivative of the polarization [156]

$$\frac{d\mathbf{P}}{dR} = e\hbar \sum_n^{\text{occ.}} \int \frac{d^3k}{(2\pi)^3} 2 \text{Im} \langle \partial_R u_{n\mathbf{k}} | \sum_m^{\text{unocc.}} \frac{1}{E_{n\mathbf{k}} - E_{m\mathbf{k}}} |u_{m\mathbf{k}}\rangle \langle u_{m\mathbf{k}}| \nabla_{\mathbf{k}} |u_{n\mathbf{k}}\rangle, \quad (1.4.20)$$

where the two summations run over the occupied and unoccupied bands, respectively, and the integration runs over the full BZ.

For the last step towards the Berry curvature, we note that $\mathbf{v}_{\mathbf{k}} = \frac{1}{\hbar}\nabla_{\mathbf{k}}H_{\mathbf{k}}$, which may be derived from $H_{\mathbf{k}} = e^{-i\mathbf{k}\cdot\mathbf{r}}He^{i\mathbf{k}\cdot\mathbf{r}}$ and the Heisenberg equation of motion, and which is substituted into Eq. 1.4.20. To further simplify $\langle u_{m\mathbf{k}}|\nabla_{\mathbf{k}}|u_{n\mathbf{k}}\rangle$, we introduce the relation [122]

$$E_n \langle u_{m\mathbf{k}}|\nabla_{\mathbf{k}}u_{n\mathbf{k}}\rangle = \langle u_{m\mathbf{k}}|\nabla_{\mathbf{k}}(H_{\mathbf{k}}u_{n\mathbf{k}})\rangle = \langle u_{m\mathbf{k}}|\nabla_{\mathbf{k}}H_{\mathbf{k}}|u_{n\mathbf{k}}\rangle + E_m \langle u_{m\mathbf{k}}|\nabla_{\mathbf{k}}u_{n\mathbf{k}}\rangle, \quad (1.4.21)$$

which holds for orthogonal nondegenerate states, implying $m \neq n$, that

$$\langle u_{m\mathbf{k}}|\nabla_{\mathbf{k}}u_{n\mathbf{k}}\rangle = \frac{\langle u_{m\mathbf{k}}|\nabla_{\mathbf{k}}H_{\mathbf{k}}|u_{n\mathbf{k}}\rangle}{E_n - E_m}. \quad (1.4.22)$$

With this, the derivative of the polarization can be expressed as [162]

$$\frac{d\mathbf{P}}{dR} = e \sum_n^{\text{occ}} \int \frac{d^3k}{(2\pi)^3} 2 \text{Im} \langle \partial_R u_{n\mathbf{k}} | \nabla_{\mathbf{k}} u_{n\mathbf{k}} \rangle = -e \sum_n^{\text{occ}} \int \frac{d^3k}{(2\pi)^3} \boldsymbol{\Omega}_{R\mathbf{k}}^n, \quad (1.4.23)$$

where we have introduced the mixed Berry curvature $\boldsymbol{\Omega}_{R\mathbf{k}}^n$, where derivatives with respect to two different, hence mixed, parameters of the Hamiltonian are taken. Remember, that here the starting point is the same as for the Berry connection, i.e., a periodic evolution in the parameter R , which is a 1D version of the parameter vector \mathbf{R} as introduced in Eq. 1.4.2. The change of polarization, i.e., the total current, can be obtained by combining Eqs. 1.4.18 and 1.4.23, which gives

$$|\Delta\mathbf{P}| = \int dt |\mathbf{J}| = -e \sum_n^{\text{occ}} \oint dR \int \frac{d^3k}{(2\pi)^3} |\boldsymbol{\Omega}_{R\mathbf{k}}^n| = -e \sum_n^{\text{occ}} \nu_n, \quad (1.4.24)$$

where the external parameter R returns to its initial value after one period. The last equality follows from the Chern theorem that states that the integral of the Berry curvature over the closed manifold equals to $2\pi\nu_n$, with the Chern number ν_n of the band n [156]. Thus, the original statement that a quantized charge is transported per cycle in R has been rederived [165].

In the context of the Berry connection, we have discussed the matrix-valued Wilson loop as a function of two independent parameters, k_1 and k_2 . Like the Berry curvature, which also requires to independent indices, the Chern number can be obtained from the Wilson loop, Eq. 1.4.16. In the next section we will elaborate on the relation between the Berry curvature and the Chern number.

Sources of Berry curvature

In the following we discuss the similarity between the Berry curvature and the electromagnetic field. Hereby, we consider a curvature only with derivatives with respect to the components of the crystal momenta, i.e., as a geometric quantity of static systems. The Berry curvature in three dimensions can be understood as the curl of the connection, and for a closed loop in parameter space the Berry curvature through the enclosed surface relates to the Berry phase. Weyl points can be identified as sources (and sinks) of Berry curvature, by considering surfaces without a boundary.

First, we want to relate the Berry phase γ_n on a loop \mathcal{L} to the Berry curvature $\boldsymbol{\Omega}_n(\mathbf{k})$ piercing any surface \mathcal{S} bounded by \mathcal{L} [122]. Hereby, the parameter \mathbf{R} is taken as a vector \mathbf{k} in the three-dimensional BZ. We find

$$\gamma_n = \oint_{\mathcal{L}=\partial\mathcal{S}} d\mathbf{k} \cdot \mathbf{A}_n(\mathbf{k}) \stackrel{\text{Stokes}}{=} \int_{\mathcal{S}} d\mathbf{S} \cdot (\nabla_{\mathbf{k}} \times \mathbf{A}_n(\mathbf{k})) = \int_{\mathcal{S}} d\mathbf{S} \cdot \boldsymbol{\Omega}^n(\mathbf{k}), \quad \text{with} \quad (1.4.25)$$

$$\boldsymbol{\Omega}^n(\mathbf{k}) = \nabla_{\mathbf{k}} \times \mathbf{A}_n(\mathbf{k}), \quad \mathbf{A}_n(\mathbf{k}) = i \langle n(\mathbf{k}) | \nabla_{\mathbf{k}} n(\mathbf{k}) \rangle, \quad (1.4.26)$$

where the use of Stokes theorem in Eq. 1.4.25 requires a continuous differentiable connection on the surface \mathcal{S} that is enclosed by the loop \mathcal{L} . If we regard the Berry vector potential as analog to the electromagnetic vector potential, then the Berry curvature corresponds to an effective magnetic field.

Before proceeding to the discussion of monopoles within this description, we need to show that Eqs. 1.4.26 and 1.4.23 are equivalent if the external parameters of the mixed curvature are both chosen as components of \mathbf{k} , e.g., k_b and k_c . The a component of the Berry curvature can be rewritten as

$$\begin{aligned}\Omega^n(\mathbf{k})_a &= (i\nabla_{\mathbf{k}} \times \langle n | \nabla_{\mathbf{k}} n \rangle)_a = i\epsilon_{abc} \nabla_b (\langle n | \nabla_c n \rangle) \\ &= i\epsilon_{abc} (\langle \nabla_b n | \nabla_c n \rangle + \langle n | \nabla_b \nabla_c n \rangle) = i\epsilon_{abc} \langle \nabla_b n | \nabla_c n \rangle \\ &= -\text{Im} \epsilon_{abc} \langle \nabla_b n | \nabla_c n \rangle = -2 \text{Im} \langle \nabla_b n | \nabla_c n \rangle = \Omega_{bc}^n,\end{aligned}\quad (1.4.27)$$

where we omitted the \mathbf{k} dependency of the eigenstates, abbreviated the components of $\nabla_{\mathbf{k}}$, e.g., we write ∇_c for ∂_{k_c} , and sum over repeated indices. In the second to last steps, the summations are replaced by fixed values for the variables using $\epsilon_{abc} = 1$. This reproduces the curvature as introduced in Eq. 1.4.23. In this form it is easy to see that the Berry curvature is gauge invariant with respect to transformations of the form given in Eq. 1.4.6.

As it is useful for anomalous Hall effect, see Sec. 1.4.3, to represent the Berry curvature with velocity matrix elements, we adapt Eq. 1.4.22 to the present notation and obtain

$$\langle m | \nabla_a n \rangle = \frac{\langle m | \nabla_a H | n \rangle}{E_n - E_m}.\quad (1.4.28)$$

If one combines Eq. 1.4.27 and 1.4.28 after inserting a partition of unity one obtains

$$\Omega^n(\mathbf{k})_a = -\text{Im} \epsilon_{abc} \sum_m \langle \nabla_b n | m \rangle \langle m | \nabla_c n \rangle = -\text{Im} \epsilon_{abc} \sum_m \frac{\langle n | \nabla_b H | m \rangle}{E_n - E_m} \frac{\langle m | \nabla_c H | n \rangle}{E_n - E_m}\quad (1.4.29)$$

$$= -\text{Im} \epsilon_{abc} \sum_m \frac{\langle n | \nabla_b H | m \rangle \langle m | \nabla_c H | n \rangle}{(E_n - E_m)^2}\quad (1.4.30)$$

Although no Thouless charge pumping process is considered here and all involved parameters are the lattice momenta k_i , which are not tuned by external perturbation, the presence of the terms $\langle n | \nabla_b H | m \rangle$, which are proportional to the velocity matrix, indicates a prevalent connection to transport, as will be shown in Sec. 1.4.3.

If one takes the newly introduced form of the curvature $\Omega^n(\mathbf{k})$ as curl of $\mathcal{A}^n(\mathbf{k})$ seriously, then $\nabla \cdot \Omega^n(\mathbf{k}) = 0$, i.e., the field should be free of sources and sinks as long as the derivatives are well defined. We will illustrate that the latter condition is not always fulfilled. To do so let us consider a general model with two eigenstates described by the Hamiltonian

$$H = \mathbf{d} \cdot \boldsymbol{\sigma} = d_x \sigma_x + d_y \sigma_y + d_z \sigma_z,\quad (1.4.31)$$

where d_i with $i \in \{1, 2, 3\}$ are arbitrary real parameters. Its eigenstates are given by [122]

$$|E_{\pm}\rangle = \frac{1}{\sqrt{2d(d \pm d_3)}} \begin{pmatrix} d_3 \pm d \\ d_1 - id_2 \end{pmatrix}, \quad (1.4.32)$$

which correspond to the eigenvalues $E_{\pm} = \pm \sqrt{d_1^2 + d_2^2 + d_3^2} = \pm d$. The Berry curvature can be expressed as derivatives of the functions d_i [166]

$$\Omega_{ij}^{\pm} = \pm \frac{1}{2d^3} \epsilon_{abc} d_a \partial_i d_b \partial_j d_c. \quad (1.4.33)$$

If we take the derivatives with respect to the parameters d_i , the result is simplified and we obtain for the curvature [121, 123]

$$\Omega_{ij}^{\mp} = \pm \frac{1}{2d^3} \epsilon_{abc} d_a \delta_{ib} \delta_{jc} = \pm \frac{1}{2d^3} \epsilon_{aij} d_a, \quad (1.4.34)$$

$$\mathbf{\Omega}^{\mp} = \pm \frac{\mathbf{d}}{2d^3}, \quad (1.4.35)$$

which is reminiscent to the field of an electric (or magnetic) monopole. For a general two-band model $d_i = d_i(\mathbf{k})$ the field would not look like a monopole in reciprocal space unless we adopt the specific choice $d_i = k_i$, which yields the low-energy description of a Weyl point, see Sec. 1.1. If one integrates the curvature $\mathbf{\Omega}^- = \frac{\mathbf{k}}{2k^3}$ of the lower band on a sphere S enclosing the origin, for example by switching into spherical coordinates, one obtains the Chern number ν , which is identified with the chirality of the Weyl point,

$$\frac{1}{2\pi} \int_S \mathbf{dS} \cdot \mathbf{\Omega} = 1 \equiv \nu. \quad (1.4.36)$$

In analogy to electrostatics the Weyl point acts as a point charge to the curvature field, $\nabla_{\mathbf{k}} \mathbf{\Omega} = 2\pi \delta_{\mathbf{k}}$. This non-zero Chern number indicates that the sphere S as a subset of the three-dimensional BZ is a topological insulator. If two Weyl points of opposite charge are embedded in an otherwise gapped band structure, one finds that some 2D planes cutting through the BZ are topological. We will give a simple example of such a system in Sec. 1.4.4.

So far we have only considered Weyl points of single charge, but suppose we choose $d_{x,y} = (k_x \pm ik_y)^n = k_{\perp}^n e^{\pm in\varphi}$ and $d_z = k_z$ instead of $d_i = k_i$, cf. [40, 167]. Note, this choice of \mathbf{d} leads to internal derivatives in the step from Eq. 1.4.33 to Eq. 1.4.34. By switching into cylindrical coordinates one may evaluate Eq. 1.4.36 and one obtains the chirality as [167]

$$\nu = \frac{1}{2\pi} \int_S \mathbf{dS} \cdot \mathbf{\Omega} = n. \quad (1.4.37)$$

Such Weyl points, also known as multi-Weyl nodes [168], i.e., those with Chern numbers $\nu > 1$ can not only be found for low-energy models, but also in lattice models with specific crystalline symmetries, see chapters 2 and 3. Generally, the presence of long-range hopping terms is needed to achieve large Chern numbers [169].

Numerical Chern number calculation

In our study of the topology of various tight-binding models, it is necessary to numerically implement the calculation of the Chern number for different integration surfaces. Our most frequently used method determines the lattice Chern number by calculating small Wilson loops on a discretized integration surface as introduced in Ref. [170]. To calculate the Chern number for M bands that are separated by gaps to other bands, one takes the corresponding eigenstate matrix $\psi = (|n_1\rangle, \dots, |n_M\rangle)$ and defines the normalized link variable [170]

$$U_\mu(k_l) = \frac{\psi^\dagger(k_l)\psi(k_l + \hat{\mu})}{|\det \psi^\dagger(k_l)\psi(k_l + \hat{\mu})|}, \quad (1.4.38)$$

where $\hat{\mu} \in \{\hat{e}_1, \hat{e}_2\}$ is a step from one corner of a plaquette to another and both are connected to each other by an edge of the plaquette. Plaquettes can be, for example, chosen to be little squares that tile the complete surface, on which the Chern number shall be calculated. The lattice Chern number $\tilde{\nu}$ is then obtained by summing the lattice field strength \tilde{F}_{12} , which corresponds to the Berry curvature, as given by [170]

$$\tilde{F}_{12}(k_l) = \ln U_1(k_l) U_2(k_l + \hat{e}_1) U_1(k_l + \hat{e}_2)^{-1} U_2(k_l)^{-1}, \quad (1.4.39)$$

$$\tilde{\nu} = \frac{1}{2\pi i} \sum_l \tilde{F}_{12}(k_l). \quad (1.4.40)$$

The main idea of this approach is that the limit of vanishing plaquette size does not need to be reached to obtain accurate results, because the (lattice) Chern number is quantized, already a rough mesh of plaquettes is sufficient. Hereby, the resolution must be good enough to ensure that the logarithm in Eq. 1.4.39 is evaluated well within its principal branch. For a surface with a size equal to $\frac{(2\pi)^2}{a_1 a_2}$, where a_1 and a_2 are in the simplest case the lattice constants in real space, the critical mesh size N_B^c , which must be reached for the method become accurate, is estimated to be [170]

$$N_B^c \approx \mathcal{O}\left(\sqrt{\frac{2\tilde{\nu}}{a_1 a_2}}\right). \quad (1.4.41)$$

Note, that this estimate assumes an approximately uniformly distributed Berry curvature. If instead a Weyl point is situated very close to the integration surface the method becomes less accurate.

Symmetries restrict the curvature

By considering how $\Omega(\mathbf{k})$ transforms with the crystal symmetries, we will not only be able to make exact statements regarding the anomalous Hall conductivity, Eq. 1.4.48, but we will

also have the basics to understand how chiralities of Weyl points are related by symmetry. It is generally known that the Berry curvature is a pseudovector, due to its definition as a curl in Eq. 1.4.25, which means it behaves as a vector under proper rotations U with $\det D_U = 1$ but does not inverse its direction for improper rotations with $\det D_U = -1$. As it is important for the latter chapters of this work, we shall explicitly consider the action of symmetries on the Berry curvature.

Spatial and sublattice symmetries act like unitary matrices U on the Hilbert space and by their representation D_U on the reciprocal space. To study the symmetries of the curvature $\mathbf{\Omega}(\mathbf{k})$ and the connection $\mathbf{A}(\mathbf{k})$, we will introduce the unitary matrix U into an expectation value by using $U^\dagger U = \mathbb{1}$, and aim to relate the result to the same functions at a different coordinate. We denote the state obtained by the action of U by $U |\psi(\mathbf{k})\rangle = |\psi'(D_U \mathbf{k})\rangle$. For a symmetric Hamiltonian $|\psi'(D_U \mathbf{k})\rangle$ is an eigenstate, has the same energy, and is in the same eigenspace as $|\psi(D_U \mathbf{k})\rangle$. To refine the relation between $|\psi\rangle$ and $|\psi'\rangle$ we split the rotation \tilde{U} in the eigenspace from the full action of U , i.e., we obtain $U |\psi(\mathbf{k})\rangle = \tilde{U}(\mathbf{k}) |\psi(D_U \mathbf{k})\rangle$. In the simplest case of nondegenerate bands $\tilde{U}(\mathbf{k})$ is just a phase. Independent of its size, this matrix $\tilde{U}_{ij} = \langle \psi_i(D_U \mathbf{k}) | U \psi_j(\mathbf{k}) \rangle$ may encode a nontrivial winding of the eigenstates, where we use a single-valued eigenbasis $\{|\psi_i(\mathbf{k})\rangle\}$.

In the next step we want to get rid of \tilde{U}_{ij} by choosing an appropriate gauge, but before doing so let us consider to what extent this is possible. The expression for \tilde{U}_{ij} resembles the time reversal polarization $\langle \psi_i(D_U \mathbf{k}) | T \psi_j(\mathbf{k}) \rangle$ [171], such matrix elements with respect to states at different positions are commonly called ‘‘sewing matrix’’ [119, 122]. If one chooses a smooth gauge, which is only possible with vanishing Chern number $\nu = 0$ or for 1D systems with a vanishing Berry phase, then one may use the sewing matrix to define \mathbb{Z}_2 invariants for topological insulators [120, 171]. In the presence of topological band crossings, the gauge will generally not be smooth and the following relation will be violated for a set of \mathbf{k} with vanishing measure.

$$U |\psi(\mathbf{k})\rangle = |\psi(D_U \mathbf{k})\rangle \quad (1.4.42)$$

In the following we study the implications of the symmetry U for Berry connection and curvature. The action of the symmetry in Eq. 1.4.42 affects the argument in the state but not the variable with respect to which the differentiation is performed. One finds that the gradient transforms as a vector

$$\nabla_{\mathbf{k}} |\psi(D_U \mathbf{k})\rangle = \frac{\partial(D_U \mathbf{k})}{\partial \mathbf{k}} \frac{\partial}{\partial(D_U \mathbf{k})} |\psi(D_U \mathbf{k})\rangle = \frac{\partial(D_U \mathbf{k})}{\partial \mathbf{k}} \frac{\partial}{\partial \mathbf{k}'} |\psi(\mathbf{k}')\rangle \Big|_{\mathbf{k}'=D_U \mathbf{k}} = D_U |\nabla_{\mathbf{k}} \psi(D_U \mathbf{k})\rangle, \quad (1.4.43)$$

where $|\nabla_{\mathbf{k}}\psi(D_U\mathbf{k})\rangle$ denotes the derivative of the state $|\psi(\mathbf{k})\rangle$ at the point $D_U\mathbf{k}$. With this result we can obtain the transformation of the Berry connection

$$\mathbf{A}(\mathbf{k}) = i\langle\psi(\mathbf{k})|\nabla_{\mathbf{k}}\psi(\mathbf{k})\rangle = i\langle U\psi(\mathbf{k})|U\nabla_{\mathbf{k}}\psi(\mathbf{k})\rangle = i\langle\psi(D_U\mathbf{k})|D_U\nabla_{\mathbf{k}}\psi(D_U\mathbf{k})\rangle = D_U\mathbf{A}(D_U\mathbf{k}), \quad (1.4.44)$$

where we have assumed that U does not depend on the position in reciprocal space \mathbf{k} . With this result we can understand, how mirror and inversion symmetries quantize the Berry phase. Along a path normal to the mirror plane the contribution $\mathbf{A}(\mathbf{k})$ to the Berry phase is canceled by $-\mathbf{A}(-\mathbf{k})$, so the total would be zero, unless the gauge is not smooth. In the latter case one may quantify the jumps of the phase by the inversion or mirror eigenvalue at the center or the surface of the BZ, which themselves only take two values and lead to a Berry phase of either $\gamma = 0$ or $\gamma = \pi$ [119].

Since nonsymmorphic symmetries, which prove to be useful to understand topological band crossings in the following chapters, generally require a \mathbf{k} -dependence of $U = U_{\mathbf{k}}$ we give a generalization of Eq. 1.4.44 in Appendix B.

For antiunitary symmetries an additional complex conjugation must be considered. Time-reversal yields $\mathbf{A}(\mathbf{k}) = \mathbf{A}(-\mathbf{k})$, because the introduced complex conjugation cancels with the minus sign due to D_U , which acts as $\mathbf{k} \rightarrow -\mathbf{k}$.

With Eq. 1.4.44 the action of a symmetry on the Berry curvature is

$$\mathbf{\Omega}(\mathbf{k}) = \nabla_{\mathbf{k}} \times \mathbf{A}(\mathbf{k}) = (D_U\nabla_{\mathbf{k}}) \times (D_U\mathbf{A}(D_U\mathbf{k})), \quad (1.4.45)$$

which simplifies to $\mathbf{\Omega}(\mathbf{k}) = D_U\mathbf{\Omega}(D_U\mathbf{k})$ for rotations, whereas the curvature is invariant $\mathbf{\Omega}(\mathbf{k}) = \mathbf{\Omega}(-\mathbf{k})$ for inversion, and a mirror symmetry switches the sign of components of $\mathbf{\Omega}(\mathbf{k})$ within their mirror plane. Time-reversal symmetry leads to $\mathbf{\Omega}(\mathbf{k}) = -\mathbf{\Omega}(-\mathbf{k})$ and the combination of TRS and inversion leads to $\mathbf{\Omega}(\mathbf{k}) = 0$.

1.4.3. Anomalous Hall conductivity

The simplest approach to the electric response is a response expanded up to linear order in the electric fields, i.e., the current $\mathbf{j} = \sigma\mathbf{E}$, where the conductivity tensor σ is for our purposes a 3 by 3 matrix. We will focus only on the antisymmetric part of the conductivity, i.e., $\sigma_{\alpha\beta} = -\sigma_{\beta\alpha}$, which describes Hall currents perpendicular to the applied electrical field. Among the first results in the study of topology in solids is that for 2D, gapped systems in an applied magnetic field the Hall conductivity $\sigma_{xy} = \frac{\nu e^2}{h}$ [121] is quantized and can be expressed in terms of the Chern number ν [165, 172, 173]. As we have discussed above, Chern numbers also occur in topological insulators, and thus imply a nontrivial response. Chern insulators exhibit in

principle a Hall effect without an external magnetic field. Hereby, it is the Berry curvature that leads to an intrinsic, anomalous contribution to the Hall effect, which is independent of impurities [48, 49]. Note, that when creating a Chern insulator one must break time-reversal symmetry, and if this is done by the presence of magnetism [114–117] there will also be an extrinsic contribution to the Hall effect due to scattering.

Our focus on topological (semi)metals in three dimensions makes a quantized Hall response an exception. Instead we have to consider partially filled bands for which the anomalous Hall conductivity takes the form given below, see Eq. 1.4.48 [174]. The description of a charge pump in Sec. 1.4.2 already contains the necessary steps to obtain the conductivity tensor for a general single particle Hamiltonian [121]

$$H(\mathbf{q}, t) = H(\mathbf{q} + \frac{e}{\hbar}\mathbf{A}(t)), \quad (1.4.46)$$

where the electromagnetic vector potential $\mathbf{A}(t)$ is added by minimal coupling to describe an electric field $\partial_t \mathbf{A}(t) = -E$. In a semiclassical description the new momentum $\mathbf{k} = \mathbf{q} + \frac{e}{\hbar}\mathbf{A}(t)$ follows the equation of motion $\frac{d\mathbf{k}}{dt} = -\frac{e}{\hbar}E$. And thus the derivative with respect to $R = t$ in Eq. 1.4.23 can be replaced by

$$\partial_R = \partial_t = \frac{d\mathbf{k}}{dt} \cdot \nabla_{\mathbf{k}} = -\frac{e}{\hbar}E \cdot \nabla_{\mathbf{k}}. \quad (1.4.47)$$

To simplify the determination of derivatives, we rewrite the Berry curvature $\Omega_{ij}^n(\mathbf{k})$ of the n th band with derivatives of the Hamiltonian $H(\mathbf{k})$ by using Eq. 1.4.30. For numerical implementations this decouples the calculation of derivatives from the matrix diagonalization. Overall the anomalous Hall conductivity is given by [175, 176]

$$\sigma_{ij} = -\frac{e^2}{\hbar} \int \frac{d^3k}{(2\pi)^3} \sum_n f(E_n(\mathbf{k})) \Omega_{ij}^n(\mathbf{k}), \quad (1.4.48)$$

$$\sum_l \Omega_l \epsilon_{ijl} = \Omega_{ij}^n(\mathbf{k}) = \sum_{m \neq n} \frac{2 \operatorname{Im}(\langle n | \frac{\partial H(\mathbf{k})}{\partial k_i} | m \rangle \langle m | \frac{\partial H(\mathbf{k})}{\partial k_j} | n \rangle)}{(E_n(\mathbf{k}) - E_m(\mathbf{k}))^2}, \quad (1.4.49)$$

where the integration runs over the full BZ, $f(E_n(\mathbf{k})) = 1/(\exp(\frac{E_n(\mathbf{k}) - \mu}{k_B T}) + 1)$ denotes the Fermi-Dirac distribution, and $|m\rangle, |n\rangle$ are \mathbf{k} dependent eigenstates of the Hamiltonian. The vectorial notation $\mathbf{\Omega}$ of the Berry curvature is given with the Levi-Civita symbol ϵ_{ijl} .

The action of crystalline symmetries on the Berry curvature, see Eq. 1.4.45, restricts the anomalous Hall conductivity σ_{ij} . Prefactors from the velocity matrix elements may lead to a cancellation of the curvature, whereas the other terms in Eq. 1.4.48 also reflect the symmetry, due to the presence of $E_n(\mathbf{k})$, but they do not affect the overall sign. We list in the following the most relevant cases. In the presence of TRS, $\mathbf{\Omega}(\mathbf{k}) = -\mathbf{\Omega}(-\mathbf{k})$, the integration adds up to zero,

i.e., $\sigma_{ij} = 0$. A mirror symmetry M_z yields $\sigma_{yz} = 0$ and $\sigma_{zx} = 0$. If there is a rotation symmetry around the z -axis, we can consider the star of the curvature vector $\mathbf{\Omega}$ for each \mathbf{k} , i.e., the repeated application of the rotation to $\mathbf{\Omega}$. Adding all resulting vectors of the star yields a vector that is parallel to the k_z -axis, and thus only $\sigma_{xy} \neq 0$. The combination of TRS with a twofold rotation C_2^z yields $(k_x, k_y, k_z) \rightarrow (k_x, k_y, -k_z)$ while mapping $(\Omega_x, \Omega_y, \Omega_z) \rightarrow (\Omega_x, \Omega_y, -\Omega_z)$ and thus $\sigma_{xy} = 0$. Our last observation restricts the anomalous Hall effect in topological nodal plane materials, see Sec. 3.3.

Within the scope of our work, we consider only the antisymmetric contribution to the conductivity tensor, due to its close relation with the topology. Nevertheless, intrinsic contributions must be considered to obtain the full conductivity tensor, which describes also the diagonal, longitudinal conduction including intraband and symmetric interband terms [177]. While these terms depend on the derivative $f'(E)$ of the Fermi-Dirac distribution, i.e., their contributions stem from the Fermi surface, the antisymmetric term given in Eq. 1.4.48 contains contributions from all occupied states. For topological insulators and semimetals, which have no or just a small Fermi surface, respectively, the antisymmetric contributions should be expected to dominate the response.

1.4.4. Weyl semimetal: surface states and chirality

In this section we want to combine the abstract discussion of the bulk-boundary correspondence with the Chern numbers in Weyl semimetals, by illustrating the central features with the toy model [122]

$$H(\mathbf{k}) = \sin k_x \sigma_x + \sin k_y \sigma_y + (M - \cos k_x - \cos k_y - \cos k_z) \sigma_z, \quad (1.4.50)$$

where two Weyl points exist if the variable M is chosen as $-1 < M < 3$, see Fig. 1.5a. A 3D Weyl semimetal can be understood as 2D Chern insulators that are stacked in the third direction, which is k_z in Eq. 1.4.50. In between the Weyl points the Chern number for each 2D subsystem is non-zero, Figs. 1.5b and 1.6a, which can be calculated by the spectral flow using Wilson loops, see Fig. 1.5c. In the example for the spectral flow we have chosen a value of k_z in between the Weyl points, such that the winding for the phase of the Wilson loop eigenvalue corresponds to the Chern number of $\nu = 1$, as seen in Fig. 1.5b. Note that for one occupied band in the model of Eq. 1.4.50 the Wilson matrix is just a number.

By the bulk-boundary correspondence the non-zero topology in the bulk implies the existence of surface states, cf. Fig. 1.6a for a visualization. In the case of Weyl semimetals helicoid bands [178], which belong to states localized on the surfaces, connect the Weyl cones in the bulk band structure, see Fig. 1.6b. If the surface state spectrum of a conventional Weyl semimetal

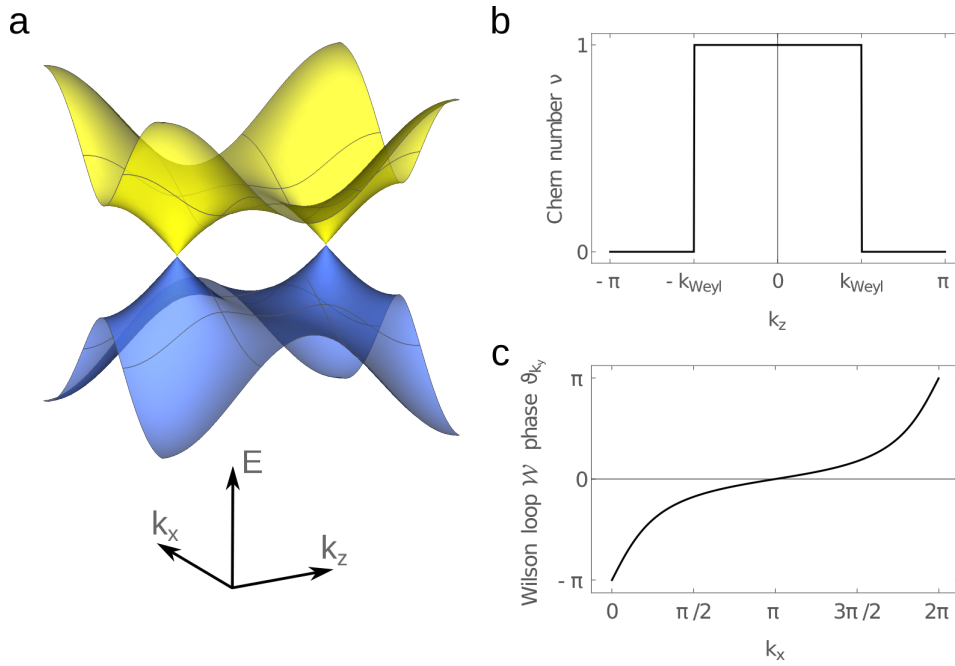


Figure 1.5.: Weyl points and their topological charge for the Weyl semimetal given in Eq. 1.4.50 for $M = 2$. **a** Band structure on the plane $k_y = 0$, which contains the two Weyl points at $\pm k_z = k_{\text{Weyl}} = \frac{\pi}{2}$ with $k_x = 0$. **b** The Chern number on planes of constant k_x is non-zero between the Weyl points. **c** Winding of complex phases of the Wilson loop eigenvalues in the $k_z = 0$ plane for a loop in k_y direction.

is considered at a given energy, i.e, if one takes a equal energy cut of the helicoid surface band, one finds the so-called Fermi arcs instead of the closed Fermi surfaces of regular electron or hole pockets, see Fig. 1.6c. While the full spectrum in Fig. 1.6b exhibits two additional surface states, when compared to Fig. 1.5a, each surface exhibits only one chiral surface state, as shown in Fig. 1.6c. Although the presence of Fermi arcs follows from the bulk invariant, the exact connectivity depends on the details of the systems. This becomes relevant in the case of a Weyl semimetal with four Weyl points, for which a Fermi arc starting at the projection of one Weyl point with charge $\nu = +1$ may end at either of the two Weyl points with the charge $\nu = -1$ [179]. Lifshitz transitions, i.e., changes in the Fermi surface topology, between different Fermi arc connectivities can be tuned, for example, by additional atoms added to the surface of the semimetal [54, 179, 180].

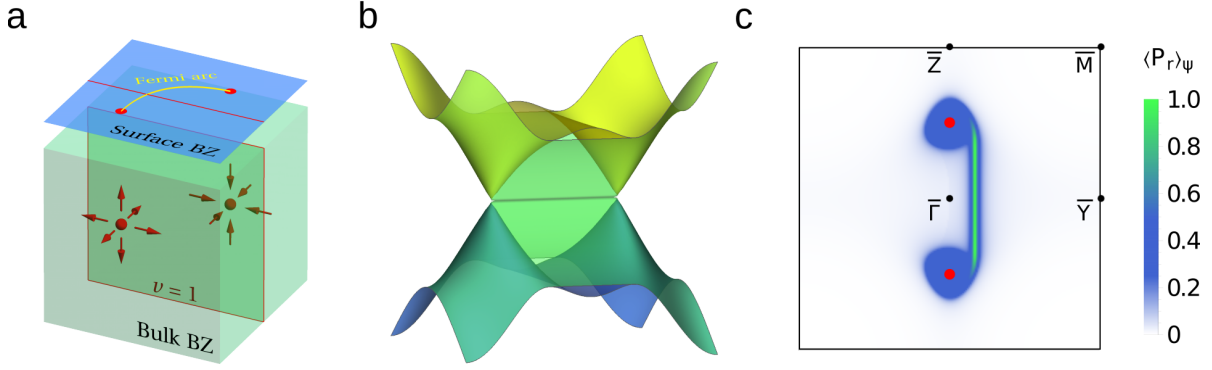


Figure 1.6.: Surface states for the Weyl semimetal of Eq. 1.4.50 with $M = 2$. **a** Bulk and surface Brillouin zones. The Fermi arc can be understood as an ensemble of surface states for 2D subsystems with the non-zero Chern number $\nu = 1$, which must exist due to the Berry curvature (red arrows) emitted from the Weyl points (red spheres), adapted from [181]. **b** Energy bands for a slab with open boundaries in k_x direction, cf. Fig. 1.5a. Between the highest occupied (blue) and lowest empty (yellow) bands with pure bulk character, there are two energy levels associated to the Fermi arcs (green). **c** Surface density of states at one of the two surfaces for the x -terminated slab with 50 layers at the energy $E = -0.5$, cf. Sec. 1.4.6. A single Fermi arc (green) connects the pockets (blue) around the projections of the Weyl points.

1.4.5. Constructing tight-binding models

In the previous section we used a well-known Hamiltonian, but once we look beyond established results we need new models. We want to study the enforced topologically band crossings in materials specified by their spatial symmetries with and without time reversal. To support the analysis of the following chapters, we devise corresponding toy models of arbitrary hopping length, which allow us to double-check that enforced band crossings are not hidden or obstructed by other features. Such generic tight-binding models not only illustrate the band crossings, but also yield information about chiralities, symmetry eigenvalues, topological invariants, surface states, and accidental crossings as well as which terms must be included to avoid the latter.

As we have constructed several dozen generic tight-binding models over the course of this work, we implemented an automatic algorithm, which generates a generic model from the input of generating symmetries in Seitz notation and a representant of a Wyckoff position. Hopping terms are included up to a freely selectable distance between the sites. To this end, we first generate all remaining symmetries and sites of the Wyckoff position, which is represented

as a point in real space with a spin-1/2 spinor attached to it. Then, all symmetry operations are reformulated in terms of the action on the tight-binding orbital basis as well as a matrix specifying the real space action. The action on the orbital basis combines the action on the Wyckoff positions, the phase factors, e.g., from spin matrices, and the information whether the symmetry contains the complex conjugation. This procedure is a transparent way to obtain band structures, which do not contain any superfluous orbitals or hopping terms unless they are explicitly introduced. For one reference site O_1 all hopping terms to other sites within a specified range are collected and represented by tuples like

$$\tilde{t} = (\Delta_x, \Delta_y, \Delta_z, O_1, O_2, t_{O_1, O_2}), \quad (1.4.51)$$

where $\Delta_{x,y,z}$ correspond to the components of the vector connecting two orbitals O_1 and O_2 , which are related by a hopping term t_{O_1, O_2} . By application of the symmetries onto the hopping \tilde{t} one obtains all symmetry allowed terms, whereas forbidden hopping terms cancel in this process. The list of real space hopping is then subjected to the discrete Fourier transformation resulting in the Hamiltonian $H(\mathbf{k})$ and the corresponding symmetries can be obtained by adding phase factors of the form $\exp(i\mathbf{k} \cdot \Delta\mathbf{r})$, whenever translation or rotations, acting on the sites in real space, move them outside of the original unit cell.

1.4.6. Determination of surface states

To study surface states in the framework of tight-binding models, we undo the discrete Fourier transformation in one direction to remove the corresponding periodic boundary conditions, while choosing a finite number of layers. The result is a slab, but naturally the process can be repeated to obtain a rod or a parallelepiped geometry for a finite crystal under consideration.

For example, suppose we want to construct the model of a slab for a given bulk system $H(\mathbf{k})$, which is described by the primitive basis vectors $\mathbf{a}_1, \mathbf{a}_2, \mathbf{a}_3$. The slab shall for concreteness be spanned by the vectors $\mathbf{a}_1, \mathbf{a}_2$, and we choose \mathbf{a}_3 as the direction, which will be finite. When we undo the Fourier transform corresponding to \mathbf{a}_3 for a Hamiltonian given in block-diagonal form, comprising the matrices $H(\mathbf{k})$, then all terms including k_3 , the crystal momentum corresponding to \mathbf{a}_3 , will couple different layers of the slab. To see this, we sort the Hamiltonian $H(\mathbf{k})$ into terms of identical powers of k_3 , i.e., of the same translation $\delta r_3 \in \mathbb{Z}$, where we give components in their corresponding length scale, i.e., r_3 and δr_3 are given in units of $|\mathbf{a}_3|$. Hereby, the distances δr_i should not be confused with r_i , which gives the absolute real space coordinate of a unit cell. Thus, we obtain the Hamiltonian H_{slab} for a slab with N layers, where each layer

by [81]

$$\begin{aligned}\rho_n(\omega, \mathbf{k}_\perp) &= -\frac{1}{N} \text{Im} \frac{\phi_n(\mathbf{k}_\perp)^\dagger P_{\text{surface}} \phi_n(\mathbf{k}_\perp)}{\omega + i\Gamma/N - E_n(\mathbf{k}_\perp)}, \\ \rho(\omega, \mathbf{k}_\perp) &= \sum_n \rho_n(\omega, \mathbf{k}_\perp),\end{aligned}\tag{1.4.54}$$

where E_n is the eigenvalue corresponding to ϕ_n , and P_{surface} is the projector onto the surface, which we typically define to contain the first five unit cells. For topological surface states, with an exponential decay of the wave function into the bulk, the choice of surface thickness has no qualitative effect. Here, Γ is just introduced to broaden the weight of a single eigenstate in energy. This reflects to some extent experimental reality as well as the numerical necessity that only a finite number of parameters k_x, k_y can be taken into account. The contribution $\rho_n(\omega, \mathbf{k}_\perp)$ of all bands has to be summed, because the surface density of states can also be dominated by bulk states, which happens if they fall on top of each other in energy. If the surface contribution shall be highlighted, one may show only the largest value at each position, i.e., $\max(\{\rho_n(\omega, \mathbf{k}_\perp) \mid n = 1, \dots, NM\})$.

To characterize the surface states, it can be useful to consider in place of the projector P_{surface} another observable. In the context of topological insulators or Weyl semimetals, we will use in the course of this work also spin matrices as well as projectors on specific orbitals in combination with the original surface projection.

1.4.7. Topological versus trivial surface states

Most topologically non-trivial systems with open boundary conditions must have a surface state that corresponds to the value of their topological invariant. The converse is generally not true, because there are several trivial ways to obtain surface states.

Two types of surface states are commonly distinguished, Tamm-Goodwin [182] and Maue-Shockley states [183]. While both decay exponentially as a function of the distance from the surface, the former type originates from localized surface effects, e.g., disorder at the termination, hereby a potential splits a state from the bulk and localizes it on the surface [184, 185]. In real solid state systems one must also consider surface reconstruction, when cutting a crystal to describe the surface there will be dangling bonds, which are energetically unfavorable. To minimize their free energy the surface atoms may form new bonds or reconfigure their oxidation state [186]. During the synthesis also adatoms may attach to the surface, which together with dangling bonds may contribute to surface states [187]. If the Tamm-Goodwin states occur without such defects, there must be some effective defects due to a modulation of

the lattice [188, 189]. A potential truncated away from its symmetry centers, would also lead to Tamm-Goodwin states [190].

The Maue-Shockley states are situated within the bulk gap and occur as a result of a crossing of bulk bands [183, 185]. As a band inversion is often an indication of topology, it should be expected in this context. Here, the cell potential is truncated in a symmetric fashion, which distinguishes the Maue-Shockley states from the previous type of surface states [184]. Depending on the symmetry eigenvalues and the position of the truncation, Maue-Shockley states may or may not exist [190]. It has been pointed out that it is important that a single wave function must be cut when a surface is created to obtain a boundary state, naturally that is only possible if the state is not centered at an atom [191]. Consider for example an SSH chain, which may have surface states in a certain parameter range as long as the chain is cut at the right bond [192].

Even if topological surface states exist, they may not be dominating the surface physics. Consider, for example, the persistent currents implied by the chiral edge states of a Chern insulator, which may exist in the ground state since their total momentum vanishes for a finite system with both surfaces [86]. Recently, it has been predicted that occupied bulk states give an equally sized but opposite contribution to continuous topology surface currents [193]. In summary, the study of surface effects appears to be far from completed, because recently new insights have been obtained from theoretical approaches as well as from study of real materials.

To follow up on the last point, regarding the input from real materials, we will consider the implications of a nonsymmorphic symmetry at the surface. For the layered semimetal ZrSiS it has been discussed that a bulk symmetry that is broken at the surface leads to floating bands localized at the surface [73]. Although the compound contains nodal lines, the floating band is not connected to them, and the weak topological invariant also does not apply to the termination that exhibits the floating bands. The states appear as truly trivial. It has been shown that the surface makes atomic sites inequivalent, which in the bulk are related by nonsymmorphic symmetries, thus breaking the symmetries, and lifting the degeneracy of bands along one of the high-symmetry lines. In the next chapter the idea that nonsymmorphic symmetries may lead to surface states and a nontrivial topology will be studied in more detail by considering the enforced topological band crossings, which result from nonsymmorphic symmetries.

2. Topological band crossings

The crossing of bands near the Fermi energy can be important in many regards. It may dominate the low-energy behavior for properties which require transitions from filled to empty states, hence offering the possibility to find a simplified model description. Topological (semi)metals can give an additional twist to such descriptions by correlating crystal momentum to spin polarization. Furthermore, topology leads to characteristic features in the response functions and the surface spectra, see chapter 1. Here, we will show that band crossings in topological (semi)metals may be obtained in various ways. At topological phase transitions, as we discussed in Sec. 1.3.4, the band gap must close. They may occur protected by symmetry or fine tuning of parameters. Their existence may be even concluded from the symmetries by general arguments, as well as from band indicators or compatibility relations, once a specific order of representations, i.e., a specific material is considered. Those approaches may include a calculation or inference of topological invariants indicating the presence of crossings without fixing their exact positions.

As several seminal approaches in the literature [142, 194, 195] have used a specific material as a starting point for which the realized band structure is analyzed and compared to all possibilities arising from how orbitals may be placed on a lattice, we present in this chapter a complementary approach [1–3, 196]. We focus on compatibility relations and bypass a choice of specific orbitals, hence all our features must exist in any band structure obtained from a specific symmetry. In this chapter we aim to give a comprehensive picture of all symmetry arguments that imply band crossings and highlight any topological content in the process. While our approach lacks the generality to detect for example fragile topological phases, it will be easier to conclude what type of band crossings lead to the realized dimensionality of an elementary band representation, due to the direct use of space group elements.

2.1. Preliminaries

Before diving into the details of the different ways to combine symmetries to obtain band crossings, we shall give here some preliminary remarks. Generally, we count the number b of

occupied states up to the band in question and consider after the crossing the energy level with the same value of b to belong to the same band. Alternatively, when following bands through the BZ we may follow an energy eigenvalue through a gapless crossings by considering its symmetry content to recognize the original band after the crossing. Both descriptions will prove useful in the following sections.

2.1.1. Enforced and accidental features

The following discussions will have several different goals. One might be interested in the smallest set of connected bands, searching for the simplest arrangement of *enforced* crossings, which follows the spirit of elementary band representations. We regard a crossing to be enforced, if the connectivity of bands requires its existence even in the simplest arrangement of bands. An arrangement is simple if it incorporates the fewest crossings. In addition, one might want to consider the possible *accidental* crossings, in the hope to find those by chance in the vicinity of the Fermi energy. Accidental crossings commonly arise between bands of different representations. In that case, a difference in the symmetry eigenvalues prohibits the introduction of a coupling term between the intersecting bands, which would create a band gap. In principle, accidental crossings may be obtained by fine-tuning even without symmetry protection, but in the large parameter spaces underlying condensed matter systems they are of vanishing probability [10].

In our discussions of enforced topological semimetals, we must not overlook the fact that the topological content of enforced features may be qualitatively changed if accidental crossings occur. This will play a crucial role in our considerations about the topology associated to nodal planes. In this spirit crossings of different dimensions may influence each other, i.e., nodal lines may coexist with nodal points at the same energy or even overshadow them if their intersection is non-empty.

2.1.2. Kramers theorem

We have discussed in Sec. 1.2.4 the double group representations, which arise when time-reversal is added to a crystallographic group. The possible representations have been comprehensively determined [88] and have recently been made accessible in an online database [137]. For our study of topological band crossings it is mandatory to consult these tables. But to understand the emerging crossings, to predict which symmetries are actually relevant for a given representation, to infer topological charges, and directly access the compatibility relations it turned out to be fruitful to rely on a more hands-on approach. We will explicitly construct

representations and retain their symmetry labels. To perform this approach we must understand how symmetry eigenvalues are paired by the various other symmetries. In this section we discuss the effects of time-reversal symmetry (TRS) and present extensions of Kramers theorem (cf. Sec. 1.2.4).

The notation for time reversal in the context of fundamental physics is \mathcal{T} or T , but since we use $T(x, y, z)$ for a translation with the vector (x, y, z) , we use θ for time-reversal in the following chapters, to avoid any confusion. Although we call time reversal a symmetry, it is not a symmetry in the same sense of spatial operations, because it contains the complex conjugation and it does not share common eigenstates with the Hamiltonian. If a TRS is present we have to consider whether Kramers theorem applies [197–199]. Originally, the Kramers degeneracy was derived for atomic energy levels in the presence of an electric field, where the levels retain a twofold degeneracy if the total spin has a half-integer value. Kramers theorem was formalized by Wigner [110] and states that the time-reversal operation acting on a state with an odd number of electrons creates a second state that is orthogonal to the first, but has an identical energy. In the course of this work we will reconsider this result for spinless and spinful systems, where TRS may also include a translation due to magnetic order [2].

Independent of the details, time reversal θ is antiunitary and must always contain the complex conjugation K . To be specific it can be written as $\theta = UK$, where U is a unitary matrix. The first condition for the proof of Kramers theorem is that $\theta^2 |\psi\rangle = a |\psi\rangle$, with $a \in \mathbb{C}$ and $a \neq 1$. Additionally, TRS shall be fulfilled with $\theta H(\mathbf{k}) = H(-D_U \mathbf{k})\theta$ for the Hamiltonian $H(\mathbf{k})$ in reciprocal space, where D_U is an orthogonal matrix representing the group element U in reciprocal space. This symmetry leads to a symmetry of the band structure $E(\mathbf{k}) = E(-D_U \mathbf{k})$. We consider in the following points in the BZ with $\tilde{\mathbf{k}} = -D_U \tilde{\mathbf{k}}$, which holds up to a reciprocal lattice vector, and omit the \mathbf{k} dependency to simplify the notation. Let $|\psi\rangle$ be an eigenstate of the Hamiltonian $H |\psi\rangle = E |\psi\rangle$ and one finds

$$\langle \psi | \theta \psi \rangle = \langle \theta^2 \psi | \theta \psi \rangle = a^* \langle \psi | \theta \psi \rangle, \quad (2.1.1)$$

where we have used the antiunitary property of $\langle \psi | \phi \rangle = \langle \theta \phi | \theta \psi \rangle$. As long as $a^* \neq 1$ we can conclude from Eq. 2.1.1 that $\langle \psi | \theta \psi \rangle = 0$ and thus $|\psi\rangle$ and $|\theta \psi\rangle$ are two orthogonal eigenstates of H with the same energy. Thus, one finds the point $\tilde{\mathbf{k}}$ hosts a degeneracy of the band structure.

To illustrate Kramers theorem we consider different possible time reversal operations θ . Without spin $\theta = K$ thus $\theta^2 = +1$, hence Kramers theorem does not apply. Still, $\theta = K$ pairs complex eigenvalues at TRIMs, e.g., in trigonal, hexagonal, or cubic space groups without Kramers theorem. Nevertheless, if time reversal is a combination of a spatial operation with the complex conjugation K , Kramers theorem can still be fulfilled, e.g., when combined with a twofold screw rotation we have: $\theta = C_2^z(0, 0, 1/2)K$, where $a^* = -1$ at $k_z = \pi$. This will proof

to be a valuable asset in our discussion of nodal planes in Sec. 2.2.3. Beyond this example one may consider even symmorphic symmetries leading to a degeneracy once combined with a TRS without spin. Take the composite symmetry PC_4K including a rotoinversion PC_4 , which leaves the lines (k, k, k_z) for $k \in \{0, \pi\}$, $k_z \in [-\pi, \pi]$ invariant. The symmetry squares to $(PC_4K)^2 = C_2$, which has the eigenvalues $\lambda_{C_2} = \{1, -1\}$. It is no accident that we have stated the first condition of Kramers theorem with $\theta^2 |\psi\rangle \neq |\psi\rangle$ instead of $\theta^2 \neq 1$, because here one finds that the theorem applies if $C_2 |\psi\rangle$ yields its -1 eigenvalue. Thus if $\lambda_{C_2} = -1$ bands will be Kramers degenerate and remain nondegenerate for $\lambda_{C_2} = 1$, as it occurs in space group (SG) 111 ($P\bar{4}2m$) with time reversal, which contains the necessary symmetry.

For spinful representations $\theta = i\sigma_y K$ is a valid representation of time reversal, which can be deduced by demanding that spin matrices $\propto \sigma_i$ have to obtain a minus sign when commuted with θ [110]. In the following we discuss several different examples with a spinful TRS. Since $\theta^2 = -1$ already holds, all TRIMs are twofold degenerate. Again, $\theta' = C_2^z(0, 0, 1/2)\theta$ will lead to the same degeneracy at $k_z = \pi$ as before. Here, the spin representation of a twofold screw rotation $C_2^z(0, 0, 1/2)$ contributes $i\sigma_y$ and thus it also squares to -1 and one obtains $\theta'^2 = -1$. An important combination is $P\theta$ with $(P\theta)^2 = -1$, which leaves any \mathbf{k} invariant, resulting in an at least twofold band degeneracy of all bands, which occurs in any centrosymmetric space group. To gain an intuitive understanding of type IV magnetic space groups, which include some possible types of antiferromagnetic order, one must consider $\theta' = T(x, y, z)\theta$ with $x, y, z \in \{0, \frac{1}{2}\}$, where at least one component x, y, z is non-zero. Then $\theta'^2 = -1$ only if $(x, y, z)^T \cdot \mathbf{k} = 0$, which excludes, for example, in a primitive cubic BZ four out of eight TRIMs. The remaining four TRIMs would be at least twofold degenerate by Kramers theorem. As before, one may consider $PC_4\theta$, where now the degeneracy is not eigenvalue dependent, because $\lambda_{C_2} \in \{+i, -i\}$ and thus $a^* \neq 1$ is always true. In this case Kramers theorem becomes independent of the paired eigenvalues and all magnetic corepresentations are twofold degenerate, cf. [88, 137].

Note that for the spinful case, the above arguments of additional degeneracies may become obsolete if the case with inversion P symmetry holds. Then, PT already pairs the bands and any other combination of symmetries may not lead to additional independent states.

Finally, we note that also within the spinful representations eigenvalue dependent pairing still occurs, for example due to $\theta' = C_4^z(a, b, c)\theta$ with $c = \frac{1}{4}$ or $\frac{3}{4}$. In this case $\lambda_{C_2} \in \{+1, -1\}$ at $k_z = \pi$ and due to $\theta'^2 = -1$ one concludes that only if $\lambda_{C_2} = +1$ Kramers theorem holds with $a = -1$ and the bands are paired. We will see that this principle leads to double Weyl points in the tetragonal SG 80 ($I4_1$), cf. Sec. 3.2.

For completeness we want to discuss a common proof by contradiction of Kramers degeneracy. Suppose we hypothesize a linear dependency between the time-reversal related state $\theta |\psi\rangle$ and the original eigenstate, $\theta |\psi\rangle = \exp(i\varphi) |\psi\rangle$ with some phase $\varphi \in \mathbb{R}$. It follows from repeated

substitution that

$$\begin{aligned} |\psi\rangle &= \exp(-i\varphi)\theta|\psi\rangle = \exp(-i\varphi)\theta(\exp(-i\varphi)\theta|\psi\rangle) = \theta^2|\psi\rangle \\ &= a|\psi\rangle \end{aligned} \tag{2.1.2}$$

and thus $|\psi\rangle$ cannot be a non-zero eigenstate of the Hamiltonian. The assumption is found to be wrong and thus $\theta|\psi\rangle$ and $|\psi\rangle$ must be linearly independent. One finds that as both states have the same energy, the bands are at least twofold degenerate. The proven statement is weaker than the original formulation using Eq. 2.1.1, because the orthogonality is not shown, but for the purpose of band topology this formulation also suffices.

Equipped with arguments like those illustrated above, one can understand already different types of point/line/plane crossings and anticipate band degeneracies without an extensive browsing of group representation tables.

2.1.3. Topological charges

In our endeavor to find topological (semi)metals, the topological charges and invariants to classify band structures play a crucial role. With the tools described in Sec. 1.4 we can quantify the topology. A complete analysis should check that the Nielsen-Ninomiya theorem is satisfied [83], which enables us to infer the presence of additional band crossings. This shall be illustrated by two examples.

Consider SG 1 ($P1$), which only contains eight Weyl points at the TRIMs due to Kramers theorem. If we have a specific system given within DFT or as a tight-binding model then we have no handle to infer symmetry enforced relations between these topological crossings as no symmetry other than TRS is present. But should an explicit calculation tell us that the total charges contributed by all Weyl points do not add up to zero but to two, then one can infer that there must be two additional Weyl points away from TRIMs, which carry the opposite charge to cancel those one finds at the TRIMs. Such a simple argument gives an indication when it is worth to search away from high-symmetry paths, here, away from high-symmetry points, for accidental crossings.

While the previous example only considered an accidental feature, we will see that the charges of topological nodal planes follow a similar argument. In this case Weyl points are enforced, but cannot be canceled by any other enforced or accidental Weyl points, thus other gapless features must also be non-trivial. This raises the following question: How it can be known that other, accidental charges are not able to cancel the charges from the enforced Weyl points?

We will study in the following how symmetries affect and relate the chiralities $\nu_{\mathbf{k}}$ of Weyl points at the positions \mathbf{k} . In Sec. 1.4.2 we have considered the same for the Berry curvature and we will use these results here. The chirality is given by an integration of the Berry curvature on a surface enclosing a nodal manifold. By convention the normal vector of the surface points outward and we need to consider only the action of symmetries on the corresponding normal component of the Berry curvature and how the symmetries relate different parts of the surface to each other.

Rotation symmetries C_n map the normal component of the curvature identically to other positions on the surface of the manifold, thus rotations leave chiralities unchanged $\nu_{\mathbf{k}} = \nu_{D_{C_n}\mathbf{k}}$. Inversion does not change the curvature at all but it inverts the positions on our integration area. For a cube, as an example, that means that an outward pointing normal component of the Berry curvature is moved such that it ends up on the opposite side of the cube pointing in the same direction. Hence, the transformed vector then points inward into the cube, i.e., we have the transformation $\hat{\mathbf{n}} \cdot \boldsymbol{\Omega}(\mathbf{k}) \xrightarrow{P} (-\hat{\mathbf{n}}) \cdot \boldsymbol{\Omega}(-\mathbf{k})$. As a consequence, inversion flips the sign of the chirality $\nu_{\mathbf{k}} = -\nu_{-\mathbf{k}}$. One can obtain mirror symmetries as the combination of twofold rotations with inversion, combining their actions on the chirality to change the sign $\nu_{\mathbf{k}} = -\nu_{D_M\mathbf{k}}$. The same is true for rotoinversions. Time-reversal symmetry comprises both an inversion of \mathbf{k} to $-\mathbf{k}$ while also adding a minus sign to the curvature vector, and thus preserving the chirality, giving $\nu_{\mathbf{k}} = \nu_{-\mathbf{k}}$. Combinations of TRS with other symmetries follow in an analogous manner.

By considering how a Weyl point somewhere in the BZ is transformed by other symmetries one obtains its minimal multiplicity and gains insight into how the compensation of Chern numbers is restricted. From these considerations commonly a statement of fundamental importance is made: Weyl points may, in the presence of TRS, only occur in multiples of four [10, 20, 57, 200–203]. To obtain this result one notes that TRS relates a Weyl point with charge ν at \mathbf{k} to a second Weyl point of the same chirality ν at $-\mathbf{k}$. We know that the sum of all chiralities should cancel, therefore two additional Weyl points with a chirality of $-\nu$ must exist, and thus there must be at least four Weyl points [13, 203]. Although this is an often recited statement, it is untrue in the generality used above. We will see in Sec. 3.2 that this statement is wrong even for some nonmagnetic systems, in disagreement with the findings of Ref. [20].

Let us phrase the statement more precisely: The minimal number of Weyl points in a time-reversal invariant Weyl semimetal is four, if the band gap does only close at Weyl points and the time reversal θ fulfills $\theta^2 = -1$. Semimetals are considered in the sense that there is a direct, but not necessarily an indirect, band gap everywhere in the BZ, except at the Weyl points. There are two changes to the original statement. First, the implicit assumption that the Weyl points are different at the time-reversal related positions \mathbf{k} and $-\mathbf{k}$ is inaccurate. Consider the time-reversal invariant momenta, where $\mathbf{k} = -\mathbf{k} + \mathbf{G}$ with a reciprocal lattice vector \mathbf{G} . At

such momenta the time-reversal-related Weyl points are identical. While there are always eight TRIMs, it is possible that some of them are part of nodal lines or planes, which can reduce the number of Weyl points below four. One can exclude these cases by restricting the statement to Weyl semimetals, where only Weyl points close the band gap. Second, it matters how the time-reversal operation is represented, if one considers the case without spin, where $\theta = K$ and $\theta^2 = +1$, Kramers theorem is not fulfilled and a general TRIM will not host a Weyl point at all. A band degeneracy then depends on the presence of other symmetries. We will discuss this in more detail in the section on Kramers-Weyl points below, cf. Sec. 2.2.1, where we will show a system without SOC, i.e., with $\theta^2 = +1$, hosting Weyl points only at three out of the eight TRIMs. Once these cases are excluded as well, the original argument for the multiplicity of Weyl points holds.

In the course of this work we introduce additional cases, where Weyl points occur in multiplicities of less than four. In fact all multiplicities below four are possible [2, 3, 204]. This concludes the preliminaries and we are now equipped to understand various arguments leading to topological band crossings.

2.2. Conditions for nodal features

The Wigner-von Neumann theorem states that eigenvalues of Hermitian matrices do not cross without a reason [11]. In the following section we want to discuss what information one can obtain from global external and internal symmetries, cf. Sec. 1.2, for the existence of nodal points, lines, and planes. Before diving into the different types of crossings, we want to give a quick introduction how compatibility relations arise in the formalism used in this exposition.

The eigenvalues or representations on different paths in the BZ are not independent, they must fulfill compatibility relations. While these compatibility relations are tabulated in Ref. [88, 137], it is instructive to consider the problem independently to find out in which cases one should expect something nontrivial to happen. The principle idea is to have mutually commuting symmetries, such that the eigenstates will be simultaneously eigenstates of all involved symmetry operators. If this happens, for example, at the intersection between different rotation axes, there will be a condition that relates the symmetry eigenvalues between axes to each other. These compatibility relations connect the behavior on different axes, which can enforce additional crossings [94].

This happens, for example, if there are three twofold rotations with mutually perpendicular rotation axes which multiply to the identity operation [104, 105, 205]. The twofold screw rotations $\tilde{C}_2^x = C_2^x(\frac{1}{2}, \frac{1}{2}, 0)$, $\tilde{C}_2^y = C_2^y(0, \frac{1}{2}, \frac{1}{2})$, and $\tilde{C}_2^z = C_2^z(\frac{1}{2}, 0, \frac{1}{2})$ commute at a TRIM (k_x, k_y, k_z)

if $k_x + k_y + k_z = \pi \pmod{2\pi}$ and their product is $\tilde{C}_2^x \tilde{C}_2^y \tilde{C}_2^z = i\sigma_x i\sigma_y i\sigma_z = 1$ [205]. If one picks the TRIM (π, π, π) then the respective eigenvalues are $\lambda_{\tilde{C}_2^x}, \lambda_{\tilde{C}_2^y}, \lambda_{\tilde{C}_2^z} \in \{+1, -1\}$. To obtain a relation between the rotation eigenvalues, one applies the product of all rotations to their common eigenstate $|\lambda_{\tilde{C}_2^x}, \lambda_{\tilde{C}_2^y}, \lambda_{\tilde{C}_2^z}\rangle$. Their action onto their common eigenstate yields the product of their respective eigenvalues, whereas additionally the product of rotation operators fulfills $\tilde{C}_2^x \tilde{C}_2^y \tilde{C}_2^z = 1$, and thus one obtains

$$\begin{aligned} |\lambda_{\tilde{C}_2^x}, \lambda_{\tilde{C}_2^y}, \lambda_{\tilde{C}_2^z}\rangle &= \tilde{C}_2^x \tilde{C}_2^y \tilde{C}_2^z |\lambda_{\tilde{C}_2^x}, \lambda_{\tilde{C}_2^y}, \lambda_{\tilde{C}_2^z}\rangle = \lambda_{\tilde{C}_2^x} \lambda_{\tilde{C}_2^y} \lambda_{\tilde{C}_2^z} |\lambda_{\tilde{C}_2^x}, \lambda_{\tilde{C}_2^y}, \lambda_{\tilde{C}_2^z}\rangle \\ \Leftrightarrow \lambda_{\tilde{C}_2^x} \lambda_{\tilde{C}_2^y} \lambda_{\tilde{C}_2^z} &= 1. \end{aligned} \tag{2.2.1}$$

Eq. 2.2.1 restricts the possible eigenvalue triples to be $(1,1,1)$, $(-1,-1,1)$, $(-1,1,-1)$, or $(1,-1,-1)$. In other words, two eigenvalues determine the third. Together with the pairing of different eigenvalues at $(\pi, \pi, 0)$, $(\pi, 0, \pi)$, $(0, \pi, \pi)$ one can deduce that on the rotation axes bands must exchange an odd number of times, giving rise to at least one enforced crossing [205]. The discussed symmetries occur in SG 19.

Another possibility would be to consider two mirror symmetries and a twofold rotation. In this case we obtain, using similar arguments as above, insights into the arrangement of nodal lines for certain tetragonal space groups, see Sec. 3.2.2.

2.2.1. Nodal points

One may divide nodal points into chiral crossings including Weyl points carrying a non-zero Chern number and non-chiral crossings including Dirac points. The former are typically two-fold degenerate crossings with unit charge, but more generally they can exhibit higher degeneracies and larger values for their charge. We follow the notation of [2] and denote Weyl points as twofold (fourfold) if they consist of two (four) bands. If their charge is larger than one we refer to them as double (quadruple) Weyl points for chiralities of $\nu = 2$ ($\nu = 4$). Besides Weyl points there are multifold crossings which carry more than one Chern number as they may be enclosed at more than one value of the band index b with a gapped integration surface for the curvature.

A group without mirror or inversion symmetries is termed as chiral. If the little group at a nodal point is chiral, then a crossing at this point must be a Weyl point in the general nomenclature introduced above [104]. In this spirit the next section introduces Weyl points as results of Kramers theorem alone. As nodal points have been found early on as band crossings between different rotation eigenvalues [10], we proceed by deriving the restrictions imposed by rotation symmetry and the periodicity within reciprocal space. We then combine both and

describe the commonly found hourglass [206, 207] and accordion [208] shaped band structures and give an outlook on how Weyl points with higher chirality can be obtained.

Unlike the chiral crossings, Dirac points may also be topologically trivial. They occur enforced by mirror and inversion symmetries and we give some examples how they can arise. Perturbations of a Dirac point at the transition between a normal and a topological insulator may lead to either nodal points or lines [39].

Kramers-Weyl points

Kramers-Weyl points occur if there is a time-reversal symmetry θ fulfilling Kramers theorem or its extensions we discussed in Sec. 2.1.2. Especially in the spinless case, θ must be combined with a rotation or mirror symmetry to fulfill Kramers theorem, hence the invariant manifolds in the BZ will be planes or lines and no single point would be degenerate. In the spinful case $\theta = i\sigma_y K$ always fulfills Kramers theorem. This means that in the absence of any other symmetries there is a Weyl point of charge $\nu = \pm 1$ at each TRIM [104]. To illustrate what kind of Weyl points can be typically expected, we construct a tight-binding model for SG 1, which only contains the spinful TRS. In this minimal model there are two bands, which are split by SOC and exhibit the Kramers-Weyl points at all TRIMs, see Fig. 2.1a. All Weyl points on the plane $k_z = 0$ exhibit a chirality of $\nu = 1$, whereas at $k_z = \pi$ the charges are $\nu = -1$. The model parameters are chosen at random without fine-tuning to highlight the difficulties to obtain Weyl points at the same energy. Note that if the Weyl points are not at the same energy, one cannot observe Fermi arcs that directly connect the projections of the Weyl points, which is true independently of the chemical potential [104]. The advantage of Kramers-Weyl points on the other hand is that they always have a large separation in reciprocal space, which can lead to a large anomalous Hall effect, cf. Eq. 1.2.20.

As we explained in the previous sections, Kramers-Weyl points are not limited to TRIMs. If the lattice type is non-primitive it is possible that certain corners of the BZ can be invariant under a composite TRS. Let us consider SG 80 ($I4_1$) with TRS but without spin, cf. Sec. 3.2 for the spinful case. The point $P(\pi, \pi, \pi)$ is no TRIM, but invariant under $\theta' = \tilde{C}_4^z \theta$ with the screw rotation \tilde{C}_4^z around the z axis. If we consider $(\theta')^2 = \tilde{C}_2^z$ and the eigenvalues $\lambda_{\tilde{C}_2^z} = \pm i$ of the rotation at P, we find that Kramers theorem applies. In fact, the two possible bands with representations given by the eigenvalues $\lambda_{\tilde{C}_2^z} = i$ and $\lambda_{\tilde{C}_2^z} = -i$ are paired to each other. When searching enforced Weyl points, we must ask how the point at P transforms under the symmetries. The group is simple and only \tilde{C}_4^z remains, which relates the two distinct but equivalent points with label P to each other and thus there are two Weyl points each of charge ν_P . We are clearly missing at least one crossing. The eigenvalues of the fourfold screw rotation

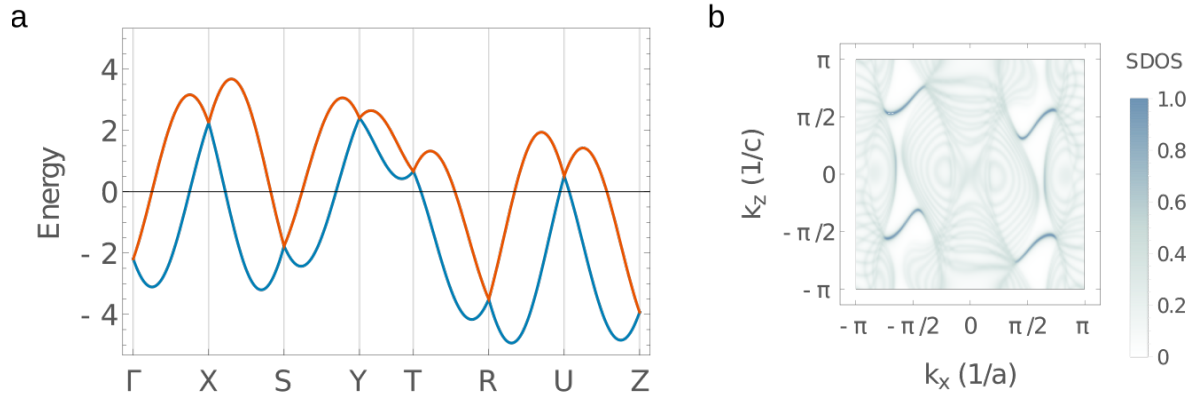


Figure 2.1.: *Generic tight-binding model of SG 1 including spinful TRS with up to third nearest neighbor hopping. **a** Band structure with orthorhombic labels, where each of the eight TRIMs hosts a Kramers-Weyl point. **b** Surface density of states for a slab in (010) termination at the energy equal to -1. Fermi arcs occur within the gap of the bulk bands.*

are $\lambda_{\tilde{c}_4} = \exp(i\frac{\pi}{2}p + ik_z/4)$ with $p \in \{0, 1, 2, 3\}$, cf. Eqs. 1.2.30 and 2.2.3. On the fourfold rotation axis at the TRIMs, Γ and M each with $k_z = 0$, the TRS will pair bands according to their eigenvalues defined by p . If we label such a degeneracy by (p_1, p_2) then the possible crossings are between $(1, 3)$. Note that a band that has a crossing with eigenvalues $(1, 3)$ at Γ will have real eigenvalues without crossing at M and vice versa.

We generate a generic tight-binding model for SG 80 without spin-orbit coupling to double check our assessment, see Fig. 2.2. In our generic model with random parameters we find that the chirality of the double Weyl point at M is $\nu_M = -2$ and each of the single Weyl points at P (or P') carries $\nu_P = +1$. The quadratic dispersion close to M along the line X - M together with the linear dispersion along M - Z_1 is a characteristic feature of the double Weyl point at M .

With this example we extended the notion of TRS enforced nodal points in two ways. We have shown that Kramers-Weyl points can also appear at points other than the TRIMs, and that time reversal may simply pair rotation values of opposite charge. Notably, we illustrated this with a space group that only enforces three Weyl points, which is a rather uncommon feature.

Rotation symmetry

In the following paragraphs we devise restrictions on the number of band crossings on rotation axes by combining the periodicity of the BZ with one-dimensional representations to label the bands. In this way one obtains the possible multiplicities of band crossings, which will be a crucial result to infer the topological character of nodal planes in Section 2.2.3. As we

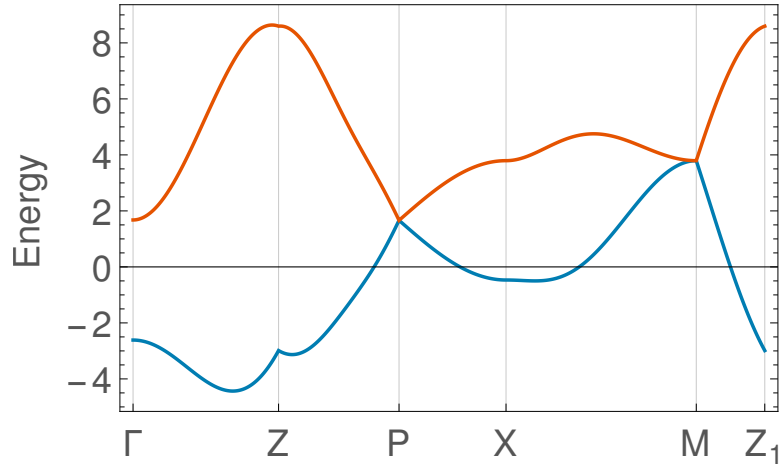


Figure 2.2.: *Generic tight-binding model of the body-centered SG 80 without spin. The Kramers-Weyl points at P and the double Weyl point at M compensate their topological charges. The used Brillouin zone labels are defined in Fig. 3.6.*

neglect time-reversal symmetry, the results of this chapter will directly apply to ferromagnetic systems with spin-polarized bands as well as models with spinless constituents. Nevertheless, the results are relevant to all chiral space groups with a rotation symmetry.

In the simplest case, in the absence of TRS, the little group is generated only by a single n -fold (screw) rotation $C_n(x, y, \frac{m}{n})$. The fractional lattice translations $x, y \in \mathbb{Q}_{\geq 0}$ play for now no further role. The translation along the rotation axis is a fraction, where $m < n$ with $m, n \in \mathbb{N}$. Note that for translation invariant systems the value n may only take the values 2,3,4, or 6. By considering the n th power of this operation, its possible eigenvalues can be found.

$$(C_n(x, y, \frac{m}{n}))^n = \exp(i\pi s) T(0, 0, m) = \exp(i\pi s + imk_z), \quad (2.2.2)$$

where $s = 1(0)$ for the spinful (spinless) case. We have used the projective representation for translations or equivalently replaced the translation operation by its eigenvalue if acting on a state of the Hilbert space. By taking the n th root on both sides one finds the following possible eigenvalues λ_{C_n} of the symmetry

$$\lambda_{C_n} = \exp\left(i \frac{2\pi p + s\pi + mk_z}{n}\right), \quad (2.2.3)$$

where $p \in \mathbb{Z}$ parametrizes the multivalued property of the complex root. The eigenvalues λ_{C_n} found with Eq. 2.2.2 and 2.2.3 can be considered as the different representations of the rotation group generated by $C_n(x, y, \frac{m}{n})$. In total there are n representations. Each representation can be labeled by its respective value of p , where $p \in \{0, 1, \dots, n-1\}$.

If the rotation is symmorphic, $m = 0$, we can already understand accidental crossings and use the eigenvalues to infer the topological charge of an accidental Weyl point or, in the presence of

TRS, of a Kramers-Weyl point [209]. The same is true for $m \neq 0$ with the caveat that there the eigenvalues exchange along high-symmetry paths through the BZ, due to their k_z dependence. If k_z is increased by 2π for the eigenvalue of a nonsymmorphic symmetry, then p must change by 1, a phenomenon known as monodromy [95]. An enforced connectivity of bands with different eigenvalues is the result, which will be discussed in the context of hourglass and accordion states in the next section, once TRS is assumed. To understand the restrictions on the eigenvalues we shall consider in the following paragraphs how the eigenvalues evolve as a function of k_z .

In the following we consider a band structure that is filled up to the band b , i.e., at each \mathbf{k} there are b energy levels occupied. The chirality of a crossing between bands labeled by λ_b and λ_{b+1} depends on the fraction λ_b/λ_{b+1} , i.e., the eigenvalues of $C_n(x, y, \frac{m}{n})$ for bands b and $b+1$. It is the change in symmetry eigenvalue that fixes the topological charges [209]. Equivalently, the topological charge is fixed by the change in phase $\Delta\varphi_{b,c} = \varphi_b(k_c + \delta) - \varphi_b(k_c - \delta)$ of the exponentials in Eq. 2.2.3, for a crossing c at k_c and a small $\delta > 0$. As we move along the rotation axis, the phase of $\lambda_b = \exp(i\varphi_b(k_z))$ of band b at k_z accumulates to

$$\varphi_b(k_z) = \frac{2\pi p + s\pi + mk_z}{n} + \sum_{k_c \leq k_z} \Delta\varphi_{b,c}, \quad (2.2.4)$$

where we include all phase changes $\Delta\varphi_{b,c}$ due to a finite number of crossings at different k_c . While in principle arbitrarily many phase changes $\Delta\varphi_{b,c}$ might occur along the rotation axis from $k_z = -\pi$ to $k_z = \pi$, the periodicity of the BZ demands that their sum compensates the nonsymmorphic winding. In other words, by the continuity of the eigenvalue one obtains $\varphi_b(-\pi) = \varphi_b(\pi) \pmod{2\pi}$ which simplifies to

$$\sum_{k_c \in [-\pi, \pi)} \Delta\varphi_{b,c} + 2\pi \frac{m}{n} = 0 \pmod{2\pi}. \quad (2.2.5)$$

Naturally, bands adjacent in energy are not independent. For a mutual crossing c' the phase changes $-\Delta\varphi_{b,c'} = \Delta\varphi_{b+1,c'}$ must be opposite in sign. We now regroup the crossings c by sorting their phase changes $\Delta\varphi_{b,c}$ of band b into the crossings c_b with the next higher band $\Delta\varphi_{b,c_b}$ and the crossings c_{b-1} with the band below $-\Delta\varphi_{b-1,c_{b-1}}$. The names of the crossings c are replaced by c_b and denote only the crossings to the next higher band. There must always be a band edge without any crossings to the bottom (or equivalently to the top) from which we will obtain iteratively conditions of the form given in Eq. 2.2.5.

To illustrate the implications of Eq. 2.2.5 for the emergence of nodal points we shall consider a minimal example. For a twofold symmorphic rotation $n = 2, m = 0$ the changes in phase are always $\Delta\varphi_c = \pi$. It follows from $\sum_{k_c \in [-\pi, \pi)} \pi = 0 \pmod{2\pi}$ that an even number of crossings with a chirality of $\nu = \pm 1$ occurs for each band [209]. One may imagine that the restriction

to an even number of band crossings can be split into an odd number of crossings with the lower band and an odd number of crossing with the higher band. But by induction starting from the lowest occupied band one finds that this is impossible. For the first band $\sum_{c_1} \Delta\varphi_{1,c_1} = 0 \pmod{2\pi}$ holds, i.e., with $\Delta\varphi_c = \pi$ it must have an even number of terms as no lower band exists. Therefore the condition on the second band $\sum_{c_2} \Delta\varphi_{2,c_2} + \sum_c \Delta\varphi_{1,c_1} = 0 \pmod{2\pi}$ reduces as well to $\sum_{c_2} \Delta\varphi_{2,c_2} = 0 \pmod{2\pi}$. The same step can be repeated indefinitely. A generalization to arbitrary symmorphic rotations follows analogously. One concludes for symmorphic rotations in the absence of other symmetries that the number of crossings to the next higher band must add up to a zero total phase, i.e.,

$$\sum_{c_b} \Delta\varphi_{b,c_b} = 0 \pmod{2\pi}. \quad (2.2.6)$$

The possible number of crossings summed in \sum_{c_b} can thus be given as a linear combination of all possible ways to choose phase changes $\Delta\varphi_{b,c_b}$ such that their total equals to $0 \pmod{2\pi}$. While the phases cannot be chosen independently without affecting the full set of intersecting bands, one can in principle encounter zero, two, or any larger even number of band crossings. If C_n and $C_{n'}$ rotations coexist on the same axis, it is possible that crossings are protected only by one of the symmetries. In case of a sixfold rotation axis implying the presence of C_6, C_3 , and C_2 it is sufficient to consider only the restrictions of Eq. 2.2.6 arising from C_6 . Notably, it is impossible to fulfill Eq. 2.2.6 with a single crossing. Other symmetries may enforce additional crossings, but they do not affect our eigenvalue analysis as long as the bands on the axis stay nondegenerate. Thus, a symmorphic rotation axis must host always either zero or at least two crossings¹ to the next higher band.

Far more interesting is the case of nonsymmorphic rotation symmetries. We begin with an example, namely a twofold screw rotation with $n = 2$ and $m = 1$. Again the distinction between phase changes due to crossings with the next higher (lower) band is denoted with $\Delta\varphi_{b,c_b}$ ($-\Delta\varphi_{b-1,c_{b-1}}$). Here, the phase changes $\Delta\varphi_{b,c_b} = \pi$ must add up to $\pi \pmod{2\pi}$. For the first band, $b = 1$, the number of crossings to the next higher band is odd, whereas it is even for the second band, $b = 2$. To see this note that the second band inherits an odd number of crossings contributing $-\sum_{c_1} \Delta\varphi_{1,c_1} = \pi \pmod{2\pi}$ to the total phase. The latter reduces the condition, Eq. 2.2.5, to the symmorphic case in Eq. 2.2.6, which requires an even number of crossings. For the third band, $b = 3$, an even number of crossings with band $b = 2$ leads to the same conditions as for the first band, $b = 1$. In conclusion, a twofold screw rotation requires that odd numbered bands exhibit an odd number of crossings to the next higher band, whereas an even numbered band has an even number of such crossings.

¹Note that the enforced crossings may also be part of nodal lines or planes.

As before the argument extends to higher-fold rotations, which shall be discussed more explicitly. By iterating the substitution one finds²

$$\begin{aligned}
 b = 1 & \quad \sum_{c_1} \Delta\varphi_{1,c_1} = -2\pi \frac{m}{n} \pmod{2\pi} \\
 b = 2 & \quad \sum_{c_2} \Delta\varphi_{2,c_2} - \sum_{c_1} \Delta\varphi_{1,c_1} = -2\pi \frac{m}{n} \pmod{2\pi} \\
 & \quad \Leftrightarrow \sum_{c_2} \Delta\varphi_{2,c_2} = -2 \cdot 2\pi \frac{m}{n} \pmod{2\pi} \\
 & \quad \vdots \\
 \text{any } b & \quad \sum_{c_b} \Delta\varphi_{b,c_b} = -b \cdot 2\pi \frac{m}{n} \pmod{2\pi} \quad (2.2.7)
 \end{aligned}$$

This result reproduces Eq. 2.2.6 for $m = 0$, the symmorphic case. With a symmorphic rotation for every b it is possible that no crossing to the next higher band occurs, whereas it is the exception for nonsymmorphic rotations. Only if $\frac{bm}{n}$ is an integer no further crossings are needed, while otherwise at least one crossing must exist, see Table 2.1. Thus, nonsymmorphic rotations require the existence of band crossings, which are nodal points in the absence of other symmetries.

n	2	3	4	4	6	6	6
m	1	1 or 2	1 or 3	2	1 or 5	2 or 4	3
# bands	2	3	4	2	6	3	2

Table 2.1.: Minimal number of connected bands for different screw rotations $C_n(x, y, \frac{m}{n})$.

The result above may also be obtained by defining bands not by the number of occupied levels but by their symmetry eigenvalue, cf. Sec. 2.1. Let us consider, for example, a band with the eigenvalue λ_{C_n} at $k_z = k_1$ on a rotation axis. The band in question shall correspond to the lower band at $k_z = k_1$ of a two-band crossing. Suppose that after the crossing at k_c the levels have switched such that the band with eigenvalue λ_{C_n} is then higher in energy at $k_z = k_2 > k_c > k_1$, which we will consider in this paragraph to be the same band. Following a single band through the whole BZ, until one returns to the starting point, results in the band multiplicities given in Table 2.1. In that description the arising phase changes would be less

² Note that if the unit cell is not primitive, the length of the rotation axis can be longer. For example in the body-centered tetragonal BZ the distance between two equivalent Γ points along z direction is 4π instead of the 2π we have considered so far. To adjust for this case, the right-hand side of Eqs. 2.2.5 and 2.2.7 must be multiplied by a factor of 2.

accessible. As a non-zero number of crossings occurs for nonsymmorphic symmetries by default, it is useful to know, whether they can be chosen such that their topological charges add up to zero. If not, there must be additional topological charges associated to other crossings in the BZ to fulfill the Nielsen-Ninomiya theorem [83]. These include Weyl points away from high-symmetry lines, like in SG 19 [104], nodal lines away from mirror symmetries [210], or nodal planes with a non-zero Chern number as we have pointed out [3].

For the analysis of Weyl point chiralities we summarize the results of [168, 209, 211] in the following table, which is adjusted to the present notation. While for twofold rotations the phase change $\Delta\varphi_{b,c} = \pi$ at a crossing does not fix the sign of the chirality $\nu_{b,c}$, threefold rotations corresponding to $\Delta\varphi_{b,c} = \pm\frac{2\pi}{3}$ yield $\nu_{b,c} = \pm 1$. Similarly, for fourfold and sixfold rotations there are phase differences, which do not only fix the magnitude of the charge but also its sign.

n	2	3	4	4	6	6	6
$\Delta\varphi_{b,c}$	π	$\pm\frac{2\pi}{3}$	$\pm\frac{\pi}{2}$	π	$\pm\frac{\pi}{3}$	$\pm\frac{2\pi}{3}$	π
$\nu_{b,c}$	1 or -1	± 1	± 1	2 or -2	± 1	± 2	3 or -3

Table 2.2.: Correspondence between changes in the phase $\Delta\varphi_{b,c}$ of the rotation eigenvalues and the chirality of the resulting point crossing. If the signs of $\nu_{b,c}$ are given with \pm there is a one-to-one correspondence between the signs used in the second and third row [209], otherwise there is a sign ambiguity.

We illustrate the generic band structures along all possible rotation axes in the absence of TRS with Fig. 2.3. Given the results presented in Table 2.2 [209] one finds that for certain values of m and n the chiralities of all enforced and accidental crossings within a connected set of bands are restricted to certain values. For $\frac{m}{n} = \frac{1}{2}$ or $\frac{m}{n} = \frac{1}{3}$ the chiralities are equal to $\pm m$. Although in most real systems several band representations overlap, the rotation symmetry fixes the possible eigenvalues such that any band belongs to one of the representations which are already considered in Fig. 2.3.

In the following we want to discuss what conclusions for the chiralities of enforced crossings on a rotation axis can be drawn from the condition that their total charges must compensate each other. To do so, we combine the results listed in Table 2.2 with all possible $\Delta\varphi_{b,c}$ fulfilling Eq. 2.2.7. If we consider $0 \neq -b \cdot 2\pi\frac{m}{n} \pmod{2\pi}$, one finds that crossings must exist. Since there is a correspondence between the absolute value of the chirality and the phase that must be compensated, it turns out not to be possible to obtain a zero total charge on the rotation axis. It is possible though to introduce accidental crossings to change the total charge by a value n that coincides with the order of the operation C_n . For example, one may introduce crossings on band b on a three-fold rotation axis such that the sum of all chiralities on the axis changes by

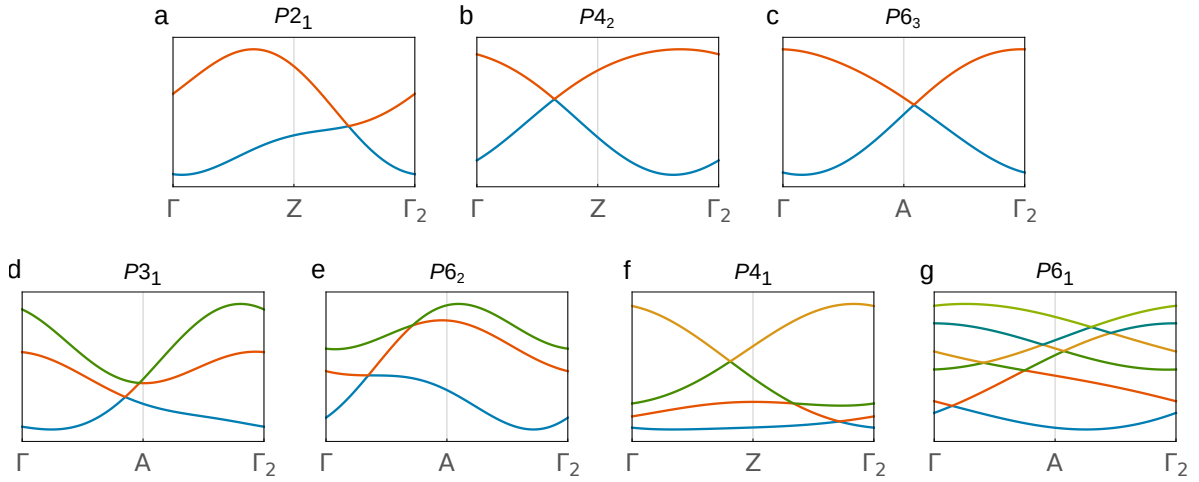


Figure 2.3.: Band structures along 2-,3-,4-, and 6-fold rotation axes for generic tight-binding models without time-reversal symmetry. For each space group a path covering the full interval $k_z \in [-\pi, \pi]$ is shown. Each color corresponds to a single band. **a,b,c** The enforced (as well as any possible accidental) Weyl points carry a chirality of $|\nu| = 1$, $|\nu| = 2$, and $|\nu| = 3$, respectively. **d,e** The enforced (as well as any possible accidental) Weyl points carry a chirality of $|\nu| = 1$, and $|\nu| = 2$, respectively. **f** Weyl points in SG $P4_1$ may carry charges of $|\nu| \in \{1, 2\}$. **g** Weyl points in SG $P6_1$ may carry charges of $|\nu| \in \{1, 2, 3\}$.

3, which however is insufficient to cancel the total charge $\nu_b = \pm 1$ according to Eq. 2.2. The necessary Weyl points to compensate the crossings on the rotation axis may also not be found at generic coordinates, since these would have also a multiplicity of at least n . One should note that the easiest possibility to resolve the mutual compensation of chiralities for a primitive unit cell would be that an even number of rotation axes of C_n occur and their contributions are equal in size but of different signs, such that they add up to zero. For our example with a three-fold rotation we will give a more detailed account in the next paragraph on how to resolve the compensation of chiral charges.

As an example to the above discussion, we use a space group with a primitive unit cell, where the charges on the screw rotation axes enforce the order of band crossings. To be specific, we are looking for the simplest configuration of Weyl points and consider the trigonal SG 144 ($P3_1$), which is equivalent to SG 145 ($P3_2$). There are three threefold rotation axes $A-\Gamma-A$, $H-K-H$, and $H'-K'-H'$, see the BZ in Fig. 3.1. The threefold screw rotation $\tilde{C}_3^z(0, 0, \frac{1}{3})$ leads for the band $b = 1$ to a accumulated phase of $-\frac{2\pi}{3} \bmod 2\pi$, which must be equal to a sum of $\Delta\varphi_{1,c} = \pm\frac{2\pi}{3}$ terms. If there is on each of the lines $A-\Gamma-A$ and $H-K-H$ only one crossing with $\Delta\varphi_{1,1} = -\frac{2\pi}{3}$, then the total charge will be $\nu_{A-\Gamma-A} + \nu_{H-K-H} = -2$. This can only be compensated

if on the third rotation axes there are two crossings with

$$\Delta\varphi_{1,1}^{\text{H}^{\prime}\text{-K-H}^{\prime}} + \Delta\varphi_{1,2}^{\text{H}^{\prime}\text{-K-H}^{\prime}} = +\frac{2\pi}{3} + \frac{2\pi}{3} = -\frac{2\pi}{3} \pmod{2\pi}, \quad (2.2.8)$$

thus fulfilling Eq. 2.2.7, while the resulting charge is $\nu_{\text{H}^{\prime}\text{-K-H}^{\prime}} = +2$. We conclude that for SG 144 it is not possible to achieve the minimal number of crossings per rotation axis, if no additional degeneracies are introduced. In principle it would be possible to have one crossing on each threefold axis, but then one must include a band crossings with the compensating charge. This may either be a movable nodal line that is invariant under the threefold rotation or three related Weyl points in the interior of the BZ.

The above discussion yielded arguments for enforced band crossings. Yet there is more to consider, because time reversal may introduce band crossings between different and identical symmetry eigenvalues, for which Table 2.2 is insufficient to infer the resulting topological charges. The combination of single a rotation symmetry with TRS at TRIMs has been considered in Ref. [209]. But combinations of more crystalline symmetries with TRS may affect the topological charges. It is even possible to obtain pinned crossings away from TRIMs between identical twofold rotation eigenvalues. Such crossings depend on the extensions of Kramers theorem discussed in Sec. 2.1.2. One example is the point P in the representation of SG 80, where one may show that the chirality is $\nu = 2$ by using tight-binding or low-energy models [196]. Despite these caveats Eq. 2.2.7 remains valid as long as bands can be labeled by their symmetry eigenvalues and applies also to off-center symmetries discussed below in the present section within the context of non-chiral little groups as well as in Sec. 2.2.2.

Rotation symmetry with time reversal

In the ensuing discussion we shall show that the presence of time-reversal symmetry does not modify the conditions on the band exchanges derived in the previous section for (screw) rotation symmetries $C_n(x, y, \frac{m}{n})$.

Time-reversal θ has several effects on the symmetry eigenvalues. Any TRS will relate the phase of the symmetry eigenvalues by complex conjugation with a simultaneous inversion of the coordinate along the rotation axis. Hereby, the phase $\varphi_b(k_z)$ of band b fulfills $\varphi_b(k_z) = -\varphi_b(-k_z)$. Additionally, there can be pinned crossings at TRIMs either because Kramers theorem applies or simply in cases where $\varphi_b(k_{\text{TRIM}}) \neq -\varphi_b(-k_{\text{TRIM}})$. In the following we assume that there are two TRIMs on the rotation axis, which must be traversed before the periodic boundary condition of the BZ takes effect. This is true for primitive unit cells.

We aim to find a tighter condition on the bands than Eq. 2.2.7, which also holds here as it is independent on whether TRS creates band crossings or they occur by any other reason. To

write the accumulated phase $\varphi_b(k_z)$ analogously to Eq. 2.2.4 as sum of the phase changes $\Delta\varphi_{b,c}$, we need to shift our reference point for the eigenvalue periodicity by an arbitrarily small length ϵ to $\varphi_b(-\pi + \epsilon) = \varphi_b(\pi + \epsilon) \bmod 2\pi$. The shift is required to ensure that one does not evaluate the phase at a crossing. With this shift the phase is well defined, but as it does not affect any considerations we omit it for simplicity. As the crossings c on the axes are related to each other by TRS, we modify the notation to include negative values of c instead of an incremental indexing. To be specific for $\Delta\varphi_{b,c}$ at k_c there exists a second crossing with a phase change of $\Delta\varphi_{b,-c}$ at $k_{-c} = -k_c$. One finds that the relative change in phase is the same for both crossings,

$$\Delta\varphi_{b,-c} = \varphi_b(-k_c + 0^+) - \varphi_b(-k_c - 0^+) = -\varphi_b(k_c - 0^+) + \varphi_b(k_c + 0^+) = \Delta\varphi_{b,c}, \quad (2.2.9)$$

where we use 0^+ as an arbitrarily small positive number to denote the limit towards the band crossing c . This result is consistent with the fact that TRS preserves the charge of Weyl points, see Sec. 2.1.3. At the TRIMs the pairing of bands depends on details of the time-reversal operation θ . Many cases can be distinguished, because θ may or may not fulfill Kramers theorem, comprise translations, mirror, or rotation symmetries. The pairing of the eigenvalues can vary depending on whether the representation is spinful or not. We shall assume in the following that we deal with either $\theta = K$ or $\theta = i\sigma_y K$. In this case the action on the phase will be simply a complex conjugation, which simplifies the phase difference $\Delta\varphi_{b,k_{\text{TRIM}}}$ at a TRIM to

$$\begin{aligned} \Delta\varphi_{b,k_{\text{TRIM}}} &= \varphi_b(k_{\text{TRIM}} + 0^+) - \varphi_b(k_{\text{TRIM}} - 0^+) = -\varphi_b(k_{\text{TRIM}} - 0^+) - \varphi_b(k_{\text{TRIM}} - 0^+) \\ &= -2\varphi_b(k_{\text{TRIM}} - 0^+). \end{aligned} \quad (2.2.10)$$

Note that for real eigenvalues with $\varphi_b(k_{\text{TRIM}} - 0^+) \in \{0, \pi\}$ the phase change will vanish, i.e., $\Delta\varphi_{b,k_{\text{TRIM}}} = 0$.

Now, we can evaluate the constraint, $\varphi_b(-\pi) = \varphi_b(\pi) \pmod{2\pi}$, due to the periodicity of the BZ, together with the accumulated phase due to the nonsymmorphic winding as in Eq. 2.2.4,

$$\varphi_b(-\pi) = \frac{2\pi p + s\pi + m(-\pi)}{n}, \quad \text{and} \quad (2.2.11)$$

$$\begin{aligned} \varphi_b(\pi) &= \frac{2\pi p + s\pi + m\pi}{n} + \sum_{k_c \in [-\pi, \pi)} \Delta\varphi_{b,c} \\ &= \frac{2\pi p + s\pi + m\pi}{n} + \sum_{c>0} 2\Delta\varphi_{b,c} + \Delta\varphi_{b,k_z=0} + \Delta\varphi_{b,k_z=\pi} \\ &= \frac{2\pi p + s\pi + m\pi}{n} + \sum_{c>0} 2\Delta\varphi_{b,c} + \Delta\varphi_{b,k_z=0} - 2\varphi_b(\pi - 0^+) \\ &= \frac{2\pi p + s\pi + m\pi}{n} + \sum_{c>0} 2\Delta\varphi_{b,c} + \Delta\varphi_{b,k_z=0} - 2 \left(\frac{2\pi p + s\pi + m\pi}{n} + \sum_{c>0} 2\Delta\varphi_{b,c} + \Delta\varphi_{b,k_z=0} \right) \\ &= -\frac{2\pi p + s\pi + m\pi}{n} - \sum_{c>0} 2\Delta\varphi_{b,c} - \Delta\varphi_{b,k_z=0} \\ &= -\frac{2\pi p + s\pi + m\pi}{n} - \sum_{c>0} 2\Delta\varphi_{b,c} - (-2) \left(\frac{2\pi p + s\pi}{n} + \sum_{c>0} \Delta\varphi_{b,c} \right) \\ &= \frac{2\pi p + s\pi - m\pi}{n}. \end{aligned} \quad (2.2.12)$$

If we compare Eqs. 2.2.11 and 2.2.12 we find that $\varphi_b(-\pi) = \varphi_b(\pi)$ holds independently of the phase changes $\Delta\varphi_{b,c}$, which have dropped out of the equation. We conclude that fulfilling time-reversal symmetry implies that also the periodic boundary conditions of the rotation eigenvalues are fulfilled. While the condition in Eq. 2.2.7 still holds, time reversal makes it possible that $\Delta\varphi_{b,\text{TRIM}} = 0$.

As our previous discussion showed, other approaches must be used to find the general symmetry enforced features, we return to the goal to find the simplest arrangement of bands that is allowed by symmetry. This will appear to be a viable substitute for the most likely band structure that should be expected. We want to discuss in the following hourglass [206, 207] and accordion states [208], which refer to band structures that are enforced by the combination of TRS and a nonsymmorphic screw rotation symmetry. All those band structures have in common that their crossings at TRIMs alternate with movable crossings on the rotation axis, if one goes through the band index b . If at one point identical eigenvalues are paired, it follows from the continuity of the symmetry eigenvalues of the screw rotation $C_n(x, y, \frac{m}{n})$, that each of the paired band must traverse the BZ a number of times that is given by the denominator of the fully reduced fraction $\frac{m}{n}$. The bands cannot wind into each other, because if their eigenvalues are paired with the same value at one point, their respective factors of $\exp(i\frac{m}{n}k_z)$, c.f. Eq. 2.2.3, will evolve identically, when traversing the BZ. Therefore, with TRS that pairs identical eigenvalues

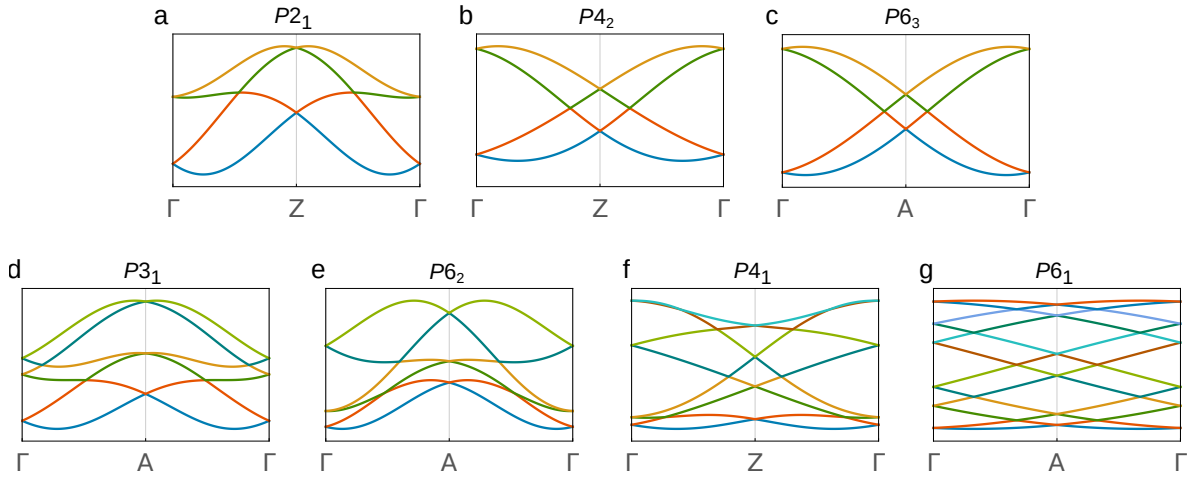


Figure 2.4.: Hourglass and accordion states on 2-,3-,4-, and 6-fold rotation axes for generic tight-binding models including time-reversal symmetry and spin-orbit coupling. Each color corresponds to a single band. For each space group a path covering the full interval $k_z \in [-\pi, \pi]$ is shown. **a, b, c** Hourglass states. **d, e, f, g** Accordion states.

at one point there will be twice the number of bands as stated in Table 2.1.

To illustrate these enforced features we consider tight-binding models for the same SGs as in the previous section but with the spinful time-reversal symmetry, see Fig. 2.4. TRS leads to mirror symmetric band structures and doubles the number of connected bands compared to Fig. 2.3. In these hourglass and accordion band structures several crossings with non-zero Chern numbers must occur. The generic band structures along screw rotation axes for the case without SOC has been discussed in Ref. [95].

Non-chiral little group

Once mirror symmetries or inversion are introduced the little groups may become non-chiral, which fixes Chern numbers to be zero, see Sec. 2.1.3. To our knowledge, in the presence of mirror inversion symmetry, no point-like crossings between two nondegenerate bands may occur without fine-tuned parameters, rather any twofold degeneracy will be part of some nodal line, see Sec. 2.2.2. But this restriction only excludes Weyl points. There are also Dirac points, which may, but do not need to carry a topological charge [211, 212].

Dirac points may be obtained in several ways. They occur at the phase boundary between different phases of strong TIs [211]. Here, we discuss the approach to obtain them by spatial symmetries. A necessary ingredient is the presence of inversion symmetry P , which in composition with time-reversal θ fulfills Kramers theorem everywhere in the BZ. Hereby, it is

also possible that the TRS contains a translation $\theta' = \theta T(x, y, z)$, which fulfills $(P\theta')^2 = -1$ in the whole BZ. Commonly, the absence of SOC leads as well to uniformly twofold degenerate bands away from the Dirac point, e.g., in graphene [41].

With the $P\theta$ -symmetry present one needs a new mechanism to pair bands to achieve a Dirac point. Suppose we have a rotation symmetry $C_n(x, y, \frac{m}{n})$ with the order n of the rotation axis larger than 2. Its eigenvalues are then paired corresponding to at least two different representations. Thus accidental crossings may occur. It is possible that a different symmetry relates the twofold representations at a TRIM, yielding a pinned Dirac point.

This raises the question, whether it is possible to enforce movable Dirac points. We will see that this is indeed possible. Suppose that $P\theta$ pairs identical eigenvalues of $C_n(x, y, \frac{m}{n})$. This means the bands have the same symmetry label as if they were unpaired. For this to happen the values of the translations x and y perpendicular to the rotation axis must be nonzero. Identical eigenvalues are then paired for all points of the form (k_x, k_y, k_z) on a rotation axis, if the scalar product with the perpendicular translation $(x, y, 0)$ yields $(k_x, k_y, k_z)(x, y, 0)^T = xk_x + yk_y = \frac{\pi}{2}$. This condition is equivalent to the anticommutation relation between the inversion operator P and the rotation $C_n(x, y, \frac{m}{n})$. If a rotation $C_n(x, y, \frac{m}{n})$ does contain such values of x and y it is referred to as off-centered symmetry [213]. We can directly apply our previous arguments of Sec. 2.2.1, i.e., TRS pairs points at TRIMs and a nonsymmorphic rotation enforces at least one crossing. Note that since $P\theta$ already leads to Kramers pairs, the bands will only gain additional degeneracies if the eigenvalues are complex and θ can relate different eigenvalues without the use of Kramers theorem. Thus there are no hourglass states with the given assumptions.

Nevertheless, one may obtain hourglass band structures for twofold degenerate bands similar to those in Fig. 2.4. Hereby the bands are labeled by the eigenvalues of two commuting symmetries, which enlarges the set of distinct representations to allow for Kramers pairing at two TRIMs and an enforced band exchange with a movable Dirac point.

Examples of such movable Dirac points will be discussed in more detail in our analysis of the tetragonal SGs, see Sec. 3.2.

Special cases

In the previous section we began to consider more combinations of symmetries, which leads to more detailed arguments, involving commutation relations of various symmetries. As such, we cannot claim to discuss all (topological) band crossings in appropriate detail. Nevertheless, we shall summarize a variety of cases and possible arguments how to find them.

The composite symmetry $\theta' = \theta C_2^x(\frac{1}{2}, 0, \frac{1}{2})$ fulfills Kramers theorem with $(\theta')^2 = -1$ on the plane $k_x = \pi$. If the SG also contains the symmetry $C_2^y(0, \frac{1}{2}, \frac{1}{2})$, then each of its eigenvalues $\lambda_{C_2^y}$

are paired with a copy of itself along the line (π, k_y, π) . Identical eigenvalues are related, because the commutation relation of the two symmetries obtains in total six minus signs. Four minus signs arise, due to the partial translations, when the spatial parts of the rotations are commuted, one minus sign from complex conjugation, and a sixth minus due to the anticommutation of spin matrices. As a result, identical eigenvalues are paired and a twofold band exists, which can be understood by a single eigenvalue of the nonsymmorphic symmetry $C_2^y(0, \frac{1}{2}, \frac{1}{2})$. Thus the band exhibits at least one crossing in the BZ, as discussed above. The resulting Weyl point is fourfold degenerate and as two time-reversal copies of a single Weyl point it will carry a charge of $\nu = \pm 2$, see Sec. 3.3 for more details. By similar arguments it is possible to combine two double Weyl points into a fourfold crossing with a charge of $\nu = \pm 4$, cf. Sec. 3.2.

All point crossings discussed so far had the implicit property that there is only one band index with a gap on every \mathbf{k} -point on a manifold around the point. In these cases a single Chern number characterizes the crossing, because the upper band has the opposite charge of the lower band. The latter must be the case because a completely filled Weyl point is trivial. But once we consider crossings of more than two bands, there is the possibility to have several well-defined gaps. Both crossings with multiple gaps and those with more involved bands, can be identified by consulting tables of irreducible corepresentations [88, 137]. Some of their low-energy models are described with spin matrices like a Weyl point, albeit for larger spin values [214]. There are threefold spin-1 fermions, fourfold spin-3/2, also called Rarity-Schwinger fermions due to its similarity to high-energy physics [215], doubled spin-1, and eightfold degeneracies. Except for the eightfold crossing, each of the crossings exhibit nonzero Chern numbers as long as they do not occur on a mirror plane.

On the other side of the spectrum there are points, which cannot be enclosed by any 2D manifold in the BZ, where the gap closes. These *nexus fermions* occur where a band associated to a 2D irreducible representation crosses another band with a 1D representation, which can be achieved in groups where a threefold rotation axis intersects a mirror plane [216]. Nexus fermions are, due to the twofold degenerate bands, comprised out of nodal lines, which will be the topic of the next section.

2.2.2. Nodal lines

Nodal lines are, unlike Weyl points, unstable without a symmetry that protects them. When the degeneracy of a nodal line is lifted, several other phases may emerge [76]. Let us begin with a nodal line without spin-orbit coupling, i.e., a fourfold degenerate Dirac nodal line. Adding SOC while preserving TRS can lead to a strong TI phase. If TRS or inversion is broken but a mirror symmetry is present, twofold degenerate Weyl nodal lines appear and are protected as

a crossing of different mirror symmetries. For the case that SOC is strong enough to remove the nodal line, mirror Chern numbers may occur indicating Weyl points away from the mirror planes like in the TaAs material class [74]. A nodal line can have a non-zero Berry phase, defined on a loop encircling the nodal line, and then it is protected as long as the inversion or mirror symmetry that quantizes the Berry phase to π is preserved [10, 62]. Like for the fourfold nodal points, it is possible to obtain Dirac nodal lines by off-centered mirror symmetries [213].

After this brief overview of nodal lines, we discuss in the following possible arguments on how nodal lines may be enforced. The approaches to enforce nodal lines follow the same main principles we discussed in Sec. 2.2.1, i.e., nodal lines can occur as a Kramers degeneracy or a crossing of different symmetry eigenvalues. For both types of arguments we consider a concrete mirror symmetry $M^x(\frac{m_x}{2}, \frac{m_y}{2}, \frac{m_z}{2})$ that inverts the x direction while adding a translation $(\frac{m_x}{2}, \frac{m_y}{2}, \frac{m_z}{2})$ with $(m_x, m_y, m_z) \in \{0, 1\}$. Since mirror symmetries are naturally twofold operations, one can obtain the possible eigenvalues by squaring the mirror symmetry

$$(M^x(x, y, z))^2 = \exp(i\pi s) T(0, y, z) = \exp(i\pi s + i(m_y k_y + m_z k_z)), \quad (2.2.13)$$

where $s = 1(0)$ for the spinful (spinless) description. By taking the square root on both sides one finds that possible eigenvalues λ_{M^x} of the symmetry are given by

$$\lambda_{M^x} = \exp\left(i \frac{2\pi p + s\pi + (m_y k_y + m_z k_z)}{2}\right), \quad (2.2.14)$$

where $p \in \{0, 1\}$ distinguishes the two possible eigenvalues of a mirror symmetry. Analogously to rotation symmetries and nodal points, it is possible that nodal lines occur if several symmetries leave the same line in the BZ invariant. When we described our basic method in Sec. 1.2.3 we found such an enforced nodal line pinned to the intersection of two mirror planes, as a result of the spinful representation of mirror symmetries and the contribution of glide translations. Similarly, it is possible to obtain a pinned nodal line from the anticommutation of spatial operations, if a rotation axis lies within a mirror plane. If more symmetries work together to relate different mirror eigenvalues, it is possible to obtain fourfold nodal lines, which in the presence of inversion and time-reversal symmetry are commonly called Dirac nodal lines [25, 50]. Nodal lines of this type can be easily spotted by the increased dimensionality of irreducible representations.

Kramers-nodal lines

Let us begin by considering the connection between Kramers theorem and nodal lines. The composite operation $\theta' = \theta M^x(\frac{m_x}{2}, \frac{m_y}{2}, \frac{m_z}{2})$ leaves lines in the BZ invariant, i.e., $\mathbf{k}_{\text{TRIM}} + (\delta k, 0, 0)$ with $\delta k \in [-\pi, \pi)$. More generally, the symmetry θ' acts as a rotation in reciprocal space, i.e.,

$(k_x, k_y, k_z) \rightarrow (k_x, -k_y, -k_z)$. As it is still antiunitary one may wonder, whether at the invariant \mathbf{k} -points Kramers theorem applies, which we check by squaring the operation and obtain

$$(\theta M^x(x, y, z))^2 = \exp(i(m_y k_y + m_z k_z)). \quad (2.2.15)$$

From this one finds that a glide symmetry combined with time reversal, which is defined by non-zero y or z , fulfills Kramers theorem if $(m_y, m_z)(k_y, k_z)^T = \pi$. If such a symmetry θ' is present and inversion combined TRS with $(P\theta)^2 = -1$ is absent, there are straight nodal lines that intersect certain TRIMs. Those nodal lines are usually easy to spot in corepresentation tables as 2D entries.

Mirror symmetry

To discuss nodal lines on the basis of mirror symmetry eigenvalues, we shall consider in the following a mirror plane that is left invariant by $M^x(\frac{m_x}{2}, \frac{m_y}{2}, \frac{m_z}{2})$. Without TRS one finds due to the periodicity of the eigenvalues an analogous condition as the one formulated in Eq. 2.2.7. Since mirror symmetries are also twofold, $n = 2$, we can write

$$\sum_{c_b} \Delta\varphi_{b,c_b}(k_z) = -b \cdot \pi m_y \quad \text{mod } 2\pi \quad (2.2.16)$$

$$\sum_{c_b} \Delta\varphi_{b,c_b}(k_y) = -b \cdot \pi m_z \quad \text{mod } 2\pi, \quad (2.2.17)$$

where the phase changes $\Delta\varphi_{b,c_b}$ at the crossings c_b between the bands b and $b + 1$ can be dependent on the second in-plane coordinate of the considered 2D mirror plane. The occurring crossings c_b depend on the exact path that is chosen within the mirror plane. In other words, for a rotation only the interval $k_z \in [-\pi, \pi]$ needed to be considered, whereas for the periodicity of mirror eigenvalues any non-contractible loop within the mirror plane yields a condition of the form Eq. 2.2.16 or 2.2.17.

If we have, for example, the nonsymmorphic mirror symmetry $M^x(0, \frac{1}{2}, 0)$, we find, analogously to twofold screw rotations, that the possible phase differences fulfill $\Delta\varphi_{b,c_b} = \pi$. Thus, there must be an odd number of band crossings c_b on any path traversing the BZ from $k_y = -\pi$ to $k_y = \pi$ for b odd, whereas an even number of crossings c_b must occur for even b . If the mirror plane is crossed in the perpendicular direction, i.e., along the k_z , the number of band crossings must be even for any band index b . The nodal lines of this type are generally movable and can easily be missed when only the compatibility relations along high-symmetry lines are checked.

Mirror symmetry with time reversal and special cases

In this section we want to combine time-reversal and mirror symmetries. Besides nodal lines exhibiting an hourglass band structure for glide mirror symmetries, any single mirror symmetry

will lead to partially movable nodal lines. Furthermore, unlike crossings due to rotation symmetry, nodal lines on mirror planes do not need to occur between high-symmetry points. It is just as well possible to obtain nodal lines between points and lines, or lines and other lines of higher symmetry [217]. Another example of a band structure with nodal lines is the nexus fermion, where the nodal lines cross at the three-band degeneracy of the nexus fermion.

For concreteness we use the mirror symmetry $M^x(\frac{m_x}{2}, \frac{m_y}{2}, \frac{m_z}{2})$ in its spinful representation. Thus, its eigenvalues are $\lambda_{M^x} = \pm 1$ at points (k_x, k_y, k_z) for which $(m_y, m_z)(k_y, k_z)^T = \pi$ and $\lambda_{M^x} = \pm i$, where $(m_y, m_z)(k_y, k_z)^T = 0 \pmod{2\pi}$. Among the points that fulfill these conditions there are the TRIMs, which means that we immediately can tell how TRS pairs the bands. The symmetry eigenvalues are paired identically if $\lambda_{M^x} = \pm 1$, and if they are $\lambda_{M^x} = \pm i$ the complex conjugation relates different eigenvalues. These eigenvalues characterize the band representation on the full mirror plane and there are always TRIMs, where different representations are paired. If one picks any path connecting a TRIM with a pairing of the first kind with a TRIM of the second, one finds in the simplest case an hourglass like band structure as seen in Fig. 2.4a for a twofold screw rotation axis [207]. Along such paths connecting the considered TRIMs, the bands change their order to fit to the endpoint of the path. A similar situation can occur, if different representations are not just paired at TRIMs but at lines. Still, any path connecting points, where the representations are paired differently, will exhibit an hourglass band structure.

We recall that for symmorphic rotations the Kramers degeneracies due to $\theta = i\sigma_y K$ are pinned to TRIMs and there is no dependency on the details of a considered physical system. Twofold nodal lines can be obtained from the same symmetry, $\theta = i\sigma_y K$, even in symmorphic mirror planes. Let us consider a TRIM, where TRS pairs different mirror eigenvalues λ_{M^x} . If we move away from this TRIM to a point \mathbf{k}_{M^x} , but stay within the mirror plane of M^x , then the lowest band shall be labeled by the eigenvalue $\lambda_{M^x,1}$. Since we assume that TRS, $\theta = i\sigma_y K$, pairs different and thus complex conjugated eigenvalues of the mirror symmetry, there is a time-reversal related point $-\mathbf{k}_{M^x}$, which is also on the mirror plane. At $-\mathbf{k}_{M^x}$ the lowest band is described by the eigenvalue $\lambda_{M^x,2} = \lambda_{M^x,1}^*$. There is a path within the mirror plane that connects both points, \mathbf{k}_{M^x} and $-\mathbf{k}_{M^x}$, e.g., a clockwise half circle around the TRIM. As the eigenvalues are different, the bands must exchange on this path. Since the path is chosen arbitrarily, the Kramers degeneracy of a TRIM, where different mirror eigenvalues are paired, must always be part of a nodal line. By a similar argument it is clear that a nodal line between different mirror eigenvalues can never end, thus in the simplest case there are nodal lines running through all TRIMs and loop into themselves. Although, the above argument is simple, the arising nodal lines are invisible in group representation tables as well as compatibility relations. They occur as long as no additional symmetry fixes them to lie on a high-symmetry line. In Ref. [2], we

have suggested the term “almost movable” to describe these nodal lines, to express that they are like movable nodal lines not fixed to a specific position in the BZ, except at a finite number of points.

If there is TRS, inversion, and an off-centered mirror symmetry of the form $M^x(\frac{1}{2}, \frac{m_y}{2}, \frac{m_z}{2})$, then $P\theta$ will pair identical mirror eigenvalues on a plane, here $k_x = \pi$. This can be thought of as a generalization of almost movable nodal lines, which are pinned at TRIMs but otherwise movable. The difference to before is that now the enforced nodal lines will be fourfold degenerate.

Finally, we want to discuss an elusive type of nodal line that is not enforced by the symmetries alone, but determined by the overall Chern number of band crossings. If one considers a chiral space group, i.e., without mirror or inversion symmetries, and determines for each occupied band the chiralities of the present Weyl points, then it might happen that no accidental nodal points can be introduced anywhere in the BZ to fulfill the Nielsen-Ninomiya theorem [83]. This happens if the number of crossings on high-symmetry lines do not add up to zero and the multiplicity of crossings within the bulk of the BZ is too high, such that the doubling theorem cannot be fulfilled by adding accidental Weyl points.

To our knowledge there are two ways to resolve this mismatch that may be realized in a system. Either there is an accidental nodal plane, see Sec. 2.2.3 below, or there are nodal lines that exist without mirror symmetries and carry a Chern number. The idea is that the rotation symmetries and TRS of the considered SG map the nodal lines to themselves. If such a nodal structure is placed in the BZ, it spreads a charge ν over a closed, symmetry invariant nodal line around a rotation axis. Comparing this again to an accidental Weyl point, it can only exist together with several copies of the same charge as long as the symmetries are preserved. This has been identified in the material AgF_3 that forms in SG $P6_122$. For a band far away from the Fermi energy of this material the total charge of Weyl points along high-symmetry lines is compensated by two nodal lines, which each carry a charge of $\nu = +1$ [210]. In this specific case accidental Weyl points in the bulk of the hexagonal BZ may only occur in multiples of at least six, whereas the charged nodal line occurs with a multiplicity of 2.

2.2.3. Nodal planes

Nodal surfaces or nodal planes, which are 2D manifolds in the BZ where the bands cross, have been theorized as (topologically) protected nodal features [27–29, 104, 204, 218–220]. If a nodal surface falls into the vicinity of the Fermi energy the emergence of superconductivity has been discussed [221]. In a different approach, starting from nodal even-parity superconductors with spontaneously broken TRS, the emergence of topological Bogoliubov Fermi surfaces has been

proposed [222]. Commonly, a \mathbb{Z}_2 invariant applies [28, 29], which indicates that nodal surfaces with a nontrivial charge can annihilate pairwise. Several realizations have been discussed in photonic [223] and acoustic [224, 225] systems and there are several proposals of materials with nodal planes [30, 104, 226, 227]. Among them are several with weak spin-orbit coupling like ZrSiS [73] or graphene networks [218, 228]. Whereas nodal surfaces refer to arbitrary 2D gapless manifolds, we speak of nodal planes if the nodal surface is fixed to a specific plane. As nodal planes imply a fixed geometry, they must be protected by crystalline symmetries. The advantage of nodal planes is that they are enforced, whereas the generic nodal surfaces are accidental features.

In the following we show how a nodal plane can be enforced by the combination of twofold screw rotation and time-reversal symmetry. This will allow us to survey all magnetic SGs for the relevant symmetries and list the SGs hosting nodal planes in Table 2.3. We then use our arguments of Sec. 2.2.1 to infer, which nodal planes must carry a non-zero Chern number [3, 4]. Out of the 1651 magnetic SGs there are 254 with nodal planes and 33 of these are enforced to carry a topological charge. By using the database MAGNDATA [229, 230] we identify several possible candidate materials.

The composite symmetry θ' shall comprise a twofold screw rotation of the form $\tilde{C}_2^x(\frac{1}{2}, y, z)$ with $y, z \in \{0, \frac{1}{2}\}$ and a time reversal symmetry $\theta = i\sigma_y K$ or $\theta = K$. Independently on whether our representation is spinful or not, the operation θ' is antiunitary and squares to

$$(\theta')^2 = (\theta\tilde{C}_2^x(\frac{1}{2}, y, z))^2 = T(1, 0, 0) = e^{ik_x} \stackrel{k_x=\pi}{=} -1. \quad (2.2.18)$$

Before one can apply Kramers theorem, one has to consider which points of the BZ are left invariant by the operation θ' , which is illustrated in Fig. 2.5a. While both planes $k_x = 0$ and $k_x = \pi$ are invariant, the Eq. 2.2.18 states that only for $k_x = \pi$ all conditions of Kramers theorem are met and we obtain a 2D degeneracy, the nodal plane. Analogous arguments hold for magnetic screw rotations $\theta\tilde{C}_2^y$ and $\theta\tilde{C}_2^z$, leading to up to three nodal planes in a primitive BZ. Note that nodal planes are only flat in reciprocal space but dispersive in energy. Whether this is a drawback or not is still part of on-going research, but a dispersive nodal plane has at least the advantage, that it is far more likely to find them at the Fermi energy compared to Weyl points, which only exist at one energy.

With these preparations we can find all possible SGs with enforced nodal planes. Our search criteria are:

- Presence of at least of magnetic screw rotation $\theta\tilde{C}_2^q$ with $q \in \{x, y, z\}$.
- Presence of a reciprocal lattice vector G such that $k_q = \pi = -k_q + G$. This means that the plane, where Kramers theorem can hold, is also invariant under $\theta\tilde{C}_2^q$.

- Absence of the composite symmetry of inversion and TRS, $P\theta$, with $(P\theta)^2 = -1$. This restriction prevents the twofold degeneracy of all bands in the BZ, which would otherwise make the degeneracy due to $\theta\tilde{C}_2^q$ obsolete.

To systematically check all magnetic space groups, we use the ISO-MAG database [231], which contains the symmetry elements of all magnetic space groups that we can survey with our list of criteria. Within the 1651 SGs we find nodal planes in 32 grey SGs with TRS, 94 black-white SGs without TRS, and 129 black-white SGs where TRS is combined with a translation. These SGs can be understood to describe paramagnetic, ferri- and ferromagnetic, and antiferromagnetic phases. Note that it is possible to conceive an antiferromagnetic order, which is not described by an antiferromagnetic SG. This could be achieved by having opposite moments forming on positions, which are on lattice sites that are not connected by a full translation. The used terminology can be understood in the sense that if a single magnetic Wyckoff position of a (an anti-)ferromagnetic SG is occupied by magnetic moments, the resulting structure will be a (an anti-)ferromagnet.

Our analysis yields space groups with one, two, or three nodal planes. For two and three nodal planes, which we call nodal plane duos and trios, respectively, we give arguments which predict a non-zero Chern number for the nodal planes, which we will discuss in the following. To test the chiralities we compare our arguments with tight-binding models with up to fifth-nearest-neighbor hopping terms, which we choose at random. Note that trios of topological nodal planes exhibit no surface states, because the unpaired Weyl points in the bulk of the BZ are projected on the nodal planes if a surface is opened. Duos of topological nodal planes differ in this respect, because for them the Fermi arcs do exist, see Sec. 3.3.

Trios of nodal planes

A trio of nodal planes is enforced by the simultaneous presence of all three magnetic screw rotations $\theta\tilde{C}_2^x$, $\theta\tilde{C}_2^y$ and $\theta\tilde{C}_2^z$, while all the planes $k_{x,y,z} = \pi$ must be at the surface of the BZ. This is only possible in paramagnetic or antiferromagnetic SGs, because a non-zero total magnetic moment breaks at least one of the required symmetries. Also non-primitive unit cells must be excluded as their BZs violate the second condition.

To obtain topologically charged nodal planes we require that there must be unpaired Weyl points in the interior of the BZ, see Fig. 2.5b. This can be achieved if TRS is spinful and exists as a group element by itself, $\theta = i\sigma_y K$, because this leads to a single unpaired Weyl point at the origin of reciprocal space, Γ . This is the case for 6 paramagnetic SGs: 19.26, 92.112, 96.144, 198.10, 212.60, and 213.64, cf. [204], and for 13 antiferromagnetic SGs: 16.6, 17.14, 18.21, 19.28, 89.94, 90.100, 91.109, 93.126, 94.132, 95.141, 195.3, 207.43,

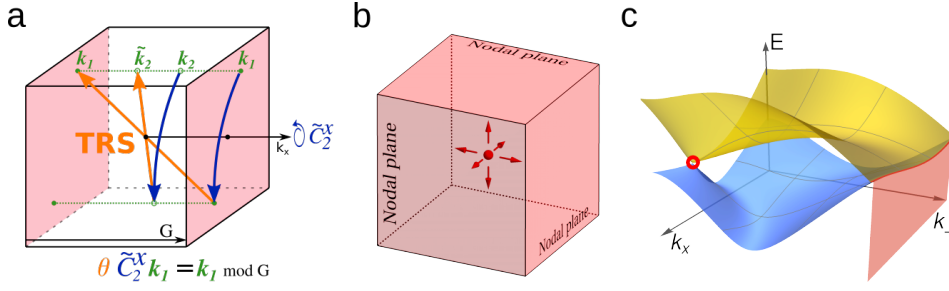


Figure 2.5.: Symmetry enforced nodal planes. **a** Action of the combination of time reversal θ and the twofold screw rotation \tilde{C}_2^x . The plane left invariant by $\theta\tilde{C}_2^x$ is shaded in red. **b** Topological nodal plane trio as red planes on the boundary of a primitive Brillouin zone with a single unpaired Weyl point, red sphere, emitting Berry flux. **c** Band structure of a generic tight-binding model including a topological nodal plane duo. k_\perp is normal to the nodal plane. The intersection of plot range and nodal plane is a line (red).

and 208.47. For an antiferromagnetic space group TRS is $\tilde{\theta} = \theta T(x, y, z)$, which squares to $\tilde{\theta}^2 = -\exp(i2(x, y, z)^T \cdot \mathbf{k}) = -1$ at Γ . The charge of the single Weyl point at Γ cannot be canceled by accidental Weyl points, because TRS or fourfold rotations increase the multiplicity of accidental points to a value higher than the charge of the crossing at Γ . In comparison to the introduction of an accidental, charged nodal line, it is simpler if the charge is compensated by the nodal plane that is already enforced. This is also the only case we have found in our generic tight-binding models.

By consulting the MAGNDATA database [229, 230] we identify the compounds CoNb_2O_6 (SG 19.28) and $\text{Ba}(\text{TiO})\text{Cu}_4(\text{PO}_4)_4$ (SG 94.132) as possible realizations of trios of nodal planes.

Duos of nodal planes

Duos of nodal planes occur if two out of the three symmetries $\theta\tilde{C}_2^x$, $\theta\tilde{C}_2^y$, and $\theta\tilde{C}_2^z$ are present. If the unit cell is primitive it follows that two out of three of its distinct planes with $k_{x,y,z} = \pi$ host nodal planes. There are two ways to obtain topologically charged nodal planes, which follow directly from our previous discussions. According to the conclusions we drew from Eq. 2.2.7, a screw rotation axis parallel to the enforced nodal planes will have crossings with an odd total chirality in the absence of TRS. We illustrate this idea in Fig. 2.5c, where the bands are plotted in a direction perpendicular to a nodal plane. Additionally, there is an unpaired movable Weyl point (red circle) on the screw rotation axis. The second possibility is to consider an antiferromagnetic SG with the TRS $\tilde{\theta} = \theta T(x, y, z)$, which creates only one Kramers-Weyl point

away from the nodal planes. This is equivalent to the condition that $\tilde{\theta}^2 = -\exp(i2(x, y, z)^T \cdot \mathbf{k})$ equal only at Γ to -1 . With either possibility realized the argument is then analogous to the nodal plane trios, i.e., the enforced crossings cannot be compensated by accidental crossings and thus the most likely resolution is a topologically nontrivial nodal plane. Note that the charge of the topological nodal plane and the number of expected Fermi arcs is not necessarily odd, because fourfold screw rotations \tilde{C}_4^z may enforce charges of up to $\nu = 2$.

There are 13 such SGs: 17.15, 18.22, 19.27, 91.110, 92.114, 92.115, 92.116, 94.130, 95.142, 96.146, 96.147, and 96.148. As potential material realizations, which exhibit the needed magnetic order, we find: $\text{Cu}_3\text{Mo}_2\text{O}_9$ (SG 19.27), Nd_5Si_4 (SG 92.114), AgNiO_2 (SG 18.22), and CoNb_3S_6 (SG 18.22) as well as the likely nonmetallic magnetic phases of TbFeO_3 (SG 19.27) and BaCrF_5 (SG 19.27).

Two additional SGs, 94.128 and 93.125, exhibit charged nodal planes. With SOC both SGs contain a TRS that creates Kramers-Weyl points at two TRIMs away from the nodal planes, i.e., at Γ and Z of the primitive tetragonal unit cell. We have shown in Ref. [3] that for these SGs the nodal planes still carry a nonzero Chern number, by combining the results of Eq. 2.2.7 with the enforced chirality at TRIMs due to the paired eigenvalues [209]. Both SGs contain a fourfold screw rotation $\tilde{C}_4^z(x, y, \frac{1}{2})$, which relates the chiralities at the TRIMs such that they add up to $\nu_\Gamma + \nu_Z = \pm 2$, which then cannot be canceled. Interestingly, SG 94.128 is to our knowledge the only known example of a nodal plane duo in a paramagnetic SG.

4.8 [t]	17.8 [t]	18.17 [t]	19.26 [T]	20.32 [t]	26.67	29.100	31.124	33.145
36.173	76.8 [t]	78.20 [t]	90.96 [t]	91.104 [t]	92.112 [T]	94.128 [T]	95.136 [t]	96.144 [T]
113.268	114.276	169.114 [t]	170.118 [t]	173.130 [t]	178.156 [t]	179.162 [t]	182.180 [t]	185.198
186.204	198.10 [T]	212.60 [T]	213.64 [T]					
4.9 [t]	11.54	14.79	17.10 [t]	18.18 [t]	18.19 [t]	19.27 [T]	20.34 [t]	26.68
26.69	29.101	29.102	31.125	31.126	33.146	33.147	36.174	36.175
51.294	51.296	52.310	52.311	53.327	53.328	54.342	54.344	55.357
55.358	56.369	56.370	57.382	57.383	57.384	58.397	58.398	59.409
59.410	60.422	60.423	60.424	61.436	62.446	62.447	62.448	63.463
63.464	64.475	64.476	90.98 [t]	90.99 [t]	92.114 [T]	92.115 [T]	94.130 [T]	94.131 [t]
96.146 [T]	96.147 [T]	113.269	113.271 [t]	114.277	114.279 [t]	127.390	127.393	128.402
128.405	129.414	129.417	130.426	130.429	135.486	135.489	136.498	136.501
137.510	137.513	138.522	138.525	169.115 [t]	170.119 [t]	173.131 [t]	176.147	178.157 [t]
178.158 [t]	179.163 [t]	179.164 [t]	182.181 [t]	182.182 [t]	185.199	185.200	186.205	186.206
193.258	193.259	194.268	194.269					
3.5 [t]	3.6 [t]	4.10 [t]	16.4 [t]	16.5 [t]	16.6 [T]	17.11 [t]	17.13 [t]	17.14 [T]
17.15 [T]	18.20 [t]	18.21 [T]	18.22 [T]	18.24 [t]	19.28 [T]	19.29 [t]	20.36 [t]	21.42 [t]
21.44 [t]	25.61	25.64	25.65	26.71	26.72	26.76	27.82	27.85
27.86	28.94	28.95	28.96	28.98	29.104	29.105	29.109	30.118
30.119	30.120	30.122	31.128	31.129	31.133	32.139	32.142	32.143
33.149	33.150	33.154	34.161	34.162	34.164	35.169	35.171	36.178
37.184	37.186	75.4 [t]	75.6 [t]	76.11 [t]	77.16 [t]	77.18 [t]	78.23 [t]	81.36 [t]
81.38 [t]	89.92 [t]	89.93 [t]	89.94 [T]	90.100 [T]	90.102 [t]	91.109 [T]	91.110 [T]	92.116 [T]
92.117 [t]	93.124 [t]	93.125 [T]	93.126 [T]	94.132 [T]	94.134 [t]	95.141 [T]	95.142 [T]	96.148 [T]
96.149 [t]	99.168	99.170	100.176	100.178	101.184	101.186	102.192	102.194
103.200	103.202	104.208	104.210	105.216	105.218	106.224	106.226	111.256
111.257	111.258	112.264	112.265	112.266	113.272	113.274	114.280	114.282
115.288	115.290	116.296	116.298	117.304	117.306	118.312	118.314	168.112 [t]
171.124 [t]	172.128 [t]	177.154 [t]	180.172 [t]	181.178 [t]	183.190	184.196	195.3 [T]	207.43 [T]
208.47 [T]	215.73	218.84						

Table 2.3.: *Comprehensive list of magnetic space groups with enforced nodal planes [3]. All SGs are given in the BNS setting. The table is split into three sections corresponding, from top to bottom, to paramagnetic SGs, where time-reversal is an element of the group, followed by ferromagnetic SGs, where time-reversal symmetry occurs at most only in combinations with other point group symmetries, and at the bottom antiferromagnetic SGs, which contain time-reversal symmetry combined with a translation. [t] indicates groups without inversion or mirror symmetries, i.e., chiral space groups, that may host topological nodal planes. [T] denotes that the nodal planes are enforced to be topologically charged. The latter is determined by the arguments presented in the text and confirmed by the explicit calculation of the Chern numbers in generic tight-binding models for each highlighted SG.*

3. Band crossings in solids

In the previous chapter we discussed various arguments to predict and understand enforced band degeneracies from the underlying crystal symmetries. These principles are now applied to guide the analysis of full band structures.

The first two sections on the trigonal [1] and tetragonal [2] crystal systems aim to identify space groups, which necessarily lead to enforced topological band crossings. Our analysis of trigonal space groups shows that the expected accordion-like band structures and hourglass nodal lines exist. The investigation of tetragonal space groups, on the other hand, is conceived more broadly and aims to classify all topological band crossings by positions, multiplicities, charge, and underlying symmetries. For the tetragonal space groups we highlight exceptional features like Weyl points with a large chirality or with multiplicities of less than four, intricate arrangements of nodal lines, and enforced weak topological invariants.

The third and the fourth sections focus on specific materials, which we study by symmetry analysis, determination of topological charges, and comparisons between DFT and tight-binding calculations. We have supported the experimental identification of nodal planes in ferromagnetic MnSi, where the results of the de Haas-van Alphen measurements are traced back to the underlying magnetic space group [3]. A comparison of the symmetry eigenvalues from DFT calculations with the theoretical expectations of chapter 2 shows a complete agreement. Furthermore, we study the implications of the topological nodal planes that exist in MnSi. The second experimental collaboration focuses on Eu_3PbO , which exhibits multiple magnetic phases. In the paramagnetic state gapped Dirac points are the only feature at the Fermi energy. We study how the onset of magnetic order changes the electronic band structure, investigate surface states, and calculate the anomalous Hall conductivity.

Finally, we consider the magnetic phases of SmB_6 , where we identify the topological band features of the different magnetic phases.

3.1. Topological crossings in trigonal space groups

The results presented in chapter 2, cf. Figs. 2.3 and 2.4, are most valuable if the band structures of real materials are reasonably simple, such that the enforced crossings may be identified and hopefully found close to the Fermi energy. Our study [1] of trigonal materials will show that the expected features are indeed visible in DFT calculations and recent ARPES measurements support our analysis [232]. We focus here on systems with strong spin-orbit coupling, because topological features like accordion band structures are more prevalent in the presence of spinful representations. Furthermore, nonzero SOC is realized in all materials at least to a certain degree. We begin our discussion by general remarks on the implications of the symmetries available in trigonal space groups.

There are 25 trigonal space groups, 8 of them contain inversion symmetry, and 12 groups contain at least one nonsymmorphic symmetry. All groups with a rotoinversion, PC_3^z , contain also inversion P itself, because $(PC_3)^3 = -P$. The centrosymmetric, i.e., inversion symmetric, trigonal space groups can be split into those with and without nonsymmorphic symmetries. Since the combination of inversion and time-reversal, $P\theta$, squares to $(P\theta)^2 = -1$, symmorphic SGs with inversion lead to twofold degenerate bands and have no enforced crossings at all. Hence, we can neglect five SGs, i.e., SGs 147, 148, 162, 164, and 166, such that three centrosymmetric SGs remain, namely SGs 163, 165, and 167. Each of these three groups contains off-centered rotations, which lead to Dirac points at A and L for SGs 163 and 167 and only at A for SG 165. While the point L occurs three times in the BZ, see Fig. 3.1a, the point A occurs only once yielding a single Dirac point. So far this information is accessible from character or representation tables.

Now we shall move towards non-centrosymmetric, trigonal SGs. Similar to before, symmorphic space groups have no means to increase the size of their elementary band representations besides TRS, because there are no products of symmetries that multiply to the identity operation, which could lead to additional compatibility relations. This implies that only two bands must be connected in the simplest arrangement of bands. Hereby, it is possible that the two bands are connected by pinned nodal lines besides the Kramers-Weyl points at TRIMs, but other than that, no additional band crossings are enforced. This is consistent with the tables of elementary band representations with spinful TRS [137]. Note that one eigenvalue of the symmorphic threefold rotation exhibits Kramers-Weyl points of charge $\nu = 3$ at the TRIMs Γ and A or Z [226], which would apply to SGs 143, 146, 149, 150, and 155.

After we have dealt with the symmorphic, non-centrosymmetric SGs, we are left with the 9 SGs, where something nontrivial can happen. We list these groups and their characteristic features in Table 3.1.

Space group	Weyl nodal points	Weyl nodal lines	Materials
144 ($P3_1$)	$\Gamma\Delta A(6)$, H-K-H(3)		$\text{Cu}_2\text{SrSnS}_4$
145 ($P3_2$)	$\Gamma\Delta A(6)$, H-K-H(3)		$\text{Cu}_2\text{SrGeS}_4$
151 ($P3_112$)	$\Gamma\Delta A(6)$, H-K-H(3)		Ag_2HPO_4
152 ($P3_121$)	$\Gamma\Delta A(6)$, H-K-H(3)		Te, Se
153 ($P3_212$)	$\Gamma\Delta A(6)$, H-K-H(3)		
154 ($P3_221$)	$\Gamma\Delta A(6)$, H-K-H(3)		
158 ($P3c1$)		$k_x k_y$ plane	
159 ($P31c$)		$k_x = \pi$	
161 ($R3c$)		$k_x = -k_y$	$\text{Te}_{16}\text{Si}_{38}$

Table 3.1.: Nonsymmorphic band crossings in trigonal space groups for the case of time-reversal symmetry and strong spin-orbit coupling. The first column states the nontrivial space groups. The second and third columns list the high-symmetry lines and planes, respectively, with movable band crossings, cf. Fig. 3.1. In the last column example materials are given.

3.1.1. Accordion-like band structure

In the following we discuss movable Weyl points due to the presence of $\tilde{C}_3^z(0, 0, \frac{1}{3})$ or equivalently its chiral partner $\tilde{C}_3^z(0, 0, \frac{2}{3})$. A threefold screw rotation by itself leads to an exchange of bands as seen in Fig. 2.3d. We are considering also TRS, but as no point on the line H-K-H and H'-K'-H' is a TRIM, the features of Fig. 2.3d also occur here.

The high-symmetry line Γ -A, which is labeled by Δ , is invariant under the screw rotation and mapped to itself by TRS. In chapter 2 we were able to make some general statements on how an accordion structure arises from these symmetries, but it is instructive to actually go through the process. We do this in two ways: first we shall use the abstract representations provided by the BANDREP tool of the Bilbao crystallographic server [97, 136], then we replace the abstract labels with k_z -dependent rotation eigenvalues and extend the analysis to the remaining rotation axes. For concreteness we choose SG 144, which is generated by $\tilde{C}_3^z(0, 0, \frac{1}{3})$ and translations, and add TRS.

To derive the accordion states as a possible band connectivity of the bands along the axis $(0, 0, k_z)$ with $k_z \in \{-\pi, \pi\}$, i.e., $\Gamma - \Delta - A$, we need to consider the double group representations

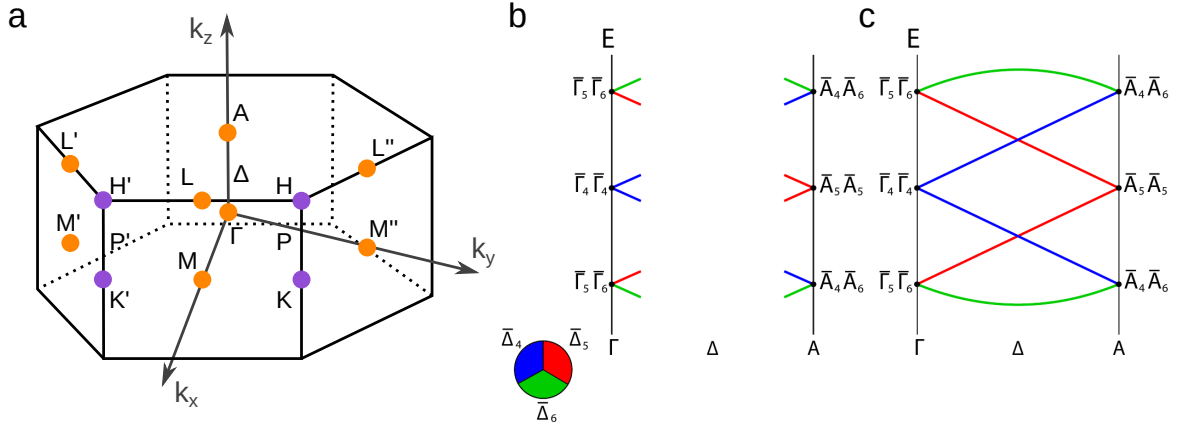


Figure 3.1.: Band crossings for trigonal crystals. **a** Hexagonal unit cell for primitive trigonal space groups [1]. Orange dots denote time-reversal invariant points, while purple dots denote high-symmetry points not invariant under time reversal. **b** Irreducible representations and their compatibility relations at Γ and A . The representations $\bar{\Delta}$ are encoded by the indicated colors. **c** Accordion-like band structure fulfilling the compatibility relations.

of the little groups of Γ and A , and their compatibility relations [97, 136]:

$$\bar{\Gamma}_4\bar{\Gamma}_4, \bar{\Gamma}_5\bar{\Gamma}_6 \qquad \bar{A}_5\bar{A}_5, \bar{A}_4\bar{A}_6 \qquad (3.1.1)$$

$$\bar{\Gamma}_4\bar{\Gamma}_4 \rightarrow 2\bar{\Delta}_4 \qquad \bar{A}_5\bar{A}_5 \rightarrow 2\bar{\Delta}_5 \qquad (3.1.2)$$

$$\bar{\Gamma}_5\bar{\Gamma}_6 \rightarrow \bar{\Delta}_5 \oplus \bar{\Delta}_6 \qquad \bar{A}_4\bar{A}_6 \rightarrow \bar{\Delta}_4 \oplus \bar{\Delta}_6. \qquad (3.1.3)$$

Each irreducible representations given in Eq. 3.1.1 is two-dimensional and splits into two of the 1D representations $\bar{\Delta}_4$, $\bar{\Delta}_5$, and $\bar{\Delta}_6$. None of the compatibility relations given in Eqs. 3.1.2 and 3.1.3 yield representations $\bar{\Delta}$ that directly match another compatibility relation, hence bands of different representations must exchange and cross. An elementary band representation on the line Δ must be connected consistently to the representations from both sides, i.e., from Γ and A .

In Fig. 3.1**b** we give a possible configuration of representations at Γ and A . Now the next step must be to match the lines in the simplest possible way, to obtain a set of enforced crossings. One should note that the order of representations in energy is material dependent and thus it is not obvious that we have chosen an arrangement that only produces enforced crossings. By using straight lines for the bands we can avoid additional accidental crossings and obtain the accordion-like bands in Fig. 3.1**c**. Thus, we have obtained the accordion state. Although this is just a sketch, we see that the connectivity is the same as for the tight-binding model with a threefold screw rotation, which we have shown in Fig. 2.4**d**.

We are interested in enforced crossings, which have to be present for all band configurations.

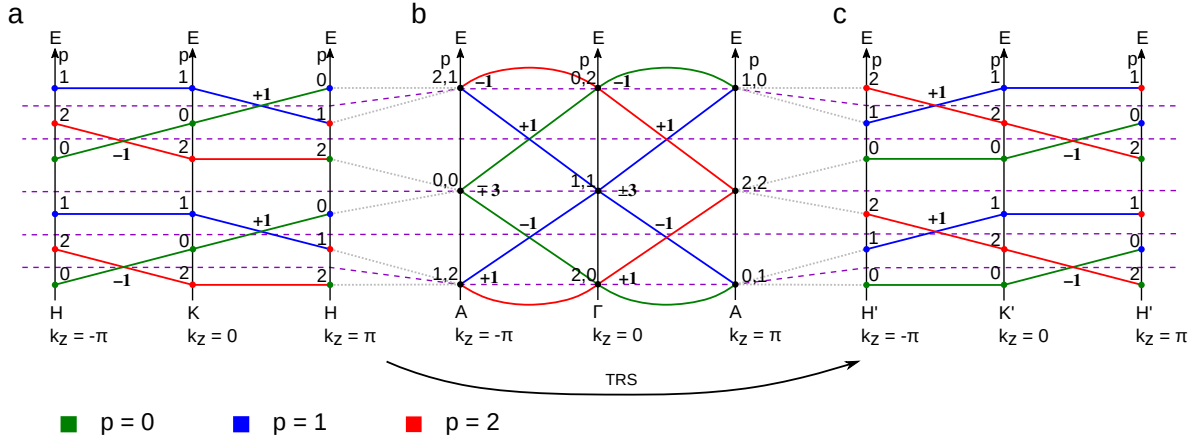


Figure 3.2.: Band connectivities and how they relate to each other on the three threefold rotation axes of trigonal space groups, reproduced from [1]. **a, c** Simplest band structure on the two rotation axes H - K - H and H' - K' - H' subject to the symmetry $\tilde{C}_3^z(0, 0, \frac{1}{3})$. The bands in **a** and **c** are related by time-reversal symmetry (TRS). **b** Accordion state on the rotation axis A - Γ - A with $\tilde{C}_3^z(0, 0, \frac{1}{3})$ and time-reversal symmetry. Purple lines indicate levels of equivalent filling, where the total chiralities of all Weyl points must add up to zero. The dotted gray lines indicate the connectivity of bands through the Brillouin zone away from high-symmetry paths.

Commonly, there might be additional accidental crossings, but there should never be fewer crossings than we have predicted. Thus we must show that the arrangement in Fig. 3.1 cannot be simplified. Let us recall Eq. 2.2.7, which gives a condition for the phase changes $\Delta\varphi_{b,c_b}$ of band b , for bands on the rotation axes of $\tilde{C}_3^z(0, 0, \frac{1}{3})$:

$$\sum_{c_b} \Delta\varphi_{b,c_b} = -b \cdot \frac{2\pi}{3} \pmod{2\pi}. \quad (3.1.4)$$

Each crossing c_b of band b to the next higher band $b + 1$ changes the phase of the complex rotation eigenvalue of band b by $\Delta\varphi_{b,c_b} = \pm\frac{2\pi}{3}$. Thus there must be at least one band crossing for each band b that is not a multiple of 3, i.e., $b \neq 0 \pmod{3}$. If we begin by considering the line Γ and A again, then we know that due to TRS every odd-numbered band has crossings at both Γ and A with the next higher band due to Kramers degeneracy. Together these two pieces of information imply that all even numbered bands in the set of connected bands, i.e., bands 2 and 4, must have at least one crossing that is not at a TRIM, because there are already the Kramers degeneracies at TRIMs and a degeneracy larger than two would be accidental. A crossing for even-numbered bands at $k_z = k_c$ with $0 < k_c < \pi$ implies a second crossing at $k_z = -k_c$. In summary, each band $b \in \{1, 2, 3, 4, 5\}$ has at minimum two crossings, which we did not exceed in the accordion state derived from compatibility relations in Fig. 3.1.

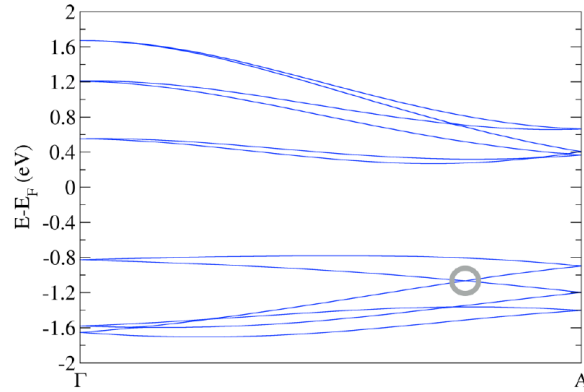


Figure 3.3.: Band structure along Γ to A for trigonal tellurium as obtained from DFT calculations [1]. The first movable Weyl point below the Fermi energy is highlighted by the gray circle.

To ensure that our arrangement of band representations is valid and does not require additional accidental crossings to fulfill the Nielsen-Ninomiya theorem, we need to check that the chiralities compensate each other. The eigenvalues of the threefold screw rotation are

$$\lambda_{\tilde{C}_{3,p}} = \exp\left(i\frac{2\pi p + \pi + k_z}{3}\right), \quad (3.1.5)$$

see Eq. 2.2.3 for details. If we label our bands by p , then we can describe band crossings by tuples (p_1, p_2) . At Γ time-reversal pairs $(0, 2)$ and $(1, 1)$, whereas at A the degeneracies are $(0, 1)$ and $(2, 2)$. To fulfill Eq. 3.1.4 for band $b = 3$, we must use the two crossings at TRIMs, which may either have each a vanishing phase change or $\Delta\varphi_{3,c_b} = 0$ or opposite contributions $\Delta\varphi_{3,\Gamma} = -\Delta\varphi_{3,A}$. This allows for two combinations $(0, 2)$ at Γ and $(0, 1)$ at A, or $(1, 1)$ at Γ and $(2, 2)$ at A. While both are possible we will choose the second one in the following discussion. With this choice we can reproduce the accordion-like bands with the symmetry eigenvalues as shown in Fig. 3.2b.

Now we want to check, whether for a given band the Weyl point chiralities add up to zero. The Weyl points that are described by a crossing of different eigenvalues have a chirality of $\nu = +1$, if the phase increases by $\Delta\varphi_{b,c_b} = +\frac{2\pi}{3}$, and a chirality of $\nu = -1$ otherwise, i.e., when $\Delta\varphi_{b,c_b} = -\frac{2\pi}{3}$ [209]. At TRIMs the crossings between identical eigenvalues, $(1, 1)$ and $(2, 2)$, carry a charge of $\nu = \pm 3$ but the sign is not fixed by symmetry. Away from TRIMs identical eigenvalues may only form avoided crossings. In Fig. 3.2 we give the chiralities for all enforced crossings. We can then infer how the bands must be aligned on the axes H-K-H and H'-K'-H', which are related to each other by TRS, to compensate the charges on the lines A- Γ -A. Time

reversal maps k_z to $-k_z$ and complex conjugates the eigenvalues resulting in

$$\lambda_{\tilde{C}_{3,p}}(k_z) = \exp\left(i\frac{2\pi p + \pi + k_z}{3}\right) \quad (3.1.6)$$

$$\xrightarrow{TRS} \exp\left(-i\frac{2\pi p + \pi + k_z}{3}\right) = \exp\left(i\frac{2\pi(-p-1) + \pi + (-k_z)}{3}\right) \quad (3.1.7)$$

$$= \lambda_{\tilde{C}_{3,p'=-p-1}}(-k_z), \quad (3.1.8)$$

which means the time-reversal related band is defined by $p' = -p - 1 \pmod{3}$. A band with $p = 0$ on the line H-K-H is related to $p' = 2$ at $-k_z$ on the axis H'-K'-H', whereas the same mapping would relate $p = 1$ to $p' = 1$. These relations are encoded in the colors of Figs. 3.2a and c.

In conclusion, we find that the charges on the threefold screw rotation axes, A- Γ -A, H-K-H, and H'-K'-H', compensate each other and no additional crossings are required. The remaining TRIMs L and M as well as their related crossings of equal charge L', L'' and M', M'', have to host oppositely charged Kramers-Weyl points to complete the compensation of chiralities for the full BZ. We have thus shown that the accordion state is the simplest arrangement of bands for SG 144, and our results can be applied equivalently to all other groups with threefold screw rotations, i.e., SGs 145, 152, 152, 153, and 154. A possible material realization of the accordion band structure is trigonal tellurium [1, 233], which belongs to SG 152, see Fig. 3.3. These accordion-like bands in trigonal tellurium have been found by ARPES measurements after the publication of our results [232].

3.1.2. Hourglass nodal lines

We study the nodal lines of the trigonal space groups by repeating the investigation of elementary band representations for the mirror plane D, highlighted in Figs. 3.5b to c. The three SGs 158, 159, and 161 each contain a mirror symmetry of the form $M^x(0, 0, \frac{1}{2})$, albeit with different normal vectors within the xy-plane. Thus, we must expect twofold hourglass nodal lines, because the bands must exchange between TRIMs of different eigenvalue pairing, see Fig. 3.5a.

To determine their connectivity one may consider different paths through the mirror plane, see, for example, the band connectivity of SG 158 in Fig. 3.4. Note that the point A (corresponding to Z for the rhombohedral unit cell type) hosts either twofold and fourfold degenerate representations [97, 136].

The result of this analysis is shown in Figs. 3.5b - d. SG 158 illustrates the general scheme of hourglass nodal lines, see Fig. 3.5b, where nodal lines occur between TRIMs, where the mirror eigenvalues are paired differently. The same eigenvalues are paired at TRIMs marked

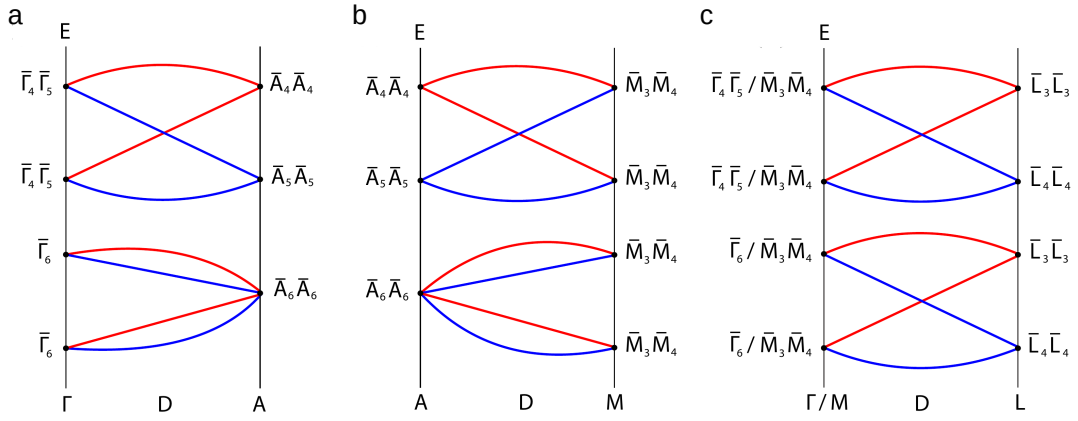


Figure 3.4.: Irreducible representations and connectivity on the mirror plane D [1]. Since the shown path through the nodal plane D is arbitrary, the occurring crossings are part of nodal lines.

with a blue circle, while TRIMs with opposite pairing are marked in red. As long as the point A is not fourfold degenerate the nodal lines must occur somewhere between blue and red TRIMs. For SG 159 there are two mirror planes, but the one containing the TRIMs Γ and A does not need to exhibit nodal lines between TRIMs, if the point A is fourfold degenerate, see Fig. 3.5c. In the last remaining trigonal space group with enforced hourglass nodal lines, SG 161, the connectivity is the same as for SG 158, but the unit cell is rhombohedral rather than hexagonal and thus the shape of the BZ must be adjusted.

Note that there are also pinned nodal lines, due to the composite symmetry $\theta M(0, 0, \frac{1}{2})$ of TRS and the glide mirror operation, as well as almost movable nodal lines if at a TRIM different eigenvalues are paired by TRS. These crossings occur at a band index of $b = 1$ and $b = 3$, whereas the hourglass nodal lines occur for band $b = 2$.

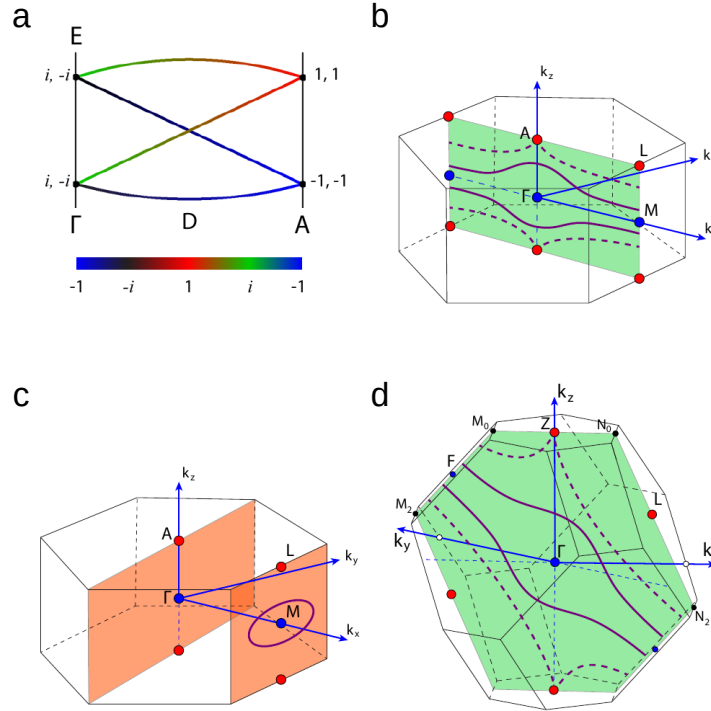


Figure 3.5.: Hourglass nodal lines of the trigonal space groups [1]. **a** Band connectivity for SG 158 along a path in the $k_x k_y$ -plane. **b - d** Weyl nodal lines (purple curves) protected by glide-mirror symmetry. **b** SG 158, **c** SG 159, and **d** SG 161. If the representation at A (or Z) is fourfold degenerate the nodal line is described by the dashed curve, whereas for twofold representations at A (or Z) the solid curves describe the simplest arrangement of nodal lines. Red and blue colored TRIMs correspond to a pairing of equal and different mirror eigenvalues, respectively.

3.2. Topological crossings in tetragonal space groups

With the following analysis of tetragonal space groups we aim to give a comprehensive description of enforced nodal features, which then serves as a starting point of a search for suitable materials [2]. Here, we give an excerpt of the work [2], highlighting some of the more unusual findings.

Our work comprises all notions of band crossings that are not directly evident from the dimensions of irreducible little group representations. To be specific we study the movable Weyl/Dirac points, hourglass and accordion band structures, chiral point crossings of higher topological charge, the number of Weyl points at the same energy, movable twofold and fourfold nodal lines, fourfold nodal lines in the absence of inversion symmetry, nodal lines not accessible from compatibility relations, and (topological) nodal planes. The analysis is

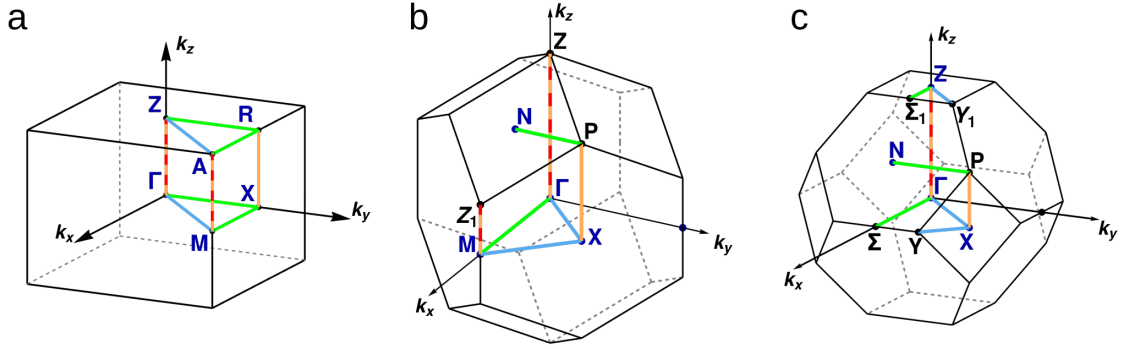


Figure 3.6.: Brillouin zones of the tetragonal crystal system [2, 87]. TRIMs are labeled in dark blue. Lines of high-symmetry, i.e., sections of rotation axes, are highlighted for the fourfold rotation (red) along $[001]$, and the twofold rotations along $\langle 100 \rangle$ (green), $\langle 110 \rangle$ (light blue), and $[001]$ (orange). **a** Primitive BZ. **b** Body-centered BZ for $c < a$, BCT_1 . **c** Body-centered BZ for $c > a$, BCT_2 .

performed for spinful systems with strong spin-orbit coupling. Our results are listed in Table 3.2 for the tetragonal SGs without inversion symmetry and in Table 3.3 for the SGs with inversion symmetry. Besides band crossings, we consider enforced nontrivial strong topology, i.e., an inversion of bands that is enforced by the crystal symmetries.

In our tables we use the labels of high-symmetry points as introduced in Fig. 3.6. We use the notation “ Γ -Z-R” to denote the straight lines that connect the point Γ to Z and Z to R on the shortest path. This is used if some point on the line is of interest. E.g., in the second column of Table 3.2 we write “ Γ -Z(8)” to denote the movable Weyl points as part of an accordion band structure comprising 8 bands on the fourfold rotation axis Γ -Z. If we need to refer to a degeneracy along the complete line we write \overline{MA} for all points on the line M-A. To denote movable lines, we give the TRIMs that exhibit the same pairing of eigenvalues. E.g., “(Γ -Z-R ; X)(4)” tells us that all points on the line Γ -Z-R have different mirror eigenvalues paired, whereas at X identical eigenvalues are related by TRS. The number of connected bands in this hourglass nodal line structure is thus 4 as given in brackets. In other words, any line in the mirror plane exhibits an hourglass structure if it connects a point given on the left hand-side of the semicolon in “(Γ -Z-R ; X)(4)” with a point of the right hand-side. Almost movable nodal lines do not need the right hand-side and occur always if there is a point on the left hand-side that is not part of a nodal line. For example “(N, Γ -Z, M-Z₁; -)(2)” indicates that an almost movable nodal line passes through the point N. If a point is on a line of certain pairing, but is actually fourfold degenerate we write it in *italic*, see Figs. 3.4 and 3.5. Any path that connects

to such a fourfold point does not need to exhibit an hourglass band structure. A high-symmetry point marked with a “(*)” has representations of different dimensionality, e.g., twofold and fourfold degenerate bands at the same point.

The defining property of tetragonal space groups are fourfold rotations C_4^z around the z-axis. This symmetry leaves the lines Γ -Z and M-A invariant, where one should expect the largest number of connected bands. Together with time-reversal symmetry this reduces the independent region of the BZ to one octant, i.e., the fraction where we have labeled the BZ in Fig. 3.6. The space groups fall into categories depending on their point group. If the point group is 4 (SGs 75 - 80), $\bar{4}$ (SGs 81-82), or 422 (SGs 89-98), there will be at least Kramers-Weyl points. Once screw rotations are involved, various movable or Weyl points with higher charge and degeneracy will occur. For point groups 4mm (SGs 99 - 110) nodal lines in various configurations arise, whereas it is more complex for the point group $\bar{4}2mn$. In the latter SGs the topological features depend on whether the mirror planes fall onto TRIMs or not. Cases arise where nodal lines and Weyl points coexist at the same band index. The SGs associated to point groups with inversion behave, for our purposes, rather similar to each other and we will only discuss some SGs as special cases.

3.2.1. The flavors of chiral point crossings

Since we have already given a detailed account on point crossings with a non-zero Chern number for the trigonal SGs, see Sec. 3.1.1, we want to use the next paragraphs to summarize the different types of crossings appearing in the tetragonal SGs.

In the fifth columns of Table 3.2 we list the number of enforced Weyl points that occur in the same gap between the same bands, i.e., at the same band index b . The Chern numbers of crossings at the same band number must compensate each other to fulfill the Nielsen-Ninomiya theorem [21] and depending on the specific parameters of a material realization they may exist at the same energy. For a primitive unit cell, one often finds eight Kramers-Weyl points. If there is an accordion band structure, the movable crossings on the rotation axes will have a lower multiplicity at half filling, since there are only two fourfold rotation axes of the same orientation. This yields four Weyl points at the same energy. In our discussion on 2D band degeneracies, see Sec. 2.2.3, also paramagnetic SGs were shown to exhibit topological nodal planes. Some of the topological nodal planes of Table 2.3 reappear in our list, i.e., the trios of nodal planes in SGs 92 and 96, as well as the duo of nodal planes in SG 94.

SG	movable Weyl points	movable Weyl lines	fourfold points	# Weyl	nodal planes	notable features
75 ($P4$)				8		
76 ($P4_1$)	Γ -Z(8), M-A(8), X-R(4)			4,8	$k_z = \pi$	double Weyl
77 ($P4_2$)	Γ -Z(4), M-A(4)			4,8		double Weyl
78 ($P4_3$)	Γ -Z(8), M-A(8), X-R(4)			4,8	$k_z = \pi$	double Weyl
79 ($I4$)				10		Weyl at P
80 ($I4_1$)	Γ -Z-M(4)			4,8		double Weyl, Weyl at P(*)
81 ($P\bar{4}$)				4		
82 ($I\bar{4}$)				6		
89 ($P422$)				8		
90 ($P42_12$)	Γ -X(4), Z-R(4)		A, M	2,10	$k_x, k_y = \pi$	fourfold Weyl
91 ($P4_122$)	Γ -Z(8), M-A(8), X-R(4)			4,8	$k_z = \pi$	double Weyl
92 ($P4_12_12$)	Γ -Z(8), Γ -X(4)		M, R, A(*)	1,3,9	$k_x, k_y, k_z = \pi$	top. nodal plane, twofold/fourfold (double/quadruple) Weyl
93 ($P4_222$)	Γ -Z(4), M-A(4)			4,8		double Weyl
94 ($P4_22_12$)	Γ -Z(4), Γ -X(4), Z-R(4)		A, M	2,12	$k_x, k_y = \pi$	top. nodal plane, double/fourfold Weyl
95 ($P4_322$)	Γ -Z(8), M-A(8), X-R(4)			4,8	$k_z = \pi$	double Weyl
96 ($P4_32_12$)	Γ -Z(8), Γ -X(4)		M, R, A(*)	1,3,9	$k_x, k_y, k_z = \pi$	see SG 92
97 ($I422$)				10		Weyl at P
98 ($I4_122$)	Γ -Z-M(4)			4,8		Weyl at P(*)
99 ($P4mm$)						
100 ($P4bm$)		(Γ -Z ; X, R)(4)	M, A			
101 ($P4_2cm$)			Z, A, R			
102 ($P4_2nm$)		(Γ -Z-R ; X)(4), (X-M-A ; R)(4)	Z, M			nodal chain metal
103 ($P4cc$)			Z, R, A			
104 ($P4nc$)		(Γ -Z-R ; X)(4), (X-M-A ; R)(4)	Z, M, A			nodal chain metal
105 ($P4_2mc$)			Z, A			
106 ($P4_2bc$)		(Γ -Z ; X, R)(4)	Z, A, M, M-A(8)			movable fourfold point
107 ($I4mm$)		(N, Γ -Z, M-Z ₁ ; -)(2)				
108 ($I4cm$)		(Γ -Z, M-Z ₁ ; N)(4)	P			fourfold at P
109 ($I4_1md$)		(Γ -Z ; X)(4), (N, Γ -Z, M-Z ₁ ; -)(2)	M			P(*), nodal chain metal
110 ($I4_1cd$)		(Γ -Z, P ; X)(4), (Γ -Z, X ; P)(4), (X-M ; P)(4), (Γ -Z, M-Z ₁ ; N)(4), (P, Γ -Z ; -)(2), (P, X-M-Z ₁ ; -)(2)	M			8N bands, in-gap nodal lines
111 ($P\bar{4}2m$)				4		
112 ($P\bar{4}2c$)			Z, A	4		
113 ($P\bar{4}2_1m$)	Γ -X(4), Z-R(4)		$\bar{M}A$	8	$k_x, k_y = \pi$	fourfold line
114 ($P\bar{4}2_1c$)	Γ -X(4)		Z, $\bar{M}A$	4	$k_x, k_y = \pi$	fourfold line
115 ($P\bar{4}m2$)						
116 ($P\bar{4}c2$)			Z, A, R			
117 ($P\bar{4}b2$)		(Γ -Z ; X, R)(4)	A, M			
118 ($P\bar{4}n2$)	A-R(4), R-X(4)	(Γ -Z-R ; X)(4) (X-M-A ; R)(4)	Z, M			nodal chain metal
119 ($I\bar{4}m2$)		(N, Γ -Z, M-Z ₁ ; -)(2)		2		
120 ($I\bar{4}c2$)	X-P(4)	(Γ -Z, M-Z ₁ ; N)(4)		2		
121 ($I\bar{4}2m$)				4		
122 ($I\bar{4}2d$)		(Γ -Z ; X)(4)	M	4		nodal chain metal

Table 3.2.: Band crossings in non-centrosymmetric tetragonal crystals with strong spin-orbit coupling [2]. The first column lists the tetragonal space groups (SG) that lack inversion symmetry. The second and third columns list the positions of Weyl points, and Weyl nodal lines, respectively, which are movable on the indicated rotation axis or mirror plane. The fourth column denotes points in reciprocal space with a fourfold degeneracy. The fifth column gives the number of enforced point crossings with non-zero chirality at the same band index. The second to last column lists conditions on \mathbf{k} for nodal planes. The last column contains a selection of noteworthy features of the respective SG.

SG	Dirac points	Dirac lines	accidental points	accidental lines	notable features
83 ($P4/m$)					
84 ($P4_2/m$)	Z, A				
85 ($P4/n$)	X, A, M, R		X-R		
86 ($P4_2/n$)	X, Z, M, R		X-R		
87 ($I4/m$)					
88 ($I4_1/a$)	X, M		X-P		
123 ($P4/mmm$)					
124 ($P4/mcc$)	A, Z, R		Z-R, Z-A, R-A		
125 ($P4/nbm$)	M, A, X, R		X-R, X-M, R-A		
126 ($P4/nnc$)	X, Z, A, R, M		X-R, X-M, Z-R, Z-A		
127 ($P4/mbm$)		$\overline{MX}, \overline{AM}, \overline{AR}$		$k_x, k_y = \pi$	
128 ($P4/mnc$)	Z	$\overline{AM}, \overline{MX}$	Z-R, Z-A, R-A	$k_x, k_y = \pi$	
129 ($P4/nmm$)		$\overline{RX}, \overline{AM}$		$k_x, k_y = \pi$	
130 ($P4/ncc$)	Z, R-Z(4)	$\overline{RX}, \overline{AM}, \overline{AR}$	Z-R, Z-A	$k_x, k_y = \pi$	movable Dirac; eightfold A
131 ($P4_2/mmc$)	Z, A		Z-A		
132 ($P4_2/mcm$)	Z, R, A		Z-R, R-A		
133 ($P4_2/nbc$)	X, Z, A, R, M, A-M(4)		X-R, X-M, Z-A, R-A		movable Dirac
134 ($P4_2/nmm$)	X, Z, M, R		X-R, X-M, Z-R		
135 ($P4_2/mbc$)	Z	$\overline{MX}, \overline{AM}, \overline{AR}$	Z-A	$k_x, k_y = \pi$	eightfold A
136 ($P4_2/nmm$)	Z	$\overline{MX}, \overline{AM}$	Z-R	$k_x, k_y = \pi$	
137 ($P4_2/nmc$)	Z	$\overline{AM}, \overline{RX}$	Z-A	$k_x, k_y = \pi$	
138 ($P4_2/ncm$)	Z, R-Z(4)	$\overline{AR}, \overline{AM}, \overline{RX}$	Z-R	$k_x, k_y = \pi$	movable Dirac
139 ($I4/mmm$)					
140 ($I4/mcm$)	N, P		N-P		
141 ($I4/amd$)	X, M		X-P, X-M		
142 ($I4_1/acd$)	X, M, N, P(*)		X-P, X-M, N-P		Dirac at P(*)

Table 3.3.: Classification of enforced band crossings in centrosymmetric tetragonal crystals with strong spin-orbit coupling [2]. The first column lists the tetragonal space groups including inversion symmetry by their number and symbol. The second and third column lists the positions of Dirac points and Dirac lines, respectively. The fourth and fifth column list lines and planes on which accidental points and lines are possible, respectively. Here, the fourfold rotation axis Γ -Z and M-A are omitted, because they always allow accidental crossings except when they host a Dirac line. The last column indicates some noteworthy features.

Pinned Weyl points away from TRIMs

Weyl points at TRIMs are a direct consequence of Kramers theorem, but Kramers-Weyl points away from TRIMs are rare but not impossible. Let us consider SG 79, which we list with 10 Weyl points at the same band index. Eight of these are regular Kramers-Weyl points occupying the TRIMs of the body-centered unit cell. Two additional Weyl points occur, because the combination θC_4^z of a symmorphic fourfold rotation C_4^z and TRS θ leaves the point $P(\pi, \pi, \pi)$ invariant, which occurs in two symmetry related copies, and fulfills Kramers theorem, see Sec. 2.1.2. For this example both eigenvalues of the twofold rotation are affected by Kramers theorem and are paired forming a Kramers-Weyl point at P.

If one replaces the fourfold rotation of SG 79 with a fourfold screw rotation one obtains SG 80, which is generated by $C_4^z(0, \frac{1}{2}, \frac{1}{4})$. This makes one of the eigenvalues at the point P

equal to 1, which is not affected by Kramers theorem anymore. In the simplest case there will be just one double Weyl point at P, which closes the same gap as the hourglass Weyl points on the fourfold rotation axis. Note that the rotation axis Γ -Z-M is longer than in a primitive cell, due to the body-centered unit cell. Effectively the accumulated phase change corresponds to what a fourfold screw rotation $C_4^z(0, 0, \frac{2}{4})$, i.e., $m = 2$ in the notation of Ch. 2, would obtain in a primitive unit cell. Thus, a minimal band structure contains four double Weyl points at half-filling. The fact that P hosts a double Weyl point in SG 80 deserves more attention, because here identical rotation eigenvalues are paired, which happens for any twofold screw rotation. But for a twofold screw rotation \tilde{C}_2^z in a primitive BZ, there are always nodal planes such that the crossing between identical rotation eigenvalues is not a Weyl point. In SG 80, on the other hand, there is no plane invariant under the composite symmetry $\theta\tilde{C}_2^z$, and thus there is no nodal plane.

The SGs 97 and 98 are the same as SG 79 and 80, respectively, but with additional symmorphic twofold rotations that do not affect the above arguments.

Two Weyl points in the presence of time reversal

To find space groups where the multiplicity of Weyl points at the same energy is smaller than four, one must consider Weyl points at TRIMs, because all other momenta have a distinct time-reversal partner and thus there would be four points in total. It is possible to have only three Weyl points, like in SGs 92 and 96, where one of the three Weyl points is a double Weyl point of charge $\nu = \pm 2$, whereas the remaining two crossings have a charge of $\nu = \mp 1$.

If we want to find an even smaller number of Weyl points, we need to look at TRIMs. For example, in SG 90 a nodal plane duo covers all TRIMs except the two points Γ and Z. The Kramers-Weyl points at Γ and Z may mutually compensate their charges, and thus there would be just two Weyl points in the BZ for an odd number of filled bands. Note that if one terminates a system obeying SG 90, the Weyl points would overlap in the surface spectrum for a [001] termination and for the $\langle 100 \rangle$ direction the bulk gap around the Fermi arc would be closed due to the nodal planes.

Instead of considering cases, where a nodal plane to removes some of the Kramers-Weyl points, one may also consider mirror planes that coincide with some but not all of the TRIMs. This happens for SGs 111 - 114 and 119 - 122. The body-centered SGs 119 and 120 are optimal for this approach, because here only two inequivalent copies of the TRIM X are away from mirror planes, i.e., the TRIMs Γ , M, and all points N are on mirror planes, and thus they carry no chirality but are instead part of nodal lines, see Fig. 3.6. Due to the rotoinversion and mirror symmetries the points X and X' carry opposite Chern numbers.

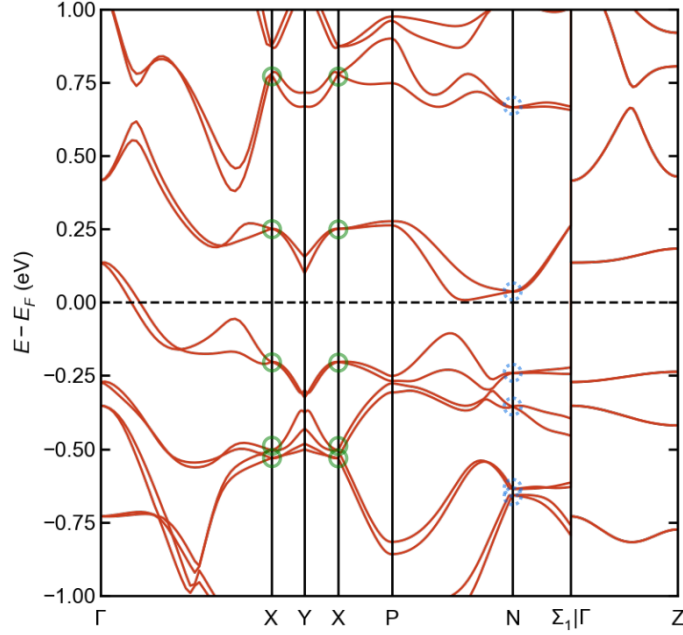


Figure 3.7.: Band structure of Cs_2Tl_3 (SG 119) calculated by DFT. [2]. Green circle: Kramers-Weyl point of multiplicity 2 at TRIMs. Blue dashed circle: almost movable nodal line crossing a TRIM.

The hypothetical compound Cs_2Tl_3 has the symmetries of SG 119 and exhibits the enforced crossings close to the Fermi energy, but sadly it does exhibit additional accidental Weyl points on the rotation axis Γ -X, see Fig. 3.7. To study the surface states of a material with just two enforced Weyl points we devise two generic tight-binding models and choose the $(1\bar{1}0)$ surface as termination. For this surface orientation one X point is projected onto Γ of the surface BZ and at its edge the second TRIM with a Weyl point, X' , is found. Although the Weyl points carry only integer charge, we find two Fermi arcs instead of one in the SDOS, which is unexpected at first, see Fig. 3.8. The charges of the Weyl points are well defined by calculating the Chern number on a surface enclosing them. If we consider planes parallel to the plane spanned by the lines Γ -Z and Γ -X we find, that we do not obtain a plane in between the two Weyl points unlike in Fig. 1.6, where we discussed the Fermi arcs as surface state due to a non-zero Chern number. Instead, due to geometry of the body-centered BZ, such a plane will cross both lines Γ -X' and its time-reversal counterpart X' - Γ . Any Chern number calculated on such a plane will be zero for SG 119. This means for our SDOS that if we assign a direction to each Fermi arc, e.g., when we follow it from positive to negative charged Weyl points, then the arcs will cross the projection of the plane with zero Chern number an even number of times. Hereby, each crossing through the nodal plane is implied by a crossing in the opposite direction somewhere

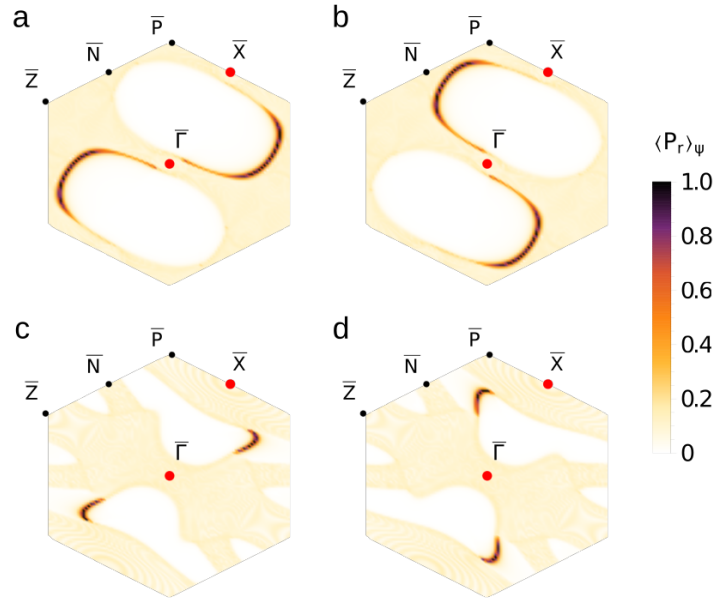


Figure 3.8.: Surface density of states, with the localization of the eigenstates indicated by the colors, for two tight-binding models subject to the symmetries of SG 119 with Fermi arcs [2]. **a,b** (**c,d**) the model contains up to 2nd (3rd) nearest neighbor hoppings. **a,c** (**b,d**) show the top (bottom) surface of the slab geometry.

else in the surface BZ. In Fig. 3.8 the projections of such planes occur as lines parallel to $\bar{\Gamma}$ - \bar{Z} , and we find indeed two Fermi arcs with the expected orientation. In summary, we find that this approach yields two Weyl points with an unusual configuration of Fermi arcs. But due to the presence of nodal lines that cross the Fermi energy as well as possible accidental nodal lines, an experimental identification of such a feature could prove to be difficult. In the next section, Sec. 3.3, we will discuss symmetries, which allow in principle for occurrence of *single* Fermi arcs.

Double and quadruple fourfold crossing

We list in Table 3.2 space groups without mirror or inversion symmetries that nevertheless exhibit fourfold point crossings, i.e., SGs 90, 92, 94, and 96. Since no symmetry fixes their topological charges to zero, one should expect something nontrivial to occur.

In the SGs 90 and 94 at M and A, as well as in SGs 92 and 96 at M and R, we find that these are fourfold double Weyl points, i.e., fourfold degenerate crossings with a total charge of $\nu = \pm 2$. These crossings can be understood by the eigenvalues of twofold rotation $C_2^z(0, 0, \frac{m}{2})$ that are paired by time reversal $\theta = i\sigma_y K$ and the composite symmetry $\theta \tilde{C}_2^x$. For SGs 90 the exact operations are $C_2^z(0, 0, 0)$ with the eigenvalues $\lambda_{C_2^z} = \pm i$ and $\theta \tilde{C}_2^x(\frac{1}{2}, \frac{1}{2}, 0)$. At both A and

M time-reversal symmetry pairs $+i$ and $-i$ eigenvalues. Kramers theorem is also fulfilled by $\theta\tilde{C}_2^x(\frac{1}{2}, \frac{1}{2}, 0)$, which gains a total of 4 sign changes for the relation of $C_2^z(0, 0, 0)$ eigenvalues,

$$C_2^z(0, 0, 0) \theta\tilde{C}_2^x(\frac{1}{2}, \frac{1}{2}, 0) |\pm i\rangle = -\theta\tilde{C}_2^x(\frac{1}{2}, \frac{1}{2}, 0) C_2^z(0, 0, 0) \exp(i(-k_x + k_z)) |\pm i\rangle \\ \stackrel{\mathbf{k} \in \text{M-A}}{=} \pm i \theta\tilde{C}_2^x(\frac{1}{2}, \frac{1}{2}, 0) |\pm i\rangle, \quad (3.2.1)$$

one due to spin, two from the full translations as a result of the commutation of nonsymmorphic operations for $\mathbf{k} \in \text{M-A}$, and a fourth sign change due to the complex conjugation applied to imaginary eigenvalues. Since we have just shown that $\theta\tilde{C}_2^x(\frac{1}{2}, \frac{1}{2}, 0)$ pairs identical eigenvalues on the rotation axis, one may understand the fourfold crossings at M (or A) as two superimposed copies of a Kramers-Weyl point, thus their charge is found to be $\nu = \pm 2$ [2, 234]. Exactly the same argument applies to SG 94, whereas for SGs 92 and 96 the operation $C_2^z(0, 0, 0)$ is replaced by $C_2^z(0, 0, \frac{1}{2})$. The latter means that for SGs 92 and 96 Eq. 3.2.1 only applies to the M point, while at $k_z = \pi$ the real eigenvalues require that $\theta\tilde{C}_2^x$ pairs different instead of identical eigenvalues, and thus the fourfold double Weyl is at R instead of A.

One last crossing remains, namely the fourfold degenerate A point in SGs 92 and 96. To understand these one must consider how the twofold rotation commutes with $\theta\tilde{C}_2^x$. It is found that at the A point TRS pairs the eigenvalues of the fourfold rotation labeled by $p \in \{0, 1, 2, 3\}$, as introduced in Eq. 2.2.3, namely as (0,2), (1,1), and (3,3), whereas $\theta\tilde{C}_2^x$ pairs (0,2) and (1,3), thus yielding a fourfold degeneracy labeled by (1,1,3,3). Here, bands of different degeneracies occur at the same point, although Kramers theorem applies independently of the symmetry eigenvalues upon which the antiunitary operation acts. The different pairing is a result of the different action of complex conjugation on real and imaginary eigenvalues. The total charge is ± 4 and, like for a double Weyl point, the dispersion becomes quadratic along the perpendicular directions to the rotation axis. Therefore one may think of this fourfold quadruple Weyl point as two superimposed double Weyl points [2, 235].

3.2.2. Weyl nodal lines

This section will be concerned with Weyl nodal lines, which is used synonymously to twofold degenerate nodal lines. Fourfold degenerate lines, which occur except for two SGs solely in centrosymmetric systems, are always pinned to high-symmetry axes. Therefore, at this point we will refer to the Tables 3.2 and 3.3 for the fourfold degenerate lines and focus here on the Weyl nodal lines.

Before we turn to a material realization of a nodal chain and an armillary sphere of nodal lines, we start by looking at almost movable nodal lines. We want to make a point that they are easy to miss. In fact, Figs. 3.7 and 3.8, which we discussed for SG 119, already contained

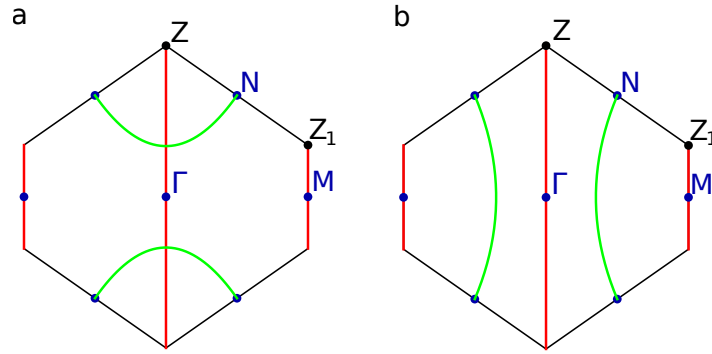


Figure 3.9.: Possible configuration of almost movable nodal lines (green) and pinned nodal lines (red) for the SGs 107, 109, and 119 [2]. **a** and **b** show different possible arrangements of almost movable nodal lines with and without a crossing of a pinned nodal line, respectively.

almost movable nodal lines. SG 119 contains the symmorphic mirror symmetry M^x with the two imaginary symmetry eigenvalues $\pm i$, which are paired at the TRIM N, see Fig. 3.7. A degeneracy at a TRIM is expected, but as we have discussed in Sec. 2.2.2 the pairing of identical eigenvalues leads to a nodal line through the TRIM, along which the bands cross and the eigenvalues are exchanged. The bulk bands associated to these nodal lines can be seen in the SDOS given in Fig. 3.8 for our tight-binding model of SG 119. In Figs. 3.8**a, b** the nodal line is straight and connects \bar{Z} to \bar{P} , whereas with an additional hopping term the line extends from \bar{N} half-way towards $\bar{\Gamma}$ and then curves towards an unlabeled point equivalent to \bar{N} , see Figs. 3.8**c, d**. We have visualized the latter case in Fig. 3.9**a**. The almost movable nodal lines may cross the pinned nodal lines of the same eigenvalue pairing, but a different connectivity like in Fig. 3.9**b** is possible as well. Such almost movable nodal lines will reappear in the next section as part of a more complex structure of nodal lines.

Nodal armillary sphere

In the following we want to discuss a nodal armillary sphere in SG 110, i.e., a crossing of two nodal lines around the point P in a body-centered tetragonal BZ. The term nodal armillary sphere is chosen due to its similarity to the armillary sphere, a mechanical device to represent the motion of celestial bodies [226]. The basic idea is to label the bands on the path X-P by the eigenvalues of three mutually commuting symmetries, $M^{1\bar{1}0}(\frac{1}{2}, 0, \frac{1}{4})$, $M^{110}(0, \frac{1}{2}, \frac{3}{4})$, and $\tilde{C}_2^z(\frac{1}{2}, \frac{1}{2}, \frac{1}{2})$.

Each eigenvalue is determined by its value of p and each band can be represented by the triple composed of the three variables $(p_{M^{1\bar{1}0}}, p_{M^{110}}, p_{\tilde{C}_2^z})$ with $p_{M^{1\bar{1}0}}, p_{M^{110}}, p_{\tilde{C}_2^z} \in \{0, 1\}$. Actually,

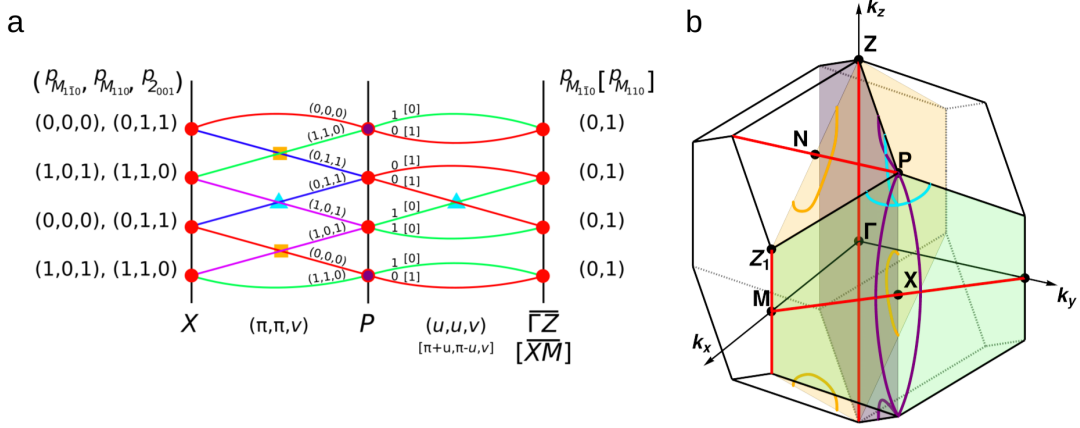


Figure 3.10.: Nodal lines enforced by SG 110 [2]. **a** Schematic band connectivity diagram for the line parametrized by (π, π, ν) and the mirror planes given by (u, u, ν) and $(\pi + u, \pi - u, \nu)$. The band labels are given next to each band and are stated for the latter plane in square brackets. Torquoise triangles: Nodal armillary sphere. Yellow squares: Hourglass nodal lines. Red circles: pinned nodal lines, which when overlapped by a purple circle denote an intersecting almost movable nodal line. **b** Qualitative arrangement of nodal lines in the 3D body-centered tetragonal BZ. The colors of the nodal lines correspond to the colored labels in **a**. Additional nodal lines related by fourfold rotation symmetry are omitted here for clarity.

only two of these variables are independent and determine the third, but we keep all three to have them accessible to infer the symmetry eigenvalues on the intersecting mirror planes. With this representation time-reversal and its combinations with spatial operations must be considered. For further details we refer to our publication [2].

If we search for the simplest way to arrange the crossings, we find an accordion-like structure along the line X-P and hourglass band structures and unpaired bands on the mirror planes on arbitrary paths to the lines $\overline{\Gamma Z}$ and \overline{XM} , see Fig. 3.10a. To identify the band structure on mirror planes, we monitor the crossings between different eigenvalues of the mirror symmetries M^{110} and $M^{1\bar{1}0}$ along the line X-P, which then imply line degeneracies within the mirror planes. With this insight we depict the resulting arrangement of the nodal lines in Fig. 3.10b. Note that the size of the turquoise armillary sphere is not fixed by symmetry and depends on the details of the system. In summary, SG 110 exhibits pinned, almost movable, movable, and interlinked nodal lines, and thus nearly any type of twofold nodal line in a single set of connected bands.

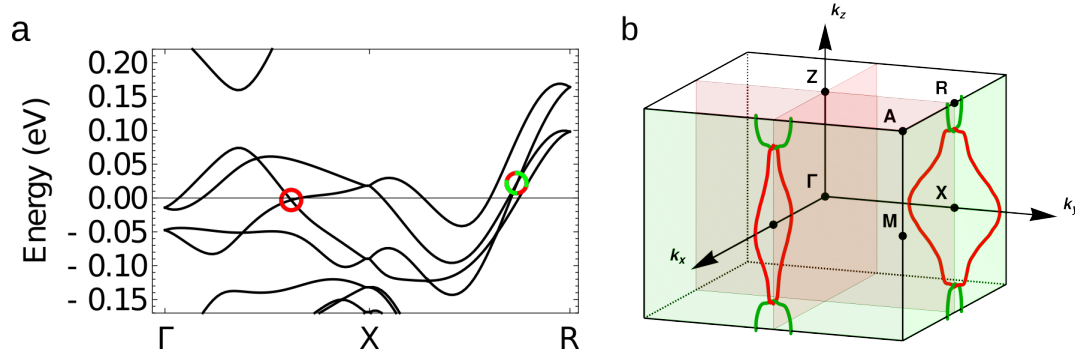


Figure 3.11.: Nodal chain metal $Ba_5In_4Bi_5$ in SG 104 [2]. **a** Electronic band structure from DFT calculation. Intersections between the nodal chain and the plotted path are marked by circles. **b** Position of the nodal line in the primitive Brillouin zone. The crossing marked by the red circle in **a** corresponds to the red nodal line encircling X in **b**. The crossing marked by the red/green dashed circle in **a** is the junction of the chain on the path X-R in **b**. The red mirror planes are defined by $k_x = 0$ or $k_y = 0$. The green mirror planes are defined by $k_x = \pi$ or $k_y = \pi$.

Nodal chains

Nodal chains are structures of intersecting nodal lines that extend over the full BZ [236]. Space groups which exhibit them have already been classified in Ref. [236] and we highlight them for completeness in Table 3.2. A nodal chain occurs if two mirror planes intersect and a TRIM within the intersection of both has a different pairing for each mirror plane. Along the intersection line there must be a second TRIM with a different pairing than the first, such that an hourglass band structure occurs on the intersection line. For example for SG 104 the hourglass nodal lines are given by $(\Gamma-Z-R ; X)(4)$ and $(X-M-A ; R)(4)$, where the point R has a pairing of identical eigenvalues for the first but different eigenvalues for the second nodal plane.

Here, we want to highlight the material $Ba_5In_4Bi_5$ as a result of our material screening, which exhibits the nodal lines of the nodal chains at the Fermi energy, see Fig. 3.11a. We map out the nodal lines in the BZ to confirm the nodal chain structure in Fig. 3.11b.

3.2.3. Trivial fourfold crossings and their proximity to Weyl semimetals

Among the tetragonal SGs there are four with movable fourfold point crossings, which are SG 106 without inversion and SGs 130, 133, and 138 with inversion symmetry. All of these occur in hourglass structures along a rotation axis, see Fig. 3.12. They can be distinguished

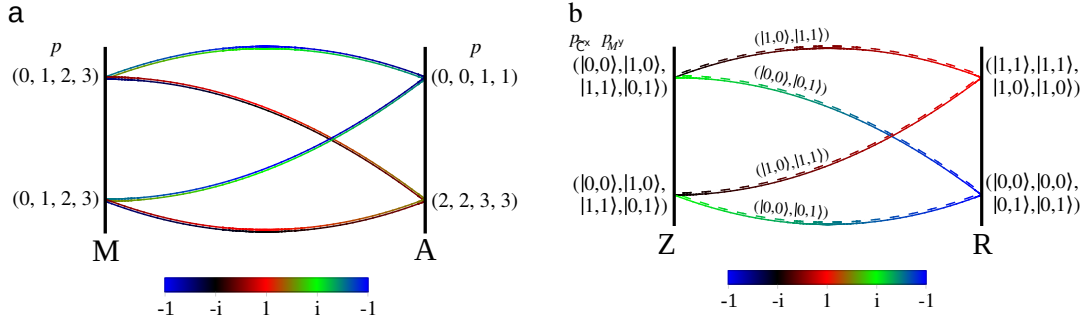


Figure 3.12.: The movable fourfold crossings of the tetragonal space groups [2]. **a** Enforced fourfold crossing on the fourfold rotation axis M-A for SGs 106 and 133. Bands are colored by their rotation eigenvalues $\lambda_{\bar{C}_4}$ and the values of p are denoted in brackets. **b** Enforced Dirac point on the twofold rotation axis Z-R for SGs 130 and 138. The colors encode the eigenvalue of the twofold screw rotation $\lambda_{\bar{C}_2}$, while the dashed distinguishes the mirror eigenvalues.

by how the eigenvalues are paired. For the SGs 106 and 133, the crossing occurs on the fourfold rotation axis M-A, due to a combination of TRS θ and a glide mirror symmetry like $M^y(\frac{1}{2}, 0, 0)$. The mirror symmetry relates $p \in \{0, 1, 2, 3\}$, as introduced in Eq. 2.2.3, into the tuples $(0,1)(2,3)$ anywhere on the rotation axis, since bands of different rotation eigenvalues are orthogonal we need no Kramers theorem here. At the TRIMs, however, Kramers theorem applies and pairs $(0,3)(1,2)$ at $k_z = 0$, whereas at $k_z = \pi$ it pairs $(0,1)(2,3)$. The combination of both symmetries, $\theta M^y(\frac{1}{2}, 0, 0)$, pairs $(0,2)(1,3)$ at $k_z = 0$ and each eigenvalue to itself at $k_z = \pi$. The result is illustrated by Fig. 3.12a. One may understand this fourfold crossing as two movable Weyl points, which are built from bands belonging to different representations of the fourfold rotation. Due to mirror symmetry they overlap, such that Weyl points of opposite Chern numbers form the fourfold crossings in SGs 106 and 133. Since the fourfold crossings of SGs 106 and 133 may occur as the only crossings in the vicinity of the Fermi energy, we study them with generic tight-binding models. These SGs, which realize the superposition of two topological phases, exhibit Fermi arcs, which are gapped and form closed energy contours, since the Chern numbers are trivial, see Fig. 3.13. Their arcs should in general take different shapes, because the two overlapping Weyl semimetals are made from different representations. As long as the Fermi arcs do not intersect in the surface band structure their exchange terms are unlikely to be strong enough to gap them out.

For the SGs 130 and 138 the fourfold crossing on the line Z-R comprises two identical representations and no such surface states occur. To understand their existence one must consider the eigenvalues of two commuting symmetries, an off-centered twofold screw rotation

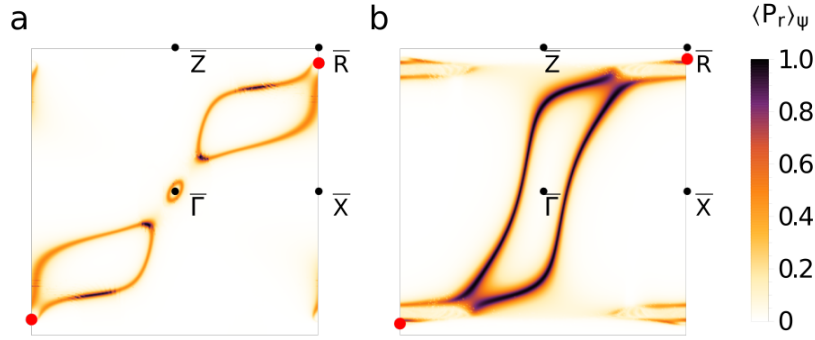


Figure 3.13.: Surface density of states for the tight-binding models of **a** SG 106 and **b** SG 133, with the localization of the eigenstates indicated by the color. The tight-binding models include hopping up to fourth nearest neighbors [2]. Gapped Fermi arcs are visible between $\bar{\Gamma}$ and \bar{R} . Red circles represent the projections of the fourfold crossings onto the surface Brillouin zone. Note that the path M - A in the bulk is projected onto \bar{X} - \bar{R} in the surface Brillouin zone.

like $\tilde{C}^x(\frac{1}{2}, 0, \frac{1}{2})$ and a glide mirror symmetry $M^y(0, \frac{1}{2}, \frac{1}{2})$. We label the states by the combination of different values of p as for SG 110. The states are related by time-reversal, inversion, and their combination, see our publication for details [2]. We illustrate the eigenvalues for the enforced hourglass band structure in Fig. 3.12**b** and we show the band structures of two example materials in Fig. 3.14.

To summarize the results, there are enforced fourfold band crossings among the tetragonal SGs and they occur in principle at half filling, without any other enforced crossings at the same energy.

3.2.4. Enforced \mathbb{Z}_2 topology

The space group 138 of the previous section does not only exhibit enforced movable Dirac points, but also an enforced nontrivial \mathbb{Z}_2 invariant on a 2D subset of the 3D BZ. Topological insulators with time-reversal symmetry exhibit a \mathbb{Z}_2 invariant, which can be calculated in the presence of inversion by its inversion eigenvalues [120]. Within one elementary band representation there can be a gapped submanifold of the BZ, which can be considered to be a TI, even if the whole system is a semimetal. Here, we will discuss how the pairing of inversion eigenvalues enforces such a topological subsystem for SG 138.

In SG 138 every TRIM except Γ is fourfold degenerate and the bands can be labeled by inversion and mirror eigenvalues at the same time. Using this we can distinguish bands by their mirror eigenvalues to find four orthogonal states at the TRIMs, while monitoring

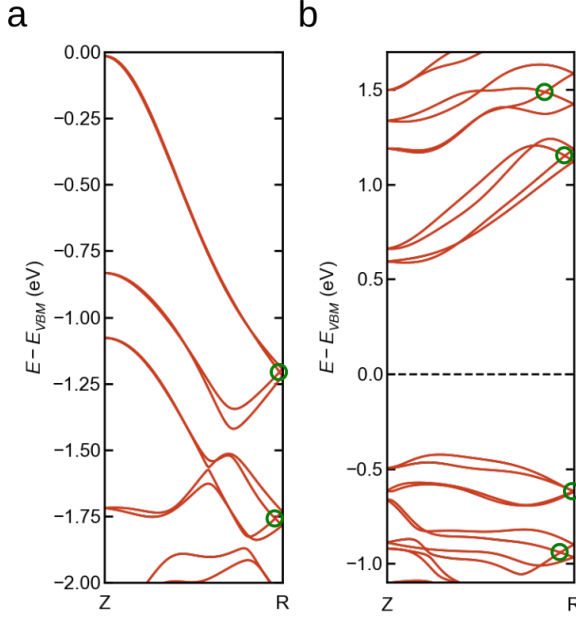


Figure 3.14.: Dirac points (green circles) on the Z-R line for AuBr (SG 138) and Tl_4PbSe_3 (SG 130) as calculated by DFT calculations [2].

how the inversion eigenvalues are paired in the process. We adopt the original notation of [120], where the inversion eigenvalue of band m at Γ_i is labeled by $\xi_m(\Gamma_i)$ with a TRIM $\Gamma_i \in \{\Gamma, X, Z, M, R, A\}$. To compute the invariant we must first consider the numbers $\delta_{\Gamma_i} = \prod_{m=1}^N \xi_{2m}(\Gamma_i)$. The enforced topology occurs at half-filling, $N = 4$. We note that due to time reversal equal inversion eigenvalues are paired at each TRIM, such that writing $2m$ in $\xi_{2m}(\Gamma_i)$ is well defined.

At the TRIMs X, Z, M, and R different inversion eigenvalues are paired and thus $\delta_X = \delta_Z = \delta_M = \delta_R = \xi_2(R)\xi_4(R) = -1$. This is different at A, where equal eigenvalues are paired, $\delta_A = \xi_2(A)\xi_4(A) = 1$. In other words, everything needed to evaluate the \mathbb{Z}_2 invariant is determined by symmetries and we do not need to assume an accidental inversion of bands. Note that this does not automatically imply a band inversion and if a inversion of bands occurs, it does not affect the topological invariant. With the δ_{Γ_i} , one can obtain the time-reversal polarization π_a , which implies a surface state if its value changes on a path in the surface BZ. Its change can be understood as a change in the number of occupied states by one, when traversing a path through the BZ in a region where occupied and filled bands are separated by a band gap. It thus leads to at least one surface state.

Suppose we have a slab of a system invariant under SG 138, which is terminated in z direction. In this case the TRIMs X and R as well as M and A are projected onto each other in the surface BZ. Then the relevant time-reversal polarizations are given by $\pi_{\bar{X}} = \delta_X \delta_R = +1$

and $\pi_{\bar{A}} = \delta_M \delta_A = (-1)(+1) = -1$, respectively. The \mathbb{Z}_2 invariant $\nu_{\mathbb{Z}_2}$ for the gapped subsystem comprising the TRIMs X, R, M, and A is then given by the time-reversal polarization as $\pi_{\bar{X}} \pi_{\bar{A}} = (-1)^{\nu_{\mathbb{Z}_2}}$. For the considered subsystem we find $\nu_{\mathbb{Z}_2} = 1$, and thus we obtain a nontrivial topological invariant without the need to assume a specific order of bands. Note that none of the involved products of inversion eigenvalues change if we would switch the order of bands.

We verify this assessment of enforced topology by comparing tight-binding models for SGs 130 and 138. Whereas we found for the latter that the topology is enforced, there are eight band crossings at R for SG 130 such that the plane XRMA is not gapped and no surface state should occur. The surface spectra for z and x terminations are given in Fig. 3.15. The above argument is formulated for the z termination and we indeed find that only for SG 138, see Fig. 3.15c, the number of surface states between \bar{X} and \bar{M} changes. Whereas SG 138 exhibits a Dirac surface state at \bar{X} , there is none for SG 130 in Fig. 3.15a. For the x termination we have to project the TRIMs X and M onto each other as well as A and R, which corresponds to the same topological subsystem of the BZ, which is again reflected in the surface states for SG 138 but not SG 130, see Figs. 3.15b and d.

We summarize that the SG 138 requires a pairing of inversion eigenvalues, such that a subsystem of a connected set of bands is always topologically nontrivial.

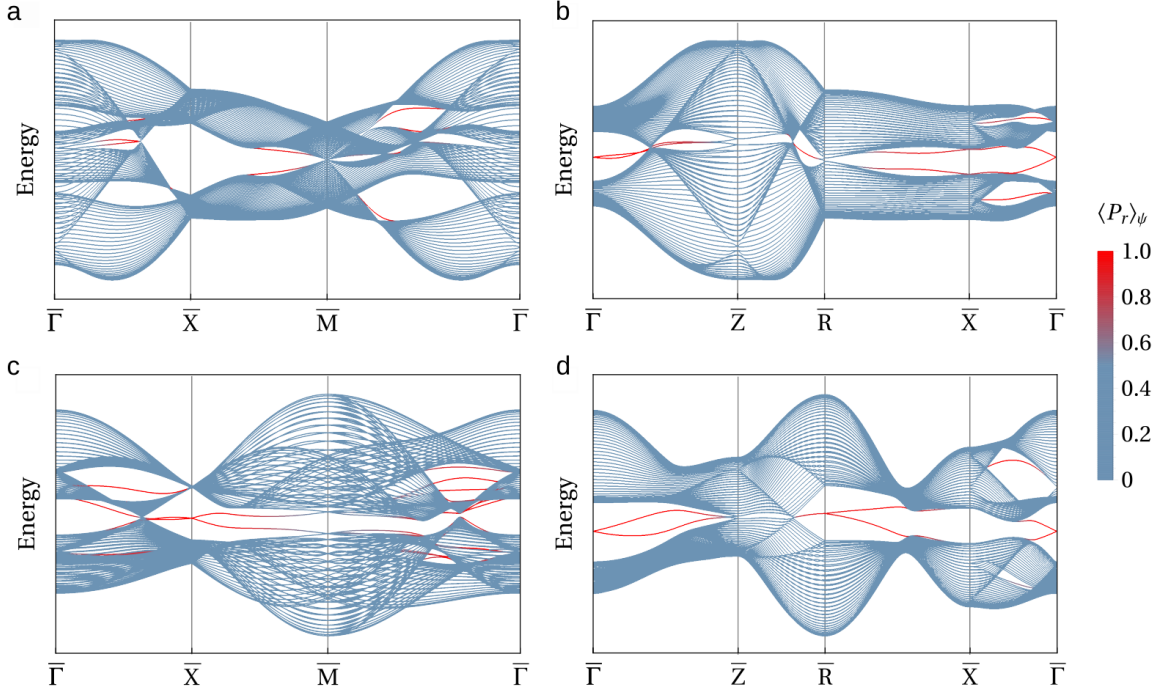


Figure 3.15.: Band structures of two generic tight-binding models in slab geometry, which are invariant under (a, b) SG 130 and (c, d) SG 138 [2]. Up to 7th nearest neighbor hopping terms are included. The color indicates the expectation value of surface projector, with red corresponding to fully localized at the surface. Left column (a, c): slab with z termination. Right column (b, d): slab with x termination.

3.3. Topological nodal planes in ferromagnetic MnSi

Although the possibility of two-dimensional band crossings, i.e., nodal surfaces, has been known since beginning of band structure theory [10], their actual existence and topological character has to our knowledge remained unproven in solid state systems. Recently, nodal planes exhibiting an enforced topological charge have been proposed [204]. But independently of the exact physical realization they lack characteristic surface states associated to their non-zero chirality. In the following section we remedy both shortcomings by not only presenting the experimental identification of gapless nodal planes in ferromagnetic MnSi, but also by applying our general arguments, see Sec. 2.2.3, to deduce their enforced non-zero topological charge [3]. The basic idea is the presence of a nodal plane duo as a result of two magnetic screw symmetries $\theta\tilde{C}_2^x$ and $\theta\tilde{C}_2^z$, if the magnetic field is aligned in y direction, [010].

MnSi is a magnetic transition metal compound, which is cubic with a B20 structure and described by SG 198. Below a temperature of 30 K, MnSi exhibits itinerant magnetism with a

helical order and by an external field a ferromagnetic state with a weak moment of $0.4\mu_B$ per Mn atom can be induced [237]. At the boundary between the paramagnetic and the helimagnetic order a phase exists, which hosts skyrmions, topological vortex structures in the magnetization texture [238]. The related nonmagnetic compounds RhSi and CoSi have been shown in ARPES studies to exhibit Fermi arc surface states [239–241]. Without magnetism they belong also to SG 198, which hosts trios of topological nodal planes, and thus none of the Fermi arcs originate from the nodal planes.

After a discussion of the experimental identification of nodal planes with de Haas-van Alphen spectroscopy, we revisit our topological arguments [3]. Hereby, DFT calculations support our analytic results for the specific band structure of MnSi. We devise a generic tight-binding model and compare it with the results of DFT calculations considering the band structure, its symmetry content, surface states, and Berry curvature. The symmetry analysis is found to be valid and we exemplify the tunability of topological properties by considering different field directions. In the latter process it becomes evident that nodal planes in the presence of weak symmetry breaking result in small band gaps at the Fermi energy yielding an enhanced Berry curvature.

3.3.1. Identifying nodal planes by de Haas-van Alphen spectroscopy

Ferromagnetic MnSi has 10 Fermi surfaces, including 6 sheets that cross the nodal plane, and hence exhibit a twofold degeneracy, see Fig. 3.16. Our goal is to show that these “topological protectorates” (TP) of a Fermi surface degeneracy exist. Since the nodal plane is a degeneracy for all bands, a change in the chemical potential would not remove the degeneracy as long as Fermi surfaces cross the boundary of the BZ, hence the term “protectorate”.

De Haas-van Alphen (dHvA) spectroscopy yields the required resolution in energy and reciprocal space to prove that the TPs are actually present [3]. A sample of MnSi is placed on a cantilever and an external field \mathbf{B} is applied, which creates Landau levels for each Fermi surface within the material. In a semiclassical description electrons move on cyclotron orbits or one introduces ladder operators to map the problem on the quantum mechanical harmonic oscillator, either way one obtains quantized states. This leads to quantized energies and cross-section areas of the electron orbits, where one needs to consider that there is also an underlying band structure. If then the magnetic field strength is varied the quantization conditions change. Every time a Landau level moves through the Fermi energy, i.e., a quantized orbit becomes equal to an orbit on the Fermi surface, a large number of low-lying electronic excitations is accessible. This affects physical properties in a periodic fashion as function of $1/|\mathbf{B}|$, whereby the frequency of this periodic modulation of physical quantities depends on the enclosed area of the orbit. For

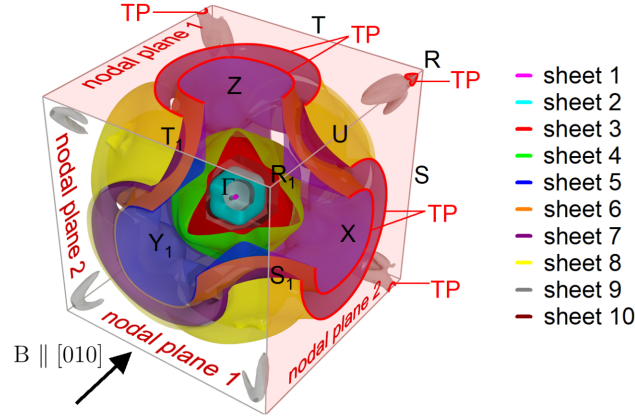


Figure 3.16.: Fermi surfaces of ferromagnetic MnSi, with the external field \mathbf{B} aligned in [010] direction [3]. The Fermi surfaces are enumerated as sheets 1 to 10. Intersection lines between the Fermi surface and the nodal planes are gapless, topologically nontrivial protectorates of the Fermi surface.

the dHvA spectroscopy the resulting oscillations are considered for the magnetization \mathbf{m} , which is measured as a torque of the cantilever due to $\tau = \mathbf{m} \times \mathbf{B}$, see Figs. 3.17a, b. By comparison to DFT calculations the observed frequencies, cf. Fig. 3.17c, are assigned to the orbits in the band structure. The behavior of the magnetization is given by the Lifshitz-Kosevich formalism as a function of parameters such as the observed dHvA frequency, temperature, the associated cross-sectional area of an orbit in the BZ, and the effective mass m^* of the electron orbit, cf. Fig. 3.17d. By fitting the theory to the data the effective masses m^* are obtained and then used to calculate the Sommerfeld coefficient γ of the specific heat $C_p = \gamma T$. The calculated coefficient is then compared to direct measurements of the specific heat, which is done to check whether the analysis of the dHvA frequencies has found all the relevant Fermi surfaces.

From these experiments it can be concluded that a duo of nodal planes does indeed exist, which is done by analyzing the oscillation frequencies and thus the sizes of cyclotron orbits, see Fig. 3.18. In the simplest case an orbit comprises only one band, but if bands come close to each other, a switch of bands can occur, which is called magnetic breakdown. The probability p of such a breakdown is given by $p = \exp\left(-\frac{B_0}{B}\right)$ with the breakdown field [3]

$$B_0 = \frac{\pi\hbar}{2e} \sqrt{\frac{k_g^3}{a+b}}, \quad (3.3.1)$$

where k_g is the distance of the two Fermi sheets in reciprocal space and a, b are the curvatures of the trajectories at the breakdown junction. While in general the possibility of magnetic breakdown results in a complex frequency spectrum, due to the many ways in which a cyclotron orbit may be spread over several bands, it is simple for an orbit that only crosses a nodal plane.

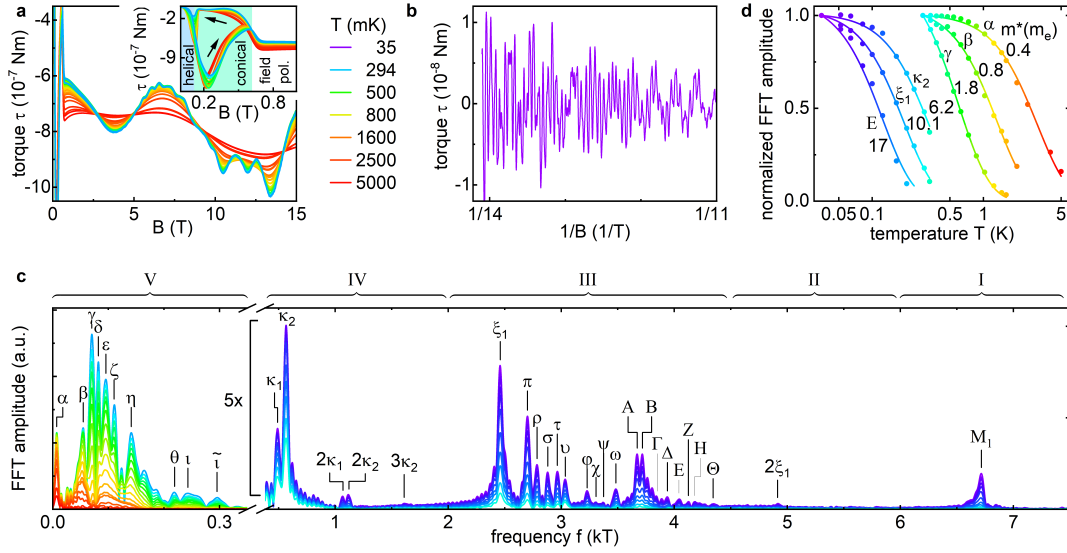


Figure 3.17.: Excerpt of the de Haas-van Alphen data for ferromagnetic MnSi [3]. **a** Torque exerted by the sample on a cantilever due to its field dependent magnetization for a fixed direction of the magnetic field $\phi = 82.5^\circ$ with temperatures from 0.035 K to 5 K. **b** Magnetic torque at high-fields for a temperature of 35 mK. **c** Fast Fourier transform (FFT) of the curves shown in **a**. The identified de Haas-van Alphen frequencies correspond to the extremal orbits. **d** Temperature dependence of the normalized FFT amplitudes for six of the peaks in **c**. The lines are fitted to the data according to the Lifshitz-Kosevich formula, which yields the effective masses m^* for the extremal orbits.

At the degeneracy, due to the nodal plane, the distance between bands is $k_g = 0$, thus $B_0 = 0$ and $p = 1$, i.e., the orbit must always switch the band when it passes through the nodal plane.

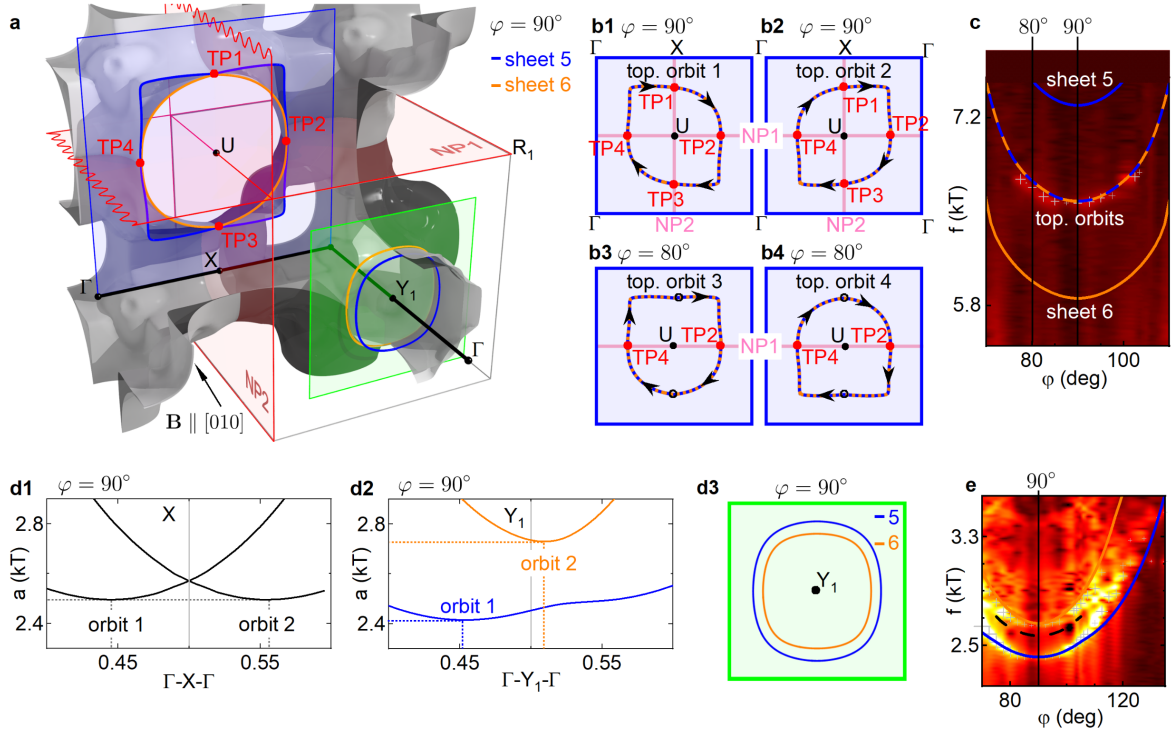


Figure 3.18.: Signatures of nodal planes at the Fermi energy seen in the extremal orbits that determine the de Haas-van Alphen spectra [3]. **a** Fermi surface sheets 5 and 6 for a magnetic field \mathbf{B} along $[010]$, which corresponds to the angle $\phi = 90^\circ$. Planes (blue, green) perpendicular to the magnetic field host orbits, which comprise line segments situated on sheet 5 (blue) or 6 (orange). The orbits enclosing the point U intersect the nodal planes (red), whereas the loops in the vicinity of Y_1 do not cross a nodal plane. **b1 - b4** Possible topological orbits for different orientations of the magnetic field. **c** Intensity map of the measured de Haas-van Alphen spectra, lines correspond to the orbits on sheet 5 (blue), sheet 6 (orange), and the topological orbits (dashed in blue and orange), which yield the best agreement with the data. **d1** Area of a Fermi surface cross-section if a field could be applied in the $[100]$ direction without removing the nodal planes, whereas **d2** shows the actual behavior along the magnetic field, where the bands become asymmetric and two orbits of different cross-sections occur. The latter results in the orbits given in the green plane in **a** and **d3**. **e** Intensity map of de Haas-van Alphen spectra for the trivial orbits at Y_1 .

Let us consider the Fermi sheets 5 and 6, cf. Fig. 3.18a, which yield two topological orbits, crossing the nodal plane, see Figs. 3.18b1-b4. The frequency associated to these orbits that switch the bands at the nodal planes fits to the measured dHvA frequency, see Fig. 3.18c. To falsify the statement that there are no nodal planes, we must consider the orbits in their absence, see Figs. 3.18d1 - d3, and e, which yield different frequencies that lie far away from the measured frequencies in Fig. 3.18c. One concludes that the observed dHvA spectra can only be explained if the nodal planes are indeed gapless.

3.3.2. Symmetry eigenvalues

The experimental analysis has shown that the nodal planes exist, and thus the symmetry argument appears to be a valid approach. This motivates us to draw further conclusions for the topology of ferromagnetic MnSi. We begin with an analysis of the present symmetries, enforced crossings, and compare these with DFT calculations.

Paramagnetic phase with SG 198.10

The following discussion on the paramagnetic case also applies to CoSi, which we have analyzed in more detail in Ref. [4]. In its paramagnetic phase MnSi is described by SG 198, which corresponds to the magnetic space group 198.10 if time-reversal symmetry θ and all its combinations with the spatial symmetry operations are added to the group. Its generating symmetries are a twofold screw rotation $\tilde{C}_2^z(\frac{1}{2}, 0\frac{1}{2})$ around the z axis, and a threefold rotation $C_3^{xyz}(0, 0, 0)$ around the [111] axis. The combination of the threefold rotation with $\theta\tilde{C}_2^z(\frac{1}{2}, 0, \frac{1}{2})$ yields the three antiunitary twofold operations $\theta\tilde{C}_2^x$, $\theta\tilde{C}_2^y$, $\theta\tilde{C}_2^z$. Each enforce a nodal plane, because the material lacks inversion symmetry, cf. Sec. 2.2.3. The trio of nodal planes is topologically charged, due a topological crossing at Γ , that would be uncompensated without the nodal plane. At Γ there are, besides the Kramers-Weyl points, also spin-3/2 fermions due to the threefold rotation. The former carry a Chern number of $\nu_\Gamma = \pm 1$, whereas the spin-3/2 fermions contribute a charge of $\nu_\Gamma = \pm 3$ at the band index of the nodal planes [239].

To prove that the nodal planes cannot be compensated by accidental Weyl points, we shall consider the multiplicities of such crossings. If a Weyl point is placed on a twofold or threefold rotation axis, it will occur with a multiplicity of 6 or 8, respectively. The composite symmetries, e.g., $\theta\tilde{C}_2^z$, act like mirror symmetries on reciprocal space, $(k_x, k_y, k_z) \rightarrow (k_x, k_y, -k_z)$, while preserving the sign of the chirality, cf. Fig. 2.5a. A Weyl point at a generic position in the effective mirror plane $k_z = 0$ exists in four copies due to $\theta\tilde{C}_2^x$ and $\theta\tilde{C}_2^y$. The threefold rotation relates the mirror planes and thus the multiplicities of these points is 12. At a generic position in the BZ, the mirror symmetries yield eight copies of an accidental crossing, each of which

has three distinct copies due to the threefold rotation, thus a generic point occurs with a multiplicity of 24. We can thus express the compensation condition for Chern numbers due to the Nielsen-Ninomiya theorem [21] as

$$6\nu_6 + 8\nu_8 + 12\nu_{12} + 24\nu_{24} + \nu_\Gamma + \nu_{\text{npt}} = 2\mu + \nu_\Gamma + \nu_{\text{npt}} = 0, \quad (3.3.2)$$

where $\nu_i \in \mathbb{Z}$ encodes the total chirality of all accidental Weyl points with multiplicity i . All accidental crossings add up to an even number $2\mu \in 2\mathbb{Z}$ and thus the odd chirality ν_Γ can only be compensated by the charge ν_{npt} of the nodal plane trio.

One may also consider a topologically charged nodal line that would need to form an armillary sphere around Γ . To exclude such a more complex solution, the charge of the nodal planes should be directly calculated. In a recent work [4] we show that CoSi, which is in the same SG as paramagnetic MnSi, does also exhibit nodal planes as expected from the symmetry. By DFT calculations we check the charges of all Weyl points to confirm the topology of the nodal planes explicitly, which is enhanced due to the presence of additional uncompensated, accidental Weyl points. Due to the large multiplicity of accidental crossings, some nodal planes of CoSi obtain charges up to $\nu_{\text{npt}} = 80$, see [4] for further details.

Ferromagnetic phase with SG 19.27

Now we want to focus on the ferromagnetic case of MnSi. If a magnetic field is applied along one of the twofold rotation axes, e.g., the [010] direction, the space group reduces to 19.27, see Fig. 3.19. A further rotation of the magnetic field in the xy-plane yields SG 4.9 and an arbitrary field alignment corresponds to SG 1.1.

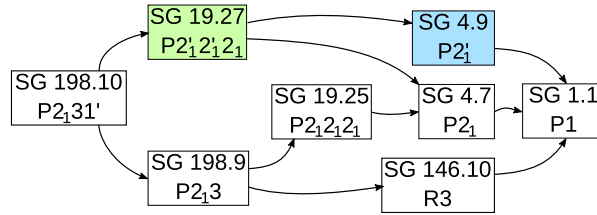


Figure 3.19.: Space groups for MnSi with different orientations of the magnetic field [3]. In the paramagnetic SG 198 reduces to SG 19.27 if the field is aligned in [010] and reduces to SG 4.9 if the field is rotated in a plane with the normal vector $\langle 001 \rangle$.

In the following we want to discuss the symmetry eigenvalues of MnSi for the field orientations preserving SG 19.27. We must consider only the three symmetries $\theta\tilde{C}_2^x$, $\theta\tilde{C}_2^z$, and \tilde{C}_2^y , where only the latter is unitary and yields symmetry eigenvalues on its rotation axes in the BZ. Three different rotation axes must be distinguished $Y_1\text{-}\Gamma\text{-}Y$, $R_1\text{-}\Gamma\text{-}R$, and $S_1\text{-}\Gamma\text{-}S$, where we find

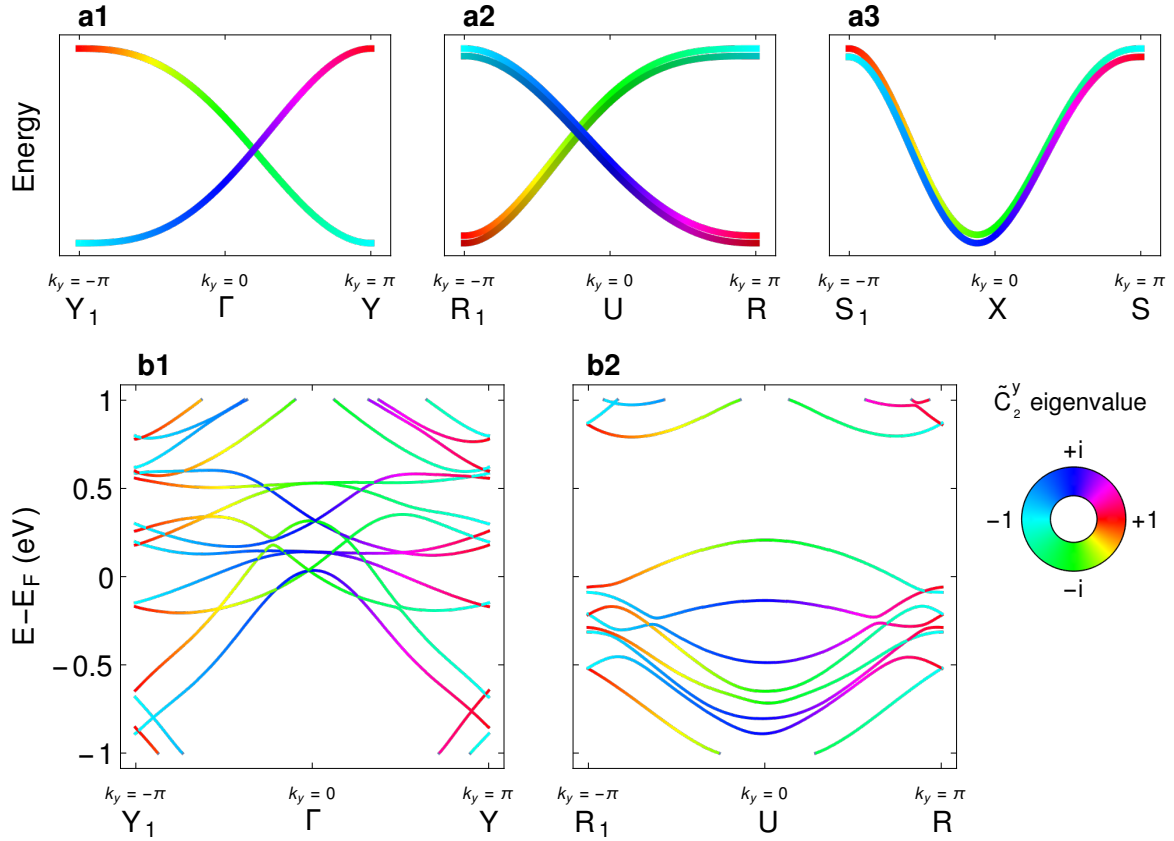


Figure 3.20.: Momentum dependence of the \tilde{C}_2^y eigenvalues, which is indicated by the color code [3]. **a1 - a3** Schematic band connectivity for a minimal set of bands along the three distinct rotation axes in SG 19.27, cf. Fig. 3.17. **b1 - b2** Band structure of MnSi from DFT calculations for a field in the $[010]$ direction. Crossings between bands of different color are Weyl points on Y_1 - Γ - Y and fourfold double Weyl points on R_1 - U - R , respectively.

the unmodified screw rotation, doubling of bands without a change in the connectivity, and a doubling of bands with trivial connectivity, respectively. In this magnetic space group our results presented in Eq. 2.2.7 can be directly applied to the twofold screw rotation \tilde{C}_2^y :

$$\begin{aligned} \sum_{c_b, b \text{ odd}} \Delta\varphi_{b, c_b} &= -(2j + 1) \cdot \pi \pmod{2\pi} \\ &= \pi \pmod{2\pi}, \end{aligned} \quad (3.3.3)$$

$$\begin{aligned} \sum_{c_b, b \text{ even}} \Delta\varphi_{b, c_b} &= -2j \cdot \pi \pmod{2\pi} \\ &= 0 \pmod{2\pi}, \end{aligned} \quad (3.3.4)$$

where $j \in \mathbb{N}$ is used to rewrite $b = 2j + 1$ and $b = 2j$, respectively, for the two equations. Equations 3.3.3 and 3.3.4 correspond to odd- and even-numbered bands, respectively. For a

twofold rotation the phase changes are $\Delta\varphi_{b,c_b} = \pi$ for any band b . It follows from Eq. 3.3.3 that on the line $Y_1-\Gamma-Y$ each odd-numbered band has an odd number of band crossings such that there will be a non-zero total charge that must be canceled by the nodal plane. This is illustrated in Fig. 3.20a1 and found to be true for each odd-numbered band of MnSi, see Fig. 3.20b1. The charges for any Weyl point on the line $Y_1-\Gamma-Y$ is $\nu = \pm 1$. No accidental Weyl points may compensate the charge on the rotation axis, because they must occur with an even multiplicity, even if they lie in one of the effective mirror planes of the symmetries $\theta\tilde{C}_2^x$ or $\theta\tilde{C}_2^z$. The condition on the chiralities, analogous to Eq. 3.3.2, takes the form

$$2\nu_2 + 4\nu_4 + \nu_{Y_1-\Gamma-Y}^{\text{odd}} + \nu_{\text{npd}} = 0, \quad (3.3.5)$$

where the total charge $\nu_{Y_1-\Gamma-Y}^{\text{odd}}$ of an odd-numbered band includes all Weyl points on the line $Y_1-\Gamma-Y$. As in the paramagnetic case, the charge ν_{npd} of the nodal plane duo is non-zero, because $\nu_{Y_1-\Gamma-Y}^{\text{odd}}$ is odd. For even-numbered bands Eq. 3.3.4 requires an even number of crossings, which can be fully compensated by other Weyl points.

On the rotation axis $R_1-\Gamma-R$, which is in the nodal plane, the antiunitary symmetry $\theta\tilde{C}_2^x$ fulfills Kramers theorem and pairs identical eigenvalues of \tilde{C}_2^y , see Fig. 3.20a2. The twofold degenerate bands along $R_1-\Gamma-R$ can still be labeled by the same eigenvalues as for those on the axis $Y_1-\Gamma-Y$, and thus must fulfill the same conditions, Eqs. 3.3.3 and 3.3.4, when the two degenerate bands are counted as one. Indeed, the twofold degenerate bands in Fig. 3.20b2 exhibit an odd number of crossings for each odd-numbered band and an even number of crossings otherwise. The crossings on $R_1-\Gamma-R$ are doubled due to a symmetry that preserves the chirality and pairs two identical representations, hence the occurring crossings are fourfold double Weyl points with $\nu = \pm 2$. These movable crossings are situated in every second gap between nodal planes and require two Weyl points in a mirror plane to compensate them. On the line $S_1-\Gamma-S$ the antiunitary operation $\theta\tilde{C}_2^x$ pairs different eigenvalues of \tilde{C}_2^y and thus there is only one distinct band and no crossings can be protected by symmetry, see Fig. 3.20a3.

3.3.3. Surface States

In the previous section, we have seen that there are several enforced Weyl points. With the realization of nodal plane duos in ferromagnetic MnSi it has become, in principle, possible to access surface states associated to topological nodal planes. Here, we want to compare the result of DFT calculations with the expectations provided by the generic four-band tight-binding model described in Appendix C.

For our minimal model the surface states are readily identified in the SDOS of a slab in (010) termination. The twofold rotation axis $Y_1-\Gamma-Y$ of the bulk system corresponds to the

center of the surface BZ, whereas the line $R_1-\Gamma-R$ projects onto the corners of the surface BZ. In Fig 3.21**a1** and **a2** a single Fermi arc connects the bands of the nodal plane to an unpaired Weyl point in the bulk, see Fig. 2.5c. The fourfold double Weyl has Fermi arcs associated to it, that connect the corner of the BZ to some bulk bands at its center, where two Weyl points occur on a mirror plane, see Figs. 3.21**b1** and **b2**. While the analysis of symmetry eigenvalues posed no problem in DFT calculations of MnSi, the surface spectra exhibit the full complexity of the ten overlapping Fermi sheets. Several surface states occur in Fig. 3.21**c1**, **c2**, and **d2**. The SDOS at the Fermi energy exhibits two Fermi arcs, which connect to a small pocket at the center of the BZ. Two arcs would indicate that these correspond to the fourfold double Weyl point. But that is unlikely, because they connect to a small pocket, which after closer inspection belongs to Weyl points that should compensate the nodal plane, which are denoted by turquoise circles in Fig. 3.21**d1** close to $E = E_F$. If we consider the energy resolved surface spectrum along high-symmetry paths, Fig. 3.21**d2**, it appears that the corresponding surface states end at the turquoise arrow. This would mean the crossing at the turquoise Weyl point in Fig. 3.21**d1** is the one, which should have an arc that connects to the nodal plane, but no such surface state could be identified.

Let us consider instead what we find in Fig. 3.21**d2** as a starting point. Two surface states with a strong localization end on the line Z-U close to $U(\pi, \pi)$, green arrows. These may at most be surface states of the fourfold double Weyl points, because they overlap with the projection of the nodal planes, i.e., the line Z-U. A surface state that belongs to a nodal plane should end and merge into the bulk bands somewhere on the lines $\Gamma-Z$, $\Gamma-X$, and $\Gamma-U$. We know from our generic model, Fig. 3.21**a2**, that not all of these three paths must exhibit the surface state. On the path $\Gamma-Z$ there is a promising surface state that may connect to the nodal planes, because it ends shortly before Z, marked by a blue arrow, and its starting point corresponds to four of the blue encircled Weyl points in the bulk BZ, Fig. 3.21**d1**.

In summary, we predict several surface states and gave arguments to which nodal features they are likely related, but further research would be needed to exclude the possibility of trivial surface states and to identify beyond doubt the corresponding bulk crossings.

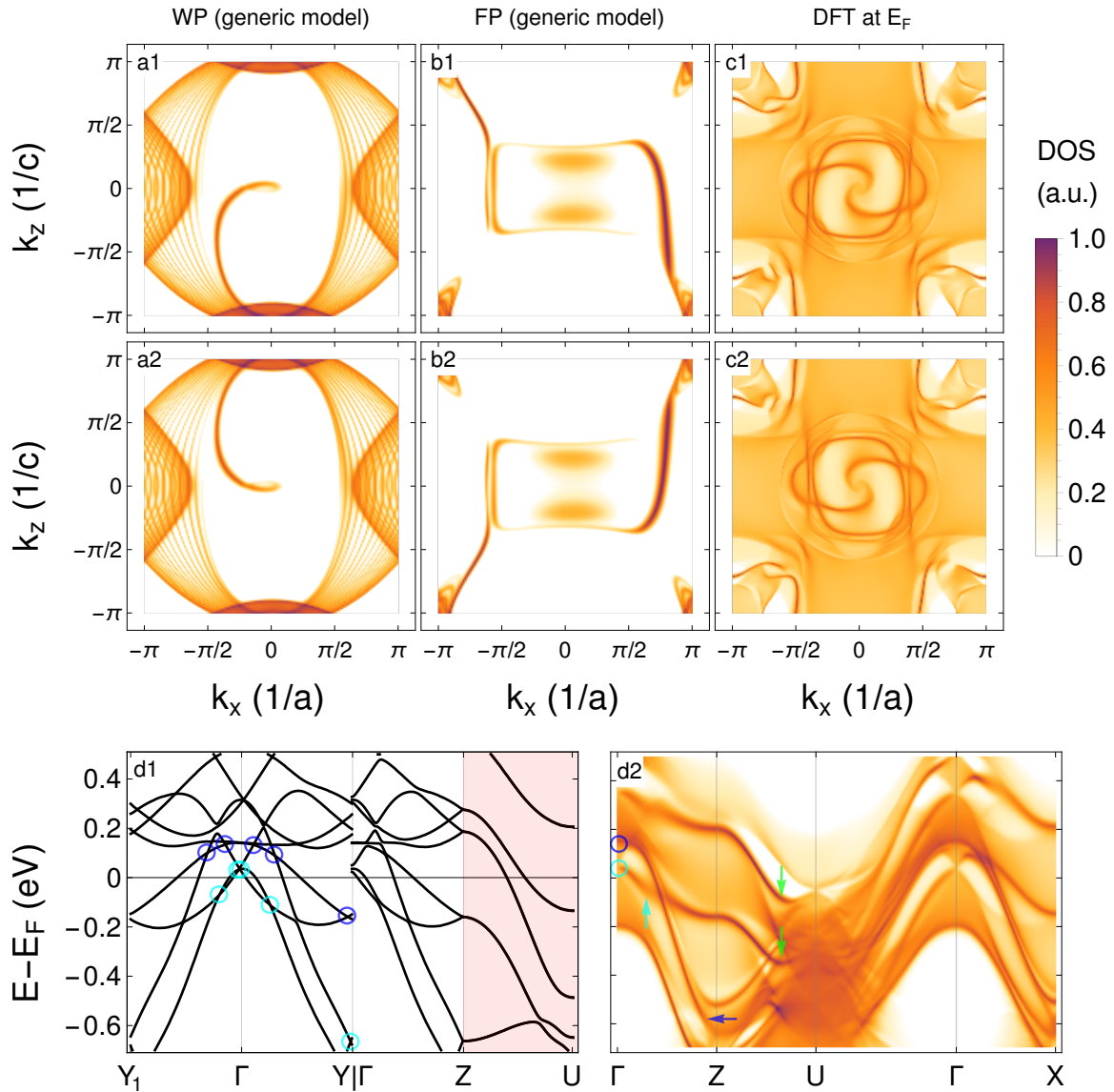


Figure 3.21.: Topological surface states for MnSi from DFT calculations (**c1**, **c2**, **d1**, **d2**) and a generic model (**a1**, **a2**, **b1**, **b2**), cf. Appendix C, on the (010) surface [3]. **a1**, **a2** Surface density of states (SDOS) at the energy of the unpaired single Weyl point (WP). **b1**, **b2** SDOS at the energy of the fourfold double Weyl point (FP). **c1**, **c2** SDOS at the Fermi energy of MnSi. **d1** Bulk band structure of MnSi, where the colored circles mark the Weyl points that must be compensated by the nodal plane. The red shading indicates the region with nodal planes. **d2** Band structure for MnSi with a (010) surface termination. The SDOS reveals several surface states.

3.3.4. Berry curvature

Weyl points are well known as sources or sinks of Berry curvature, cf. Sec. 1.4.2. A topological nodal plane with a non-zero Chern number on an enclosing surface must also be a source or a sink of Berry flux. While a Weyl point corresponds to a divergence of the curvature, the nodal plane does not need a divergence and the curvature may be in comparison rather small close to the nodal plane. This can be understood when considering how a integration area of the Berry curvature needs to look like for the computation of Chern numbers of Weyl points or nodal planes. For a Weyl point one could consider a sphere that can be arbitrarily close to the nodal point and since the Chern number must have the same value for every radius of the sphere, the curvature must increase close to the Weyl point. To enclose, for example, a trio of nodal planes one may use a cube that is nearly the size of the BZ. When it approaches the nodal plane its surface area approaches that of the nodal plane, hence no divergence is needed.

In the following we want to consider a generic tight-binding model of SG 19 with eight bands, which includes spin. We then apply a Zeeman term to reduce the symmetry again to SG 19.27 and determine the Berry curvature for the resulting nodal planes. Due to the effective mirror symmetries that protect the nodal plane, one finds local extrema in the transversal Berry curvature components at a nodal plane, see Fig. 3.22a1. The normal component of the curvature is antisymmetric at the nodal plane and flips its sign. Overall, the absolute value of the curvature at the nodal planes at $k_x = \pi$ and $k_z = \pi$ exhibit no unusual features, see Fig. 3.22a2. Yet, with our eight-band model we can rotate the direction of the magnetic field. If this is done by a small angle in the xy -plane, one of the nodal planes, $k_x = \pi$, becomes gapped, while the other nodal plane is still symmetry protected. Before it is gapped we know from Kramers theorem for the symmetry $\theta\tilde{C}_2^x$ that the eigenstates in orbital space at (k_x, k_y, k_z) and $(-k_x, k_y, k_z)$ are orthogonal to each other. At a (gapless) nodal plane, two bands switch and there is a discontinuous change between orthogonal states. After we have turned the field into the xy -plane the states all over the Brillouin are unlikely to exhibit a drastic change, which means that at the nodal planes, the eigenstates for the gapped bands must interpolate between two formerly exactly orthogonal states. The result is a large value of the Berry curvature as illustrated with our generic tight-binding model in Figs. 3.22b1 and b2. Note that this diverging Berry curvature should mostly cancel when integrated over an area that encloses the surface of the BZ, because in the simplest case a topologically charged nodal plane is replaced by a Weyl points of an equal charge if the protecting symmetry is gapped. Nevertheless, independently of the whereabouts of the chirality, a small gap and a large Berry curvature at the Fermi energy for a gapped nodal plane should be a property of nodal plane metals that represents a general feature of nodal planes beyond the discussion of MnSi.

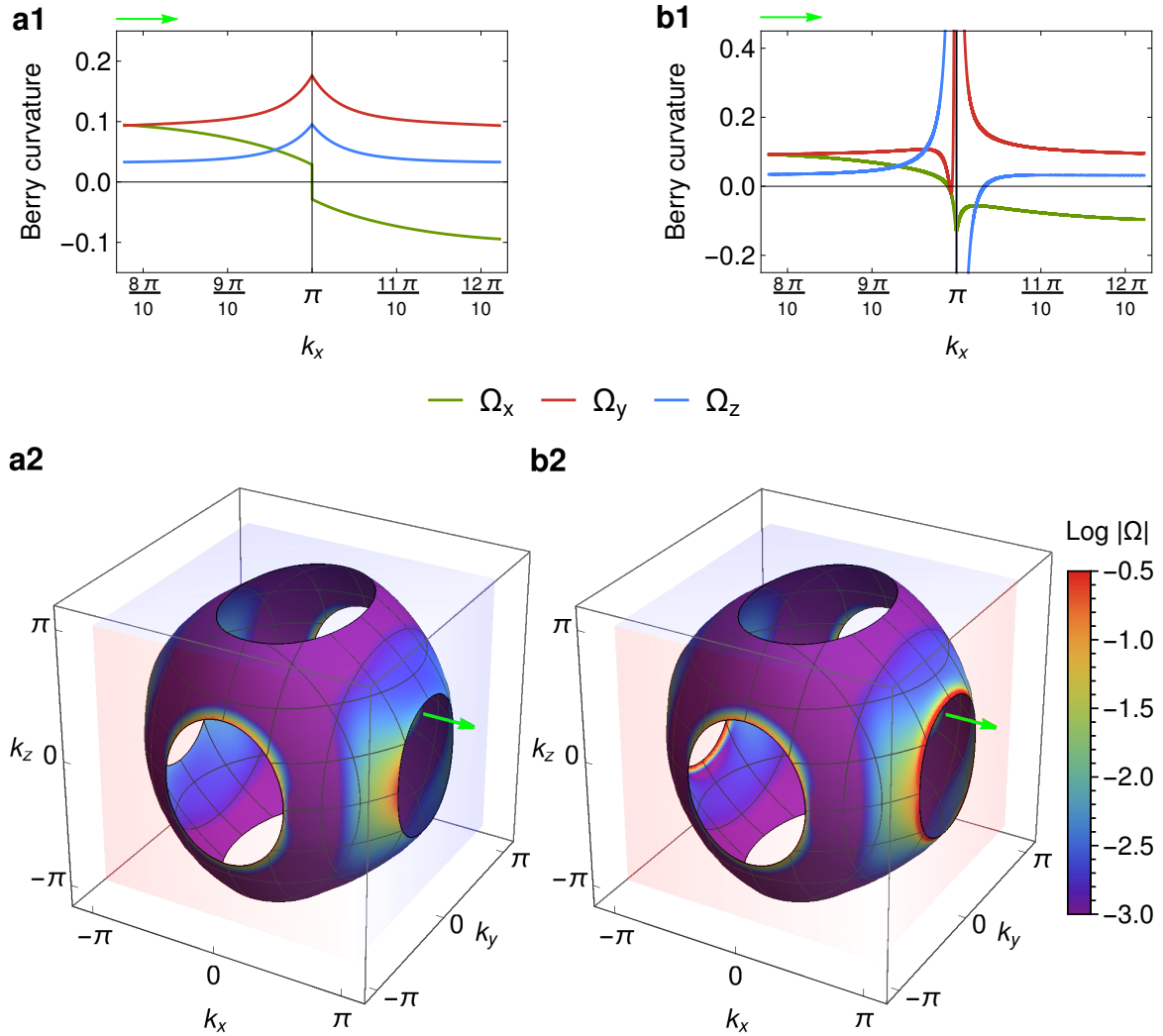


Figure 3.22.: Berry curvature at the Fermi surface of nodal planes described by the eight-band tight-binding model, see Appendix D [3]. **a1** Berry curvature $\Omega_i(\mathbf{k})$ in the vicinity of nodal planes of SG 19.27. **a2** A possible Fermi surface (only one band shown) of the same model colored by the logarithm of the absolute value of the Berry curvature $\log |\Omega_i(\mathbf{k})|$. The green arrow in **a2** marks the path chosen in **a1**. **b1**, **b2** correspond to **a1**, **a2** once the magnetic field is rotated into the xy -plane.

3.4. The magnetic antiperovskite Eu_3PbO

In the final section of this chapter we want to present unpublished work [5] on the magnetic antiperovskite compound Eu_3PbO . The corresponding family of antiperovskite compounds are known to be Dirac semimetals. Additionally, Eu^{3+} exhibits a large magnetic moment due to its half-filled f orbitals. Experimental analysis has suggested different ferro-, ferri- and antiferromagnetic phases, which due to the time-reversal symmetry breaking are expected to be Weyl metals. We use the insights collected in chapter 2 to identify the band crossings found by DFT calculations. A tight-binding model is then adapted by the author to reproduce the DFT results. Where the tight-binding model is found to be valid, surface states are calculated for different terminations. We study the effect on the surface states due to magnetic atoms within the surface layer. Finally, we show that the field alignment makes it possible to tune the topological contribution to the anomalous Hall effect by performing an explicit calculation in the ferromagnetic regime.

3.4.1. Antiperovskites: structure, materials, topology

The perovskite structure named after an eponymous mineral CaTiO_3 [242] with structure formula ABX_3 comprises corner sharing octahedra of atom type X, inscribed in a cuboid unit cell with A atoms at the center and B atoms at its corners [243]. Hereby, A and B atoms are cations and the X element acts as anion in the compound. Depending on the exact composition the crystal type may be cubic in the idealized structure, but more common are tetragonal, orthorhombic or hexagonal distortions of the perovskite structure [243, 244].

Our work is concerned with *antiperovskites*, which are synonymously referred to by the term inverse perovskites, which exhibit the same structure as perovskites but where the positions of cations A and anions X are switched [243], cf. the inset of Fig. 3.23c. This may lead to unusual oxidation states of the A atom [245]. Some antiperovskites have been discussed as candidates for TIs [246, 247], higher-order topology [248] and in the context of Dirac points and lines [249].

We focus on a family of oxides with the antiperovskite structure, which exhibit Dirac points gapped by SOC at or in close vicinity of the Fermi energy, like Sr_3PbO , Sr_3SnO , Ca_3SnO and Ca_3PbO [250–258]. At the Γ point of the BZ the bands are inverted, albeit unlike for TIs not due to spin-orbit coupling. By analysis of the parity eigenvalues [120] it was shown that, despite this inverted gap, the strong topological invariant is zero. Nevertheless, the four example materials discussed in this paragraph are topological crystalline insulators [120, 259]. There is a full gap within the mirror planes and a mirror Chern number ν_M can be defined. ν_M is

calculated as the regular Chern number but using only states with the same eigenvalue of mirror symmetry [120, 259]. In this subspace the Hamiltonian exhibits nondegenerate bands because the composite symmetry of inversion and time reversal relates different mirror eigenvalues. Although the combination of inversion and time-reversal excludes a spin polarization of the bands, the presence of spin-orbit coupling leads to weak antilocalization, which can be observed by magneto-conductance measurements in thin films [260]. Synthesis can be done by various methods for bulk crystals and thin-films, including flux growth [261, 262], molecular-beam epitaxy [263], and pulsed-laser deposition [264], where the air sensitivity of the antiperovskite oxides must be taken into consideration.

Out of the same family of compounds $\text{Sr}_{3-x}\text{SnO}$ with hole doping has been discussed as a possible odd-parity superconductor [265, 266] and is of increased interest due to the $J = 3/2$ states in the vicinity of the Fermi energy [267]. At lower carrier density, i.e., with a Fermi level closer to the Dirac points, no superconductivity has been found [255]. Also, magnetic order has been shown to occur in several compounds [268–270], which will be the focus of the following sections.

3.4.2. Magnetic order in Eu_3PbO

The main idea is to consider an oxide antiperovskite, i.e., Eu_3PbO , which comprises internal magnetic moments. These order at low temperatures and different magnetic structures can be obtained with an applied external magnetic field. Thereby, the exchange coupling splits the bands forming the gapped Dirac points in the vicinity of the Fermi energy to a larger extent than it would be possible without the magnetic order. Preliminary discussions of this approach to magnetic Weyl metals have been pursued [258, 270], but they were limited to the ferromagnetic case, hence neglecting other possible magnetic phases. The present work is the continuation of [258], where first arguments for the existence of a rich magnetic phase diagram have been presented.

To determine the realized magnetic order, as a first step, we consider some of the bulk material properties, such as resistivity and susceptibility, see Fig 3.23. With the Fermi energy at a Dirac point theoretical [33] and experimental [37, 38] results indicate an increase of the resistivity for a Dirac semimetal at low temperatures. But the actual resistivity data for Eu_3PbO measured with a pressed powder sample indicates a semimetallic resistivity with a weak temperature dependence, see Fig. 3.23a. No increase of resistivity at lower temperatures is found for Eu_3PbO . This is in agreement with the intrinsic hole doping of the synthesized material for which the relaxation due to Coulomb interaction should be suppressed, because of imbalance between electron and hole charge carriers [271]. Interestingly, there is a sudden

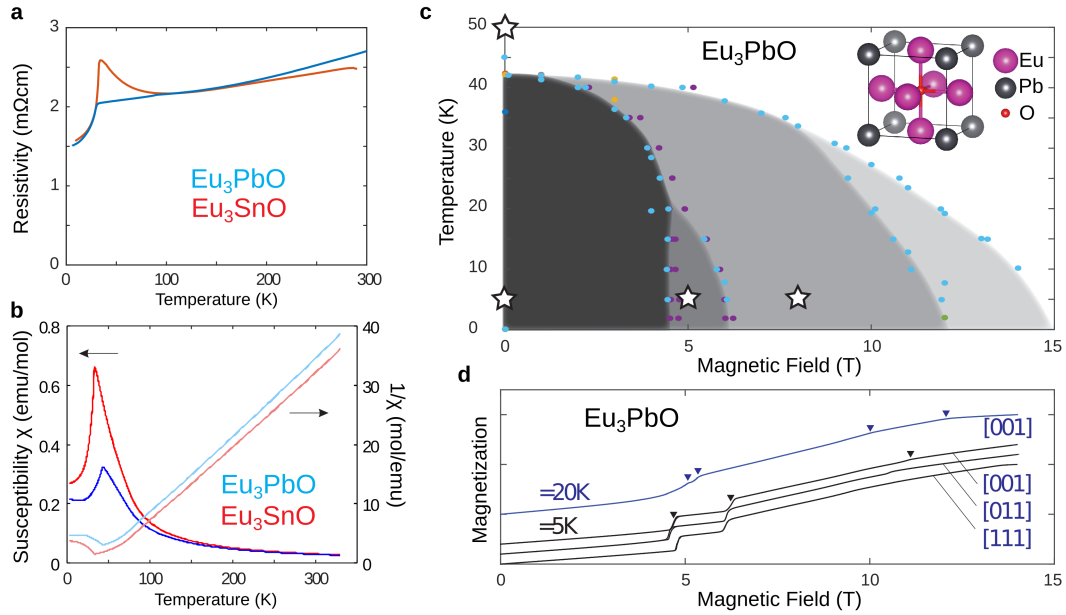


Figure 3.23.: Measurements on Eu_3PbO . **a** Resistivity over temperature. **b** Magnetic susceptibility over temperature. **c** Magnetic phase diagram with respect to the external magnetic field and temperature. **d** Magnetization curves for different alignments of the external field. (a,b adapted from [258])

change of the resistivity at low temperatures, which indicates a significant coupling between magnetic and electronic degrees of freedom and thus motivates our calculation of the anomalous Hall conductivity in the magnetically ordered phase, see Sec. 3.4.5. The DFT calculation for the emerging phase, which will be discussed below, yields a larger Fermi surface than for the paramagnetic case, which is consistent with a decrease in the resistivity at the phase transition, see Figs. 3.25a and g.

Signatures of the magnetic phase are found in the magnetic susceptibility χ , which exhibits Curie-Weiss behavior $\chi \propto 1/(T - \theta)$ with a Weiss temperature of $\theta = 36.5$ K. This increase of susceptibility is commonly related to ferromagnetic fluctuations. Nevertheless, the transition results in an overall antiferromagnetic order at a Néel temperature of $T_N = 42.9$ K [258], see Fig. 3.23b. The related antiperovskite Eu_3SnO exhibits an upturn in the resistivity and a stronger increase of the susceptibility below ≈ 100 K. Hence, one must consider that also magnetic fluctuations may contribute to the resistivity at low temperatures besides the explanation discussed above [33].

Together with magnetization measurements, see Fig. 3.23d, the compound is shown to exhibit several magnetic phase transitions summarized in Fig. 3.23c. To unveil the exact structure realized for the different magnetic phases neutron diffraction measurements at the

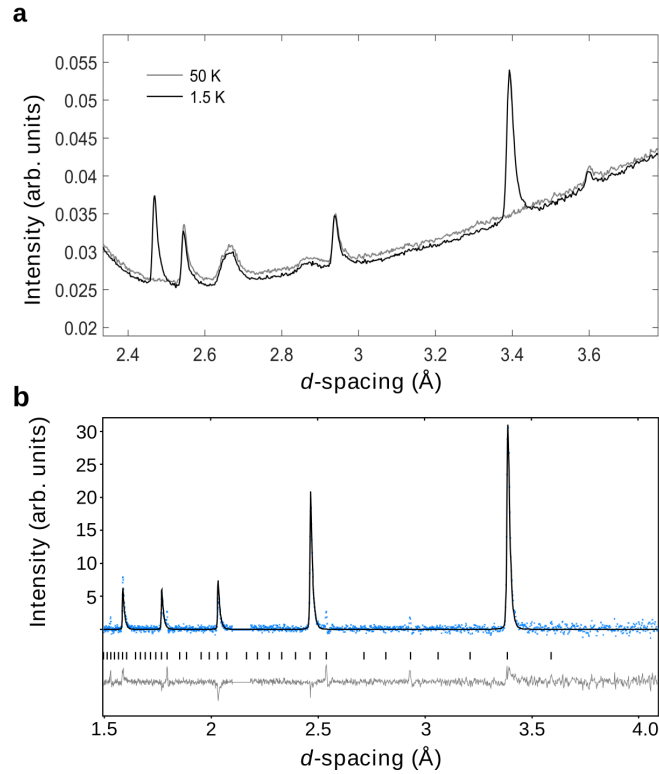


Figure 3.24.: Neutron diffraction data for Eu_3PbO . **a** Raw data for temperatures of 1.5 K and 50 K with a background signal due to the used quartz ampule. At 1.5 K the antiferromagnetic phase emerges. **b** Intensity at 1.5 K with a curve obtained by the Rietveld refinement under the assumption of the antiferromagnetic order. The differences between data and fitted curve are shown below.

WISH beamline of ISIS, Oxfordshire UK, have been performed on powder samples. The stars at temperatures 50 K and 1.5 K inscribed in the phase diagram Fig. 3.23c mark the temperatures and field strengths, which have been accessible in the neutron diffraction measurements.

Several peaks of the diffraction intensity emerge within the magnetic phases, see Fig. 3.24a. A Rietveld refinement was performed using the software *FullProf* [272] and *Jana2006* [273], which includes the consideration of possible magnetic subgroups [274] of the paramagnetic SG $Pm\bar{3}m$ (No. 221) starting from higher symmetry SGs. These are then tested on how well they reproduce the observed neutron diffraction data. Thereby, $P1a\bar{3}$ (No. 205.36) has been identified and the result of the refinement is shown in Fig. 3.24b.

Repeating the procedure for the other two magnetic phases yields two ferrimagnetic structures. At an external field of 5 T the phase “Ferri5T” with magnetic SG $P4/m'm'm'$ (No. 123.345) and at 8 T the phase “Ferri8T” with magnetic SG $Pm'm'm$ (No. 47.252) have been obtained.

Note, a third ferrimagnetic phase exists, see Fig. 3.23c but could not be reached for the

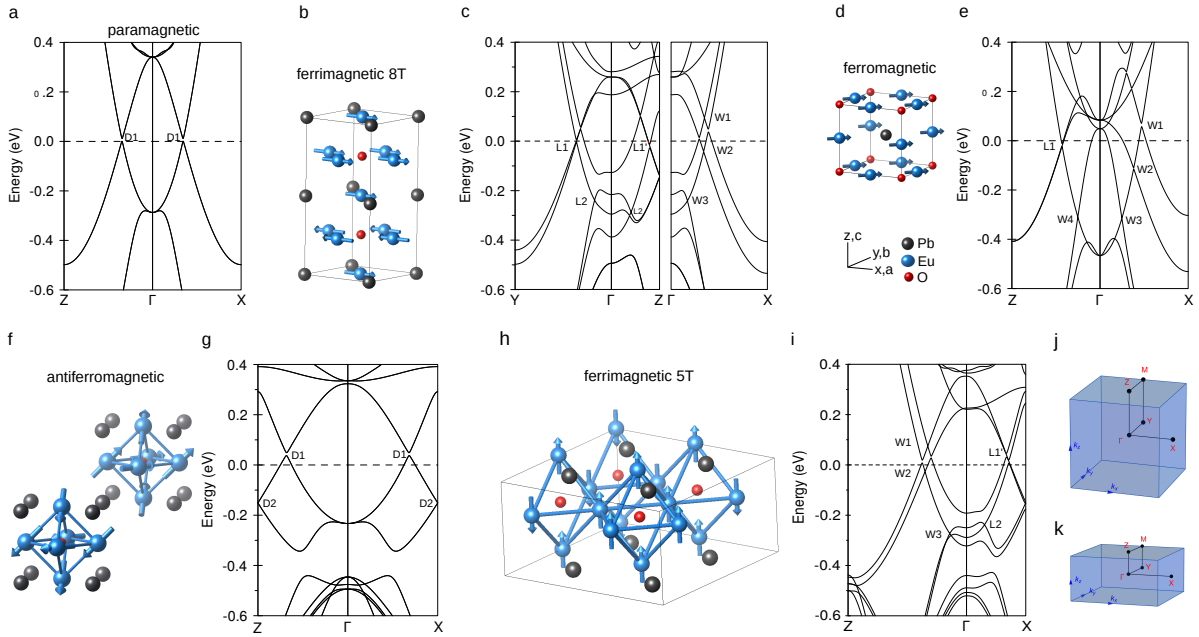


Figure 3.25.: *Electronic band structures, magnetic orders, and Brillouin zones of Eu_3PbO . (a), (c), (e), (g), (i) Electronic band structures of the paramagnetic and magnetic phases of Eu_3PbO along the high-symmetry lines of the Brillouin zones. The dashed lines at 0 eV mark the Fermi energy. Topological band crossings are labeled by “D”, “L1”. “L2”, and “W1”-“W5”, for Dirac points, nodal lines, and Weyl points, respectively, see Table 3.4. (b), (d), (f), (h) Crystal and magnetic structures of the magnetic phases Ferri8T, FM, AFM, and Ferri5T, respectively. The blue arrows indicate the orientations of the magnetic moments on the Eu atoms and each structure is shown in the basis of the paramagnetic, primitive cubic cell. (j), (k) Brillouin zones for (j) the paramagnetic, antiferromagnetic and ferromagnetic phases and (k) for the ferrimagnetic phase Ferri8T.*

neutron scattering experiment with the available magnetic fields. While this analysis is limited by the use of powder samples for the neutron diffraction experiments, the data represents the best approximation to the real structure at the time.

3.4.3. Band topology

Here, we want to discuss the DFT band structures given in Fig. 3.25 for the different magnetic phases. Their positions in the BZ and relative to the Fermi energy are given alongside their multiplicity in Table 3.4.

The paramagnetic phase of Fig. 3.25a exhibits six gapped Dirac points, “D1”, one on each

direction equivalent to Γ -X. As the space group $Pm\bar{3}m$ is symmorphic and includes inversion, all bands are twofold degenerate, except for possible fourfold degeneracies at Γ and R given by the $J = 3/2$ representation. The strong invariant for class \mathbb{Z}_2 is trivial but due to the band inversion of Eu- d and Pb- p orbitals a nontrivial mirror Chern number can be defined like in Ca_3PbO [252, 259].

At zero field for temperatures below the Néel temperature the antiferromagnetic phase emerges, see Fig. 3.25f. In SG 205.36 time-reversal symmetry is now reduced to the composite operation $\tilde{\theta} = \theta T(\frac{1}{2}, \frac{1}{2}, \frac{1}{2})$, where θ is the regular time reversal and $T(\frac{1}{2}, \frac{1}{2}, \frac{1}{2})$ a translation by less than a full lattice vector of the enlarged antiferromagnetic cell. Due to the backfolded bands in the larger unit cell, the band structure Fig. 3.25g exhibits a curious additional Dirac point, “D2”, at X, Y, and Z that is only indirectly protected by symmetry. Inversion symmetry is preserved with inversion centers at the oxygen sites. The composition of inversion P with time-reversal $\tilde{\theta}$ fulfills $\forall \mathbf{k} : (P\tilde{\theta})^2 = -1$, i.e., the twofold degeneracy of bands is not lifted by the onset of magnetic order. While the fourfold rotation symmetry is broken by the magnetic moments, twofold screw rotations $\tilde{C}_x(\frac{1}{2}, \frac{1}{2}, 0)$ remain, different symmetry eigenvalues are paired by $P\tilde{\theta}$ along the rotation axes Γ -X. Between identical representations no crossing is expected, yet the gap is smaller than 1 meV. This can be understood by considering that the involved bands exhibit only Pb- p character and the Pb site exhibits a vanishing magnet moment, because it is an inversion center. Any splitting of “D2” must be mediated by other states, which are far away in energy, and thus it is effectively zero.

With increasing field the Eu_3PbO reaches the ferrimagnetic order, Figs. 3.25b and h, where inversion P and time reversal θ are broken. Several Weyl points and twofold nodal lines appear. Among them “W1” and “W2”, which emerge as anticipated from the Dirac point in the vicinity of the Fermi energy. Nodal lines appear and are protected by mirror symmetry while carrying a Berry phase, cf. Figs. 3.25c and i and Table 3.4. With a non-zero total magnetic moment, the nonsymmorphic symmetries of the antiferromagnetic phase are gone, all magnetic corepresentations and the magnetic elementary band representations are one-dimensional [137], i.e., all crossings are accidental.

As the magnetic moments generally follow the external field in the ferromagnetic phase, we consider a [110] field alignment to extend the discussions in the literature, where a [100] moment direction was considered [258, 270]. One obtains the symmorphic SG $Cmm'm'$ (No. 65.486), which has a base-centered orthorhombic instead of cubic unit cell although no lattice constants have changed. To see this, one may consider that the structure, Fig. 3.25d, breaks threefold and fourfold rotations, so the cell type must be orthorhombic. The moments are perpendicular to a mirror plane such that [110] must be a principal axis in the new lattice basis. Hence, there exists a translation $T(\frac{1}{2}, \frac{1}{2}, 0)$ as a symmetry and the cell type is base-centered

orthorhombic. Nevertheless, to simplify the comparison with the previous magnetic structures we continue to use the primitive cubic basis. Three Weyl points “W1”, “W2”, and “W3” occur in the vicinity of the old rotation axes, displaced by varying degree relative to the ferrimagnetic phases, see Table 3.4. As the Γ -Z axis lies within the mirror plane (110) the crossings “L1” and “L2” are nodal lines.

phase	position	E (eV)	type	top. inv.	#
PM	(0.18, 0, 0)	0.017	Dirac (D1)	mir. Chern	6
AFM	(0.35, 0, 0)	0.05	Dirac (D1)	mir. Chern	6
AFM	$(\pi, 0, 0)$	-0.15	Dirac (D2)	–	3
Ferri5T	(0, 0, 0.17)	0.07	WP (W1)	Chern	2
Ferri5T	(0, 0, 0.18)	-0.03	WP (W2)	Chern	2
Ferri5T	(0, 0, 0.07)	-0.27	WP (W3)	Chern	2
Ferri5T	$k_x k_y$ -plane	-0.24	Line (L2)	Berry	1
Ferri5T	$k_x k_y$ -plane	0.05	Line (L1')	Berry	1
Ferri8T	(0.17, 0, 0)	0.09	WP (W1)	Chern	2
Ferri8T	(0.16, 0, 0)	-0.04	WP (W2)	Chern	2
Ferri8T	(0.07, 0, 0)	-0.25	WP (W3)	Chern	2
Ferri8T	$k_y k_z$ -plane	-0.24	Line (L2)	Berry	1
Ferri8T	$k_y k_z$ -plane	-0.003	Line (L1)	Berry	1
Ferri8T	$k_y k_z$ -plane	-0.29	Line (L2)	Berry	1
Ferri8T	$k_y k_z$ -plane	-0.007	Line (L1')	Berry	2
FM [110]	(0.23, 0.015, 0)	0.06	WP (W1)	Chern	4
FM [110]	(0.19, -0.001, 0)	-0.12	WP (W2)	Chern	4
FM [110]	(0.12, 0, 0)	-0.32	WP (W3)	Chern	4
FM [110]	(0.003, 0.003, 0.13)	-0.31	WP (W4)	Chern	4
FM [110]	(110)-plane	-0.31	Line (L1)	Berry	1

Table 3.4.: *Types of topological band crossings. This table lists the positions and energies of the topological band crossings in the first Brillouin zone (BZ) for the paramagnetic phase (PM), the antiferromagnetic phase (AFM), the ferrimagnetic phases (Ferri5T and Ferri8T), and the ferromagnetic phase with magnetization in [110] direction (FM [110]). The positions of the band crossings $\mathbf{k} = (k_x, k_y, k_z)$ are given in units of $2\pi/a_i$, where a_i denotes the lattice constant of the respective real space direction. All energies are given in eV relative to the Fermi energy. The type of band crossing is indicated in the fourth column, while the fifth column states the topological invariant that protects the crossings. The last column gives the multiplicity of the crossings, i.e., the number of symmetry related crossings at the same energy.*

3.4.4. Surface states

Among the different magnetic phases, there are mirror Chern insulators as well as Weyl metals. In the following we aim to answer the question, how their surface states are affected by the increasing degree of magnetization. To do so we implement a tight-binding model, including the orbitals Pb- p_x, p_y, p_z and Eu- $d_{xy}, d_{x^2-y^2}$ resulting in 18 bands, once spin is included. This model is sufficient to capture topological band crossings and respective topological invariants for the paramagnetic, antiferromagnetic and ferromagnetic phases, but lacks relevant orbitals for the ferrimagnetic cases. For the ferrimagnetic order the remaining Eu orbitals would need to be included. Nevertheless, the tight-binding model is sufficient for the questions posed above, see appendix E for details.

The surface states for paramagnetic, Fig 3.26a, and antiferromagnetic, Fig 3.26b, phases are the same up to slight deformations. Their spin polarization is not affected despite the non-zero magnetic moments on the surface. Due to the folding of the BZ in the antiferromagnetic case the surface states are larger relative to the total size of the Brillouin zone.

For the ferromagnetic phase, Fig 3.26c, d, there are several differences. If the surface termination includes lead atoms, then the closed Fermi surface associated to the mirror Chern number is split into Fermi arcs of similar spin polarization as before. Note that between the field alignment in [110] and [100] directions the number of Weyl points is different, because the bands do not split along a direction in reciprocal space that is perpendicular to the magnetic field, cf. appendix E. For the field in [100] direction, Fig 3.26d, only two instead of four Weyl points occur. The oxygen termination, which exhibits not lead but two of the europium sites, shows a more strongly modified Fermi arc connectivity. With the field in [110] direction the Fermi arcs connect Weyl points “W1” and “W2” next to each other on the same axis, whereas with [100] field alignment the arcs connect to the opposite side of the BZ and merge into the bulk. In both cases, the oxygen termination leads to a spin polarization nearly parallel to the applied magnetic field. This depends on the europium sites in the surface layer of the termination, which dominate the character of the surface states with Eu- d orbitals.

This analysis showed that the magnitude by which the surface states are modified, depends to a large extent on the modification of the bulk bands, but local effects depending on the details of the termination may strongly change the connectivity of the Fermi arcs.

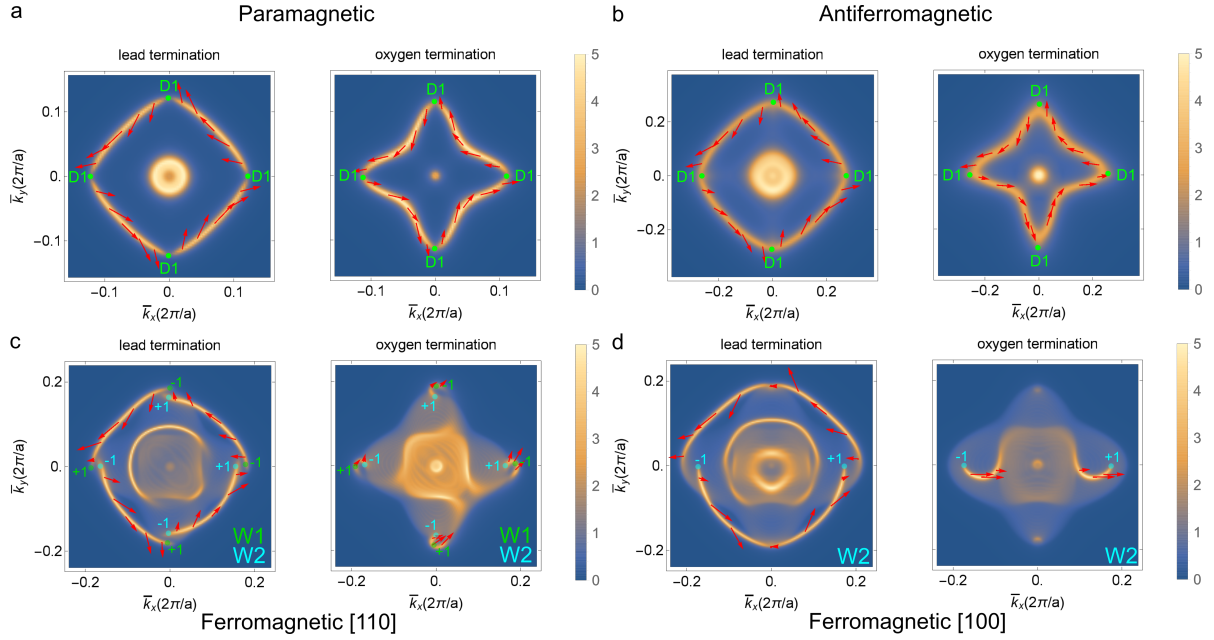


Figure 3.26.: Surface states and their spin polarization in Eu_3PbO . Calculated surface density of states (SDOS) and spin polarization for a (001) slab of Eu_3PbO with oxygen and lead termination. The color code represents the SDOS on a linear scale for the five outermost layers, while the in-plane spin polarization is indicated by the red arrows. (a),(b) show the SDOS for the paramagnetic and antiferromagnetic phases at the energy of the upper Dirac points $E = 0.017$ eV and $E = 0.05$ eV, respectively. The position of the Dirac points is marked by the label “D1” (cf. Table 3.4). The closed ring of surface states corresponds to the nontrivial mirror Chern number. (c), (d) display the SDOS for the ferromagnetic phase with magnetization in [110] and [100] directions at the energy of the Weyl points W1 and W2, respectively. The chiralities and positions of the Weyl points W1 and W2 are indicated in all panels by the green and blue dots and numbers.

3.4.5. Anomalous Hall conductivity in the ferromagnetic order

Our above study of band structures and surface states has determined the Weyl points and their splitting in energy and reciprocal space. The Weyl points of the ferromagnetic phase that are at the same energy are separated by up to nearly half of a reciprocal lattice vector, cf. Table 3.4. This distance is known to determine the size of the anomalous Hall effect in Weyl semimetals as was discussed in Section 1.2.2 and expressed in Eq. 1.2.20. But those results were only true for half filling. To obtain the conductivity for a periodic system the Berry curvature must be integrated over the full BZ weighted with the Fermi-Dirac distribution to account for the filling defined by the chemical potential μ as defined in Eq. 1.4.48.

To illustrate what to expect and to aid the interpretation of our result for Eu_3PbO , we consider a simple lattice model with two Weyl points, see Eq. 1.4.50, and calculate the Berry curvature and with it the non-zero off-diagonal components of the anomalous conductivity tensor. In Fig. 3.27a a part of the band structure is shown, where the Weyl points at zero energy can be seen. The conductivity for this model shows an anomalous Hall effect over the full range of the band width with a maximum at the position of the Weyl points.

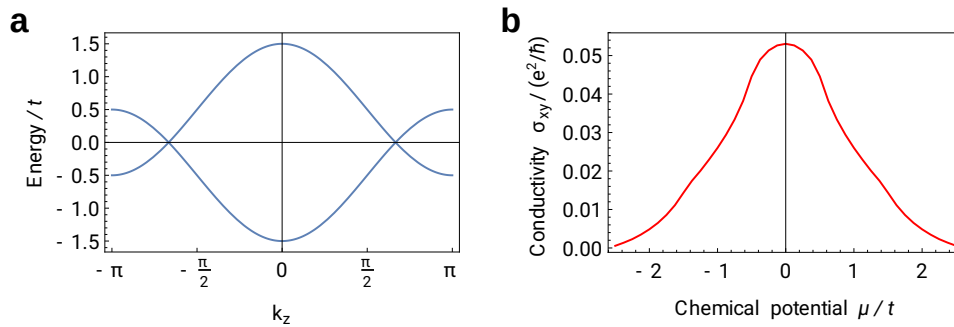


Figure 3.27.: *Weyl semimetal and its anomalous Hall conductivity. $m = -2.5, t = 1.0$ **a** Band structure along a path crossing Γ and the only two Weyl points of the system. **b** Anomalous Hall conductivity as function of the chemical potential at zero temperature.*

With the simple picture in mind, we turn to the anomalous Hall conductivity as we obtain it from our tight-binding model for Eu_3PbO for different orientations of the magnetic field, see Fig. 3.28. The overall shape of the conductivity curve exhibits broad features, as we must expect from the band widths seen in Fig. 3.25. Acknowledging this fact, the positions of Weyl points are only given as colored stripes. Depending on the alignment of local moments the conductivity may change roughly by up to a factor of 5 for some chemical potential μ , whereas at different filling the value stays approximately the same. For the experimentally expected hole doping in the order of a few 10 meV the magnitude of the relative change is up to a factor

of 2. To be specific at $\mu \approx -0.05$ eV the anomalous Hall conductivity $\sigma_{yz} \approx 50(\Omega\text{cm})^{-1}$ and $70(\Omega\text{cm})^{-1}$ for [111] and [110] magnetization, respectively, whereas for FM [100] its value is calculated to be $\sigma_{yz} \approx 110(\Omega\text{cm})^{-1}$. This can be considered to be a large value, which is of the same order as other systems like antiferromagnetic Mn_3Ge and Mn_3Sn [174, 175, 275] or ferromagnetic PrAlGe [276] and $\text{Co}_3\text{Sn}_2\text{S}_2$ [176].

We have listed the nodal features of the three considered instances of the ferromagnetic phase in Table A1. It turns out that the number of Weyl points vary for each case. FM [100] contains only “W2” and “W3”, whereas FM [110] has all “W1” to “W4” and FM [111] the crossings “W1” to “W3”. In the vicinity of the Fermi energy of the compound at $\mu = 0$, the Weyl points “W1” and “W2” are most relevant. In Fig. 3.26 we have indicated that their chiralities are opposite for adjacent crossings. For the anomalous Hall effect this means that their contributions cancel at least partially. Consequentially, at $\mu = 0$ the value of the conductivity of FM [110] and FM [111] is smaller than it is for FM [100], where no cancellation may happen due to the absence of “W1”.

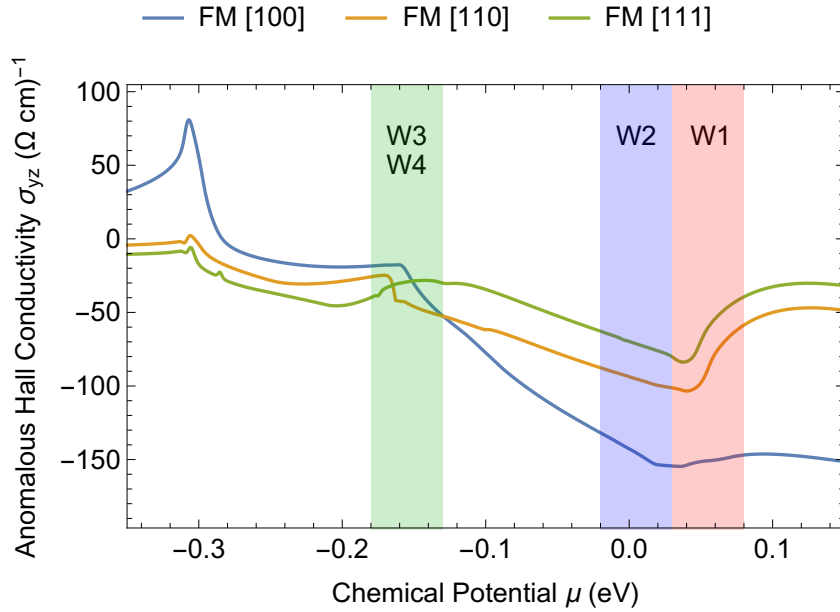


Figure 3.28.: Calculation of the intrinsic anomalous Hall conductivity σ_{yz} in the ferromagnetic phase as a function of chemical potential μ , for different orientations of the magnetic moments at a temperature of 10 K. Shaded stripes highlight the sections, where the largest contributions from different Weyl points to σ_{yz} are expected.

3.5. Topology in different magnetic phases of SmB_6

In the following we want to briefly discuss an on-going project that aims to analyze the band topology of the magnetic phases of SmB_6 [6]. The heavy-fermion compound SmB_6 has been considered as a possible realization of a topological Kondo insulator [277, 278]. It is a mixed valence compound, where the valence of Sm is at 2.56 and increases with pressure, which results in the on-set of a magnetic order [279]. The static susceptibilities indicate A-type magnetic order, while the G-type order appears as the second most likely case [6], see Fig. 3.29.

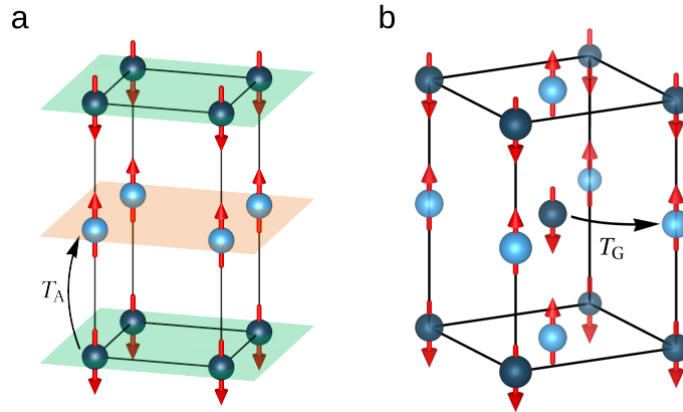


Figure 3.29.: Antiferromagnetic time-reversal symmetries for the two most likely types of magnetic order in SmB_6 under pressure [6]. **a** A-type magnetic order. **b** G-type magnetic order.

Here, we want to discuss the implications of the two different time-reversal symmetries $\theta_A = \theta T(0, 0, 1)$ and $\theta_G = \theta T(1, 0, 0)$. The paramagnetic SG of SmB_6 is 221, ($Pm\bar{3}m$) a symmorphic, centrosymmetric, cubic SG, whereas the A-type order is described by the tetragonal SG $P_{2c}4/m\bar{m}'m'$ (OG 123.15.1013) and the G-type order is described by the body-centered SG $P_14/m\bar{m}'m'$ (OG 123.19.1017). The OG setting is used here, because it states all symmetries in the basis of the parent compound, which simplifies the comparison. Both groups contain inversion P and $P\theta_A$ as well as $P\theta_G$, which fulfill Kramers theorem, hence all bands are twofold degenerate even with the onset of magnetic order. The strong topological invariant \mathbb{Z}_2 can be defined from inversion eigenvalues analogously to the paramagnetic phase [280]. For the A-type phase the very same inversion eigenvalues are folded back to the $k_z = 0$ plane, which can then be considered as a 2D subsystem with the same \mathbb{Z}_2 invariant as the 3D paramagnetic system [281].

We want to find out what happens in the $k_z = \frac{\pi}{2}$ plane, which is a mirror plane for the A-type phase at the boundary of the BZ but not for the G-type phase. Note that $k_z = \frac{\pi}{2}$ is at the boundary

of the tetragonal BZ instead of $k_z = \pi$, due to our use of the OG setting, which is in this case just a differently scaled lattice constant compared to the other parts of this work. The plane $k_z = \frac{\pi}{2}$ is left invariant by the mirror operation $M^z(0, 0, 0)$ with the symmetry eigenvalues $\pm i$. Usually different eigenvalues are paired by $P\theta$ and on the plane there is only one representation of the mirror symmetry. This does not happen here, because $P\theta_A$ obtains a factor of -1 from its commutation with $M^z(0, 0, 0)$, due to its translation in z direction. Therefore, identical mirror eigenvalues are paired at $k_z = \frac{\pi}{2}$ for the A-type magnetic order, but not for the G-type order. We find fourfold degenerate lines and associated drumhead surface states in our preliminary calculations [6]. These accidental Dirac nodal lines are different from the off-center symmetry enforced nodal lines, which require an off-centered mirror symmetry instead of $M^z(0, 0, 0)$. In fact this type of Dirac nodal lines is not possible in paramagnetic systems.

We conclude that the presence of Dirac nodal lines could be a possible criterion to distinguish A-type and G-type antiferromagnetism in pressurized SmB_6 , but it remains to be seen, whether these are experimentally accessible.

4. Semimetals with higher-order topology

The study of higher-order topology is concerned with surface states of lower dimension, i.e., states localized to hinges and corners instead of the complete surface. In the endeavor to generalize the already known concepts of topology in condensed matter systems to higher-order topology, recent approaches were made to describe semimetals and their topological band crossings in the context of higher-order topology.

We begin this chapter by a brief introduction of higher-order topology, its relation to the classification of topological insulators and superconductors, and the invariants that are associated with the higher-order topology. Then we summarize our work [7] that offers a variant of the discussed approaches. We will show surface states of a Weyl superconductor that occur only for certain terminations, which makes them a one-dimensional feature. This is different compared to regular Fermi arcs, which correspond to a non-zero Chern number and occur on any termination. We consider a two-dimensional topological superconductor that is driven by circular polarized light, which we describe by Floquet theory, and use the polarization of light as a synthetic third dimension. The emerging surface state exhibits a spin-polarization, that may be used to detect its presence.

4.1. Higher-order topology

Higher-order topology can be understood as a result of higher moments of electric polarization or as trivial bulk system that exhibits surfaces that are TIs of lower dimension themselves, according to Sec. 1.3.2. In the following we shall discuss both perspectives on higher-order topological insulators (HOTIs).

The polarization defined in Sec. 1.4.1 can be considered as the dipole moment of an electric charge distribution. If the dipole moment is zero, i.e., if inversion symmetry is present, it is possible to define a quadrupole moment, or if that one is zero one can define an octupole moment and so on [131, 132]. Let us consider a 2D quadrupole insulator, which exhibits corner

states. To obtain a non-zero quadrupole moment there must be at least two occupied bands below the band gap, and the insulating bulk must be trivial such that the edges are gapped as well. Under these conditions the quadrupole moment is characterized by nested Wilson loops [131, 132]. First a discrete Wilson loop [119] is calculated along one lattice direction, e.g., k_x . The result is a square matrix $\mathcal{W}_{x,k}$ with the number of occupied bands as dimension. Then a Wannier Hamiltonian $H_{\mathcal{W}_x}$ can be defined by

$$\mathcal{W}_{x,k} = e^{2\pi i H_{\mathcal{W}_x}}. \quad (4.1.1)$$

The eigenvalues ϑ_{k_x} of the Hamiltonian $H_{\mathcal{W}_x}$ correspond to the Wannier charge centers and when multiplied by 2π to generalized Berry phases. To obtain information about the corners of the system in real space, the idea is to use that $H_{\mathcal{W}_x}$ has the same topology as the edge spectrum for a termination in the x direction [282]. After a diagonalization of the Wannier Hamiltonian $H_{\mathcal{W}_x}$ one can express its eigenstates in the original basis of the Hamiltonian. The topology of the edge can then be characterized by a second Wilson loop that uses the eigenstates of $H_{\mathcal{W}_x}$. Finally, the edge polarization is given by the sum of eigenvalues of this second Wilson loop for all occupied bands. If no additional edge polarization independently of the bulk is present, one finds the quadrupole moment as the absolute value of the polarization.

Mirror symmetries quantize the quadrupole moment to either 0 or $\frac{e}{2}$ with e as the charge of an electron. In the nontrivial phase each corner of the 2D quadrupole insulator carries a charge of $\frac{e}{2}$. A topological transition does not need to close the bulk gap but instead the gap on the edge, whereby the bulk induced edge polarizations change.

There were several approaches to higher-order topology, including a hinge surface state that has been proposed to exist for a 3D insulator in class AIII [283] and another work that related corner and hinge states from Wannier charge centers to symmetry indicators in the presence of fourfold rotation C_4^z and mirror M^z symmetries [284].

The second interpretation of HOTI considers a D -dimensional system with an insulating, trivial bulk, which has TIs on its surface [133, 285], such that the surface of the surface hosts the gapless topological states. In 3D a 2nd order TI exhibits no surface states on its faces but they are themselves 2D TIs and their surfaces, the hinges, carry a 1D surface state. Generally, one defines n th order topology as the topology of a part of the surface with $D - n + 1$ dimensions, whereby surfaces of higher dimension than $D - n + 1$ are gapped and trivial, whereas the $D - n$ -dimensional edge or corner is gapless, as it is the boundary of the $D - n + 1$ -dimensional surface.

In principle one may apply the regular classification of topological insulators and superconductors to the surface itself, but in this case the topology would depend on the details of the surface termination. This is a difference between the two approaches to HOTIs, because the

description by the quadrupole moment is a bulk property [283]. The solution to this restriction is the addition of crystalline bulk symmetries, which fix the topology by relating different surfaces [134, 285, 286]. If we consider a 2nd order TI in two dimensions, then one may consider the edges, i.e., the gapped surfaces as 1D TIs, which are gapped by a mass term $\propto m$. To obtain a HOTI a mirror [285], inversion [134], or the combination of time-reversal and rotation [133] symmetries is needed, which relates different sections of the surface while switching the sign of the mass m . In this case the corner, i.e., the $D - 2$ dimensional boundary of the edges, is at the border between different topological phases and must thus exhibit a topological bound state. Note that in the case of inversion symmetry it is not necessary to have corners or hinges to be consistent with the symmetry [134].

Quadrupole moments have been realized in microwave resonators [287], as well as in a phononic metamaterial [288]. Bismuth has been proposed as a 2nd order TI, which is supported by scanning tunneling microscopy and transport measurements [286]. The cited approach to identify bismuth as a HOTI, is in-between the two schools of thought discussed in this chapter. One may consider the surfaces of bismuth as 2D, TRS-invariant TIs, but then an argument can be made based on the arrangement of symmetry eigenvalues within the 3D bulk system. To be specific, the authors find that the trivial Fu-Kane inversion invariant [120] can be split into contributions from two distinct eigenspaces of the threefold rotation C_3^z , which are both nontrivial by themselves. This two coincident band inversions then are shown by direct calculation to correspond to enforced gapless lines on the surface, the hinge states.

4.2. Higher-order Weyl superconductor

In the following we want to discuss a higher-order Weyl superconductor [7], which belongs to the second type of higher-order topology discussed in the previous section. The system we consider is inversion symmetric, and we show that thus its surface theory exhibits a sign change in its mass term for points related by inversion on the surface. This change of mass term then must lead to hinge states, where the mass vanishes [134, 285, 286].

We begin with a 2D higher-order topological superconductor $H = H_0 + h_\Delta$ that respects TRS and inversion with an inter-orbital s-wave pairing [7]

$$H_0(\mathbf{k}) = m(\mathbf{k})\tau_z\sigma_z + v \sin k_x s_z \sigma_x + v \sin k_y \tau_z \sigma_y - \mu\tau_z, \quad (4.2.1)$$

$$h_\Delta = \Delta_0 \tau_y s_y \sigma_x, \quad (4.2.2)$$

where $m(\mathbf{k}) = M_0 - 2m(\cos k_x + \cos k_y)$ and the Pauli matrices s_i , σ_i , and τ_i with $i \in \{x, y, z\}$ act on spin, orbital, and Nambu space, respectively. The chemical potential μ and the parameters

M_0 , m , and v are system dependent. We can represent the inversion symmetry with $\mathcal{P} = \tau_z \sigma_z$, which fulfills $\mathcal{P}H(\mathbf{k})\mathcal{P}^{-1} = H(-\mathbf{k})$.

To obtain a higher-order Weyl superconductor (HOWSC) we consider a periodic driving by an external electric field, given by the vector potential $\mathbf{A}(t) = A_0(\cos(\omega t), \sin(\omega t + \phi))$, where the phase shift ϕ determines the polarization of the incident light. We use a minimal coupling $\mathbf{k} \rightarrow \mathbf{k} \pm e\mathbf{A}(t)$ to the electromagnetic vector potential in the Hamiltonian, where the signs distinguish between electron and hole components of the Nambu spinor.

In the limit of large frequencies we use Floquet theory [289] to approximate the Hamiltonian as effectively static. To do so we note that the time-dependent Hamiltonian $H(\mathbf{k}, t)$, which we obtained from the minimal coupling procedure, is periodic in time t , i.e., $H(\mathbf{k}, t) = H(\mathbf{k}, t + T)$ with a period $T = \frac{2\pi}{\omega}$. Thus, the Hamiltonian can be expressed as a Fourier series $H(\mathbf{k}, t) = \sum_n H_n(\mathbf{k}) \exp(in\omega t)$. As we are only interested in the physics close to the Fermi energy, we proceed with the continuum description, where we replace $\sin k \rightarrow k$ and $\cos k \rightarrow 1 - k^2$. With this simplification the only non-zero matrix-valued expansion coefficients are [7]

$$H_0(\mathbf{k}) = \tilde{m}(\mathbf{k})\tau_z\sigma_z + vk_x s_z \sigma_x + vk_y \tau_z \sigma_y - \mu\tau_z + \Delta_0 \tau_y s_y \sigma_x, \quad (4.2.3)$$

$$H_{\pm 1}(\mathbf{k}) = eA_0 m(k_x \mp ik_y e^{\pm i\phi})\tau_z\sigma_z + \frac{1}{2}eA_0 v s_z \sigma_x \mp \frac{i}{2}eA_0 v e^{\pm i\phi} \tau_z \sigma_y, \text{ and} \quad (4.2.4)$$

$$H_{\pm 2}(\mathbf{k}) = \frac{1}{4}e^2 A_0^2 m(1 - 2e^{\pm 2i\phi})\tau_z\sigma_z, \quad (4.2.5)$$

with $\tilde{m}(\mathbf{k}) = m_0 + mk_x^2 + mk_y^2 + e^2 A_0^2 m$, and $m_0 = M_0 - 4m$. An effective static Hamiltonian is then given by [289]

$$H_{\text{eff}} = H_0(\mathbf{k}) + \sum_{n \geq 1} \frac{[H_{+n}(\mathbf{k}), H_{-n}(\mathbf{k})]}{n\omega} + \mathcal{O}\left(\frac{1}{\omega^2}\right). \quad (4.2.6)$$

To first order in $\frac{1}{\omega}$ and reverted to the periodic description, the effective Hamiltonian H_{eff} takes the form

$$h(\mathbf{k}) = h_0(\mathbf{k}) + \gamma(\mathbf{k}) \cos \phi, \quad (4.2.7)$$

$$h_0(\mathbf{k}) = \left((m(\mathbf{k}) + m\mathcal{I})\sigma_z + v \sin k_x \sigma_x + v \sin k_y \sigma_y - \mu \right) \tau_z - \Delta_0 \tau_x \sigma_x, \quad (4.2.8)$$

$$\gamma(\mathbf{k}) = \frac{2m\mathcal{I}}{\omega} \left(v \sin k_x \sigma_x + v \sin k_y \sigma_y - \frac{v^2}{2m} \sigma_z \right), \quad (4.2.9)$$

where $\mathcal{I} = e^2 A_0^2$ corresponds to the intensity of the light.

In the following we will study the surfaces states of the HOWSC described by Eq. 4.2.7. Let us consider a disc geometry that is finite in x and y directions, for which the phase shift ϕ of the polarization acts as a third dimension with periodic boundary conditions, see Fig. 4.1. The

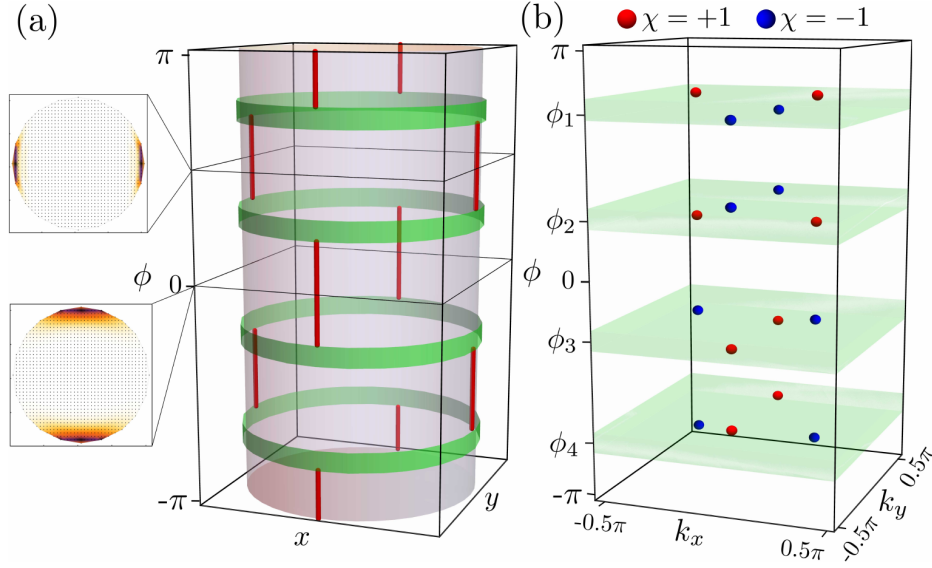


Figure 4.1.: Higher order topology and Weyl points of the effectively 3D Brillouin zone [7]. **a** Qualitative arrangement of surface states for the model defined in Eq. 4.2.7. Insets show parameter regions with different second-order topology, where the intensity map depicts the localization of the hinge state (red lines) in a circular system at the indicated value of ϕ . Green stripes mark regions with first-order topology, where the system exhibits chiral edge states, due to a non-zero Chern number. **b** The 16 Weyl points of the HOWSC are denoted with red and blue spheres according to their chirality. Four sets of Weyl points occur and are labeled by ϕ_1, \dots, ϕ_4 . They lie on the boundaries of the green regions that correspond to the stripes in **a**.

disc becomes a cylinder, when it is stacked in the ϕ direction, which we use to illustrate the ϕ dependence of the surface state, see Fig. 4.1a. We find that there are two parameter regions with higher-order topology, which are characterized by different positions of a 0D surface state, i.e., a line in ϕ direction. These hinge states comprise Majorana bound states and may either be localized in x or y directions. The transition between the two possibilities happens in a region where the surface and the bulk become gapless, due to the emergence of Weyl points, see Fig. 4.1b.

Previous proposals for higher-order Weyl semimetals have considered stacked quadrupole insulators [290, 291]. But such a description does not apply to our model, because the Wannier centers ϑ_{k_x} as eigenvalues of the Wannier Hamiltonian H_{W_x} , see Eq. 4.1.1, cross, and thus one cannot calculate the nested Wilson loop. For our model the surface states can be understood as overlapping Fermi arcs of two Weyl semimetals, which are protected from opening a band gap

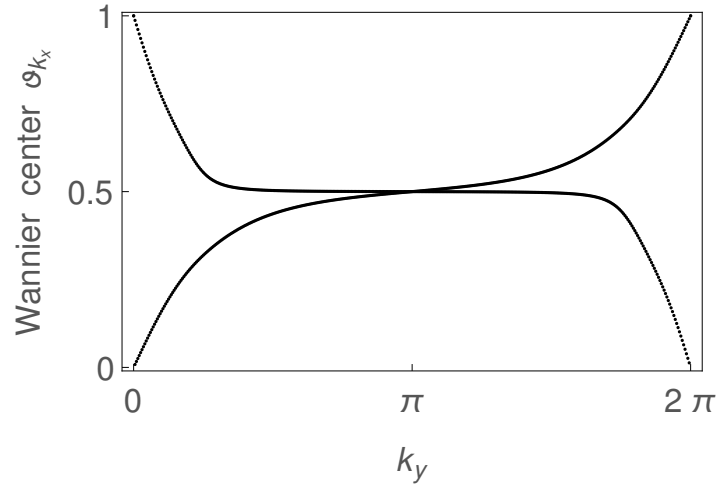


Figure 4.2.: Eigenvalues of the Wannier Hamiltonian H_{W_x} at $\phi = 0$ as function of the remaining coordinate k_x . There is no spectral flow and thus the Chern number vanishes at $\phi = 0$. Due to the crossing of eigenvalues at $k_y = \pi$, the quadrupole moment remains undefined for a nested Wilson loop.

at two points on the edge of a finite system, which then become Majorana bound states.

The hinge states of a quadrupole insulator would only exist on the hinges as 1D subsets of its surface. This is not the case for our model of a HOWSC, where surface states can also be found in the 2D surface BZ, see Figs. 4.3**b-d**. Depending on the choice of a surface termination, which corresponds to a straight edge in real space together with ϕ a second coordinate, we find different connectivities of the Fermi arcs. We illustrate the Chern number for constant ϕ in Fig. 4.3**a**, where we find a result consistent with the green regions of Fig. 4.1**a**. If ϕ lies in a region ϕ_i the system hosts surface states for all terminations, due to the non-zero Chern number. The (100) termination exhibits surface states around $\phi = \pm\frac{\pi}{2}$, whereas the (010) termination exhibits them around $\phi = 0$ and $\phi = \pi$, and the (110) termination corresponds to the intermediate case, where none of the Fermi arcs occur. In conclusion, the model exhibits Fermi arcs of Majorana bound states, but only for certain orientations of the surface. Hence, this is not a regular Weyl semimetallic phase, but indeed a phenomenon characteristic to higher-order topology.

Since we break TRS with the periodic driving, we ask ourselves whether these Fermi arcs obtain a spin-polarization. This is indeed the case and can be seen in Fig. 4.4. We find that the expectation value of $\langle S_z \rangle$ is largest for a given ϕ in the vicinity of a phase transition between differently oriented hinge states. At $\phi = \pm\frac{\pi}{2}$ the induced spin-polarization flips its sign. While the Majorana bound states are composed of equal electron- and hole-like parts and are thus charge neutral, the spin-polarization may be a useful property to measure the Majorana bound

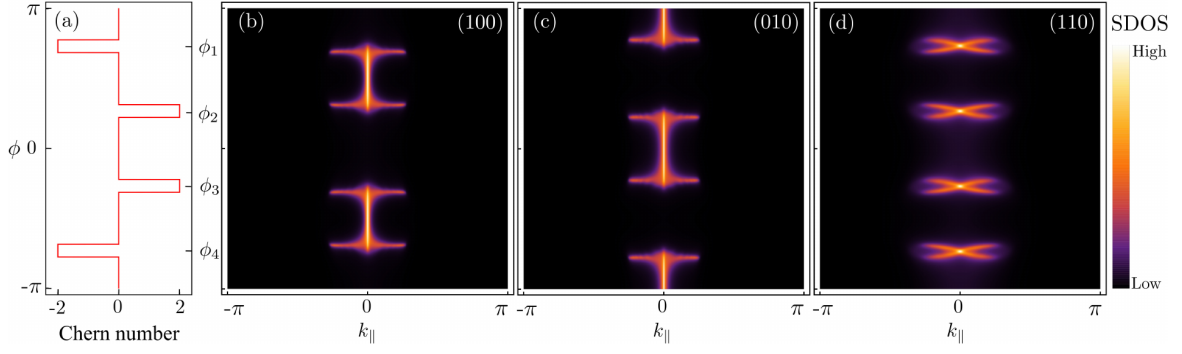


Figure 4.3.: Termination dependent surface state connectivity of the HOWSC [7]. **a** Chern numbers in the $k_x - k_y$ plane as a function of the phase ϕ of the incident light. **b**, **c**, and **d** Surface Brillouin zones including ϕ as independent coordinate for (100), (010), and (110) directions, respectively. The density of states on the surface (SDOS) at zero energy is given by the intensity map. k_{\parallel} denotes the reciprocal lattice direction within the surface BZ.

states in the HOWSC.

To show that our higher-order 1D surface states are indeed protected by inversion symmetry and to confirm the tight-binding calculations, we consider an effective surface model corresponding to the continuum model that precedes Eq. 4.2.7. Hereby, we find without the superconducting pairing two boundary states and then reintroduce the pairing to obtain the effective boundary Hamiltonian

$$h_{\text{eff}} = \begin{pmatrix} |v^+|k_{\parallel} - \mu & \tilde{\Delta}(\theta) \\ \tilde{\Delta}(\theta)^* & -|v^-|k_{\parallel} + \mu \end{pmatrix}, \quad (4.2.10)$$

where $v^{\pm} = v(1 \pm 2m\mathcal{I} \cos \phi/\omega)$, θ is the angle of polar coordinates and defines the considered position on the surface, and k_{\parallel} is the momentum tangential to the surface. The effective pairing in this basis

$$\tilde{\Delta}(\theta) = \frac{i}{2} \mathcal{F} \Delta_0 \text{sgn}(v^-) (\text{sgn}(v^+ v^-) e^{i\theta} - e^{-i\theta}) \quad (4.2.11)$$

is dependent on the angle θ , where \mathcal{F} is some non-zero overlap between wave functions. For $\mu = 0$ the pairing $\tilde{\Delta}(\theta)$ determines whether the energy spectrum of the boundary theory is gapless or not. Inversion symmetry leads to $\tilde{\Delta}(\theta + \pi) = -\tilde{\Delta}(\theta)$. This sign change implies that there exist two values for θ , where $\tilde{\Delta}(\theta)$ vanishes, i.e., the surface spectrum is gapless and a Majorana bound state appears. This is in accordance with the emergence of 1D surface states in the tight-binding model as, illustrated in Fig. 4.1. As a possible realization we suggest a cold atom system, where internal states and the layer index can be used to represent spin and orbit degrees of freedom [7].

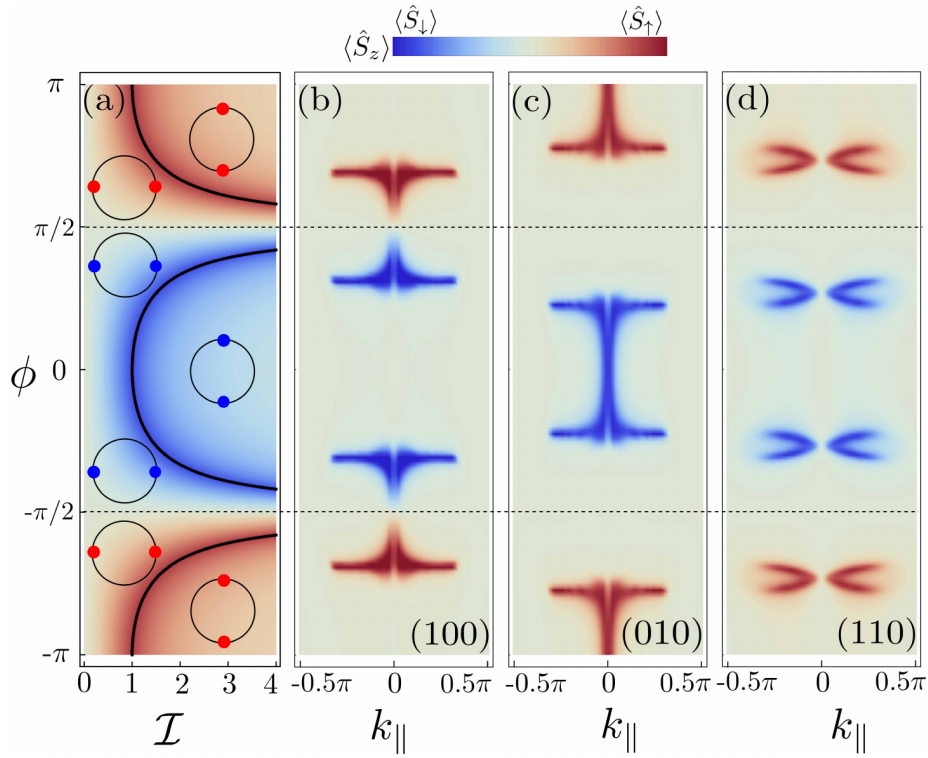


Figure 4.4.: Spin polarization of Majorana bound states [7]. **a** Phase diagram of the position of Majorana zero modes, which is denoted by the schematic insets. The intensity \mathcal{I} is given in units of $\frac{\omega}{2m}$. **b**, **c**, and **d** correspond to the spin-resolved surface density of states for the system with (100), (010), and (110) termination, respectively. k_{\parallel} denotes the reciprocal lattice direction within the surface BZ.

5. Exceptional topology

In this section we leave the regular Hermitian quantum mechanics behind us and discuss topology in the context of non-Hermitian models. Non-Hermitian Hamiltonians may occur as effective descriptions of systems that lose or gain (quasi)particles. It is one of the principles of regular quantum mechanics that each physical quantity is represented by a Hermitian operator. By dropping this restriction one loses several useful properties and encounters peculiarities, including complex eigenvalues for the used operators. For example, the Hamiltonian has non-orthogonal eigensystems even for nondegenerate eigenvalues, as well as exceptional points, where the eigenvalues become degenerate and the Hamiltonian is not diagonalizable anymore. But in return intrinsic topological features emerge and basic principles, like the bulk-boundary correspondence, have to be revisited.

After a general introduction to non-Hermitian systems, we discuss the Kitaev chain in the presence of gain and loss [8]. In this work we investigate whether the Pfaffian invariant of the Hermitian system remains well-defined for non-Hermitian, but \mathcal{PT} -symmetric systems. We find that the invariant can still be used and the strength of the non-Hermitian perturbation enters on an equal footing as the other parameters to tune the topological phase. Finally, we discuss in the second work, published in Ref. [9], the opposite case, where the non-Hermitian perturbation invalidates the bulk-boundary correspondence and enhances the topological phase. We find that the bulk invariant is insufficient to capture the emergence of topological surface states and the bulk-boundary correspondence is dependent on the chosen termination.

5.1. Non-Hermitian quantum mechanics

Non-Hermitian quantum mechanics is an extensively studied field of physics [292–294]. We will begin, in this section, by introducing some of the basic features of the theory of non-Hermitian quantum systems. But first, we shall consider the possible realizations of non-Hermitian systems. Theoretical descriptions of open systems and dissipation are often intricate, which limits their applicability in practical cases. For example, one may consider the Lindblad formalism that gives a master equation for the time-evolution of the density matrix of an open

system [295]. In this case it can be useful to approximate the formalism by an effective non-Hermitian matrix [296, 297]. The non-reciprocal energy transfer in a cryogenic optomechanical device can be described by an effective non-Hermitian Hamiltonian [298]. In a photonic system, used to implement a quantum walk, a localization of the walker to a phase boundary has been experimentally identified and related to the effectively non-Hermitian dynamics [299]. With mechanical metamaterials [300] or electrical circuits non-Hermitian physics can be readily implemented [301]. For a more complete exposition of possible applications of non-Hermitian physics, we refer to the recent reviews [293, 294].

A non-Hermitian Hamiltonian results in a non-unitary time-evolution. To illustrate this, we assume that there is an eigenstate $|\psi\rangle$ with an eigenvalue $E \in \mathbb{C}$ for a time-independent Hamiltonian H . Note, the Hamiltonian must be at least normal, i.e., $H^\dagger H = HH^\dagger$, to be diagonalizable with a unitary matrix, which generally is not the case for a non-Hermitian H . The time-dependent eigenstate is then given by $|\psi(t)\rangle = \exp(iEt) |\psi\rangle = \exp(-\text{Im } Et) \exp(i \text{Re } Et) |\psi\rangle$, which exhibits a decay for $\text{Im } E > 0$ or an increase for $\text{Im } E < 0$ in amplitude. This may be interpreted as gain or loss of (quasi)particles in the system [292], but it is then a priori unclear how quantum mechanical probabilities have to be calculated if the states are not normalized.

5.1.1. \mathcal{PT} -symmetric quantum mechanics

The generically complex energy spectra of non-Hermitian Hamiltonians can be avoided within the framework of \mathcal{PT} -symmetric quantum mechanics, where \mathcal{P} denotes inversion symmetry and \mathcal{T} refers to time-reversal symmetry [302–304]. Note that we adjust our notation to the literature and use in the following \mathcal{T} instead of θ to denote the time-reversal operation. The main idea of \mathcal{PT} -symmetric quantum mechanics is to constrain the Hamiltonian H by $[H, \mathcal{PT}] = 0$ instead of hermiticity. Suppose we have an eigenstate $|\psi\rangle$ of the Hamiltonian H with $H|\psi\rangle = E|\psi\rangle$, then one finds

$$H\mathcal{PT}|\psi\rangle = \mathcal{PT}H|\psi\rangle = E^*\mathcal{PT}|\psi\rangle. \quad (5.1.1)$$

In other words, $\mathcal{PT}|\psi\rangle$ is an eigenstate with eigenvalue E^* . One may conclude from this equation that the spectrum of the Hamiltonian must be real if $|\psi\rangle$ is an eigenstate of the operator \mathcal{PT} with eigenvalue 1. Here, we suppose the representation fulfills $\mathcal{P}^2 = \mathcal{T}^2 = +1$ and that \mathcal{P} commutes with \mathcal{T} . Let us begin more general and assume $|\psi\rangle$ is an eigenstate of the antiunitary operation \mathcal{PT} with the eigenvalue λ and thus

$$|\psi\rangle = (\mathcal{PT})^2|\psi\rangle = \mathcal{PT}\lambda|\psi\rangle = \lambda^*\mathcal{PT}|\psi\rangle = \lambda^*\lambda|\psi\rangle. \quad (5.1.2)$$

We find that the eigenvalue is just a complex number with unit modulus, i.e., $\lambda = \exp(i\varphi_\lambda)$, which can be removed by setting $|\psi'\rangle = \exp\left(i\frac{\varphi_\lambda}{2}\right)|\psi\rangle$, yielding

$$\mathcal{PT}|\psi'\rangle = |\psi'\rangle. \quad (5.1.3)$$

One concludes that a \mathcal{PT} -symmetric Hamiltonian yields a real energy spectrum, as long as its eigenstates are all simultaneous eigenstates of the antiunitary symmetry \mathcal{PT} . It has been found that the Hamiltonian H may enter a \mathcal{PT} -broken phase, i.e., a phase where the eigenstates of H are no longer eigenstates of \mathcal{PT} , as a function of the system parameters [302]. The transition between the two different phases corresponds to an exceptional point in the spectrum of the Hamiltonian H [302, 305].

So far our discussion does not quite lead to a unitary time-evolution, because in the \mathcal{PT} -broken phase a transition probability is not conserved. It has been suggested to use a different inner product for \mathcal{PT} unbroken Hamiltonians, by constructing a third symmetry C . In this formalism the product $\langle f|g\rangle$, of two states $|f\rangle$ and $|g\rangle$, is defined such that the state $\langle f|$ is not obtained by Hermitian conjugation, $\langle f| \neq (|f\rangle)^\dagger$, but instead $|f\rangle$ is multiplied with the operator $C\mathcal{PT}$ [303]. The occurring time-reversal makes the inner product conserved in time and independent of the choice of the phase factor for $|\psi'\rangle$. For Hermitian systems this inner product becomes equivalent to the conventional inner product of quantum mechanics.

Two caveats are in order. First if a system is completely described by a \mathcal{PT} -symmetric Hamiltonian that shares eigenstates with the \mathcal{PT} operation, there is a similarity transformation that maps the non-Hermitian to a Hermitian Hamiltonian, obeying the conventional inner product [306]. In this case the use of \mathcal{PT} -symmetric quantum mechanics would only correspond to a reformulation instead of an extension of quantum mechanics. The alternative would be to describe only a subset of the system with a \mathcal{PT} -symmetric Hamiltonian. If one then uses the probability distributions calculated from conventional normalized quantum states, it has been found in Ref. [307] that the formalism violates the no-signaling principle, which prohibits superluminal signal transmission [308, 309].

5.1.2. Biorthogonal quantum mechanics

Instead of trying to find a formalism that yields a unitary time-evolution, one may aim to give interpretations for the peculiarities of non-Hermitian systems. This raises the question: How do we need to calculate expectation values with states defined by a non-Hermitian Hamiltonian? In the following we discuss biorthogonal quantum mechanics, which uses left and right eigenstates of the Hamiltonian [292, 310]. Let us begin with the non-Hermitian Hamiltonian H , which we assume to be diagonalizable, and its right and left eigenstates, denoted by $|\psi_{R,n}\rangle$ and $\langle\psi_{L,n}|$,

respectively, are defined as

$$H|\psi_{R,n}\rangle = E_{R,n}|\psi_{R,n}\rangle, \quad (5.1.4)$$

$$\langle\psi_{L,n}|H = E_{L,n}\langle\psi_{L,n}| \Leftrightarrow H^\dagger|\psi_{L,n}\rangle = E_{L,n}^*|\psi_{L,n}\rangle. \quad (5.1.5)$$

The set $\{|\psi_{R,n}\rangle\}$ of right eigenstates generally does not contain pairwise orthogonal states, as long as the Hamiltonian is not Hermitian. An orthogonal basis can be constructed with left and right eigenstates, by using [310]

$$\langle\psi_{L,m}|H|\psi_{R,n}\rangle = E_{R,n}\langle\psi_{L,m}|\psi_{R,n}\rangle = E_{L,m}\langle\psi_{L,m}|\psi_{R,n}\rangle. \quad (5.1.6)$$

If $E_{R,n} \neq E_{L,m}$, then $\langle\psi_{L,m}|\psi_{R,n}\rangle = 0$, i.e., the states are orthogonal. Suppose the Hamiltonian is a finite dimensional matrix, and thus both left and right eigenvectors span the same vector space. This means that for each n there is at least one value of m with $\langle\psi_{L,m}|\psi_{R,n}\rangle \neq 0$, and thus $E_{R,n} = E_{L,m}$. If we assume nondegenerate eigenvalues of H , this relation between the eigenvalues of left and right eigenvectors is one-to-one. Hence, we can identify the eigenvalues with each other $E_{R,n} = E_{L,n} = E_n$. With the assumption that the non-Hermitian Hamiltonian is diagonalizable, its left and right eigenstates form two bases, which each span the full Hilbert space, and fulfill the biorthogonality relation [310]

$$\langle\psi_{L,m}|\psi_{R,n}\rangle = \delta_{nm}\langle\psi_{L,n}|\psi_{R,n}\rangle. \quad (5.1.7)$$

This fixes several problems of non-Hermitian quantum mechanics. For example, usually one would interpret the nonzero overlap between different eigenstates, $\langle\psi_{L,n}|\psi_{R,m}\rangle \neq 0$ for $m \neq n$, as a non-zero transition probability. But without an orthogonal eigenbasis this would allow for transitions between eigenstates of different energy without any energy transfer, for example, to the environment. If one uses an inner product comprising left and right eigenstates, one finds $\langle\psi_{R,n}|\psi_{R,m}\rangle = 0$ for $m \neq n$. By normalizing the eigenstates to fulfill $\langle\psi_{L,m}|\psi_{R,n}\rangle = \delta_{nm}$, this state overlap becomes a well-defined transition probability. In conclusion, probabilities becomes well defined if one expands “ket”-states $|\phi\rangle$ in the right eigenbasis and associate to them “bra”-states $\langle\tilde{\phi}|$ with

$$|\phi\rangle = \sum_n c_n |\psi_{R,n}\rangle, \quad \text{and} \quad \langle\tilde{\phi}| = \sum_n c_n^* \langle\psi_{L,n}|. \quad (5.1.8)$$

The expectation value of an operator A with respect to the state $|\phi\rangle$ is then calculated by [310]

$$\langle A \rangle_\phi = \frac{\langle\tilde{\phi}|A|\phi\rangle}{\langle\tilde{\phi}|\phi\rangle}. \quad (5.1.9)$$

Exceptional points

In the following we illustrate the emergence of an exceptional point, a degeneracy of energy eigenvalues that can only be encountered in non-Hermitian systems. Let us consider a minimal model that exhibits an exceptional point in its parameter space given by the Hamiltonian [293]

$$H = \begin{pmatrix} 0 & 1 \\ \alpha & 0 \end{pmatrix}, \quad (5.1.10)$$

with $\alpha \in \mathbb{C}$. If $\alpha \neq 0$, the matrix H can be diagonalized, yielding the left and right eigenstates

$$\langle \psi_{L,\pm} | = (\pm \sqrt{\alpha} \quad 1), \quad \text{and} \quad | \psi_{R,\pm} \rangle = \begin{pmatrix} 1 \\ \pm \sqrt{\alpha} \end{pmatrix}. \quad (5.1.11)$$

The corresponding eigenvalues of Eq. 5.1.10 are $E_{\pm} = \pm \sqrt{\alpha}$. Consider the limit of $\alpha \rightarrow 0$, where the two energies and the eigenstates become equal. At $\alpha = 0$ the Hamiltonian is not diagonalizable anymore and Eq. 5.1.10 corresponds to the Jordan normal form with the eigenvalue $E = 0$. In this case the Hamiltonian has an algebraic multiplicity of two and a geometric multiplicity of one, because there is only one linearly independent right eigenvector. The entirety of these features are the defining properties of an exceptional point in the spectrum of a non-Hermitian system. Note that the left and right eigenvectors have become orthogonal independent of the corresponding eigenvalue, i.e., $\langle \psi_{L,+} | \psi_{R,+} \rangle = 0$ at $\alpha = 0$, while at $\alpha \neq 0$ they fulfill, as expected, the biorthogonality relation given in Eq. 5.1.7. This so-called self-orthogonality of eigenstates implies a divergence of at least one entry in normalized eigenvectors [292].

There is an inherently nontrivial topology connected to such exceptional points. Suppose we change the phase of the parameter $\alpha = |\alpha| \exp(i \arg \alpha)$ from $\arg \alpha = -\pi$ to $\arg \alpha = +\pi$. The eigenvalues $E = \pm \sqrt{|\alpha|} \exp\left(i \frac{\arg \alpha}{2}\right)$ change in the process by a factor of -1 , i.e., they exchange and so do their eigenstates. Only after the phase $\arg \alpha$ is varied from 0 to 4π one obtains the original eigenvalue. If a Berry phase is calculated with the regular formula, cf. Eq. 1.4.5, but expressed with left and right eigenstates, a phase of $\pm \frac{\pi}{2}$ is accumulated.

5.1.3. Topology in non-Hermitian systems

To discuss topology in the context of non-Hermitian Hamiltonians, we begin by introducing the spectral winding number. Then we want to summarize recent developments regarding the extension of the Hermitian classification of topological phases to the non-Hermitian case.

Whereas for Hermitian systems a continuous energy spectrum may be split into different intervals that are separated by energy gaps, non-Hermitian systems exhibit, in general, energy

spectra that fill a region within the complex plane. The latter gives rise to two different notions of complex energy gaps [311]: There can be a point in the complex plane that does not correspond to an eigenenergy, but which is enclosed by the eigenvalues of the system, a so-called point gap. If there is a line in the complex plane that divides the spectrum into two disjoint sets of eigenenergies, then this is called a line-gap. A line gap is topologically similar to the gap in a Hermitian system as it leads to disconnected sets within an otherwise continuous energy spectrum.

Non-Hermitian systems are sensitive to boundary conditions. Hermitian systems exhibit a well-defined interior, in the absence of periodic boundary conditions, that is approximately described by the periodic Hamiltonian. Switching from periodic to open boundary conditions for non-Hermitian systems may lead to drastic changes for all bands. This is related to the energy winding around the exceptional point, we discussed for Eq. 5.1.10, once the complex phase of α is replaced by the crystal momentum k [312]. Suppose we have a point gap in the complex energy spectrum at E_{pg} , then one can define the spectral winding number as

$$W(E_{pg}) = \frac{1}{2\pi i} \int_0^{2\pi} dk \frac{d}{dk} \log \det(H(k) - E_{pg}). \quad (5.1.12)$$

$W(E_{pg})$ captures the number of times the energies wind around the point E_{pg} within the complex plane as a function of the crystal momentum k . A non-zero value of $W(E_{pg})$ implies the emergence of the non-Hermitian skin effect, which corresponds to a localization of all eigenstates of the open system at one of the surfaces [312, 313]. Note that this is understood as a diminishing size of the components for right and left eigenstates towards the bulk of the open system. The effect vanishes once the expectation value is calculated according to Eq. 5.1.9 [7, 293]. Nevertheless, it occurs together with drastic changes among the energies of bulk bands, and thus complicates the inference of topological surface states from bulk invariants. This has been explained by the emergence of exceptional points, i.e., points where the band gap closes, once the periodicity of the system is removed [314]. We will show in Sec. 5.3.2 that the topology of a system depends on the chosen surface termination.

It is possible to extend the classification of topological insulators and superconductors to non-Hermitian systems. For a non-Hermitian matrix H one may consider the matrix

$$\tilde{H} = \begin{pmatrix} 0 & H \\ H^\dagger & 0 \end{pmatrix}, \quad (5.1.13)$$

which is Hermitian and thus can be treated with the conventional classification scheme [315]. Another approach uses the fact that the operations of complex conjugation and matrix transposition are inequivalent for a non-Hermitian matrix. Hereby, the time-reversal and particle hole

symmetry, which define the 10 Altland-Zirnbauer classes, split into different symmetries. The resulting classification comprises 43 distinct symmetry classes [316]. This has been used to classify non-Hermitian topological insulators and exceptional points [311, 317].

In the following sections we want to discuss our contributions to the field that predate some of the discussed general approaches to topology in non-Hermitian systems.

5.2. Non-Hermitian Kitaev chain

Here we study whether the sign of the Pfaffian as a \mathbb{Z}_2 invariant for topological superconductors is still well-defined if a non-Hermitian perturbation is added to the Hamiltonian [8]. To do so, we consider the Kitaev chain, which was introduced as a 1D toy model for a quantum wire on top of a 3D p-wave superconductor [318]. In its topological phase this Hermitian model exhibits Majorana bound states localized to the end points of the wire.

The Hamiltonian for the Kitaev chain is given by

$$H_0 = \sum_n \left(t c_n^\dagger c_{n+1} + \tilde{\Delta} c_n c_{n+1} - \frac{\mu}{2} c_n^\dagger c_n + H.c. \right), \quad (5.2.1)$$

with the hopping amplitude t , the superconducting pairing amplitude $\tilde{\Delta} = \Delta \exp(i\theta)$ with $\Delta \geq 0$, the chemical potential μ , and the Hermitian conjugate $H.c.$ of the preceding terms. c_n and c_n^\dagger denote the fermionic ladder operators at the site $n \in \{1, \dots, N\}$ of a chain with N sites. We choose the phase $\theta = \pm \frac{\pi}{2}$ to obtain a \mathcal{PT} -symmetric model. Hereby, we choose the action of inversion as $\mathcal{P}c_n\mathcal{P} = c_{N+1-n}$ and time reversal \mathcal{T} shall commute with the ladder operators but act as complex conjugation on scalars. With the specific choice for the gap parameter $\tilde{\Delta}$ the Hamiltonian takes the form [8]

$$H_0 = \sum_n \left(t c_n^\dagger c_{n+1} + i\Delta c_n c_{n+1} - \frac{\mu}{2} c_n^\dagger c_n + H.c. \right). \quad (5.2.2)$$

To introduce a non-Hermitian term to the model, we consider the \mathcal{PT} -symmetric potentials

$$U_1 = \sum_n (-1)^n i\gamma c_n^\dagger c_n, \quad (5.2.3)$$

$$U_2 = i\gamma \left(- \sum_{n=1}^{N/2-f} c_n^\dagger c_n + \sum_{n=N/2+f}^N c_n^\dagger c_n \right) \quad (5.2.4)$$

with $\gamma \in \mathbb{R}$. While the potential U_1 breaks hermiticity at each site by alternating gain and loss, the potential U_2 introduces a non-Hermitian term for the $f \in \mathbb{N}$ first and last sites of the chain. The full Hamiltonian for our \mathcal{PT} -symmetric Kitaev chain is given by

$$H = H_0 + U, \quad (5.2.5)$$

with $U \in \{U_1, U_2\}$.

5.2.1. Pfaffian invariant

In the following we shall discuss the sign of the Pfaffian, which corresponds to the topological invariant of the Hermitian Kitaev chain, as system in class D. The introduction of the non-Hermitian potential U , may lead to an ill-defined sign and thus the fate of the invariant is a priori unclear. To investigate this, we use in the following the non-Hermitian perturbation U_1 , which preserves the translation invariance of the system for an enlarged unit cell. Accordingly, we introduce sublattices A and B for even and odd-numbered sites, respectively. To obtain the Pfaffian we need to rewrite the Hamiltonian, see Eq. 5.2.5, in the Majorana basis [318]

$$c_{\eta,n} = \frac{1}{2} (a_{\eta,2n-1} + ia_{\eta,2n}), \quad c_{\eta,n}^\dagger = \frac{1}{2} (a_{\eta,2n-1} - ia_{\eta,2n}), \quad (5.2.6)$$

where the Majorana operators fulfill $\{a_{\eta,m}, a_{\eta',n}\} = 2\delta_{nm}\delta_{\eta\eta'}$ and $a_{\eta,m}^\dagger = a_{\eta,m}$, with $\eta, \eta' \in \{A, B\}$. After this substitution and a discrete Fourier transformation one obtains

$$H = \frac{i}{4} \sum_k b_k^\dagger A(k) b_k, \quad (5.2.7)$$

with the four-component spinors b_k comprising the Fourier transformed Majorana operators a for sublattices A and B , see Ref. [8] for details. The Majorana number \mathcal{M} as topological invariant is then given by [109, 318]

$$\mathcal{M} = \text{sgn}(\text{Pf}[A(0)]\text{Pf}[A(\pi)]) = \text{sgn}(\mu^2 + \gamma^2 - 4t^2), \quad (5.2.8)$$

where the Pfaffian Pf is defined for a screw-symmetric matrix A , i.e., $A^T = -A$, by

$$\text{Pf}A = \frac{1}{2^N N!} \sum_{\tau \in S_{2N}} \text{sgn}(\tau) A_{\tau(1),\tau(2)} \cdots A_{\tau(2N-1),\tau(2N)}, \quad (5.2.9)$$

with S_{2N} as the set of all permutations of $2N$ elements. We find a nontrivial Majorana number $\mathcal{M} = -1$ for $\mu^2 + \gamma^2 < 4t^2$, which matches the result obtained from a real space calculation, see Fig. 5.1. The non-Hermitian perturbation, given by γ , enters the formula in the same way as the chemical potential μ . Large values for either parameter, μ or γ , contribute to a suppression of the topological phase. Thus, we find that in principle the invariant can be well-defined for our \mathcal{PT} -symmetric Hamiltonian.

Next we investigate under which conditions an arbitrary, particle-hole symmetric Hamiltonian H , with $H = \psi^\dagger \tilde{H} \psi$, leads to a well-defined Pfaffian invariant. To write the Hamiltonian more concise, we have introduced the Nambu spinors ψ and the matrix of coefficients \tilde{H} . After the transformation M , a $N \times N$ matrix, to the Majorana basis one obtains a skew-symmetric matrix X

$$\begin{aligned} \psi^\dagger \tilde{H} \psi &= i\psi^\dagger M^\dagger M(-i)\tilde{H}M^\dagger M\psi \equiv i\gamma X\gamma \\ &\Rightarrow -iM\tilde{H}M^\dagger = X, \end{aligned} \quad (5.2.10)$$

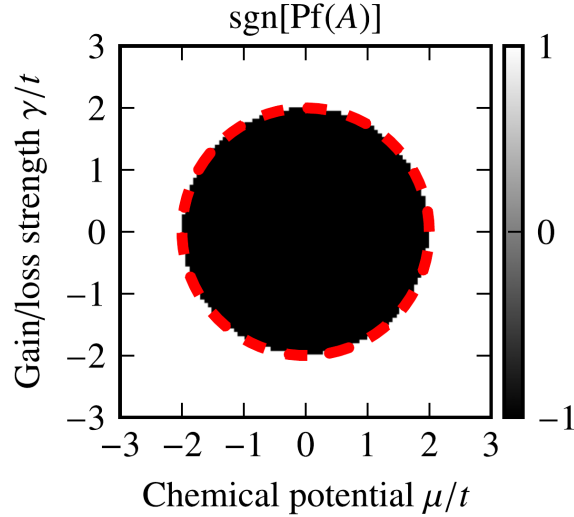


Figure 5.1.: Topological phase diagram for the non-Hermitian Kitaev chain with the potential U_1 [8]. The color map indicates the sign of the Pfaffian in a numerical real-space calculation with $N = 1$, $t = 1$, and $\Delta = 1$, where -1 (black) and $+1$ (white) correspond to the topological and trivial phases, respectively. The dashed line represents the result of the analytic calculation shown in the main text.

where we introduced the spinors γ containing the Majorana operators. Due to \mathcal{PT} -symmetry $[\mathcal{PT}, H] = 0$, one obtains the anticommutation relation $\{U, X\} = 0$, for U as the antiunitary operation representing \mathcal{PT} in the Majorana basis. In the simplest case the \mathcal{PT} -symmetry acts with an orthogonal matrix u , i.e., $u^T u = \mathbb{1}$, on the ladder operators, while in the general case u is unitary. With this we write $U = u \otimes \sigma_z K \equiv OK$, where K is the complex conjugation and σ_z acts within the Majorana states associated to an original site. It follows that the Pfaffian is a real quantity, since

$$\text{Pf}(X)^* = \text{Pf}(X^*) = \text{Pf}(-OXO^T) = \text{Pf}(-X) \det(O) = \text{Pf}(-X) \det(u)^2 \det(-\mathbb{1}) = \text{Pf}(X), \quad (5.2.11)$$

where we have used in the last step the assumption that u is an orthogonal matrix and that the Pfaffian $\text{Pf}(-X)$ has the same sign as the determinant $\det(-\mathbb{1})$ of the negative unity matrix. Since we have shown that the Pfaffian is a real number, its sign and thus the topological invariant can be defined. It is possible to show that this is also true if the action of \mathcal{PT} -symmetry relates different sites only by an inversion operation, see Ref. [8] for details.

5.2.2. Localized zero mode

After we have discussed the topological invariant in the previous section, we will now consider the end states on the quantum wire described by Eq. 5.2.5 with the potential U_2 [8]. We assume that the region of length f with a homogenous non-Hermitian potential $i\gamma$ is long enough to enclose most of the surface states. With this assumption we can perform an analytic calculation using the local generating function [319].

In the following we consider a semi-infinite system starting at the site $j = 1$. To solve the stationary Schrödinger equation $H|\psi\rangle = E|\psi\rangle$ we begin with the ansatz $|\psi\rangle = \sum_{j=1}^N (c_j^\dagger \psi_j^1 + c_j \psi_j^2) |0\rangle$, where $|0\rangle$ corresponds to the superconducting ground state and $\psi_j^1, \psi_j^2 \in \mathbb{C}$. We obtain a set of coupled equations for the vector $\psi_j = (\psi_j^1, \psi_j^2)^T$:

$$\Gamma_2 \psi_{j+1} + \Gamma_2^\dagger \psi_{j-1} - \Gamma_1 \psi_j = 0, \quad \text{with} \quad (5.2.12)$$

$$\Gamma_1 = \begin{pmatrix} \mu + i\gamma + E & 0 \\ 0 & -\mu - i\gamma + E \end{pmatrix}, \quad \text{and} \quad (5.2.13)$$

$$\Gamma_2 = \begin{pmatrix} t & -i\Delta \\ i\Delta & -t \end{pmatrix}. \quad (5.2.14)$$

To find the surface states with Eq. 5.2.12 we multiply it by z^j with $z \in \mathbb{C}$ and sum over j yielding

$$(\Gamma_2 - z\Gamma_1 + z^2\Gamma_2^\dagger)^{-1} \Gamma_2 \psi_1 = g(z) \equiv \sum_j z^{j-1} \psi_j. \quad (5.2.15)$$

The defined local generating function $g(z)$ is expected to have poles for surface states, because a localized state exhibits an exponential decay in j , $\psi_j \propto 1/z^j$, of its amplitude. Thus, we can identify surface states as the poles of $g(z)$, which may only arise due to the inverse matrix, which contains the denominator $\det(\Gamma_2 - z\Gamma_1 + z^2\Gamma_2^\dagger)^{-1}$ [319]. For $E = 0$ we find four poles of the generating function at

$$z_{a,b} = \frac{i\gamma + \mu + a \sqrt{4(-t^2 + \Delta^2) + (\mu + i\gamma)^2}}{2(t + b\Delta)}, \quad (5.2.16)$$

with $a, b \in \{-1, 1\}$. Only two of the decay constants given by the poles in Eq. 5.2.16, i.e., those with $|z| > 1$, correspond to states that decay into the bulk of our semi-infinite system, see Fig. 5.2. At $\gamma = \mu = 0$ perfectly localized end states of the quantum wire occur. Coincidentally, one finds for $t = \Delta$ the same condition as for the non-Hermitian potential U_1 , i.e., $\mu^2 + \gamma^2 = 4t^2$, for which no localized surface states exists. Nevertheless, overall the potential U_1 and U_2 yield different results.

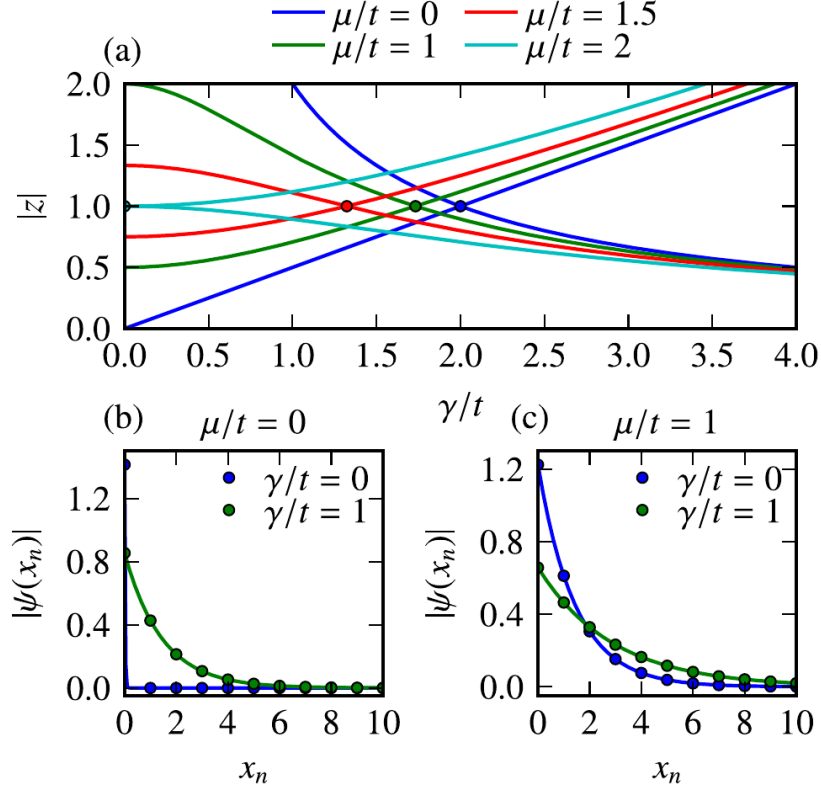


Figure 5.2.: Surface states and their decay constants for $t = \Delta$ [8]. **a** Modulus of the decay constant $|z|$ as function of the strength of the non-Hermitian potential γ , cf. Eq. 5.2.4. The intersections at $|z| = 1$ (filled dots) correspond to the phase transition points as calculated from the Pfaffian. **b** and **c** show the unnormalized edge states in a system with $N = 100$ sites as dots. The corresponding analytic results are given as lines.

In our discussion we have learned that it is indeed possible to apply the Pfaffian invariant to non-Hermitian Hamiltonians, with some restrictions, and to thereby obtain insights into non-Hermitian topology. The conventional topological phase of the Kitaev chain is not immediately destroyed by the application of non-Hermitian on-site potentials, but rather affected in a similar fashion as for the real chemical potential μ . For the energy spectrum rather drastic changes occur in our model, see Ref. [8]. We will discuss the effect of non-Hermitian terms on the band structure in the following section for a higher-dimensional system.

5.3. Non-Hermitian semimetals

In this section we study topological band crossings known from Hermitian systems, i.e., Weyl points, in the context of non-Hermitian topology [9]. We will encounter a violation of the conventional bulk-boundary correspondence and a termination-dependent topology. For a system with open boundary conditions we will see that the topological invariant of the periodic system is insufficient. Then, we will discuss a method to derive for a given finite system the corresponding bulk Hamiltonian with the same topology as the finite system. The latter enables us to calculate a bulk invariant, a Chern number, that captures the emergence of topological surface states.

5.3.1. Non-Hermitian Weyl semimetal

As an exemplary model we consider the toy model of a Weyl semimetal, see Eq. 1.4.50, together with a non-Hermitian term $\propto \lambda \in \mathbb{R}$:

$$H(\mathbf{k}) = \sin k_x \sigma_x + \sin k_y \sigma_y + (m - \cos k_x - \cos k_y - \cos k_z) \sigma_z + i\lambda \sigma_y. \quad (5.3.1)$$

The band structure of the Hamiltonian in Eq. 5.3.1 is illustrated in Fig. 5.3. We have chosen $m = 2.5$, such that for $\lambda = 0$ there are two Weyl points on the line $(0, 0, k_z)$. If we add the non-Hermitian potential $i\lambda \sigma_y$ with $\lambda = 0.4$, the Weyl points are replaced by regions with a flat real spectrum, $\text{Re } E = 0$, and non-zero complex part, $\text{Im } E \neq 0$. The boundary of the flat region consists of exceptional points.

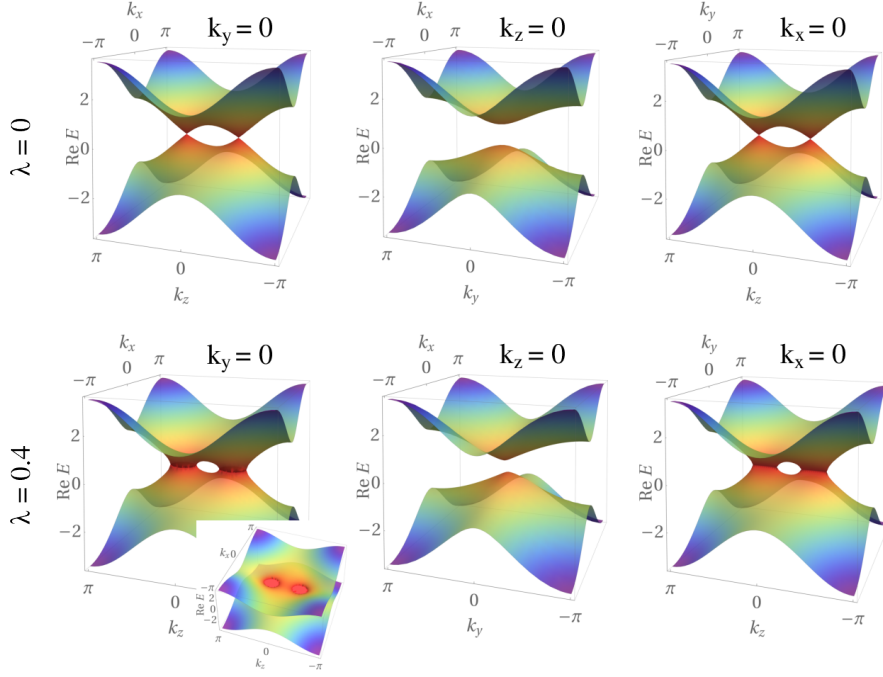


Figure 5.3.: Band structure of the Weyl semimetal model given in Eq. 5.3.1 on different planes in the Brillouin zone as indicated by $k_i = 0$ with $i \in \{x, y, z\}$. Only the real part of the energy is shown and color coded by its absolute value. All plots for $m = 2.5$. Top row: $\lambda = 0$. Bottom row: $\lambda = 0.4$, where the inset shows the band structure on the $k_y = 0$ plane from a second view point to illustrate the circular exceptional lines at $\text{Re } E = 0$.

5.3.2. Termination dependent topology

In this section we will discuss how the Chern number is insufficient to predict the surface states of the model defined in Eq. 5.3.1, once the periodic boundary conditions are lifted. The Berry curvature may be defined using any combination of left and right eigenstates in Eq. 1.4.27. Even though the local values of the Berry curvature depend on the chosen definition, the resulting Chern number is the same for all four possible choices [320]. Although we can find a unique, non-zero Chern number on planes of constant k_z , it is insufficient to predict the presence of surface states. By calculating the expectation value of the projector onto the surface according to Eq. 5.1.9, we can check whether the Chern number of the bulk Hamiltonian with periodic boundary conditions, see Eq. 5.3.1, is in accordance with the surface states.

To investigate the bulk-boundary correspondence, we have determined the band structure of two slabs with terminations in x and y direction, see Fig. 5.4. Whereas the bulk-boundary correspondence is valid for the x terminated slab, except in the vicinity of the exceptional lines,

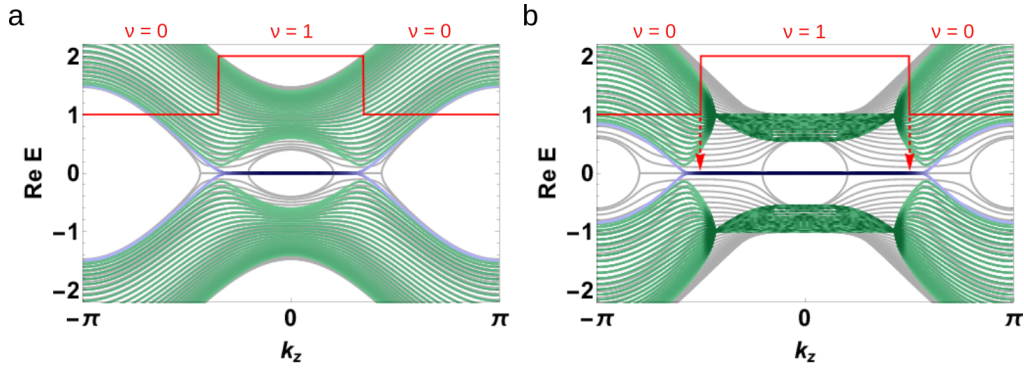


Figure 5.4.: Real part of the band structure for a slab with open boundary conditions in x direction **a** and y direction **b** for $m = 2$ and $\lambda = 0.8$. The bulk bands (gray) are shown together with the bands of the open system (green and blue), whereby for the latter a darker color corresponds to a larger expectation value of the projector on the surface layers. The red line represents the Chern number ν as a function of k_z . The arrows in **b** indicate a mismatch between the extension of the Fermi arc and the topological invariant.

cf. Fig. 5.4**a**, the converse is true for the termination in y direction, where the bulk states for open and closed boundary conditions do not coincide for any value of k_z , see Fig. 5.4**b**. Furthermore, we find that the surface state in the case with invalid bulk-boundary correspondence extends beyond the range expected from the Chern number. Interestingly, there is an increased surface density for all states with the onset of the non-zero Chern number, as seen by the darker color of the bulk bands. This is unexpected, because we calculate the localization according to Eq. 5.1.9, which should suppress the non-Hermitian skin effect. Note that close to the end of the Fermi arc states in Fig. 5.4**b**, two exceptional points occur and approximately half of all bands coalesce in each of these two degeneracies. These exceptional points have a macroscopically large order, i.e., each is a degenerate point of $\mathcal{O}(N)$ many bands for N layers in the slab. They indicate that the system undergoes a drastic change, once the periodic boundary conditions are lifted. Between these exceptional points the magnitude of state localization is fluctuating, possibly due to a numeric instability of the calculation.

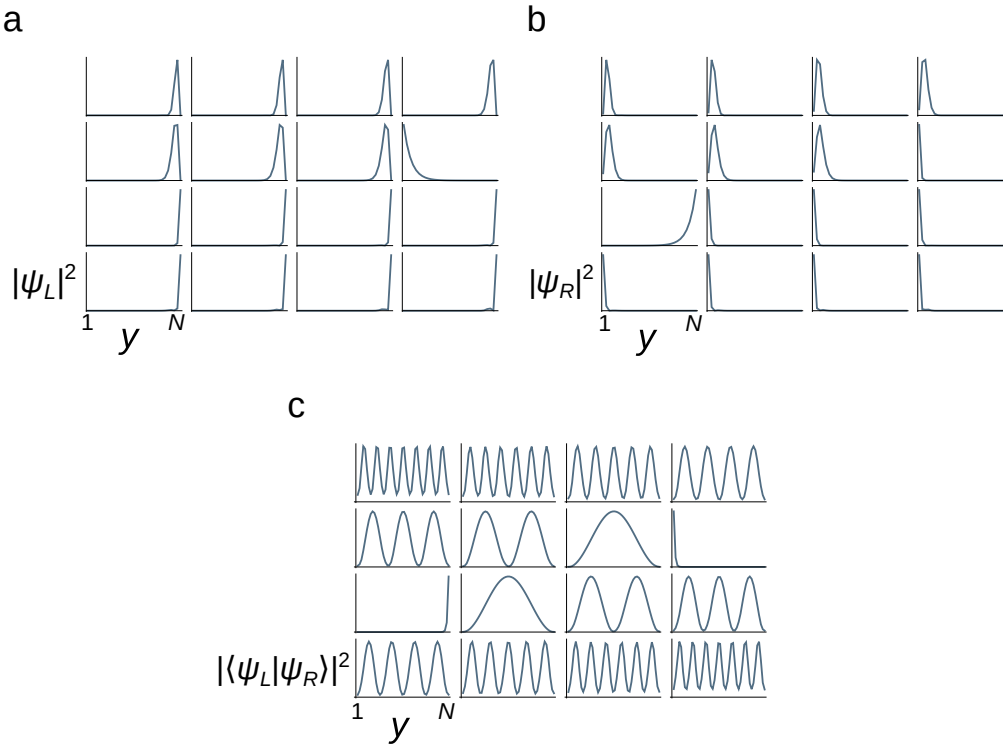


Figure 5.5.: Qualitative localization of left and right eigenfunctions $\psi_{L/R}(y) = \langle y | \psi_{L/R} \rangle$ with the coordinate y within the slab. **a**, **b**, and **c** each show the square of the wave function amplitude for 16 different states with an energy close to $\text{Re } E = 0$ for the open system. The axes (black) denote the position y in the slab and qualitative magnitude of the square of the depicted eigenstate for each y . **a** and **b** show the localization of left and right eigenstates, respectively. Due to the skin effect all states except one are localized at either of the surfaces. **c** uses the overlap between left and right eigenstates, which is equivalent to the expectation value of a projector onto a state at a single y coordinate, according to Eq. 5.1.9. The skin effect is absent in **c** and only the topological surface states are localized.

At the surface with y termination we find the typical localization behavior of the non-Hermitian skin effect [313], see Fig. 5.5. The left and right eigenstates exhibit a localization at the surface at small y coordinate, see Fig. 5.5 **a**, and at large y coordinate, see Fig. 5.5 **b**, respectively. While all left and right eigenstates are affected by the skin effect, one of the topological states remains localized alone at the opposite edge, see Figs. 5.5 **a** and **b**. The expectation value calculated according to Eq. 5.1.9 yields the conventional spatial distribution of states, where the surface states can be clearly distinguished from states associated to trivial bulk bands, see Fig. 5.5 **c**. Even if we consider this definition of spatial distributions according to the

biorthogonal quantum mechanics, like in Fig. 5.5 c, we do not recover the topological aspect of bulk-boundary correspondence because the energy spectrum, see Fig. 5.4, is independent of this choice. Thus, it remains to be discussed how the existence of a topological surface state can be inferred from a corresponding system with periodic boundary conditions.

To determine the correct invariant and topological phase, we can perform a non-unitary transformation on the system with open boundary conditions to obtain a model without the non-Hermitian term $\propto \lambda$ [9]. We find that the model will generally not become Hermitian but will correspond to a different periodic Hamiltonian, that then in return yields the correct Chern number to describe the surface states for the y termination. After undoing the Fourier transformation in y direction, we obtain the Hamiltonian of the open system

$$H(k_x, k_z) = \frac{1}{2i}\sigma_y \otimes (S - S^\dagger) + \frac{1}{2}\sigma_z \otimes (S + S^\dagger) + h_0, \quad \text{with} \quad (5.3.2)$$

$$h_0 = \sin k_x + M_k \sigma_z + i\lambda \sigma_y, \quad (5.3.3)$$

$$M_k = m - \cos k_x - \cos k_z, \quad \text{and} \quad (5.3.4)$$

$$S_{ij} = \delta_{i,j+1}. \quad (5.3.5)$$

We can remove the term $i\lambda\sigma_y$ from the above Hamiltonian for N layers with the transformation ρ , defined by

$$H_\rho(k_x, k_z) = \rho^{-1} H(k_x, k_z) \rho, \quad \text{with} \quad (5.3.6)$$

$$\rho = \rho' \otimes \text{diag}(1, \alpha, \alpha^2, \dots, \alpha^N), \quad (5.3.7)$$

$$\rho' = \frac{1}{2\sqrt{\alpha}} ((\alpha + 1)\mathbb{1}_2 + (\alpha - 1)\sigma_x), \quad \text{and} \quad (5.3.8)$$

$$\alpha = \sqrt{\frac{M_k - \lambda}{M_k + \lambda}}. \quad (5.3.9)$$

Note that the transformation ρ is generally not unitary. The new Hamiltonian $H_\rho(k_x, k_z)$ takes the form

$$H_\rho(k_x, k_z) = \frac{1}{2i}(S - S^\dagger) \otimes \sigma_y + \frac{1}{2}(S + S^\dagger) \otimes \sigma_z + \sin k_x \sigma_1 + \sqrt{M_k^2 - \lambda^2} \sigma_z. \quad (5.3.10)$$

The corresponding periodic Hamiltonian $H_\rho(\mathbf{k})$ corresponds to a Weyl semimetal, like the original Hamiltonian in Eq. 5.3.1, but the positions of the Weyl points are shifted depending on the value of λ . We will see that this new Hamiltonian $H_\rho(\mathbf{k})$ fulfills the bulk-boundary correspondence, i.e., it can be used to determine a topological invariant that is in agreement with the surface states. The mismatch between the Chern number ν and the existence of the surface state seen in Fig. 5.4b can be resolved.

First, let us take the left and corresponding right eigenstates, $\langle \varphi_{\rho,L} |$ and $|\varphi_{\rho,R}\rangle$, of the Hamiltonian $H_\rho(k_x, k_z)$ for the open system. These states do not exhibit the non-Hermitian skin effect. But note that even if $M_k^2 - \lambda^2 > 0$, for which the Hamiltonian $H_\rho(\mathbf{k})$ is Hermitian and the left and right eigenstates are related by Hermitian conjugation, we must distinguish the left and right eigenstates. This is because the transformation we used in Eq. 5.3.6 has acted differently on left and right eigenstates, due to $\rho^{-1} \neq \rho^\dagger$. With this in mind we want to relate the left and right eigenstates, $|\psi_L\rangle$ and $\langle\psi_R|$, of $H(k_x, k_z)$ to the eigenstates of $H_\rho(k_x, k_z)$. To do so we undo the transformation ρ and consider the expectation value of the projector P_y to the site y for the eigenstates of $H_\rho(k_x, k_z)$ as

$$\langle\psi_R|P_y|\psi_R\rangle = \langle\varphi_R|\rho P_y \rho^\dagger|\varphi_R\rangle, \quad (5.3.11)$$

$$\langle\psi_L|P_y|\psi_R\rangle = \langle\varphi_L|\rho P_y \rho^{-1}|\varphi_R\rangle = \langle\varphi_L|P_y|\varphi_R\rangle. \quad (5.3.12)$$

While the transformation ρ drops out of Eq. 5.3.12, it remains in Eq. 5.3.11. Thus the expression in Eq. 5.3.11 exhibits the skin effect, see Fig. 5.5b, whereas the use of left and right eigenstates in Eq. 5.3.12 only yields a localized surface state, if the original eigenstates $\langle\varphi_L|$ and $|\varphi_R\rangle$ of the transformed Hamiltonian already correspond to a surface state of $H_\rho(k_x, k_z)$. In the latter case the restored bulk-boundary correspondence of $H_\rho(k_x, k_z)$ is related to the well defined bulk states seen in Fig. 5.5c.

We have seen so far that transformation ρ captures the decay of eigenstate amplitudes because of the non-Hermitian skin effect. Now we will show that the topological phase of $H_\rho(k_x, k_z)$, i.e., where the skin-effect has been removed, is in accordance to the existence of topological surface states seen for $H(k_x, k_z)$. With the presence of Weyl points of the Hamiltonian $H_\rho(\mathbf{k})$ for a given set of parameters m and λ , which in this case implies a non-zero Chern number, we obtain a topological nontrivial phase. This phase is denoted as "∃ Weyl points (H_ρ)" in Fig. 5.6. We find that this phase is in perfect agreement with a direct determination of surface states. Surface states exist if the decay constants fulfill $|\alpha_L \alpha_R| < 1$ with the decay constants α_L and α_R for left and right eigenstates, respectively, which have been determined by analytic calculation. We find even if the Hamiltonian $H_\rho(\mathbf{k})$ is not Hermitian, that the topological phase of the constructed, periodic Hamiltonian $H_\rho(\mathbf{k})$ exactly agrees with the direct calculation of surface states [9].

We have thus seen that the chirality of Weyl points is robust even with non-Hermitian perturbations that replace the Weyl points with exceptional lines. Yet, their topological charge is found to describe only some of the surface states, i.e., those for which the bulk-boundary correspondence applies to the corresponding terminations. The open system appears to have undergone a topological phase transition, but it can be connected adiabatically to a different bulk Hamiltonian, which can be used to calculate the relevant topological invariant.

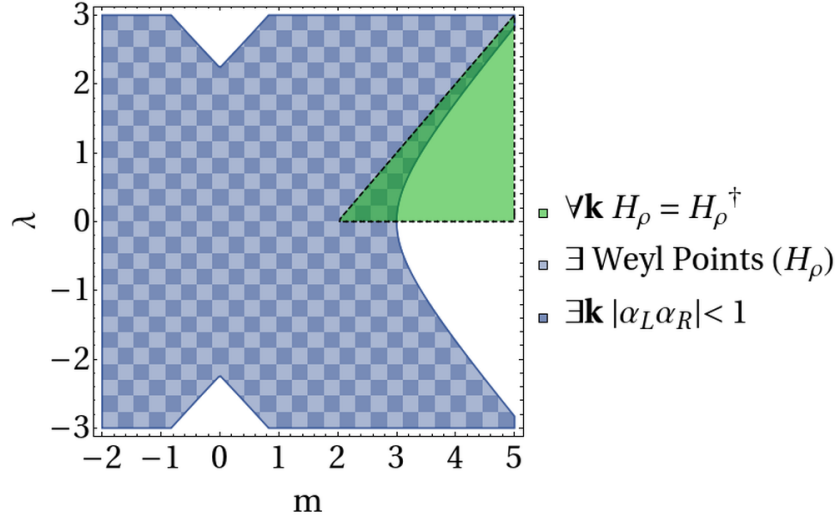


Figure 5.6.: Phase diagram for the non-Hermitian Weyl semimetal with y termination, reproduced from [9]. The green region corresponds to parameters for which $H_\rho(\mathbf{k})$ is Hermitian. The lighter blue region corresponds to a non-zero Chern number of $H_\rho(\mathbf{k})$ and identically matches the region in darker blue where surface states exist. For the latter we have calculated the decay constants α_L and α_R of left and right eigenstates of the open system given in Eq. 5.3.2 and a localized state exists if $|\alpha_L \alpha_R| < 1$.

We discuss in Ref. [9] the superposition of two Weyl systems of the type discussed in this section. Without the non-Hermitian terms this leads to a \mathcal{PT} -symmetric Dirac semimetal, whereas with a non-Hermitian term the physics is equivalent to that discussed here. In this configuration of two superimposed Weyl semimetals the non-Hermitian skin effect is modified by a mirror symmetry that relates the surfaces to each other. The eigenstates of a system with open boundary conditions are then localized to either surface at the same time.

Summary and outlook

In this work we have discussed the topological band crossings of electronic bands in condensed matter systems with a discrete translation invariance. Topological band crossings can be studied in terms of their symmetry eigenvalues, which characterize accidental and enforced crossings alike. Such crossings are of interest, especially in the context of topology, where they can be understood as transition points between qualitatively different regions in real or abstract parameter spaces. Our work revolves mainly around the existence of crossings, material search, Berry curvature, and topological surface states. In our endeavor to give a comprehensive approach to the possible band crossings that have been found so far, we have shown several extensions to Kramers theorem, which can be used to derive a significant subset of enforced crossings. The crystalline symmetries and the periodicity of the Brillouin zone imply that on high-symmetry lines and planes the bands may only exhibit certain numbers of crossings. Especially, for non-symmorphic symmetries a non-zero number of crossings is enforced to exist and cannot be removed without breaking the protecting symmetry. We discuss several exceptions to the commonly held belief that in the presence of time-reversal symmetry Weyl points must appear in sets of at least four. In the spinful case, there can be nodal lines or planes, i.e., extended regions of band degeneracy within the Brillouin zone, such that they include six out of the eight time-reversal invariant momenta. Thus only the two remaining momenta each host a Weyl point. In effectively spinless systems, Weyl points generally only occur at time-reversal invariant momenta if they are enforced by other spatial symmetries. For certain space groups two Weyl points are compensated by a third, which carries two times the opposite charge, totaling three Weyl points instead of four.

In our discussions we have used the inference of topological charges from symmetry eigenvalues to great effect. A logical next step is to extend the discussion presented in the literature by considering all possible combinations of one or more rotation symmetries with or without time-reversal symmetry. We have already found in a few cases unusually high topological charges for certain combinations of rotation and time-reversal symmetry [196].

Comprehensive study of space groups and material search

As a guide for band structure calculations with density functional theory it is helpful to predict beforehand in which space groups potentially interesting band crossings may occur. To interpret band crossings found on high-symmetry paths, one must understand, whether nodal points, lines, or planes have to be expected or whether they may occur at least accidentally. With our work on trigonal [1] and tetragonal [2] space groups, we aim to condense this analysis. In the process we discuss Weyl and Dirac points, their charges and multiplicities, nodal lines that are pinned, movable, or almost movable, as well as nodal planes. We have proposed several material candidates as examples, where these band crossings occur.

Furthermore, we have discovered some peculiar enforced band topologies in certain space groups, which to the best of our knowledge have not been reported previously. Among those are enforced \mathbb{Z}_2 topologies, i.e., 2D subspaces of the Brillouin zone, which exhibit an enforced weak \mathbb{Z}_2 index. This occurs in semimetals in the presence of inversion symmetry with bulk Dirac points that do not exhibit surface states. Yet, we find that due to the enforced nontrivial \mathbb{Z}_2 invariant, surface states analogously to a topological insulator must occur in these semimetals, i.e., Dirac cones pinned at time-reversal invariant momenta of the surface Brillouin zone. Closely related to this are fourfold crossings built from two Weyl points of opposite topological charges and of different symmetry representations. We have shown that these features appear in the space groups 106 and 133, which exhibit trivial fourfold crossings. These fourfold crossings are accompanied in the surface spectrum by two Fermi arcs that form avoided (gapped) crossings, leading to van Hove singularities.

Currently, we are finalizing the symmetry analysis of topological band crossings for orthorhombic space groups [321]. To extend the breadth of our material search, we also consider space groups for systems with weak or negligible spin-orbit coupling in addition to the case with strong spin-orbit coupling. Again, we search for systems with a small number of enforced Weyl points, movable Weyl and Dirac points, the various types and arrangements of nodal lines, nodal planes, and enforced \mathbb{Z}_2 invariants. Among the orthorhombic space groups movable fourfold nodal lines must exist due to off-centered mirror symmetries, this is unlike the tetragonal SGs, which restricted such lines to high-symmetry axes. In Ref. [321] the comparative discussion of effectively spinless and spinful systems leads to an extension of our results presented in this thesis. Suppose we can completely infer the inversion eigenvalues at time-reversal invariant momenta in the absence of spin-orbit coupling, then one should expect the same order of bands for material realizations, where spin-orbit coupling is not strong enough to change the order of bands. As a result we find space groups and exemplary materials, where a nontrivial \mathbb{Z}_2 topology is inherited from the limit of vanishing spin-orbit coupling.

In our work on Eu_3PbO we have performed a band topology analysis and gave a prediction of the topological contribution to the anomalous Hall current [5]. Furthermore, we have investigated SmB_6 in its pressure-induced phases, which exhibit either A-type or G-type antiferromagnetic order. We have shown that the A-type order exhibits Dirac nodal lines that are protected by a specific combination of symmetries, which are absent for the G-type type order. Hence, these two different band topologies may be used a criterion to experimentally distinguish the A-type from the G-type magnetic order [6].

Nodal planes and their topology

A prominent result of our work is the compilation of all 254 magnetic space groups with enforced nodal planes [3]. We have derived the necessary conditions for a nodal plane to exist and have surveyed all possible symmetry groups. Furthermore, there are several space groups where topologically charged nodal planes are possible. We have shown for 33 of them that their topological charge is enforced. Among them there is even an overlooked paramagnetic space group, SG 94, which exhibits doubly charged nodal planes. Unlike previous proposals of enforced nodal planes in solid state materials, space group 94 enforces topological surface states. Unfortunately, space group 94 is very rare among real materials and corresponds only to few and unsuitable compounds among the currently known materials. This motivates us to look for further examples of nontrivial nodal planes. While our list of enforced nodal planes can be considered to be complete, we must note that we cannot claim to have found all symmetry arguments to obtain enforced topological charges associated to the planes. Indeed, among the hexagonal space groups there are certain band representations that imply the necessity of topological nodal planes. In other words, by assuming more details of the system in question we find additional topological nodal planes. The goal of this on-going work is the systematic identification of paramagnetic, chiral space groups that host topological nodal planes [322].

We have also recently performed a study on CoSi , a non-magnetic compound with trios of nodal planes [4]. By symmetry arguments and density functional theory calculations we have determined the realized topological charges, and thus refined previous discussions in the literature that did not consider the nodal planes or all relevant Weyl points for each band.

At a nodal plane small symmetry breaking perturbations lead to large changes in the Berry curvature due to the orthogonality of states in the presence of a protecting symmetry. It has not yet been investigated which consequences follow from this general finding for nodal planes. Furthermore, it would be interesting to consider how a topological nodal plane compares to a Weyl semimetal of equal charges or a trivial nodal plane with respect to the contribution to the anomalous Hall effect [323].

Higher-order semimetals

In Ref. [7] we have discussed a system with trivial bulk topology that exhibits hinge surface states. To be specific, we have considered a driven topological superconductor yielding a Weyl phase with switchable Fermi arc connectivity and spin-polarized surface states. Future directions of this work include generalizations to Weyl semimetals with higher charges [324].

Topology in non-Hermitian systems

With our work on topological quantum wires with balanced gain and loss we have studied a non-Hermitian system, where for certain conditions the Hermitian topological invariant is well-defined [8]. In a subsequent project we considered models, for which the Hermitian invariant does not directly apply. We then discussed an approach to define the relevant topological invariant by taking the boundary conditions explicitly into account. It is found that the topological phase is enhanced by the presence of non-Hermitian perturbations [9]. The field of topology in non-Hermitian systems developed quickly, but transport properties of solid state systems have been rarely discussed. It would be a valuable insight to find a rigorous connection between a quantized Chern number and the Hall conductivity for a non-Hermitian system. Hereby, one must consider that the occupied and empty energies may generally be connected within the complex plane without a gap closing.

Appendix

A. Symmetries in tight-binding models

The goal of this section is to relate the action of crystalline or local symmetries in real space to a corresponding representation in reciprocal space. Thereby, one obtains the action on a symmetric Hamiltonian with periodic boundary conditions in the tight-binding approximation. We assume that the action of symmetries on the real space Hamiltonian is given by

$$H = U^\dagger H U, \quad H_{\mathbf{R}_\alpha p, \mathbf{R}_\beta q} = \sum_{\mathbf{R}_\gamma r, \mathbf{R}_\delta s} U_{\mathbf{R}_\gamma r, \mathbf{R}_\alpha p}^* U_{\mathbf{R}_\delta s, \mathbf{R}_\beta q} H_{\mathbf{R}_\gamma r, \mathbf{R}_\delta s}, \quad (\text{A.1})$$

where U is a unitary matrix that typically comprises a permutation of the localized orbitals as well as a set of complex phases. In Eq. A.1 we have also given the matrix elements $H_{\mathbf{R}_\alpha p, \mathbf{R}_\beta q}$ of the Hamiltonian H with respect to localized states $\phi_{\mathbf{R}_\alpha p}(\mathbf{r})$ labeled by the lattice vectors $\mathbf{R}_\alpha, \mathbf{R}_\beta, \mathbf{R}_\gamma, \mathbf{R}_\delta$, which point towards the corresponding unit cell, and the orbital and spin degrees of freedom p, q, r, s , which additionally distinguish the sites within a unit cell. If the symmetry is antiunitary, H and $H_{\mathbf{R}_\gamma r, \mathbf{R}_\delta s}$ are complex conjugated on the right-hand side of Eq. A.1. The stationary Schrödinger equation in the given basis has the form

$$\sum_{\mathbf{R}_\beta, q} H_{\mathbf{R}_\alpha p, \mathbf{R}_\beta q} \psi_{n, \mathbf{R}_\beta q} = E_n \psi_{n, \mathbf{R}_\alpha p}. \quad (\text{A.2})$$

For all further applications, we assume the presence of translation symmetry and choose a common eigenbasis of the Hamiltonian and the translation operators, as discussed in Sec. 1.2.3. Additionally, we assume periodic boundary conditions such that the common eigenbasis corresponds to a discrete Fourier transformation with respect to the positions in the lattice. The localized wave functions $\phi_{\mathbf{R}_\alpha p}(\mathbf{r}) = \phi_p(\mathbf{r} - \mathbf{R}_\alpha - \boldsymbol{\delta}_p)$ are centered at a lattice vector \mathbf{R}_α plus the position $\boldsymbol{\delta}_p$ of the site within the cell. One may express the basis wave functions as

$$\phi_{\mathbf{k}p}(\mathbf{r}) = \frac{1}{\sqrt{N^3}} \sum_{\mathbf{R}_\alpha} e^{i\mathbf{k} \cdot \mathbf{R}_\alpha} \phi_{\mathbf{R}_\alpha p}(\mathbf{r}), \quad \phi_{\mathbf{R}_\alpha p}(\mathbf{r}) = \frac{1}{\sqrt{N^3}} \sum_{\mathbf{k}} e^{-i\mathbf{k} \cdot \mathbf{R}_\alpha} \phi_{\mathbf{k}p}(\mathbf{r}). \quad (\text{A.3})$$

Now, we consider H with respect to the new basis $|\phi_{\mathbf{k}p}\rangle$ and then express the resulting matrix element $H_{\mathbf{k}p, \mathbf{k}'q}$ with $\langle \phi_{\mathbf{R}_\alpha p} | H | \phi_{\mathbf{R}_\beta q} \rangle$, for which the action of the symmetry is defined in Eq. A.1.

One obtains the expected block diagonal Hamiltonian, where the blocks are labeled by \mathbf{k} , as

$$\begin{aligned}
 H_{\mathbf{k}p,\mathbf{k}'q} &= \langle \phi_{\mathbf{k}p} | H | \phi_{\mathbf{k}'q} \rangle \\
 &= \frac{1}{N^3} \sum_{\mathbf{R}_\alpha, \mathbf{R}_\beta} e^{-i\mathbf{k} \cdot \mathbf{R}_\alpha} \langle \phi_{\mathbf{R}_\alpha p} | H | \phi_{\mathbf{R}_\beta q} \rangle e^{i\mathbf{k}' \cdot \mathbf{R}_\beta} \\
 &= \frac{1}{N^3} \sum_{\mathbf{R}_\alpha, \mathbf{R}_\beta} e^{-i\mathbf{k} \cdot \mathbf{R}_\alpha} H_{\mathbf{R}_\alpha p, \mathbf{R}_\beta q} e^{i\mathbf{k}' \cdot \mathbf{R}_\beta} \\
 &= \frac{1}{N^3} \sum_{\mathbf{R}_\beta, \Delta} e^{-i\mathbf{k} \cdot (\mathbf{R}_\beta + \Delta)} H_{\Delta = \mathbf{R}_\alpha - \mathbf{R}_\beta pq} e^{i\mathbf{k}' \cdot \mathbf{R}_\beta} \\
 &= \delta_{\mathbf{k}\mathbf{k}'} \sum_{\Delta} H_{\Delta, pq} e^{-i\mathbf{k} \cdot \Delta} \\
 &\equiv H_{\mathbf{k}, pq}, \tag{A.4}
 \end{aligned}$$

where it has been used that the Hamiltonian is translation invariant or in other words the matrix element depends only on the relative spatial coordinate $H_{\mathbf{R}_\alpha p, \mathbf{R}_\beta q} = H_{\mathbf{R}_\alpha - \mathbf{R}_\beta, pq}$, and $\frac{1}{N^3} \sum_{\mathbf{R}_\alpha} e^{i\mathbf{R}_\alpha \cdot (-\mathbf{k} + \mathbf{k}')} = \delta_{\mathbf{k}\mathbf{k}'}$. The relative distance Δ is defined by $\Delta = \mathbf{R}_\alpha - \mathbf{R}_\beta$ and the sum over Δ runs over the full real space lattice.

Before one may derive how the spatial symmetries act on $H_{\mathbf{k}, pq}$, it should be considered how the translation invariance modifies Eq. A.1. Since the crystalline unit cell repeats indefinitely, the elements of the matrix U do not depend on the position in space, i.e., $U_{\mathbf{R}_\alpha p, \mathbf{R}_\beta q} = U_{pq}$. Nevertheless, one must expect that generally different values of \mathbf{k} are related by symmetries like rotations or reflections, because they do not need to commute with the translation operators. The symmetry action on the position of the localized atomic sites is the regular representation on real space \tilde{D}_U , e.g., matrices corresponding to a rotation or mirror operation, to which a translation \mathbf{t}_U is added for nonsymmorphic symmetries. \mathbf{t}_U does not change the relative distance between sites, but if it moves one of the sites p or q out of the unit cell it can change the value of Δ in the Hamiltonian. This will be used in the following calculation. The spatial action of U turns the distance vector between two sites $\mathbf{R}_\beta + \delta_q - (\mathbf{R}_\alpha + \delta_p)$, corresponding to the orbitals q and p in the respective unit cells at \mathbf{R}_β and \mathbf{R}_α , into

$$\begin{aligned}
 \tilde{D}_U(\mathbf{R}_\alpha + \delta_q) + \mathbf{t}_U - \tilde{D}_U(\mathbf{R}_\beta + \delta_p) - \mathbf{t}_U &= \tilde{D}_U(\mathbf{R}_\alpha - \mathbf{R}_\beta) + \tilde{D}_U\delta_q + \mathbf{t}_U - \tilde{D}_U\delta_p - \mathbf{t}_U \\
 &= \tilde{D}_U\Delta + \delta\mathbf{R}_{pq} + \delta'_{pq}, \tag{A.5}
 \end{aligned}$$

$$\delta\mathbf{R}_{pq} = \tilde{\delta}_q - \tilde{\delta}_p, \quad \tilde{\delta}_q = [\tilde{D}_U\delta_q + \mathbf{t}_U]_{\mathbf{R}}, \quad \tilde{\delta}_p = [\tilde{D}_U\delta_p + \mathbf{t}_U]_{\mathbf{R}}, \tag{A.6}$$

$$\delta'_{pq} = \delta_{q'} - \delta_{p'}, \tag{A.7}$$

where the function $[\cdot]_{\mathbf{R}}$ returns a lattice vector, which is obtained by flooring the coefficients in the basis expansion of the function argument, while $\delta_{q'}$ and $\delta_{p'}$ are the positions of the

orbitals within the unit cell after the application of the symmetry U . The motivation behind the rearrangement of terms in Eq. A.5 is to identify the lattice vectors $\tilde{\delta}_p$ and $\tilde{\delta}_q$ that point towards the unit cells, where the orbitals, formerly labeled by p and q , are situated after the rotation. Thus, one obtains $\delta\mathbf{R}_{pq}$ as an additional change to the distance vector Δ . The explicit new positions within the unit cells, i.e., $\delta_{q'}$ and $\delta_{p'}$ are only introduced for completeness and do not affect the further calculations, because the permutations of orbitals is already encoded in the matrices U_{pq} . To summarize the symmetry action on the periodic Hamiltonian, we have obtained so far

$$H_{\mathbf{R}_{\alpha p}, \mathbf{R}_{\beta q}} = \sum_{\mathbf{R}_{\gamma r}, \mathbf{R}_{\delta s}} U_{\mathbf{R}_{\gamma r}, \mathbf{R}_{\alpha p}}^* U_{\mathbf{R}_{\delta s}, \mathbf{R}_{\beta q}} H_{\mathbf{R}_{\gamma r}, \mathbf{R}_{\delta s}} \quad (\text{A.8})$$

$$\Rightarrow H_{\Delta, pq} = \sum_{r, s} U_{rp}^* U_{sq} H_{\tilde{D}_U \Delta + \delta \mathbf{R}_{rs}, rs}. \quad (\text{A.9})$$

Now, Eqs. A.4 and A.9 must be combined and we move the action of the symmetry to the components of the matrix U to obtain the corresponding symmetry representation in reciprocal space

$$\begin{aligned} H_{pq}(\mathbf{k}) &= \sum_{\Delta} H_{\Delta, pq} e^{-i\mathbf{k} \cdot \Delta} \\ &= \sum_{\Delta, r, s} U_{rp}^* U_{sq} H_{\tilde{D}_U \Delta + \delta \mathbf{R}_{rs}, rs} e^{-i\mathbf{k} \cdot \Delta} \\ &= \sum_{\Delta, r, s} U_{rp}^* U_{sq} H_{\Delta, rs} e^{-i\mathbf{k} \cdot (\tilde{D}_U^{-1} (\Delta - \delta \mathbf{R}_{rs}))} \\ &= \sum_{\Delta, r, s} U_{rp}^* U_{sq} H_{\Delta, rs} e^{-i(\tilde{D}_U^{-1})^T \mathbf{k} \cdot (\Delta - \delta \mathbf{R}_{rs})} \\ &= \sum_{r, s} U_{rp}^* e^{-i(\tilde{D}_U^{-1})^T \mathbf{k} \cdot \tilde{\delta}_r} U_{sq} e^{i(\tilde{D}_U^{-1})^T \mathbf{k} \cdot \tilde{\delta}_s} \sum_{\Delta} H_{\Delta, rs} e^{-i(\tilde{D}_U^{-1})^T \mathbf{k} \cdot \Delta} \\ &= \sum_{r, s} \left(U_{rp} e^{i(\tilde{D}_U^{-1})^T \mathbf{k} \cdot \tilde{\delta}_r} \right)^* U_{sq} e^{i(\tilde{D}_U^{-1})^T \mathbf{k} \cdot \tilde{\delta}_s} H_{rs}((\tilde{D}_U^{-1})^T \mathbf{k}), \end{aligned} \quad (\text{A.10})$$

where we have used that the summation of Δ runs over the full lattice such that one may rearrange the order of elements, because the convergence is trivial due to the finite amount of non-zero summands, i.e., the effectively finite-range hopping in a finite system. Note that $(\tilde{D}_U^{-1})^T$ is equal to \tilde{D}_U if the matrix is orthogonal, which is the case for Cartesian coordinate systems. The latter is not always the chosen convention, e.g., in the hexagonal unit cell the non-rectangular primitive lattice vectors can also be a viable basis choice. The symmetry in reciprocal space is thus expressed with the matrices

$$\left(U((\tilde{D}_U^{-1})^T \mathbf{k}) \right)_{sq} = U_{sq} e^{i(\tilde{D}_U^{-1})^T \mathbf{k} \cdot \tilde{\delta}_s}, \quad (\text{A.11})$$

where the action on the Hamiltonian is given by

$$U \left((\tilde{D}_U^{-1})^T \mathbf{k} \right)^\dagger H \left((\tilde{D}_U^{-1})^T \mathbf{k} \right) U \left((\tilde{D}_U^{-1})^T \mathbf{k} \right) = H(\mathbf{k}) \quad (\text{A.12})$$

$$\Leftrightarrow U(\mathbf{k})^\dagger H(\mathbf{k}) U(\mathbf{k}) = H(\tilde{D}_U^T \mathbf{k}) = H(D_U \mathbf{k}), \quad (\text{A.13})$$

with the definition $D_U = (\tilde{D}_U)^T$, which denotes the action of the symmetry on reciprocal vectors. This means that for some symmetry U and its associated rotations D_U and \tilde{D}_U , given in a Cartesian coordinate system, the reciprocal vector \mathbf{k} is rotated in the opposite direction as the vector \mathbf{r} in real space. For an antiunitary symmetry $\theta = UK$ with the complex conjugation K the rotation matrix is modified by an additional inversion $D_\theta = -D_U$, due to the complex conjugation of the exponentials in Eq. A.10. The discussed representation in reciprocal space also applies to other operators. For example, if the product of two symmetry operators $U_1(\mathbf{k})$ and $U_2(\mathbf{k})$ shall be calculated, the action in k space must be considered as well, i.e., their product is $U_1(\mathbf{k})U_2(D_{U_1}\mathbf{k})$.

B. Berry curvature with arbitrary crystalline symmetries

To predict how the chiralities of Weyl points relate to each other and to anticipate which components of the anomalous Hall conductivity are non-zero, we need to understand how crystalline symmetries act on the Berry curvature. In the main text, we have already discussed the cases for symmetries that are represented by a matrix that is constant in the crystal momentum \mathbf{k} .

In the following we shall consider nondegenerate bands at generic momenta, which implies that the combination of inversion and TRS is absent, because otherwise the Berry curvature would already be identical to zero at all points of the BZ. An eigenstate $|n(\mathbf{k})\rangle$ of the Hamiltonian is related by a symmetry operation $U(\mathbf{k})$ as

$$U(\mathbf{k}) |n(\mathbf{k})\rangle = \tilde{U}_n(\mathbf{k}) |n(D_U \mathbf{k})\rangle, \quad (\text{B.1})$$

where $\tilde{U}_n(\mathbf{k})$ generally denotes a matrix acting within the subspace of eigenstates that are degenerate with the n th state. One may choose a different basis to simplify the expression $\tilde{U}_n(\mathbf{k})$, but here we consider for now an arbitrary choice of eigenstates such that we may directly use a geometrically motivated expression for U . In the present case, $\tilde{U}_n(\mathbf{k})$ is only a 1D matrix, and therefore for each band n it is a single phase factor with $|\tilde{U}_n(\mathbf{k})| = 1$. $\tilde{U}_n(\mathbf{k})$ depends on the orbital character of the basis states and the partial translations that must occur for nonsymmorphic symmetries.

In the following we want to study how Berry curvature is related by the symmetry U . The

curvature is expressed as

$$\begin{aligned}\Omega^n(\mathbf{k})_a &= -\text{Im} \epsilon_{abc} \sum_m \frac{\langle n(\mathbf{k})|\nabla_b H(\mathbf{k})|m(\mathbf{k})\rangle \langle m(\mathbf{k})|\nabla_c H(\mathbf{k})|n(\mathbf{k})\rangle}{(E_n(\mathbf{k}) - E_m(\mathbf{k}))^2} \\ &= -\text{Im} \epsilon_{abc} \sum_m \frac{V_b^{nm}(\mathbf{k})V_c^{mn}(\mathbf{k})}{(E_n(\mathbf{k}) - E_m(\mathbf{k}))^2}\end{aligned}\quad (\text{B.2})$$

where we have introduced the velocity operator $V_b^{nm}(\mathbf{k})$, which we rewrite using a symmetry U of the Hamiltonian:

$$\begin{aligned}V_b^{nm}(\mathbf{k}) &\equiv \langle n(\mathbf{k})|\frac{dH(\mathbf{k})}{dk_b}|m(\mathbf{k})\rangle \\ &= \langle n(\mathbf{k})|U^\dagger U \frac{dH(\mathbf{k})}{dk_b}|m(\mathbf{k})\rangle \\ &= \langle n(\mathbf{k})|U^\dagger \left(\frac{d(UH(\mathbf{k}))}{dk_b} - \frac{dU}{dk_b} H(\mathbf{k}) \right) |m(\mathbf{k})\rangle \\ &= \langle n(\mathbf{k})|U^\dagger \frac{d(UH(\mathbf{k}))}{dk_b} |m(\mathbf{k})\rangle - \langle n(\mathbf{k})|U^\dagger \frac{dU}{dk_b} H(\mathbf{k}) |m(\mathbf{k})\rangle \\ &= \langle n(\mathbf{k})|U^\dagger \frac{d(H(D_U \mathbf{k})U)}{dk_b} |m(\mathbf{k})\rangle - E_m(\mathbf{k}) \langle n(\mathbf{k})|U^\dagger \frac{dU}{dk_b} |m(\mathbf{k})\rangle \\ &= \tilde{U}_n^*(\mathbf{k}) \tilde{U}_m(\mathbf{k}) \langle n(D_U \mathbf{k})|\frac{dH(D_U \mathbf{k})}{dk_b}|m(D_U \mathbf{k})\rangle \\ &\quad + \langle n(\mathbf{k})|H(\mathbf{k})U^\dagger \frac{dU}{dk_b} |m(\mathbf{k})\rangle - E_m(\mathbf{k}) \langle n(\mathbf{k})|U^\dagger \frac{dU}{dk_b} |m(\mathbf{k})\rangle \\ &= \tilde{U}_n^*(\mathbf{k}) \tilde{U}_m(\mathbf{k}) D_U^{b'b} V_b^{nm}(D_U \mathbf{k}) + (E_n(\mathbf{k}) - E_m(\mathbf{k})) \langle n(\mathbf{k})|U^\dagger \frac{dU}{dk_b} |m(\mathbf{k})\rangle,\end{aligned}\quad (\text{B.3})$$

where D_U is the constant matrix that represents the action of the crystalline symmetry U within space. To study the symmetry of $\Omega^n(\mathbf{k})_a$ the energies $E_n(\mathbf{k})$ do not play a role as they are symmetric under $\mathbf{k} \rightarrow D_U \mathbf{k}$. The symmetry of the curvature can be captured by the product of velocity matrix elements, see Eq. B.2,

$$\begin{aligned}V_b^{nm}(\mathbf{k})V_c^{mn}(\mathbf{k}) &= \left(\tilde{U}_n^*(\mathbf{k}) \tilde{U}_m(\mathbf{k}) D_U^{b'b} V_b^{nm}(D_U \mathbf{k}) + (E_n(\mathbf{k}) - E_m(\mathbf{k})) \langle n(\mathbf{k})|U^\dagger \frac{dU}{dk_b} |m(\mathbf{k})\rangle \right) \\ &\quad \times \left(\tilde{U}_m^*(\mathbf{k}) \tilde{U}_n(\mathbf{k}) D_U^{c'c} V_c^{mn}(D_U \mathbf{k}) - (E_n(\mathbf{k}) - E_m(\mathbf{k})) \langle m(\mathbf{k})|U^\dagger \frac{dU}{dk_c} |n(\mathbf{k})\rangle \right) \\ &= D_U^{b'b} V_b^{nm}(D_U \mathbf{k}) D_U^{c'c} V_c^{mn}(D_U \mathbf{k}) \\ &\quad + (E_n(\mathbf{k}) - E_m(\mathbf{k})) \left(-\tilde{U}_n^*(\mathbf{k}) \tilde{U}_m(\mathbf{k}) D_U^{b'b} V_b^{nm}(D_U \mathbf{k}) \langle m(\mathbf{k})|U^\dagger \frac{d}{dk_c} |n(\mathbf{k})\rangle \right. \\ &\quad \left. + \tilde{U}_m^*(\mathbf{k}) \tilde{U}_n(\mathbf{k}) D_U^{c'c} V_c^{mn}(D_U \mathbf{k}) \langle n(\mathbf{k})|U^\dagger \frac{dU}{dk_b} |m(\mathbf{k})\rangle \right) \\ &\quad - (E_n(\mathbf{k}) - E_m(\mathbf{k}))^2 \langle n(\mathbf{k})|U^\dagger \frac{dU}{dk_b} |m(\mathbf{k})\rangle \langle m(\mathbf{k})|U^\dagger \frac{dU}{dk_c} |n(\mathbf{k})\rangle.\end{aligned}\quad (\text{B.4})$$

The first term of the last expression in Eq. B.4 corresponds to the result for constant U shown in the main text in Eq. 1.4.45, whereas here all other terms occur due to the k -dependence of the symmetry operator U . Thus, we have found that in the most general case there are additional terms, compared to the case of constant U , and there might not be a one-to-one correspondence between the Berry curvature and the crystalline symmetries.

It is known that even for some nonsymmorphic symmetries the Berry curvature obeys the corresponding crystallographic point group symmetry. We now specify the matrix U to study such cases. Let us assume the symmetry U is represented by its action on the orbitals, as discussed in Appendix A. Here, U is a generalized permutation matrix given as $U = U_{\text{perm}} \tilde{U}$. U_{perm} denotes a constant permutation matrix and \tilde{U} is a diagonal matrix with complex phase factors. Suppose U depends only on one k_a for some $a \in \{x, y, z\}$. For example, we consider a twofold screw rotation symmetry that relates s orbitals on the sites $(0, 0, 0)$ and $(0, 0, \frac{1}{2})$ and is given by

$$U' = \begin{pmatrix} 0 & e^{ik_z} \\ 1 & 0 \end{pmatrix}, \quad (\text{B.5})$$

which must be adjusted to the correct basis convention, because, while the Berry curvature is invariant under gauge choice of the eigenstates of the Hamiltonian, it depends on the choice of the tight-binding basis. The natural choice is to multiply each basis state with a phase factor corresponding to its position in the unit cell, yielding

$$U = B^\dagger U' B = \begin{pmatrix} 0 & e^{\frac{ik_z}{2}} \\ e^{\frac{ik_z}{2}} & 0 \end{pmatrix} \quad \text{with the transformation} \quad B = \begin{pmatrix} 1 & 0 \\ 0 & e^{-\frac{ik_z}{2}} \end{pmatrix}. \quad (\text{B.6})$$

Since $U \propto U_{\text{perm}}$ all off-diagonal matrix elements of $U^\dagger \frac{dU}{dk_a} \propto \mathbb{1}$ vanish in Eq. B.4 and the Berry curvature transforms like for constant U .

One may also encounter cases, where the Berry curvature is not symmetric, i.e., it does not transform as a pseudovector. This applies, for example, to the magnetic space group 94.130, which is interesting due to the presence of topological nodal planes. The group contains the fourfold screw rotation $C_4^z(\frac{1}{2}, \frac{1}{2}, \frac{1}{2})$. To define a minimal matrix U , we consider the Wyckoff position with two sites $(0, 0, 0)$ and $(\frac{1}{2}, \frac{1}{2}, \frac{1}{2})$ that carry one s orbital each such that the symmetry can be represented as

$$U(\mathbf{k}) = \begin{pmatrix} 0 & e^{i\frac{-k_x+k_y+k_z}{2}} \\ e^{i\frac{k_x+k_y+k_z}{2}} & 0 \end{pmatrix}, \quad (\text{B.7})$$

which can be obtained by considering that by applying $C_4^z(\frac{1}{2}, \frac{1}{2}, \frac{1}{2})$ once to the sites $(0, 0, 0)$ and $(\frac{1}{2}, \frac{1}{2}, \frac{1}{2})$ leads to $(\frac{1}{2}, \frac{1}{2}, \frac{1}{2})$ and $(0, 1, 1) \equiv (0, 0, 0)$, respectively, where the latter equivalence

of sites is up to the translation $T(0, 1, 1)$. The basis is then adjusted to the necessary convention, where the orbital at $(\frac{1}{2}, \frac{1}{2}, \frac{1}{2})$ is multiplied by $e^{-i\frac{k_x+k_y+k_z}{2}}$. The resulting U is also consistent with the action on real space for the repeated application of the symmetry, e.g., $U(\mathbf{k})U(D_U\mathbf{k})$. Note that the matrix U is accompanied by the simultaneous action D_U on the vector \mathbf{k} as shown in Appendix A. Thus, with Eq. B.7 we have identified a case where \tilde{U} is not proportional to unity and the additional terms in Eq. B.4 do not vanish. Note that U can be \mathbf{k} dependent even it represents a symmorphic symmetry, for example, for $C_2^z(0, 0, 0)$ in SG 94.140 with the same choice of the Wyckoff position as above.

In summary, one should not prematurely conclude the transformation properties of the Berry curvature from the underlying crystalline symmetries. While any Weyl points are still related to another by such a symmetry, since the band structure is always symmetric, the relation between the chiralities of such Weyl points cannot be concluded from the present discussion.

C. Tight-binding model for SG 19.27

In this section we describe our four-band model for SG 19.27, which is used to calculate the surface states in Fig. 3.21a1, a2, b1, and b2 [3]. Due to the fourfold point on the $R_1 - U - R$ line, the minimum number of distinct bands is four. Hence, we consider a tight-binding model with four atoms in the unit cell, which are located at the four Wyckoff positions $4a$ of SG 19.27, i.e., at $(0, 0, 0)$, $(1/2, 1/2, 0)$, $(1/2, 0, 1/2)$, and $(0, 1/2, 1/2)$, and which each contribute one s orbital to the band structure. Taking into account only nearest-neighbor hopping terms, the tight-binding Hamiltonian reads

$$H(\mathbf{k}) = \begin{pmatrix} \mu & H_{12} & H_{13} & H_{14} \\ H_{12}^* & \mu & H_{23} & H_{24} \\ H_{13}^* & H_{23}^* & \mu & H_{34} \\ H_{14}^* & H_{24}^* & H_{34}^* & \mu \end{pmatrix}, \quad (\text{C.1})$$

with

$$H_{12} = a_1 + a_1^* e^{ik_y} + a_2 e^{ik_x} + a_2^* e^{i(k_x+k_y)}, \quad H_{13} = a_3(1 + e^{ik_x}) + a_4 e^{ik_z}(1 + e^{ik_x}), \quad (\text{C.2})$$

$$H_{14} = a_5(1 + e^{ik_z}) + a_6 e^{ik_y}(1 + e^{ik_z}), \quad H_{23} = a_6(1 + e^{ik_z}) + a_5 e^{-ik_y}(1 + e^{ik_z}), \quad (\text{C.3})$$

$$H_{24} = a_4(1 + e^{-ik_x}) + a_3 e^{ik_z}(1 + e^{-ik_x}), \quad H_{34} = a_2 + a_2^* e^{ik_y} + a_1 e^{-ik_x} + a_1^* e^{i(-k_x+k_y)} \quad (\text{C.4})$$

where the hopping amplitudes a_i are complex and are arbitrarily chosen to be $a_1 = -0.612421 - 0.386933i$, $a_2 = -0.205746 + 0.0929439i$, $a_3 = -0.940811 - 0.0412139i$, $a_4 = 0.133936 + 0.344822i$, $a_5 = -0.0649457 - 0.529284i$, and $a_6 = -1.051 - 0.111635i$. The chemical potential μ is set to $\mu = 1.06929$.

This model exhibits one Weyl point along the $Y_1-\Gamma-Y$ path and a fourfold crossing point along the R_1-U-R path. As expected along the R_1-U-R path the bands are doubly degenerate, since this path is part of the nodal plane duo, i.e., at the intersection of $k_x = \pi$ and $k_z = \pi$.

D. Tight-binding model for SG 4.9

In the following we state the eight-band tight-binding model used to calculate the Berry curvature with a variable direction of the magnetic field, cf. Fig. 3.22 [3]. We need to find a tight-binding model for SG 4.9 with a variable term for the symmetry breaking. To do so we use SG 19 as a starting point, which explicitly contains the spin degree of freedom. We then add to this model a Zeeman term $H_Z = \mathbf{B} \cdot \sigma$, which lowers the symmetry from SG 19 down to SG 4.9. This allows us to study the effects of Zeeman splitting as a function of field direction \mathbf{B} . Our model contains twelve nearest-neighbor hopping terms with twelve complex hopping parameters. As in Sec. C we consider four atoms in the unit cell, located at the four Wykoff positions $4a$ of SG 19. Each atom at these four Wykoff positions contributes two s orbitals to the band structure, i.e., one for each spin up and spin down. With this, the Hamiltonian $H(\mathbf{k})$ for SG 4.9 can be written as

$$H(\mathbf{k}) = \begin{pmatrix} H_{\uparrow}(\mathbf{k}) & H^{\text{SOC}}(\mathbf{k}) \\ H^{\text{SOC}}(\mathbf{k})^{\dagger} & H_{\downarrow}(\mathbf{k}) \end{pmatrix} + \mathbf{B} \cdot \sigma \otimes \mathbb{1}_{4 \times 4}, \quad (\text{D.1})$$

where $H_{\downarrow}(\mathbf{k}) = H_{\uparrow}(-\mathbf{k})^*$, σ is the vector of Pauli matrices operating in spin space, and \mathbf{B} is the magnetic field vector. $H_{\uparrow}(\mathbf{k})$ has a similar structure as Eq. (C.1), i.e.,

$$H_{\uparrow}(\mathbf{k}) = \begin{pmatrix} 0 & H_{12}^{\uparrow} & H_{13}^{\uparrow} & H_{14}^{\uparrow} \\ H_{12}^{\uparrow*} & 0 & H_{23}^{\uparrow} & H_{24}^{\uparrow} \\ H_{13}^{\uparrow*} & H_{23}^{\uparrow*} & 0 & H_{34}^{\uparrow} \\ H_{14}^{\uparrow*} & H_{24}^{\uparrow*} & H_{34}^{\uparrow*} & 0 \end{pmatrix}, \quad (\text{D.2})$$

with

$$H_{12}^{\uparrow} = b_1 + b_1 e^{ik_x} + b_2 e^{ik_y} + b_2 e^{i(k_x+k_y)}, \quad H_{13}^{\uparrow} = b_3 + b_3^* e^{ik_z} + b_4 e^{ik_x} + b_4^* e^{i(k_x+k_z)}, \quad (\text{D.3})$$

$$H_{14}^{\uparrow} = b_5 + b_5 e^{ik_y} + b_6 e^{ik_z} + b_6 e^{i(k_y+k_z)}, \quad H_{23}^{\uparrow} = b_6^* + b_6^* e^{-ik_y} + b_5^* e^{ik_z} + b_5^* e^{-i(k_y-k_z)}, \quad (\text{D.4})$$

$$H_{24}^{\uparrow} = b_4 + b_4^* e^{ik_z} + b_3 e^{-ik_x} + b_3^* e^{-i(k_x-k_z)}, \quad H_{34}^{\uparrow} = b_2 + b_2 e^{-ik_x} + b_1 e^{ik_y} + b_1 e^{-i(k_x-k_y)}, \quad (\text{D.5})$$

where b_i are complex hopping amplitudes, which we arbitrarily set to $b_1 = -0.430005 - 0.818889i$, $b_2 = 0.139629 - 0.587502i$, $b_3 = 1.00815 - 0.17464i$, $b_4 = 0.0620589 - 0.0593171i$, $b_5 =$

$-0.226315 + 0.64551i$, and $b_6 = -0.326725 + 0.76938i$. The two spin sectors are coupled to each other via spin-orbit coupling

$$H_{\text{SOC}}(\mathbf{k}) = \begin{pmatrix} 0 & H_{12}^{\text{SOC}}(\mathbf{k}) & H_{13}^{\text{SOC}}(\mathbf{k}) & H_{14}^{\text{SOC}}(\mathbf{k}) \\ -H_{12}^{\text{SOC}}(-\mathbf{k}) & 0 & H_{23}^{\text{SOC}}(\mathbf{k}) & H_{24}^{\text{SOC}}(\mathbf{k}) \\ -H_{13}^{\text{SOC}}(-\mathbf{k}) & -H_{23}^{\text{SOC}}(-\mathbf{k}) & 0 & H_{34}^{\text{SOC}}(\mathbf{k}) \\ -H_{14}^{\text{SOC}}(-\mathbf{k}) & -H_{24}^{\text{SOC}}(-\mathbf{k}) & -H_{34}^{\text{SOC}}(-\mathbf{k}) & 0 \end{pmatrix}, \quad (\text{D.6})$$

with

$$H_{12}^{\text{SOC}} = c_1 + c_1^* e^{ik_x} + c_2^* e^{ik_y} + c_2 e^{i(k_x+k_y)}, \quad H_{13}^{\text{SOC}} = c_3 + c_3 e^{ik_z} + c_4 e^{ik_x} + c_4 e^{i(k_x+k_z)} \quad (\text{D.7})$$

$$H_{14}^{\text{SOC}} = c_5 - c_5^* e^{ik_y} - c_6^* e^{ik_z} + c_6 e^{i(k_y+k_z)}, \quad H_{23}^{\text{SOC}} = c_6 - c_6^* e^{-ik_y} - c_5^* e^{ik_z} + c_5 e^{-i(k_y-k_z)} \quad (\text{D.8})$$

$$H_{24}^{\text{SOC}} = -c_4^* - c_4^* e^{ik_z} - c_3^* e^{-ik_x} - c_3 e^{-i(k_x-k_z)}, \quad H_{34}^{\text{SOC}} = -c_2^* - c_2 e^{-ik_x} - c_1 e^{ik_y} - c_1^* e^{-i(k_x+k_y)} \quad (\text{D.9})$$

where c_i are spinflip hopping parameters, which we arbitrarily set to $c_1 = -0.0673999 - 0.0654125i$, $c_2 = 0.895971 + 0.223187i$, $c_3 = 0.397634 + 0.222339i$, $c_4 = -0.0167943 + 0.100792i$, $c_5 = 0.388337 - 0.727044i$, and $c_6 = 0.180885 - 0.0104037i$.

E. Tight-binding model for Eu_3PbO

To construct a tight-binding model for Eu_3PbO we follow the works by Kariyado and Ogata [252] and Chiu *et al.* [259]. In Ref. [259] a nine-band model for Ca_3PbO with three Pb- p orbitals and six Ca- d orbitals was constructed. This model faithfully captures the low-energy physics of Ca_3PbO . In particular, it exhibits six gapped Dirac cones along the $\Gamma - X$ direction with a non-zero mirror Chern number, in full agreement with the *ab-initio* DFT calculations. In the following we describe how this model can be adapted to the case of Eu_3PbO , both for the paramagnetic phase and the magnetically ordered phases.

Paramagnetic phase

The paramagnetic phase of Eu_3PbO can be described by the same model as in Ref. [259], albeit with different parameter values, since its band structure is qualitatively similar to Ca_3PbO . In the absence of spin-orbit coupling, this tight-binding model is written as $\mathcal{H}_{\text{PM}} = \sum_{\mathbf{k}} \psi_{\mathbf{k}}^\dagger H_{\text{PM}}(\mathbf{k}) \psi_{\mathbf{k}}$

with the nine-component spinor

$$\psi_{\mathbf{k}} = (\text{Pb}_{p_x}, \quad \text{Pb}_{p_y}, \quad \text{Pb}_{p_z}, \\ \text{Eu}_{d_{y^2-z^2}}^1, \quad \text{Eu}_{d_{z^2-x^2}}^2, \quad \text{Eu}_{d_{x^2-y^2}}^3, \\ \text{Eu}_{d_{yz}}^1, \quad \text{Eu}_{d_{zx}}^2, \quad \text{Eu}_{d_{xy}}^3)^T$$

and the 9×9 matrix $H_{\text{PM}}(\mathbf{k})$ with block form

$$H_{\text{PM}}(\mathbf{k}) = \begin{pmatrix} H_p & V_{dp}^u & V_{dp}^l \\ V_{dp}^{u\dagger} & H_d^u & 0 \\ V_{dp}^{l\dagger} & 0 & H_d^l \end{pmatrix}. \quad (\text{E.1})$$

The blocks of $H_{\text{PM}}(\mathbf{k})$ are given by

$$H_p = \begin{pmatrix} e_p - 2t_{pp}c_{2x} & 0 & 0 \\ 0 & e_p - 2t_{pp}c_{2y} & 0 \\ 0 & 0 & e_p - 2t_{pp}c_{2z} \end{pmatrix}, \quad (\text{E.2})$$

$$H_d^u = \begin{pmatrix} e_d & -4t_{dd}c_xc_y & -4t_{dd}c_zc_x \\ -4t_{dd}c_xc_y & e_d & -4t_{dd}c_yc_z \\ -4t_{dd}c_zc_x & -4t_{dd}c_yc_z & e_d \end{pmatrix}, \quad (\text{E.3})$$

and $H_d^l = e_d \mathbb{1}_3$, with $\mathbb{1}_3$ the 3×3 identity matrix. The coupling matrices between Pb- p and Eu- d orbitals read

$$V_{dp}^u = 4it_{pd} \begin{pmatrix} 0 & c_zs_x & -c_ys_x \\ -c_zs_y & 0 & c_xs_y \\ c_ys_z & -c_xs_z & 0 \end{pmatrix}, \\ V_{dp}^l = 4it_{pd} \begin{pmatrix} 0 & c_xs_z & c_xs_y \\ c_ys_z & 0 & c_ys_x \\ c_zs_y & c_zs_x & 0 \end{pmatrix}, \quad (\text{E.4})$$

where we have used the abbreviations $c_i = \cos \frac{k_i}{2}$, $s_i = \sin \frac{k_i}{2}$, and $c_{2i} = \cos k_i$.

To lowest order, spin-orbit coupling enters as an on-site term in the tight-binding Hamiltonian (E.1). For the Pb- p orbitals the on-site spin-orbit coupling reads $\sum_{\mathbf{k}} \psi_p^\dagger(\mathbf{k}) H_{\text{SO}}^p(\mathbf{k}) \psi_p(\mathbf{k})$ with the spinor

$$\psi_p(\mathbf{k}) = (\text{Pb}_{p_x}^\uparrow, \text{Pb}_{p_y}^\uparrow, \text{Pb}_{p_z}^\uparrow, \text{Pb}_{p_x}^\downarrow, \text{Pb}_{p_y}^\downarrow, \text{Pb}_{p_z}^\downarrow)$$

and

$$H_{\text{SO}}^p(\mathbf{k}) = \frac{\lambda_p}{2} \begin{pmatrix} 0 & -i & 0 & 0 & 0 & 1 \\ i & 0 & 0 & 0 & 0 & -i \\ 0 & 0 & 0 & -1 & i & 0 \\ 0 & 0 & -1 & 0 & i & 0 \\ 0 & 0 & -i & -i & 0 & 0 \\ 1 & i & 0 & 0 & 0 & 0 \end{pmatrix}.$$

The on-site spin-orbit coupling for the Eu- d orbitals is $\sum_{\mathbf{k}} \psi_d^\dagger(\mathbf{k}) H_{\text{SO}}^d(\mathbf{k}) \psi_d(\mathbf{k})$ with the vector

$$\begin{aligned} \psi_d(\mathbf{k}) = & (\text{Eu}_{d_{y^2-z^2}}^{1,\uparrow}, \text{Eu}_{d_{z^2-x^2}}^{2,\uparrow}, \text{Eu}_{d_{x^2-y^2}}^{3,\uparrow}, \text{Eu}_{d_{y^2-z^2}}^{1,\downarrow}, \text{Eu}_{d_{z^2-x^2}}^{2,\downarrow}, \text{Eu}_{d_{x^2-y^2}}^{3,\downarrow}, \\ & \text{Eu}_{d_{yz}}^{1,\uparrow}, \text{Eu}_{d_{zx}}^{2,\uparrow}, \text{Eu}_{d_{xy}}^{3,\uparrow}, \text{Eu}_{d_{yz}}^{1,\downarrow}, \text{Eu}_{d_{zx}}^{2,\downarrow}, \text{Eu}_{d_{xy}}^{3,\downarrow})^T, \end{aligned}$$

and

$$\begin{aligned} H_{\text{SO}}^d(\mathbf{k}) = & \lambda_d \tau_y \otimes \left\{ \sigma_x \otimes \begin{pmatrix} 1 & 0 & 0 \\ 0 & 0 & 0 \\ 0 & 0 & 0 \end{pmatrix} \right. \\ & \left. + \sigma_y \otimes \begin{pmatrix} 0 & 0 & 0 \\ 0 & 1 & 0 \\ 0 & 0 & 0 \end{pmatrix} + \sigma_z \otimes \begin{pmatrix} 0 & 0 & 0 \\ 0 & 0 & 0 \\ 0 & 0 & 1 \end{pmatrix} \right\}, \end{aligned} \quad (\text{E.5})$$

where τ_β and σ_α operate in the d -orbital ($d_{x_i^2-x_j^2}$ and $d_{x_i x_j}$) and spin (\uparrow and \downarrow) degree of freedom, respectively. Combining these spin-orbit coupling terms with Eq. (E.1), we obtain the full tight-binding Hamiltonian for the paramagnetic phase of Eu_3PbO

$$H_{\text{PM}}^{\text{tot}}(\mathbf{k}) = \begin{pmatrix} H_p^{\text{tot}}(\mathbf{k}) & V_{\text{tot}}(\mathbf{k}) \\ V_{\text{tot}}^\dagger(\mathbf{k}\hat{E}) & H_d^{\text{tot}}(\mathbf{k}) \end{pmatrix} + \mu \mathbb{1}_{18}, \quad (\text{E.6})$$

with

$$H_p^{\text{tot}}(\mathbf{k}) = \begin{pmatrix} H_p & 0 \\ 0 & H_p \end{pmatrix} + H_{\text{SO}}^p(\mathbf{k}), \quad (\text{E.7})$$

$$H_d^{\text{tot}}(\mathbf{k}) = \begin{pmatrix} \sigma_0 \otimes H_d^u & 0 \\ 0 & \sigma_0 \otimes H_d^l \end{pmatrix} + H_{\text{SO}}^d(\mathbf{k}),$$

and

$$V_{\text{tot}}(\mathbf{k}) = \left(\sigma_0 \otimes V_{dp}^u \quad \sigma_0 \otimes V_{dp}^l \right).$$

The outermost grading of H_p^{tot} and σ_0 in Eq. (E.7) corresponds to the spin grading. In Eq. (E.6) a diagonal term $\mu\mathbb{1}_{18}$ for the chemical potential has been added.

We have determined the nine parameters of the above tight-binding model by a fit to the *ab-initio* DFT band structure, which yields

$$\begin{aligned} e_p &= 0.0, & e_d &= 2.4, & t_{pp} &= -0.4, & t_{dd} &= -0.4, \\ t_{pd} &= -0.4, & \lambda_p &= 0.75, & \lambda_d &= 0.07, & \mu &= 0.87. \end{aligned}$$

Magnetic phases

To describe the Eu magnetic moments we introduce the magnetic splitting derived by the DFT calculations as Zeeman terms $H_{Zee,n}$ for each orbital n into the tight-binding model as

$$H_{Zee,n} = \begin{pmatrix} \sigma_x \\ \sigma_y \\ \sigma_z \end{pmatrix} \cdot \mathbf{B}_n |n\rangle \langle n|, \quad (\text{E.8})$$

where $|n\rangle \langle n|$ is the projector onto the orbitals n without spin degree of freedom. The Pauli matrices σ_i describe the spin degree of freedom and \mathbf{B}_n is the magnetic splitting energy.

The magnitude of the splitting energy \mathbf{B}_n for the different orbitals is determined from the DFT calculations of the ferromagnetic phase. For the other magnetic phases we then assume that the splitting vector \mathbf{B}_n reorients according to the respective magnetic structure, but does not change its magnitude. We have checked that this procedure leads to a tight-binding band structure that is qualitatively similar to the DFT electronic bands.

Ferromagnetic phase

In the ferromagnetic phase all moments are aligned collinearly. Therefore, also \mathbf{B} points in the same direction $\hat{\mathbf{B}}$ at all sites and we can write $\mathbf{B}_n = B_n \hat{\mathbf{B}}$. By comparing to DFT calculations, we find that the magnetic splitting B_n of the different orbitals are

$$B_{\text{Eu}} = 0.43 \text{ eV}, \quad B_{\text{Pb}} = -0.035 \text{ eV}, \quad (\text{E.9})$$

which corresponds to half the total energy splitting, as read out from the DFT band structures.

In the ferromagnetic phase the magnetization direction $\hat{\mathbf{B}}$ can be easily aligned by the external field. As explained in the main text, the topology of the electronic bands changes with magnetization direction. In particular, the position of the Weyl points, both in energy and momentum, as well as their multiplicities depend strongly on the magnetization direction. This is shown in Table A1 for the three magnetization directions [100], [110], and [111], see also

Fig. 3.25 in the main text. Note that the Weyl points W1 only exist for the [110] and [111] magnetizations, but are absent for the [100] magnetization. For the [110] magnetization W1 has multiplicity 4, i.e., there are two pairs of Weyl points, one close to the k_x axis and another one close to the k_y axis. For the [111] magnetization there are six Weyl points W1, as the symmetry is higher. I.e., there is one pair of Weyl points close to each of the three main axes k_x , k_y , and k_z . Similarly, the multiplicity of the Weyl points W2 and W3 is only 4 for the [110] magnetization, while it is 6 for the [111] magnetization. The Weyl nodal lines L2 and L1' for the [100] magnetization have multiplicity 1, as they connect the four half axes $\pm k_y$ and $\pm k_z$. For the nodal lines appearing at a magnetization in [100] and [110] direction the largest extension along one of the equivalent axes is given in the table as position. For the [110] magnetization the Weyl points W4 have also multiplicity 4, but now they are located close to the k_z axis, one pair with positive k_z and one pair with negative k_z .

Antiferromagnetic phase

The magnetic space group of the AFM phase is $P1a\bar{3}$ (No. 205.36, type IV). The unit cell is eightfold enlarged as compared to the paramagnetic phase. I.e., it is doubled in each of the three main axes x , y , and z . This leads to an eightfold back folding of the bands, and hence the tight-binding model of the AFM phase has $8 \times 18 = 144$ bands (including spin). Correspondingly, there are eight times more orbitals in the tight-binding model, leading to an 144×144 tight-binding Hamiltonian. The hopping parameters for this enlarged Hamiltonian can be determined in an automatized fashion directly in momentum space from the tight-binding model of the paramagnetic phase, Eq. (E.6). For that purpose, we first perform a unitary transformation of Hamiltonian (E.6) in order to simplify its momentum dependence. This transformation amounts to multiplying the Pb- p orbitals by $e^{i(k_x+k_y+k_z)/2}$, the Eu^1 - d orbitals by $e^{ik_x/2}$, the Eu^2 - d orbitals by $e^{ik_y/2}$, and the Eu^3 - d orbitals by $e^{ik_z/2}$. With this, all the terms in Eq. (E.6) of the form $e^{ik_n/2}$ are transformed into terms with e^{ik_n} or terms that are independent of k_n . Now, we can start to construct the tight-binding Hamiltonian for the AFM phase, which has

phase	position	E (eV)	type	top. inv.	#
FM [100]	(0.18, 0, 0)	-0.16	WP (W2)	Chern	2
FM [100]	(0.12, 0, 0)	-0.33	WP (W3)	Chern	2
FM [100]	(0, 0, 0.13)	-0.31	Line (L2)	Berry	1
FM [100]	(0, 0, 0.21)	-0.02	Line (L1')	Berry	1
FM [110]	(0.23, 0.015, 0)	0.06	WP (W1)	Chern	4
FM [110]	(0.19, -0.001, 0)	-0.12	WP (W2)	Chern	4
FM [110]	(0.12, 0, 0)	-0.32	WP (W3)	Chern	4
FM [110]	(0.003, 0.003, 0.13)	-0.31	WP (W4)	Chern	4
FM [110]	(110)-plane	-0.02	Line (L1)	Berry	1
FM [111]	(0.23, 0.008, 0.008)	0.05	WP (W1)	Chern	6
FM [111]	(0.2, -0.001, -0.001)	-0.09	WP (W2)	Chern	6
FM [111]	(0.13, 0, 0)	-0.31	WP (W3)	Chern	6

Table A1.: Weyl points of the ferromagnetic phase in different field orientations. This table lists the positions and energies of the topological band crossings in the first Brillouin zone (BZ) for the ferromagnetic phase with magnetization in [100], [110], and [111] direction (FM [100], FM [110], and FM [111], respectively). The positions of the band crossings $\mathbf{k} = (k_x, k_y, k_z)$ are given in units of $2\pi/a_i$, where a_i denotes the lattice constant of the respective real space direction. All energies are given in eV relative to the Fermi energy. The type of band crossing is indicated in the fourth column, while the fifth column states the topological invariant that protects the crossings. The last column gives the multiplicity of the crossings, i.e., the number of symmetry related crossings at the same energy.

a block structure with 8×8 blocks, where each block is an 18×18 matrix, i.e.,

$$H_{\text{AFM}}(\mathbf{k}) = \begin{pmatrix} H_{000} & H_x(\mathbf{k}) & H_y(\mathbf{k}) & H_{xy}(\mathbf{k}) & H_z(\mathbf{k}) & H_{xz}(\mathbf{k}) & H_{yz}(\mathbf{k}) & 0 \\ & H_{100} & H_y^x(\mathbf{k}) & H_y(\mathbf{k}) & H_x^z(\mathbf{k}) & H_z(\mathbf{k}) & 0 & H_{yz}(\mathbf{k}) \\ & & H_{010} & H_x(\mathbf{k}) & H_z^y(\mathbf{k}) & 0 & H_z(\mathbf{k}) & H_{xz}(\mathbf{k}) \\ & & & H_{110} & 0 & H_z^y(\mathbf{k}) & H_x^z(\mathbf{k}) & H_z(\mathbf{k}) \\ & & & & H_{001} & H_x(\mathbf{k}) & H_y(\mathbf{k}) & H_{xy}(\mathbf{k}) \\ & & H.C. & & & H_{101} & H_y^x(\mathbf{k}) & H_y(\mathbf{k}) \\ & & & & & & H_{011} & H_x(\mathbf{k}) \\ & & & & & & & H_{111} \end{pmatrix}. \quad (\text{E.10})$$

The 18×18 matrices H_{abc} (with $a, b, c \in \{0, 1\}$) on the diagonal describe hoppings within each of the eight paramagnetic unit cells. The off-diagonal entries $H_x, H_y, H_z, H_{xy}, H_{xz}, H_{yz}, H_y^x, H_x^z,$

and H_z^y describe hoppings that connect different paramagnetic unit cells. These hopping terms are modified by exponential factors e^{ik_n} , since they connect different paramagnetic unit cells.

So far, Eq. (E.10) represents just an artificial increase of the Hamiltonian, that trivially leads to folded bands. But now, we introduce the magnetic splitting $\mathbf{B}_i = B_{\text{Eu}}\hat{\mathbf{B}}_i$ to represent the antiferromagnetically ordered Eu moments. These splitting energies are added to the diagonal blocks H_{abc} in Eq. (E.10) and have all the same magnitude

$$B_{\text{Eu}} = 0.45 \text{ eV}. \quad (\text{E.11})$$

The orientation of the $\hat{\mathbf{B}}_i$ vectors on the different Eu sites is determined by the AFM ordering pattern, as determined in the neutron diffraction experiment. We can implement this pattern in the following way

$$\begin{aligned} \hat{\mathbf{B}}_{\text{Eu}^1} &= \frac{1}{\sqrt{2}}(0, (-1)^a, (-1)^b), \\ \hat{\mathbf{B}}_{\text{Eu}^2} &= \frac{1}{\sqrt{2}}((-1)^c, (-1)^a, 0), \\ \hat{\mathbf{B}}_{\text{Eu}^3} &= \frac{1}{\sqrt{2}}((-1)^c, 0, (-1)^b), \end{aligned} \quad (\text{E.12})$$

where the indices $a, b, c \in \{0, 1\}$ label the eight different paramagnetic unit cells.

Bibliography

- [1] Y.-H. Chan, Berkay Kilic, Moritz M. Hirschmann, Ching-Kai Chiu, Leslie M. Schoop, Darshan G. Joshi, and Andreas P. Schnyder. Symmetry-enforced band crossings in trigonal materials: Accordion states and Weyl nodal lines. *Phys. Rev. Materials*, 3:124204, Dec 2019.
- [2] Moritz M. Hirschmann, Andreas Leonhardt, Berkay Kilic, Douglas H. Fabini, and Andreas P. Schnyder. Symmetry-enforced band crossings in tetragonal materials: Dirac and Weyl degeneracies on points, lines, and planes. *Phys. Rev. Materials*, 5:054202, May 2021.
- [3] Marc A. Wilde, Matthias Doderhöft, Arthur Niedermayr, Andreas Bauer, Moritz M. Hirschmann, Kirill Alpin, Andreas P. Schnyder, and Christian Pfleiderer. Symmetry-enforced topological nodal planes at the Fermi surface of a chiral magnet. *Nature*, 594(7863):374–379, 2021.
- [4] Nico Huber, Kirill Alpin, Grace L. Causer, Lukas Worch, Andreas Bauer, Georg Benka, Moritz M. Hirschmann, Andreas P. Schnyder, Christian Pfleiderer, and Marc A. Wilde. Network of topological nodal planes, multifold degeneracies, and Weyl points in CoSi. *arXiv preprint arXiv:2107.02820*, 2021.
- [5] Moritz M. Hirschmann, Alex S. Gibbs, Fabio Orlandi, Dmitry Khalyavin, Pascal Manuel, Vahideh Abdolazimi, Alexander Yaresko, Jürgen Nuss, Hidenori Takagi, Andreas W. Rost, and Andreas P. Schnyder. To be submitted.
- [6] Huimei Liu, Moritz M. Hirschmann, Andreas P. Schnyder, George A. Sawatzky, and Giniyat Khaliullin. Tunable correlated topological phases in SmB₆. In preparation.
- [7] W. B. Rui, Song-Bo Zhang, Moritz M. Hirschmann, Zhen Zheng, Andreas P. Schnyder, Björn Trauzettel, and Z. D. Wang. Higher-order Weyl superconductors with anisotropic Weyl-point connectivity. *Phys. Rev. B*, 103:184510, May 2021.

- [8] Henri Menke and Moritz M. Hirschmann. Topological quantum wires with balanced gain and loss. *Phys. Rev. B*, 95:174506, May 2017.
- [9] W. B. Rui, Moritz M. Hirschmann, and Andreas P. Schnyder. \mathcal{PT} -symmetric non-Hermitian Dirac semimetals. *Phys. Rev. B*, 100:245116, Dec 2019.
- [10] Conyers Herring. Accidental degeneracy in the energy bands of crystals. *Physical Review*, 52(4):365, 1937.
- [11] Johann von Neumann and Eugene P Wigner. Über das Verhalten von Eigenwerten bei adiabatischen Prozessen. In *The Collected Works of Eugene Paul Wigner*, pages 294–297. Springer, 1993.
- [12] Paul Adrien Maurice Dirac. The quantum theory of the electron. *Proceedings of the Royal Society of London. Series A, Containing Papers of a Mathematical and Physical Character*, 117(778):610–624, 1928.
- [13] Andrei Bernevig, Hongming Weng, Zhong Fang, and Xi Dai. Recent progress in the study of topological semimetals. *Journal of the Physical Society of Japan*, 87(4):041001, 2018.
- [14] Carl D. Anderson. The Positive Electron. *Phys. Rev.*, 43:491–494, Mar 1933.
- [15] Hermann Weyl. Elektron und gravitation. I. *Zeitschrift für Physik*, 56(5-6):330–352, 1929.
- [16] Y. Fukuda, T. Hayakawa, E. Ichihara, K. Inoue, K. Ishihara, H. Ishino, Y. Itow, T. Kajita, J. Kameda, S. Kasuga, K. Kobayashi, Y. Kobayashi, Y. Koshio, M. Miura, M. Nakahata, S. Nakayama, A. Okada, K. Okumura, N. Sakurai, M. Shiozawa, Y. Suzuki, Y. Takeuchi, Y. Totsuka, S. Yamada, M. Earl, A. Habig, E. Kearns, M. D. Messier, K. Scholberg, J. L. Stone, L. R. Sulak, C. W. Walter, M. Goldhaber, T. Barszczak, D. Casper, W. Gajewski, P. G. Halverson, J. Hsu, W. R. Kropp, L. R. Price, F. Reines, M. Smy, H. W. Sobel, M. R. Vagins, K. S. Ganezer, W. E. Keig, R. W. Ellsworth, S. Tasaka, J. W. Flanagan, A. Kibayashi, J. G. Learned, S. Matsuno, V. J. Stenger, D. Takemori, T. Ishii, J. Kanzaki, T. Kobayashi, S. Mine, K. Nakamura, K. Nishikawa, Y. Oyama, A. Sakai, M. Sakuda, O. Sasaki, S. Echigo, M. Kohama, A. T. Suzuki, T. J. Haines, E. Blaufuss, B. K. Kim, R. Sanford, R. Svoboda, M. L. Chen, Z. Conner, J. A. Goodman, G. W. Sullivan, J. Hill, C. K. Jung, K. Martens, C. Mauger, C. McGrew, E. Sharkey, B. Viren, C. Yanagisawa, W. Doki, K. Miyano, H. Okazawa, C. Saji, M. Takahata, Y. Nagashima, M. Takita,

- T. Yamaguchi, M. Yoshida, S. B. Kim, M. Etoh, K. Fujita, A. Hasegawa, T. Hasegawa, S. Hatakeyama, T. Iwamoto, M. Koga, T. Maruyama, H. Ogawa, J. Shirai, A. Suzuki, F. Tsushima, M. Koshihara, M. Nemoto, K. Nishijima, T. Futagami, Y. Hayato, Y. Kanaya, K. Kaneyuki, Y. Watanabe, D. Kielczewska, R. A. Doyle, J. S. George, A. L. Stachyra, L. L. Wai, R. J. Wilkes, and K. K. Young. Evidence for Oscillation of Atmospheric Neutrinos. *Phys. Rev. Lett.*, 81:1562–1567, Aug 1998.
- [17] K Nakamura, ST Petcov, et al. Neutrino masses, mixing, and oscillations. 2018.
- [18] Xiangang Wan, Ari M. Turner, Ashvin Vishwanath, and Sergey Y. Savrasov. Topological semimetal and Fermi-arc surface states in the electronic structure of pyrochlore iridates. *Phys. Rev. B*, 83:205101, May 2011.
- [19] Alexey A Soluyanov, Dominik Gresch, Zhijun Wang, QuanSheng Wu, Matthias Troyer, Xi Dai, and B Andrei Bernevig. Type-ii weyl semimetals. *Nature*, 527(7579):495–498, 2015.
- [20] Zhijun Wang, Dominik Gresch, Alexey A. Soluyanov, Weiwei Xie, S. Kushwaha, Xi Dai, Matthias Troyer, Robert J. Cava, and B. Andrei Bernevig. MoTe₂: A Type-II Weyl Topological Metal. *Phys. Rev. Lett.*, 117:056805, Jul 2016.
- [21] Holger Bech Nielsen and Masao Ninomiya. No-go theorem for regularizing chiral fermions. Technical report, Science Research Council, 1981.
- [22] A. A. Zyuzin and A. A. Burkov. Topological response in Weyl semimetals and the chiral anomaly. *Phys. Rev. B*, 86:115133, Sep 2012.
- [23] Jan Behrends, Jun-Won Rhim, Shang Liu, Adolfo G Grushin, and Jens H Bardarson. Nodal-line semimetals from Weyl superlattices. *Physical Review B*, 96(24):245101, 2017.
- [24] Xiao-Qi Sun, Shou-Cheng Zhang, and Tomáš Bzdušek. Conversion rules for Weyl points and nodal lines in topological media. *Physical review letters*, 121(10):106402, 2018.
- [25] Motoaki Hirayama, Ryo Okugawa, Takashi Miyake, and Shuichi Murakami. Topological Dirac nodal lines and surface charges in fcc alkaline earth metals. *Nature communications*, 8(1):1–9, 2017.
- [26] Si Li, Ying Liu, Shan-Shan Wang, Zhi-Ming Yu, Shan Guan, Xian-Lei Sheng, Yugui Yao, and Shengyuan A Yang. Nonsymmorphic-symmetry-protected hourglass Dirac

- loop, nodal line, and Dirac point in bulk and monolayer $X_3\text{SiTe}_6$ ($X = \text{Ta}, \text{Nb}$). *Physical Review B*, 97(4):045131, 2018.
- [27] Meng Xiao and Shanhui Fan. Topologically charged nodal surface. *arXiv preprint arXiv:1709.02363*, 2017.
- [28] Tomáš Bzdušek and Manfred Sigrist. Robust doubly charged nodal lines and nodal surfaces in centrosymmetric systems. *Physical Review B*, 96(15):155105, 2017.
- [29] Oğuz Türker and Sergej Moroz. Weyl nodal surfaces. *Physical Review B*, 97(7):075120, 2018.
- [30] Weikang Wu, Ying Liu, Si Li, Chengyong Zhong, Zhi-Ming Yu, Xian-Lei Sheng, YX Zhao, and Shengyuan A Yang. Nodal surface semimetals: Theory and material realization. *Physical Review B*, 97(11):115125, 2018.
- [31] Naoto Nagaosa, Takahiro Morimoto, and Yoshinori Tokura. Transport, magnetic and optical properties of Weyl materials. *Nature Reviews Materials*, 5(8):621–636, 2020.
- [32] Gerd Czycholl. *Theoretische Festkörperphysik: von den klassischen Modellen zu modernen Forschungsthemen*. Springer-Verlag, 2007.
- [33] Lars Fritz, Jörg Schmalian, Markus Müller, and Subir Sachdev. Quantum critical transport in clean graphene. *Phys. Rev. B*, 78:085416, Aug 2008.
- [34] Pavan Hosur, SA Parameswaran, and Ashvin Vishwanath. Charge transport in Weyl semimetals. *Physical review letters*, 108(4):046602, 2012.
- [35] Pavan Hosur, Siddharth A. Parameswaran, and Ashvin Vishwanath. Erratum: Charge Transport in Weyl Semimetals [Phys. Rev. Lett. 108, 046602 (2012)]. *Phys. Rev. Lett.*, 123:079901, Aug 2019.
- [36] Prachi Telang, Kshiti Mishra, Giacomo Prando, AK Sood, and Surjeet Singh. Anomalous lattice contraction and emergent electronic phases in Bi-doped $\text{Eu}_2\text{Ir}_2\text{O}_7$. *Physical Review B*, 99(20):201112, 2019.
- [37] Hui Li, Hongtao He, Hai-Zhou Lu, Huachen Zhang, Hongchao Liu, Rong Ma, Zhiyong Fan, Shun-Qing Shen, and Jiannong Wang. Negative magnetoresistance in dirac semimetal Cd_3As_2 . *Nature communications*, 7(1):1–7, 2016.

- [38] Cai-Zhen Li, Li-Xian Wang, Haiwen Liu, Jian Wang, Zhi-Min Liao, and Da-Peng Yu. Giant negative magnetoresistance induced by the chiral anomaly in individual Cd_3As_2 nanowires. *Nature communications*, 6(1):1–7, 2015.
- [39] A. A. Burkov, M. D. Hook, and Leon Balents. Topological nodal semimetals. *Phys. Rev. B*, 84:235126, Dec 2011.
- [40] Bitan Roy, Pallab Goswami, and Vladimir Juričić. Interacting Weyl fermions: Phases, phase transitions, and global phase diagram. *Phys. Rev. B*, 95:201102, May 2017.
- [41] A. H. Castro Neto, F. Guinea, N. M. R. Peres, K. S. Novoselov, and A. K. Geim. The electronic properties of graphene. *Rev. Mod. Phys.*, 81:109–162, Jan 2009.
- [42] S. A. Parameswaran, T. Grover, D. A. Abanin, D. A. Pesin, and A. Vishwanath. Probing the Chiral Anomaly with Nonlocal Transport in Three-Dimensional Topological Semimetals. *Phys. Rev. X*, 4:031035, Sep 2014.
- [43] Holger Bech Nielsen and Masao Ninomiya. The Adler-Bell-Jackiw anomaly and Weyl fermions in a crystal. *Physics Letters B*, 130(6):389–396, 1983.
- [44] D. T. Son and B. Z. Spivak. Chiral anomaly and classical negative magnetoresistance of Weyl metals. *Phys. Rev. B*, 88:104412, Sep 2013.
- [45] Vivek Aji. Adler-Bell-Jackiw anomaly in Weyl semimetals: Application to pyrochlore iridates. *Phys. Rev. B*, 85:241101, Jun 2012.
- [46] Frank Arnold, Chandra Shekhar, Shu-Chun Wu, Yan Sun, Ricardo Donizeth Dos Reis, Nitesh Kumar, Marcel Naumann, Mukkattu O Ajeesh, Marcus Schmidt, Adolfo G Grushin, et al. Negative magnetoresistance without well-defined chirality in the Weyl semimetal TaP. *Nature communications*, 7(1):1–7, 2016.
- [47] Yuanbo Zhang, Yan-Wen Tan, Horst L Stormer, and Philip Kim. Experimental observation of the quantum Hall effect and Berry’s phase in graphene. *nature*, 438(7065):201–204, 2005.
- [48] Enke Liu, Yan Sun, Nitesh Kumar, Lukas Muechler, Aili Sun, Lin Jiao, Shuo-Ying Yang, Defa Liu, Aiji Liang, Qiunan Xu, et al. Giant anomalous Hall effect in a ferromagnetic kagome-lattice semimetal. *Nature physics*, 14(11):1125–1131, 2018.
- [49] Hung-Yu Yang, Bahadur Singh, Baozhu Lu, Cheng-Yi Huang, Faranak Bahrami, Wei-Chi Chiu, David Graf, Shin-Ming Huang, Baokai Wang, Hsin Lin, et al. Transition

- from intrinsic to extrinsic anomalous Hall effect in the ferromagnetic Weyl semimetal $\text{PrAlGe}_{1-x}\text{Si}_x$. *APL Materials*, 8(1):011111, 2020.
- [50] WB Rui, YX Zhao, and Andreas P Schnyder. Topological transport in Dirac nodal-line semimetals. *Physical Review B*, 97(16):161113, 2018.
- [51] Muhammad Ikhlas, Takahiro Tomita, Takashi Koretsune, Michi-To Suzuki, Daisuke Nishio-Hamane, Ryotaro Arita, Yoshichika Otani, and Satoru Nakatsuji. Large anomalous Nernst effect at room temperature in a chiral antiferromagnet. *Nature Physics*, 13(11):1085–1090, 2017.
- [52] E. J. König, H.-Y. Xie, D. A. Pesin, and A. Levchenko. Photogalvanic effect in Weyl semimetals. *Phys. Rev. B*, 96:075123, Aug 2017.
- [53] Judit Sári, Csaba Tóke, and Mark O Goerbig. Magnetoplasmons of the tilted anisotropic Dirac cone material α -(BEDT-TTF) $_2$ I $_3$. *Physical Review B*, 90(15):155446, 2014.
- [54] Jianhui Zhou, Hao-Ran Chang, and Di Xiao. Plasmon mode as a detection of the chiral anomaly in Weyl semimetals. *Physical Review B*, 91(3):035114, 2015.
- [55] Xun Jia, Maoyuan Wang, Dayu Yan, Siwei Xue, Shuyuan Zhang, Jianhui Zhou, Youguo Shi, Xuetao Zhu, Yugui Yao, and Jiandong Guo. Topologically nontrivial interband plasmons in type-II Weyl semimetal MoTe_2 . *New Journal of Physics*, 22(10):103032, 2020.
- [56] Su-Yang Xu, Ilya Belopolski, Nasser Alidoust, Madhab Neupane, Guang Bian, Chenglong Zhang, Raman Sankar, Guoqing Chang, Zhujun Yuan, Chi-Cheng Lee, Shin-Ming Huang, Hao Zheng, Jie Ma, Daniel S. Sanchez, BaoKai Wang, Arun Bansil, Fangcheng Chou, Pavel P. Shibayev, Hsin Lin, Shuang Jia, and M. Zahid Hasan. Discovery of a Weyl fermion semimetal and topological Fermi arcs. *Science*, 349(6248):613–617, 2015.
- [57] N. P. Armitage, E. J. Mele, and Ashvin Vishwanath. Weyl and Dirac semimetals in three-dimensional solids. *Rev. Mod. Phys.*, 90:015001, Jan 2018.
- [58] Young-Woo Son, Marvin L Cohen, and Steven G Louie. Half-metallic graphene nanoribbons. *Nature*, 444(7117):347–349, 2006.
- [59] Katsunori Wakabayashi, Ken-ichi Sasaki, Takeshi Nakanishi, and Toshiaki Enoki. Electronic states of graphene nanoribbons and analytical solutions. *Science and technology of advanced materials*, 2010.

- [60] Chenggang Tao, Liying Jiao, Oleg V Yazyev, Yen-Chia Chen, Juanjuan Feng, Xiaowei Zhang, Rodrigo B Capaz, James M Tour, Alex Zettl, Steven G Louie, et al. Spatially resolving edge states of chiral graphene nanoribbons. *Nature Physics*, 7(8):616–620, 2011.
- [61] Y-H Chan, Ching-Kai Chiu, MY Chou, and Andreas P Schnyder. Ca_3P_2 and other topological semimetals with line nodes and drumhead surface states. *Physical Review B*, 93(20):205132, 2016.
- [62] Chen Fang, Hongming Weng, Xi Dai, and Zhong Fang. Topological nodal line semimetals. *Chinese Physics B*, 25(11):117106, 2016.
- [63] Guang Bian, Tay-Rong Chang, Hao Zheng, Saavanth Velury, Su-Yang Xu, Titus Neupert, Ching-Kai Chiu, Shin-Ming Huang, Daniel S Sanchez, Ilya Belopolski, et al. Drumhead surface states and topological nodal-line fermions in TlTaSe_2 . *Physical Review B*, 93(12):121113, 2016.
- [64] M Mofazzel Hosen, Gyanendra Dhakal, Baokai Wang, Narayan Poudel, Klauss Dimitri, Firoza Kabir, Christopher Sims, Sabin Regmi, Krzysztof Gofryk, Dariusz Kaczorowski, et al. Experimental observation of drumhead surface states in SrAs_3 . *Scientific reports*, 10(1):1–9, 2020.
- [65] Andrew C Potter, Itamar Kimchi, and Ashvin Vishwanath. Quantum oscillations from surface Fermi arcs in Weyl and Dirac semimetals. *Nature communications*, 5(1):1–6, 2014.
- [66] Justin C. W. Song and Mark S. Rudner. Fermi arc plasmons in Weyl semimetals. *Phys. Rev. B*, 96:205443, Nov 2017.
- [67] OV Bugaiko, EV Gorbar, and Pavlo O Sukhachov. Surface plasmon polaritons in strained Weyl semimetals. *Physical Review B*, 102(8):085426, 2020.
- [68] Kota Tsuchikawa, Satoru Konabe, Takahiro Yamamoto, and Shiro Kawabata. Characterization of a Weyl semimetal using a unique feature of surface plasmon polaritons. *Physical Review B*, 102(3):035443, 2020.
- [69] Pengzi Liu, James R Williams, and Judy J Cha. Topological nanomaterials. *Nature Reviews Materials*, 4(7):479–496, 2019.

- [70] Andre K Geim and Konstantin S Novoselov. The rise of graphene. In *Nanoscience and technology: a collection of reviews from nature journals*, pages 11–19. World Scientific, 2010.
- [71] Yuanping Chen, Yuee Xie, Shengyuan A Yang, Hui Pan, Fan Zhang, Marvin L Cohen, and Shengbai Zhang. Nanostructured carbon allotropes with Weyl-like loops and points. *Nano letters*, 15(10):6974–6978, 2015.
- [72] Z. K. Liu, B. Zhou, Y. Zhang, Z. J. Wang, H. M. Weng, D. Prabhakaran, S.-K. Mo, Z. X. Shen, Z. Fang, X. Dai, Z. Hussain, and Y. L. Chen. Discovery of a Three-Dimensional Topological Dirac Semimetal, Na_3Bi . *Science*, 343(6173):864–867, 2014.
- [73] Andreas Topp, Raquel Queiroz, Andreas Grüneis, Lukas Mühler, Andreas W Rost, Andrei Varykhalov, Dmitry Marchenko, Maxim Krivenkov, Fanny Rodolakis, Jessica L McChesney, et al. Surface floating 2D bands in layered nonsymmorphic semimetals: ZrSiS and related compounds. *Physical Review X*, 7(4):041073, 2017.
- [74] Hongming Weng, Chen Fang, Zhong Fang, B Andrei Bernevig, and Xi Dai. Weyl semimetal phase in noncentrosymmetric transition-metal monophosphides. *Physical Review X*, 5(1):011029, 2015.
- [75] William Witczak-Krempa, Ara Go, and Yong Baek Kim. Pyrochlore electrons under pressure, heat, and field: Shedding light on the iridates. *Phys. Rev. B*, 87:155101, Apr 2013.
- [76] Shuo-Ying Yang, Hao Yang, Elena Derunova, Stuart SP Parkin, Binghai Yan, and Mazhar N Ali. Symmetry demanded topological nodal-line materials. *Advances in Physics: X*, 3(1):1414631, 2018.
- [77] Manfred Böhm. Symmetrien in Festkörpern. *Gruppentheoretische Grundlagen und Anwendungen Wiley-VCH*, 2002.
- [78] Hilary Greaves and Teruji Thomas. On the CPT theorem. *Studies in History and Philosophy of Science Part B: Studies in History and Philosophy of Modern Physics*, 45:46–65, 2014.
- [79] E Noether. Invariante Variationsprobleme. Nachrichten der Königlichen Gessellschaft der Wissenschaften. Mathematisch-Physikalische Klasse 2, 235–257. *Transport Theory and Statistical Physics*, pages 183–207, 1918.

- [80] Florian Scheck. *Theoretische Physik I: Mechanik*. Springer-Verlag, 2013.
- [81] Alexander Altland and Ben D Simons. *Condensed matter field theory*. Cambridge university press, 2010.
- [82] Pavan Hosur and Xiaoliang Qi. Recent developments in transport phenomena in Weyl semimetals. *Comptes Rendus Physique*, 14(9):857–870, 2013. Topological insulators / Isolants topologiques.
- [83] Holger Bech Nielsen and Masao Ninomiya. No-go theorem for regularizing chiral fermions. Technical report, Science Research Council, 1981.
- [84] Frank Wilczek. Two applications of axion electrodynamics. *Physical review letters*, 58(18):1799, 1987.
- [85] M. M. Vazifeh and M. Franz. Electromagnetic Response of Weyl Semimetals. *Phys. Rev. Lett.*, 111:027201, Jul 2013.
- [86] D. Bohm. Note on a Theorem of Bloch Concerning Possible Causes of Superconductivity. *Phys. Rev.*, 75:502–504, Feb 1949.
- [87] Wahyu Setyawan and Stefano Curtarolo. High-throughput electronic band structure calculations: Challenges and tools. *Computational materials science*, 49(2):299–312, 2010.
- [88] Stanley C Miller and William F Love. *Tables of irreducible representations of space groups and co-representations of magnetic space groups*. Pruett Press, 1967.
- [89] J. C. Slater and G. F. Koster. Simplified LCAO Method for the Periodic Potential Problem. *Phys. Rev.*, 94:1498–1524, Jun 1954.
- [90] Ivo Souza, Nicola Marzari, and David Vanderbilt. Maximally localized Wannier functions for entangled energy bands. *Phys. Rev. B*, 65:035109, Dec 2001.
- [91] Mois Ilia Aroyo, Juan Manuel Perez-Mato, Cesar Capillas, Eli Kroumova, Svetoslav Ivantchev, Gotzon Madariaga, Asen Kirov, and Hans Wondratschek. Bilbao Crystallographic Server: I. Databases and crystallographic computing programs. *Zeitschrift für Kristallographie - Crystalline Materials*, 221(1):15–27, 2006.
- [92] Mildred S Dresselhaus, Gene Dresselhaus, and Ado Jorio. *Group theory: application to the physics of condensed matter*. Springer Science & Business Media, 2007.

- [93] A Michael Glazer, Mois I Aroyo, and André Authier. Seitz symbols for crystallographic symmetry operations. *Acta Crystallographica Section A: Foundations and Advances*, 70(3):300–302, 2014.
- [94] Anja König and N David Mermin. Electronic level degeneracy in nonsymmorphic periodic or aperiodic crystals. *Physical Review B*, 56(21):13607, 1997.
- [95] L Michel and J Zak. Connectivity of energy bands in crystals. *Physical Review B*, 59(9):5998, 1999.
- [96] Johann Jakob Burckhardt. *Die Symmetrie der Kristalle*. Birkhäuser, 1988.
- [97] Luis Elcoro, Barry Bradlyn, Zhijun Wang, Maia G Vergniory, Jennifer Cano, Claudia Felser, B Andrei Bernevig, Danel Orobengoa, G Flor, and Mois I Aroyo. Double crystallographic groups and their representations on the Bilbao Crystallographic Server. *Journal of Applied Crystallography*, 50(5):1457–1477, 2017.
- [98] Conyers Herring. Effect of Time-Reversal Symmetry on Energy Bands of Crystals. *Phys. Rev.*, 52:361–365, Aug 1937.
- [99] AP Cracknell. Time-reversal degeneracy in the electronic band structure of a magnetic metal. *Journal of Physics C: Solid State Physics*, 2(8):1425, 1969.
- [100] Samuel V. Gallego, Emre S. Tasci, Gemma de la Flor, J. Manuel Perez-Mato, and Mois I. Aroyo. Magnetic symmetry in the Bilbao Crystallographic Server: a computer program to provide systematic absences of magnetic neutron diffraction. *Journal of Applied Crystallography*, 45(6):1236–1247, Dec 2012.
- [101] Michael Glazer, Gerald Burns, and Alexander N Glazer. *Space groups for solid state scientists*. Elsevier, 2012.
- [102] L Michel and J Zak. Elementary energy bands in crystalline solids. *EPL (Europhysics Letters)*, 50(4):519, 2000.
- [103] Juan L Manes. Existence of bulk chiral fermions and crystal symmetry. *Physical Review B*, 85(15):155118, 2012.
- [104] Guoqing Chang, Benjamin J Wieder, Frank Schindler, Daniel S Sanchez, Ilya Belopolski, Shin-Ming Huang, Bahadur Singh, Di Wu, Tay-Rong Chang, Titus Neupert, et al. Topological quantum properties of chiral crystals. *Nature materials*, 17(11):978–985, 2018.

- [105] J Zak. Topologically unavoidable points and lines of crossings in the band structure of solids. *Journal of Physics A: Mathematical and General*, 35(30):6509, 2002.
- [106] Mikio Nakahara. *Geometry, topology and physics*. CRC press, 2003.
- [107] George G Szpiro. *Das Poincaré-Abenteuer: ein mathematisches Welträtsel wird gelöst*. Piper, 2008.
- [108] Fellow coffee table puzzlers. How to hang a picture on a wall using two nails, such that if either nail is removed, the picture rapidly approaches the ground. *Proceedings of the office 5C14*, 2016.
- [109] Ching-Kai Chiu, Jeffrey CY Teo, Andreas P Schnyder, and Shinsei Ryu. Classification of topological quantum matter with symmetries. *Reviews of Modern Physics*, 88(3):035005, 2016.
- [110] Eugene Paul Wigner. Über die Operation der Zeitumkehr in der Quantenmechanik. In *The Collected Works of Eugene Paul Wigner*, pages 213–226. Springer, 1993.
- [111] Alexander Altland and Martin R. Zirnbauer. Nonstandard symmetry classes in mesoscopic normal-superconducting hybrid structures. *Phys. Rev. B*, 55:1142–1161, Jan 1997.
- [112] Petr Hořava. Stability of Fermi Surfaces and K Theory. *Phys. Rev. Lett.*, 95:016405, Jun 2005.
- [113] Alexei Kitaev. Periodic table for topological insulators and superconductors. *AIP Conference Proceedings*, 1134(1):22–30, 2009.
- [114] Kevin F Garrity and David Vanderbilt. Chern insulator at a magnetic rocksalt interface. *Physical Review B*, 90(12):121103, 2014.
- [115] Yujun Deng, Yijun Yu, Meng Zhu Shi, Zhongxun Guo, Zihan Xu, Jing Wang, Xian Hui Chen, and Yuanbo Zhang. Quantum anomalous Hall effect in intrinsic magnetic topological insulator MnBi_2Te_4 . *Science*, 367(6480):895–900, 2020.
- [116] Chang Liu, Yongchao Wang, Hao Li, Yang Wu, Yaoxin Li, Jiaheng Li, Ke He, Yong Xu, Jinsong Zhang, and Yayu Wang. Robust axion insulator and Chern insulator phases in a two-dimensional antiferromagnetic topological insulator. *Nature materials*, 19(5):522–527, 2020.

- [117] Guorui Chen, Aaron L Sharpe, Eli J Fox, Ya-Hui Zhang, Shaoxin Wang, Lili Jiang, Bosai Lyu, Hongyuan Li, Kenji Watanabe, Takashi Taniguchi, et al. Tunable correlated Chern insulator and ferromagnetism in a moiré superlattice. *Nature*, 579(7797):56–61, 2020.
- [118] Ching-Kai Chiu and Andreas P. Schnyder. Classification of reflection-symmetry-protected topological semimetals and nodal superconductors. *Phys. Rev. B*, 90:205136, Nov 2014.
- [119] Aris Alexandradinata, Xi Dai, and B Andrei Bernevig. Wilson-loop characterization of inversion-symmetric topological insulators. *Physical Review B*, 89(15):155114, 2014.
- [120] Liang Fu and C. L. Kane. Topological insulators with inversion symmetry. *Phys. Rev. B*, 76:045302, Jul 2007.
- [121] Shun-Qing Shen. *Topological insulators*, volume 174. Springer, 2012.
- [122] B Andrei Bernevig and Taylor L Hughes. *Topological insulators and topological superconductors*. Princeton university press, 2013.
- [123] János K Asbóth, László Oroszlány, and András Pályi. A short course on topological insulators. *Lecture notes in physics*, 919:997–1000, 2016.
- [124] Andrew M. Essin and Victor Gurarie. Bulk-boundary correspondence of topological insulators from their respective Green’s functions. *Phys. Rev. B*, 84:125132, Sep 2011.
- [125] Gian Michele Graf and Marcello Porta. Bulk-edge correspondence for two-dimensional topological insulators. *Communications in Mathematical Physics*, 324(3):851–895, 2013.
- [126] R. D. King-Smith and David Vanderbilt. Theory of polarization of crystalline solids. *Phys. Rev. B*, 47:1651–1654, Jan 1993.
- [127] Robert A Evarestov and Vyacheslav P Smirnov. *Site symmetry in crystals: theory and applications*, volume 108. Springer Science & Business Media, 2012.
- [128] Raffaello Bianco and Raffaele Resta. Mapping topological order in coordinate space. *Phys. Rev. B*, 84:241106, Dec 2011.
- [129] Marcello Davide Caio, Gunnar Möller, Nigel R Cooper, and MJ Bhaseen. Topological marker currents in Chern insulators. *Nature Physics*, 15(3):257–261, 2019.

-
- [130] Wei Chen. Scaling theory of topological phase transitions. *Journal of Physics: Condensed Matter*, 28(5):055601, jan 2016.
- [131] Wladimir A Benalcazar, B Andrei Bernevig, and Taylor L Hughes. Quantized electric multipole insulators. *Science*, 357(6346):61–66, 2017.
- [132] Wladimir A Benalcazar, B Andrei Bernevig, and Taylor L Hughes. Electric multipole moments, topological multipole moment pumping, and chiral hinge states in crystalline insulators. *Physical Review B*, 96(24):245115, 2017.
- [133] Frank Schindler, Ashley M Cook, Maia G Vergniory, Zhijun Wang, Stuart SP Parkin, B Andrei Bernevig, and Titus Neupert. Higher-order topological insulators. *Science advances*, 4(6):eaat0346, 2018.
- [134] Eslam Khalaf. Higher-order topological insulators and superconductors protected by inversion symmetry. *Physical Review B*, 97(20):205136, 2018.
- [135] Barry Bradlyn, L Elcoro, Jennifer Cano, MG Vergniory, Zhijun Wang, C Felser, MI Aroyo, and B Andrei Bernevig. Topological quantum chemistry. *Nature*, 547(7663):298–305, 2017.
- [136] MG Vergniory, L Elcoro, Zhijun Wang, Jennifer Cano, C Felser, MI Aroyo, B Andrei Bernevig, and Barry Bradlyn. Graph theory data for topological quantum chemistry. *Physical Review E*, 96(2):023310, 2017.
- [137] Luis Elcoro, Benjamin J. Wieder, Zhida Song, Yuanfeng Xu, Barry Bradlyn, and B. Andrei Bernevig. Magnetic Topological Quantum Chemistry. *arXiv preprint arXiv:2010.00598*, 2020.
- [138] Yuanfeng Xu, Luis Elcoro, Zhi-Da Song, Benjamin J Wieder, MG Vergniory, Nicolas Regnault, Yulin Chen, Claudia Felser, and B Andrei Bernevig. High-throughput calculations of magnetic topological materials. *Nature*, 586(7831):702–707, 2020.
- [139] Junyeong Ahn, Sungjoon Park, and Bohm-Jung Yang. Failure of Nielsen-Ninomiya Theorem and Fragile Topology in Two-Dimensional Systems with Space-Time Inversion Symmetry: Application to Twisted Bilayer Graphene at Magic Angle. *Phys. Rev. X*, 9:021013, Apr 2019.
- [140] Adrien Bouhon, Tomáš Bzdušek, and Robert-Jan Slager. Geometric approach to fragile topology beyond symmetry indicators. *Phys. Rev. B*, 102:115135, Sep 2020.

- [141] QuanSheng Wu, Alexey A. Soluyanov, and Tomáš Bzdušek. Non-Abelian band topology in noninteracting metals. *Science*, 365(6459):1273–1277, 2019.
- [142] Hoi Chun Po, Ashvin Vishwanath, and Haruki Watanabe. Symmetry-based indicators of band topology in the 230 space groups. *Nature communications*, 8(1):1–9, 2017.
- [143] Eslam Khalaf, Hoi Chun Po, Ashvin Vishwanath, and Haruki Watanabe. Symmetry Indicators and Anomalous Surface States of Topological Crystalline Insulators. *Phys. Rev. X*, 8:031070, Sep 2018.
- [144] JM Luttinger. Fermi surface and some simple equilibrium properties of a system of interacting fermions. *Physical Review*, 119(4):1153, 1960.
- [145] Masaki Oshikawa. Topological approach to Luttinger’s theorem and the fermi surface of a kondo lattice. *Physical Review Letters*, 84(15):3370, 2000.
- [146] Robert B Laughlin. Quantized Hall conductivity in two dimensions. *Physical Review B*, 23(10):5632, 1981.
- [147] SA Parameswaran. Topological ‘Luttinger’ invariants for filling-enforced non-symmorphic semimetals. *Journal of Physics: Condensed Matter*, 31(10):104001, 2019.
- [148] Takahiro Morimoto and Naoto Nagaosa. Weyl mott insulator. *Scientific reports*, 6(1):1–6, 2016.
- [149] Niklas Wagner, Sergio Ciuchi, Alessandro Toschi, Björn Trauzettel, and Giorgio Sangiovanni. Resistivity Exponents in 3D Dirac Semimetals From Electron-Electron Interaction. *Phys. Rev. Lett.*, 126:206601, May 2021.
- [150] Ryan Thorngren, Ashvin Vishwanath, and Ruben Verresen. Intrinsically Gapless Topological Phases. *arXiv preprint arXiv:2008.06638*, 2020.
- [151] Michael Victor Berry. Quantal phase factors accompanying adiabatic changes. *Proceedings of the Royal Society of London. A. Mathematical and Physical Sciences*, 392(1802):45–57, 1984.
- [152] Max Born and Vladimir Fock. Beweis des adiabatensatzes. *Zeitschrift für Physik*, 51(3-4):165–180, 1928.
- [153] DJ Griffiths. Introduction to Quantum Mechanics Prentice Hall. *Upper Saddle River, NJ*, 1995.

-
- [154] J Zak. Berry's phase for energy bands in solids. *Physical review letters*, 62(23):2747, 1989.
- [155] J Zak. Band center—a conserved quantity in solids. *Physical Review Letters*, 48(5):359, 1982.
- [156] David Vanderbilt. *Berry Phases in Electronic Structure Theory: Electric Polarization, Orbital Magnetization and Topological Insulators*. Cambridge University Press, 2018.
- [157] Rui Yu, Xiao Liang Qi, Andrei Bernevig, Zhong Fang, and Xi Dai. Equivalent expression of Z_2 topological invariant for band insulators using the non-Abelian Berry connection. *Physical Review B*, 84(7):075119, 2011.
- [158] Jun-Jie Zhang, Dongyang Zhu, and Boris I Yakobson. Heterobilayer with Ferroelectric Switching of Topological State. *Nano Letters*, 2020.
- [159] Xian-Kui Wei, Gustav Bihlmayer, Xiaodong Zhou, Wanxiang Feng, Yury V Kolen'ko, Dehua Xiong, Lifeng Liu, Stefan Blügel, and Rafal E Dunin-Borkowski. Discovery of Real-Space Topological Ferroelectricity in Metallic Transition Metal Phosphides. *Advanced materials*, 32(46):2003479, 2020.
- [160] F-T Huang, F Xue, B Gao, LH Wang, X Luo, W Cai, X-Z Lu, JM Rondinelli, LQ Chen, and S-W Cheong. Domain topology and domain switching kinetics in a hybrid improper ferroelectric. *Nature communications*, 7(1):1–9, 2016.
- [161] Christopher W Peterson, Tianhe Li, Wladimir A Benalcazar, Taylor L Hughes, and Gaurav Bahl. A fractional corner anomaly reveals higher-order topology. *Science*, 368(6495):1114–1118, 2020.
- [162] Stefan Blügel, Yuriy Mokrousov, Thomas Schäpers, Yoichi Ando, and Forschungszentrum Jülich. *Topological Matter: Topological Insulators, Skyrmions and Majoranas: Lecture Notes of the 48th IFF Spring School 2017, Organized by the Institute for Advanced Simulation, the Peter Grünberg Institute of the Forschungszentrum Jülich and by the Physics Institute II, University of Cologne on 27 March-7 April 2017*. Forschungszentrum Jülich GmbH, 2017.
- [163] D. J. Thouless. Quantization of particle transport. *Phys. Rev. B*, 27:6083–6087, May 1983.

- [164] Shuta Nakajima, Takafumi Tomita, Shintaro Taie, Tomohiro Ichinose, Hideki Ozawa, Lei Wang, Matthias Troyer, and Yoshiro Takahashi. Topological Thouless pumping of ultracold fermions. *Nature Physics*, 12(4):296–300, 2016.
- [165] David J Thouless, Mahito Kohmoto, M Peter Nightingale, and Marcel den Nijs. Quantized Hall conductance in a two-dimensional periodic potential. *Physical review letters*, 49(6):405, 1982.
- [166] Xiao-Liang Qi, Yong-Shi Wu, and Shou-Cheng Zhang. Topological quantization of the spin Hall effect in two-dimensional paramagnetic semiconductors. *Physical Review B*, 74(8):085308, 2006.
- [167] Renato MA Dantas, Francisco Peña-Benitez, Bitan Roy, and Piotr Surówka. Magneto-transport in multi-Weyl semimetals: A kinetic theory approach. *Journal of High Energy Physics*, 2018(12):1–25, 2018.
- [168] Chen Fang, Matthew J Gilbert, Xi Dai, and B Andrei Bernevig. Multi-Weyl topological semimetals stabilized by point group symmetry. *Physical review letters*, 108(26):266802, 2012.
- [169] Joel Röntynen and Teemu Ojanen. Topological Superconductivity and High Chern Numbers in 2D Ferromagnetic Shiba Lattices. *Phys. Rev. Lett.*, 114:236803, Jun 2015.
- [170] Takahiro Fukui, Yasuhiro Hatsugai, and Hiroshi Suzuki. Chern numbers in discretized Brillouin zone: efficient method of computing (spin) Hall conductances. *Journal of the Physical Society of Japan*, 74(6):1674–1677, 2005.
- [171] Liang Fu and Charles L Kane. Time reversal polarization and a Z_2 adiabatic spin pump. *Physical Review B*, 74(19):195312, 2006.
- [172] P Streda. Theory of quantised Hall conductivity in two dimensions. *Journal of Physics C: Solid State Physics*, 15(22):L717, 1982.
- [173] Qian Niu, David J Thouless, and Yong-Shi Wu. Quantized Hall conductance as a topological invariant. *Physical Review B*, 31(6):3372, 1985.
- [174] Hao Yang, Yan Sun, Yang Zhang, Wu-Jun Shi, Stuart SP Parkin, and Binghai Yan. Topological Weyl semimetals in the chiral antiferromagnetic materials Mn_3Ge and Mn_3Sn . *New Journal of Physics*, 19(1):015008, 2017.

- [175] Ajaya K Nayak, Julia Erika Fischer, Yan Sun, Binghai Yan, Julie Karel, Alexander C Komarek, Chandra Shekhar, Nitesh Kumar, Walter Schnelle, Jürgen Kübler, et al. Large anomalous Hall effect driven by a nonvanishing Berry curvature in the noncolinear antiferromagnet Mn_3Ge . *Science advances*, 2(4):e1501870, 2016.
- [176] Qi Wang, Yuanfeng Xu, Rui Lou, Zhonghao Liu, Man Li, Yaobo Huang, Dawei Shen, Hongming Weng, Shancai Wang, and Hechang Lei. Large intrinsic anomalous Hall effect in half-metallic ferromagnet $\text{Co}_3\text{Sn}_2\text{S}_2$ with magnetic Weyl fermions. *Nature communications*, 9(1):1–8, 2018.
- [177] Johannes Mitscherling. Longitudinal and anomalous Hall conductivity of a general two-band model. *Phys. Rev. B*, 102:165151, Oct 2020.
- [178] Chen Fang, Ling Lu, Junwei Liu, and Liang Fu. Topological semimetals with helicoid surface states. *Nature Physics*, 12(10):936–941, 2016.
- [179] HF Yang, LX Yang, ZK Liu, Yan Sun, C Chen, H Peng, M Schmidt, D Prabhakaran, Bogdan A Bernevig, C Felser, et al. Topological Lifshitz transitions and Fermi arc manipulation in Weyl semimetal NbAs. *Nature communications*, 10(1):1–7, 2019.
- [180] GE Volovik. Topological lifshitz transitions. *Low Temperature Physics*, 43(1):47–55, 2017.
- [181] Leon Balents. Weyl electrons kiss. *Physics*, 4:36, 2011.
- [182] Ig Tamm. Über eine mögliche Art der Elektronenbindung an Kristalloberflächen. *Zeitschrift für Physik*, 76(11-12):849–850, 1932.
- [183] William Shockley. On the surface states associated with a periodic potential. *Physical review*, 56(4):317, 1939.
- [184] Jarosław Kłos and Henryk Puzkarski. Conditions of coexistence of Tamm and Shockley states in a superlattice with a perturbed surface. *Physical Review B*, 68(4):045316, 2003.
- [185] N Malkova and Cun-Zheng Ning. Interplay between Tamm-like and Shockley-like surface states in photonic crystals. *Physical Review B*, 76(4):045305, 2007.
- [186] GP Srivastava. Theory of semiconductor surface reconstruction. *Reports on Progress in Physics*, 60(5):561, 1997.
- [187] John E Northrup. Origin of surface states on Si (111)(7×7). *Physical review letters*, 57(1):154, 1986.

- [188] Ivan L Garanovich, Andrey A Sukhorukov, and Yuri S Kivshar. Defect-free surface states in modulated photonic lattices. *Physical review letters*, 100(20):203904, 2008.
- [189] Ricardo A Pinto. Surface states in defect-free polyatomic lattices described by a tight-binding model. *Physical Review B*, 81(23):233404, 2010.
- [190] J Zak. Symmetry criterion for surface states in solids. *Physical Review B*, 32(4):2218, 1985.
- [191] C-K Chiu, Y-H Chan, and AP Schnyder. Quantized Berry Phase and Surface States under Reflection Symmetry or Space-Time Inversion Symmetry. *arXiv preprint arXiv:1810.04094*, 2018.
- [192] W. P. Su, J. R. Schrieffer, and A. J. Heeger. Soliton excitations in polyacetylene. *Phys. Rev. B*, 22:2099–2111, Aug 1980.
- [193] Wei Chen. Absence of equilibrium edge currents in theoretical models of topological insulators. *Phys. Rev. B*, 101:195120, May 2020.
- [194] MG Vergniory, L Elcoro, Claudia Felser, Nicolas Regnault, B Andrei Bernevig, and Zhijun Wang. A complete catalogue of high-quality topological materials. *Nature*, 566(7745):480–485, 2019.
- [195] Tiantian Zhang, Yi Jiang, Zhida Song, He Huang, Yuqing He, Zhong Fang, Hongming Weng, and Chen Fang. Catalogue of topological electronic materials. *Nature*, 566(7745):475–479, 2019.
- [196] Wan Yee Yau, Andreas Leonhardt, Moritz M. Hirschmann, Niclas Heinsdorf, and Andreas P. Schnyder. In preparation.
- [197] Hendrik Antoon Kramers. Théorie générale de la rotation paramagnétique dans les cristaux. *Proc. Acad. Amst*, 33(6), 1930.
- [198] Lev Davidovich Landau and Evgenii Mikhailovich Lifshitz. *Quantum mechanics: non-relativistic theory*, volume 3. Elsevier, 2013.
- [199] Bryan W Roberts. Kramers degeneracy without eigenvectors. *Physical Review A*, 86(3):034103, 2012.
- [200] Ling Lu, Zhiyu Wang, Dexin Ye, Lixin Ran, Liang Fu, John D Joannopoulos, and Marin Soljačić. Experimental observation of Weyl points. *Science*, 349(6248):622–624, 2015.

-
- [201] Seunghyun Khim, Klaus Koepf, Dmitry V Efremov, J Klotz, T Förster, J Wosnitzer, Mihai I Sturza, Sabine Wurmehl, Christian Hess, Jeroen van den Brink, et al. Magneto-transport and de Haas–van Alphen measurements in the type-II Weyl semimetal TaIrTe₄. *Physical Review B*, 94(16):165145, 2016.
- [202] Luyang Wang, Shao-Kai Jian, and Hong Yao. Topological photonic crystal with equifrequency Weyl points. *Physical Review A*, 93(6):061801, 2016.
- [203] Ilya Belopolski, Peng Yu, Daniel S Sanchez, Yukiaki Ishida, Tay-Rong Chang, Songtian S Zhang, Su-Yang Xu, Hao Zheng, Guoqing Chang, Guang Bian, et al. Signatures of a time-reversal symmetric Weyl semimetal with only four Weyl points. *Nature communications*, 8(1):1–7, 2017.
- [204] Zhi-Ming Yu, Weikang Wu, YX Zhao, and Shengyuan A Yang. Circumventing the no-go theorem: A single Weyl point without surface Fermi arcs. *Physical Review B*, 100(4):041118, 2019.
- [205] Akira Furusaki. Weyl points and Dirac lines protected by multiple screw rotations. *Science Bulletin*, 62(11):788–794, 2017.
- [206] Zhijun Wang, Aris Alexandradinata, Robert J Cava, and B Andrei Bernevig. Hourglass fermions. *Nature*, 532(7598):189–194, 2016.
- [207] Lin Wu, Feng Tang, and Xiangang Wan. Exhaustive list of topological hourglass band crossings in 230 space groups. *Physical Review B*, 102(3):035106, 2020.
- [208] Jonathan Zhang, Y-H Chan, C-K Chiu, Maia G Vergniory, Leslie M Schoop, and Andreas P Schnyder. Topological band crossings in hexagonal materials. *Physical Review Materials*, 2(7):074201, 2018.
- [209] Stepan S Tsirkin, Ivo Souza, and David Vanderbilt. Composite Weyl nodes stabilized by screw symmetry with and without time-reversal invariance. *Physical Review B*, 96(4):045102, 2017.
- [210] Rafael González-Hernández, Erick Tuiran, and Bernardo Uribe. Topological electronic structure and Weyl points in nonsymmorphic hexagonal materials. *Physical Review Materials*, 4(12):124203, 2020.
- [211] Bohm-Jung Yang and Naoto Nagaosa. Classification of stable three-dimensional Dirac semimetals with nontrivial topology. *Nature communications*, 5(1):1–10, 2014.

- [212] Takahiro Morimoto and Akira Furusaki. Weyl and Dirac semimetals with Z_2 topological charge. *Physical Review B*, 89(23):235127, 2014.
- [213] Bohm-Jung Yang, Troels Arnfred Bojesen, Takahiro Morimoto, and Akira Furusaki. Topological semimetals protected by off-centered symmetries in nonsymmorphic crystals. *Physical Review B*, 95(7):075135, 2017.
- [214] Barry Bradlyn, Jennifer Cano, Zhijun Wang, MG Vergniory, C Felser, Robert Joseph Cava, and B Andrei Bernevig. Beyond Dirac and Weyl fermions: Unconventional quasiparticles in conventional crystals. *Science*, 353(6299), 2016.
- [215] Long Liang and Yue Yu. Semimetal with both Rarita-Schwinger-Weyl and Weyl excitations. *Physical Review B*, 93(4):045113, 2016.
- [216] Guoqing Chang, Su-Yang Xu, Shin-Ming Huang, Daniel S Sanchez, Chuang-Han Hsu, Guang Bian, Zhi-Ming Yu, Ilya Belopolski, Nasser Alidoust, Hao Zheng, et al. Nexus fermions in topological symmorphic crystalline metals. *Scientific reports*, 7(1):1–13, 2017.
- [217] Ryo Takahashi, Motoaki Hirayama, and Shuichi Murakami. Spinless hourglass nodal-line semimetals. *Phys. Rev. B*, 96:155206, Oct 2017.
- [218] Chengyong Zhong, Yuanping Chen, Yuee Xie, Shengyuan A Yang, Marvin L Cohen, and SB Zhang. Towards three-dimensional Weyl-surface semimetals in graphene networks. *Nanoscale*, 8(13):7232–7239, 2016.
- [219] Grazia Salerno, Nathan Goldman, and Giandomenico Palumbo. Floquet-engineering of nodal rings and nodal spheres and their characterization using the quantum metric. *Physical Review Research*, 2(1):013224, 2020.
- [220] György Frank, Zoltán Scherübl, Szabolcs Csonka, Gergely Zaránd, and András Pályi. Magnetic degeneracy points in interacting two-spin systems: Geometrical patterns, topological charge distributions, and their stability. *Physical Review B*, 101(24):245409, 2020.
- [221] Pavel A Volkov and Sergej Moroz. Coulomb-induced instabilities of nodal surfaces. *Physical Review B*, 98(24):241107, 2018.
- [222] DF Agterberg, PMR Brydon, and C Timm. Bogoliubov Fermi surfaces in superconductors with broken time-reversal symmetry. *Physical review letters*, 118(12):127001, 2017.

- [223] Minkyung Kim, Dasol Lee, Dongwoo Lee, and Junsuk Rho. Topologically nontrivial photonic nodal surface in a photonic metamaterial. *Physical Review B*, 99(23):235423, 2019.
- [224] Yihao Yang, Jian-ping Xia, Hong-xiang Sun, Yong Ge, Ding Jia, Shou-qi Yuan, Shengyuan A Yang, Yidong Chong, and Baile Zhang. Observation of a topological nodal surface and its surface-state arcs in an artificial acoustic crystal. *Nature communications*, 10(1):1–7, 2019.
- [225] Meng Xiao, Liping Ye, Chunyin Qiu, Hailong He, Zhengyou Liu, and Shanhui Fan. Experimental demonstration of acoustic semimetal with topologically charged nodal surface. *Science advances*, 6(8):eaav2360, 2020.
- [226] Dexi Shao, Huaiqiang Wang, Tong Chen, Pengchao Lu, Qinyan Gu, Li Sheng, Dingyu Xing, and Jian Sun. Composite topological nodal lines penetrating the Brillouin zone in orthorhombic AgF_2 . *npj Computational Materials*, 5(1):1–8, 2019.
- [227] Tie Yang, Guangqian Ding, Zhenxiang Cheng, Xiaotian Wang, and Gang Zhang. Diverse topological states in a ternary NdAsPd compound. *Journal of Materials Chemistry C*, 8(23):7741–7748, 2020.
- [228] Shi-Zhang Chen, Siwen Li, Yuanping Chen, and Wenhui Duan. Nodal flexible-surface semimetals: case of carbon nanotube networks. *Nano Letters*, 20(7):5400–5407, 2020.
- [229] Samuel V Gallego, J Manuel Perez-Mato, Luis Elcoro, Emre S Tasci, Robert M Hanson, Koichi Momma, Mois I Aroyo, and Gotzon Madariaga. MAGNDATA: towards a database of magnetic structures. I. The commensurate case. *Journal of Applied Crystallography*, 49(5):1750–1776, 2016.
- [230] Samuel V Gallego, J Manuel Perez-Mato, Luis Elcoro, Emre S Tasci, Robert M Hanson, Mois I Aroyo, and Gotzon Madariaga. MAGNDATA: Towards a database of magnetic structures. II. The incommensurate case. *Journal of Applied Crystallography*, 49(6):1941–1956, 2016.
- [231] H. T. Stokes, D. M. Hatch, and B. J. Campbell. *ISO-MAG, ISOTROPY Software Suite*. iso.byu.edu.
- [232] G Gatti, D Gosálbez-Martínez, SS Tsirkin, M Fanciulli, M Puppini, S Polishchuk, S Moser, L Testa, E Martino, S Roth, et al. Radial Spin Texture of the Weyl Fermions in Chiral Tellurium. *Physical Review Letters*, 125(21):216402, 2020.

- [233] Motoaki Hirayama, Ryo Okugawa, Shoji Ishibashi, Shuichi Murakami, and Takashi Miyake. Weyl node and spin texture in trigonal tellurium and selenium. *Physical review letters*, 114(20):206401, 2015.
- [234] Felix Flicker, Fernando De Juan, Barry Bradlyn, Takahiro Morimoto, Maia G Vergniory, and Adolfo G Grushin. Chiral optical response of multifold fermions. *Physical Review B*, 98(15):155145, 2018.
- [235] Weikang Wu, Zhi-Ming Yu, Xiaoting Zhou, Y. X. Zhao, and Shengyuan A. Yang. Higher-order Dirac fermions in three dimensions. *Phys. Rev. B*, 101:205134, May 2020.
- [236] Tomáš Bzdušek, QuanSheng Wu, Andreas Rüegg, Manfred Sigrist, and Alexey A Soluyanov. Nodal-chain metals. *Nature*, 538(7623):75–78, 2016.
- [237] GG Lonzarich. Magnetic oscillations and the quasiparticle bands of heavy electron systems. *Journal of magnetism and magnetic materials*, 76:1–10, 1988.
- [238] Sebastian Mühlbauer, Benedikt Binz, F Jonietz, Christian Pfleiderer, Achim Rosch, Anja Neubauer, Robert Georgii, and Peter Böni. Skyrmion lattice in a chiral magnet. *Science*, 323(5916):915–919, 2009.
- [239] Peizhe Tang, Quan Zhou, and Shou-Cheng Zhang. Multiple types of topological fermions in transition metal silicides. *Physical review letters*, 119(20):206402, 2017.
- [240] Daniel S Sanchez, Ilya Belopolski, Tyler A Cochran, Xitong Xu, Jia-Xin Yin, Guoqing Chang, Weiwei Xie, Kaustuv Manna, Vicky Süß, Cheng-Yi Huang, et al. Topological chiral crystals with helicoid-arc quantum states. *Nature*, 567(7749):500–505, 2019.
- [241] Zhicheng Rao, Hang Li, Tiantian Zhang, Shangjie Tian, Chenghe Li, Binbin Fu, Cenyao Tang, Le Wang, Zhilin Li, Wenhui Fan, et al. Observation of unconventional chiral fermions with long Fermi arcs in CoSi. *Nature*, 567(7749):496–499, 2019.
- [242] HF Kay and PC Bailey. Structure and properties of CaTiO₃. *Acta Crystallographica*, 10(3):219–226, 1957.
- [243] Sergey V Krivovichev. Minerals with antiperovskite structure: a review. *Zeitschrift Fur Kristallographie*, 223(1):109–113, 2008.
- [244] CJ Ball, BD Begg, DJ Cookson, GJ Thorogood, and ER Vance. Structures in the system CaTiO₃/SrTiO₃. *Journal of Solid State Chemistry*, 139(2):238–247, 1998.

- [245] Atsutoshi Ikeda, Shun Koibuchi, Shinji Kitao, Mohamed Oudah, Shingo Yonezawa, Makoto Seto, and Yoshiteru Maeno. Negative ionic states of tin in the oxide superconductor $\text{Sr}_{3-x}\text{SnO}$ revealed by Mössbauer spectroscopy. *Physical Review B*, 100(24):245145, 2019.
- [246] Yan Sun, Xing-Qiu Chen, Seiji Yunoki, Dianzhong Li, and Yiyi Li. New family of three-dimensional topological insulators with antiperovskite structure. *Physical review letters*, 105(21):216406, 2010.
- [247] Wen Fong Goh and Warren E Pickett. Survey of the class of isovalent antiperovskite alkaline-earth pnictide compounds. *Physical Review B*, 97(3):035202, 2018.
- [248] Yuan Fang and Jennifer Cano. Higher-order topological insulators in antiperovskites. *Physical Review B*, 101(24):245110, 2020.
- [249] Rui Yu, Hongming Weng, Zhong Fang, Xi Dai, and Xiao Hu. Topological Node-Line Semimetal and Dirac Semimetal State in Antiperovskite Cu_3PdN . *Phys. Rev. Lett.*, 115:036807, Jul 2015.
- [250] Timothy H Hsieh, Junwei Liu, and Liang Fu. Topological crystalline insulators and Dirac octets in antiperovskites. *Physical Review B*, 90(8):081112, 2014.
- [251] Toshikaze Kariyado and Masao Ogata. Three-dimensional Dirac electrons at the Fermi energy in cubic inverse perovskites: Ca_3PbO and its family. *Journal of the Physical Society of Japan*, 80(8):083704, 2011.
- [252] Toshikaze Kariyado and Masao Ogata. Low-energy effective Hamiltonian and the surface states of Ca_3PbO . *Journal of the Physical Society of Japan*, 81(6):064701, 2012.
- [253] Yoshihiko Okamoto, Akira Sakamaki, and Koshi Takenaka. Thermoelectric properties of antiperovskite calcium oxides Ca_3PbO and Ca_3SnO . *Journal of Applied Physics*, 119(20):205106, 2016.
- [254] Jürgen Nuss, Claus Mühle, Kyouhei Hayama, Vahideh Abdolazimi, and Hidenori Takagi. Tilting structures in inverse perovskites, M_3TtO ($\text{M} = \text{Ca, Sr, Ba, Eu}$; $\text{Tt} = \text{Si, Ge, Sn, Pb}$). *Acta Crystallographica Section B: Structural Science, Crystal Engineering and Materials*, 71(3):300–312, 2015.
- [255] S Suetsugu, K Hayama, AW Rost, J Nuss, C Mühle, J Kim, K Kitagawa, and H Takagi. Magnetotransport in Sr_3PbO antiperovskite. *Physical Review B*, 98(11):115203, 2018.

- [256] S Suetsugu, K Kitagawa, T Kariyado, AW Rost, J Nuss, C Mühle, M Ogata, and H Takagi. Giant orbital diamagnetism of three-dimensional Dirac electrons in Sr₃PbO antiperovskite. *arXiv preprint arXiv:2011.13182*, 2020.
- [257] D Huang, H Nakamura, and H Takagi. Planar Hall effect with sixfold oscillations in a Dirac antiperovskite. *arXiv preprint arXiv:2101.05512*, 2021.
- [258] AW Rost, J Kim, S Suetsugu, V Abdolazimi, K Hayama, JAN Bruin, C Mühle, K Kitagawa, A Yaresko, J Nuss, et al. Inverse-perovskites A₃BO (A= Sr, Ca, Eu/B= Pb, Sn): A platform for control of Dirac and Weyl fermions. *Appl Materials*, 7(12):121114, 2019.
- [259] Ching-Kai Chiu, Y-H Chan, Xiao Li, Y Nohara, and AP Schnyder. Type-II Dirac surface states in topological crystalline insulators. *Physical Review B*, 95(3):035151, 2017.
- [260] H Nakamura, D Huang, J Merz, E Khalaf, P Ostrovsky, A Yaresko, D Samal, and H Takagi. Robust weak antilocalization due to spin-orbital entanglement in Dirac material Sr₃SnO. *Nature communications*, 11(1):1–9, 2020.
- [261] A Velden and M Jansen. Zur Kenntnis der inversen Perowskite M₃TO (M= Ca, Sr, Yb; T= Si, Ge, Sn, Pb). *Zeitschrift für anorganische und allgemeine Chemie*, 630(2):234–238, 2004.
- [262] Yukiko Obata, Satoru Matsuishi, and Hideo Hosono. Flux growth and magneto-transport properties of cubic antiperovskite Ca₃PbO single crystals. *Materials Research Bulletin*, 106:1–6, 2018.
- [263] D Samal, H Nakamura, and H Takagi. Molecular beam epitaxy of three-dimensional Dirac material Sr₃PbO. *APL Materials*, 4(7):076101, 2016.
- [264] Makoto Minohara, Ryu Yukawa, Miho Kitamura, Reiji Kumai, Youichi Murakami, and Hiroshi Kumigashira. Growth of antiperovskite oxide Ca₃SnO films by pulsed laser deposition. *Journal of Crystal Growth*, 500:33–37, 2018.
- [265] Mohamed Oudah, Atsutoshi Ikeda, Jan Niklas Hausmann, Shingo Yonezawa, Toshiyuki Fukumoto, Shingo Kobayashi, Masatoshi Sato, and Yoshiteru Maeno. Superconductivity in the antiperovskite Dirac-metal oxide Sr_{3-x}SnO. *Nature communications*, 7(1):1–6, 2016.
- [266] Mohamed Oudah, Jan Niklas Hausmann, Shinji Kitao, Atsutoshi Ikeda, Shingo Yonezawa, Makoto Seto, and Yoshiteru Maeno. Evolution of Superconductivity with Sr-Deficiency in Antiperovskite Oxide Sr_{3-x}SnO. *Scientific reports*, 9(1):1–9, 2019.

- [267] Takuto Kawakami, Tetsuya Okamura, Shingo Kobayashi, and Masatoshi Sato. Topological crystalline materials of $j=3/2$ electrons: Antiperovskites, dirac points, and high winding topological superconductivity. *Physical Review X*, 8(4):041026, 2018.
- [268] Enamul Haque and M Anwar Hossain. Structural, thermodynamic, electronic and magnetic properties of $\text{Sr}_3\text{Sn}_{1-x}\text{Y}_x\text{O}$ ($\text{Y} = \text{V}, \text{Fe}$) from first-principles study. *Results in Physics*, 11:283–290, 2018.
- [269] Samuel ML Teicher, Ida K Svenningsson, Leslie M Schoop, and Ram Seshadri. Weyl nodes and magnetostructural instability in antiperovskite Mn_3ZnC . *APL Materials*, 7(12):121104, 2019.
- [270] Anna Pertsova, R Matthias Geilhufe, Martin Bremholm, and Alexander V Balatsky. Computational search for Dirac and Weyl nodes in f-electron antiperovskites. *Physical Review B*, 99(20):205126, 2019.
- [271] Tian Liang, Quinn Gibson, Mazhar N Ali, Minhao Liu, RJ Cava, and NP Ong. Ultrahigh mobility and giant magnetoresistance in the Dirac semimetal Cd_3As_2 . *Nature materials*, 14(3):280–284, 2015.
- [272] Juan Rodríguez-Carvajal. Recent advances in magnetic structure determination by neutron powder diffraction. *Physica B: Condensed Matter*, 192(1):55–69, 1993.
- [273] Václav Petříček, Michal Dusek, and Lukáš Palatinus. Crystallographic Computing System JANA2006: General features. *Zeitschrift für Kristallographie - Crystalline Materials*, 229, 05 2014.
- [274] J.M. Perez-Mato, S.V. Gallego, E.S. Tasci, L. Elcoro, G. de la Flor, and M.I. Aroyo. Symmetry-Based Computational Tools for Magnetic Crystallography. *Annual Review of Materials Research*, 45(1):217–248, 2015.
- [275] Satoru Nakatsuji, Naoki Kiyohara, and Tomoya Higo. Large anomalous Hall effect in a non-collinear antiferromagnet at room temperature. *Nature*, 527(7577):212–215, 2015.
- [276] Biao Meng, Hao Wu, Yang Qiu, Chunlei Wang, Yong Liu, Zhengcai Xia, Songliu Yuan, Haixin Chang, and Zhaoming Tian. Large anomalous Hall effect in ferromagnetic Weyl semimetal candidate PrAlGe . *APL Materials*, 7(5):051110, 2019.
- [277] Maxim Dzero, Kai Sun, Victor Galitski, and Piers Coleman. Topological kondo insulators. *Physical review letters*, 104(10):106408, 2010.

- [278] Tetsuya Takimoto. SmB₆: A promising candidate for a topological insulator. *Journal of the Physical Society of Japan*, 80(12):123710, 2011.
- [279] Nicholas P Butch, Johnpierre Paglione, Paul Chow, Yuming Xiao, Chris A Marianetti, Corwin H Booth, and Jason R Jeffries. Pressure-resistant intermediate valence in the Kondo insulator SmB₆. *Physical review letters*, 116(15):156401, 2016.
- [280] Kai-Wei Chang and Peng-Jen Chen. Anomalous Z_2 antiferromagnetic topological phase in pressurized SmB₆. *Physical Review B*, 97(19):195145, 2018.
- [281] Kazuhiro Kimura, Tsuneya Yoshida, and Norio Kawakami. Reflection-Symmetry Protected Antiferromagnetic Topological Insulator in Three-Dimensional Heavy-Fermion Systems. In *Proceedings of the International Conference on Strongly Correlated Electron Systems (SCES2019)*, page 011012, 2020.
- [282] Lukasz Fidkowski, TS Jackson, and Israel Klich. Model characterization of gapless edge modes of topological insulators using intermediate brillouin-zone functions. *Physical review letters*, 107(3):036601, 2011.
- [283] Koji Hashimoto, Xi Wu, and Taro Kimura. Edge states at an intersection of edges of a topological material. *Physical Review B*, 95(16):165443, 2017.
- [284] Zhida Song, Zhong Fang, and Chen Fang. (d- 2)-dimensional edge states of rotation symmetry protected topological states. *Physical review letters*, 119(24):246402, 2017.
- [285] Josias Langbehn, Yang Peng, Luka Trifunovic, Felix von Oppen, and Piet W Brouwer. Reflection-symmetric second-order topological insulators and superconductors. *Physical review letters*, 119(24):246401, 2017.
- [286] Frank Schindler, Zhijun Wang, Maia G Vergniory, Ashley M Cook, Anil Murani, Shamashis Sengupta, Alik Yu Kasumov, Richard Deblock, Sangjun Jeon, Ilya Drozdov, et al. Higher-order topology in bismuth. *Nature physics*, 14(9):918–924, 2018.
- [287] Christopher W Peterson, Wladimir A Benalcazar, Taylor L Hughes, and Gaurav Bahl. A quantized microwave quadrupole insulator with topologically protected corner states. *Nature*, 555(7696):346–350, 2018.
- [288] Marc Serra-Garcia, Valerio Peri, Roman Süsstrunk, Osama R Bilal, Tom Larsen, Luis Guillermo Villanueva, and Sebastian D Huber. Observation of a phononic quadrupole topological insulator. *Nature*, 555(7696):342–345, 2018.

-
- [289] N. Goldman and J. Dalibard. Periodically Driven Quantum Systems: Effective Hamiltonians and Engineered Gauge Fields. *Phys. Rev. X*, 4:031027, Aug 2014.
- [290] Hai-Xiao Wang, Zhi-Kang Lin, Bin Jiang, Guang-Yu Guo, and Jian-Hua Jiang. Higher-order Weyl semimetals. *Physical Review Letters*, 125(14):146401, 2020.
- [291] Sayed Ali Akbar Ghorashi, Tianhe Li, and Taylor L Hughes. Higher-order Weyl Semimetals. *Physical Review Letters*, 125(26):266804, 2020.
- [292] Nimrod Moiseyev. *Non-Hermitian quantum mechanics*. Cambridge University Press, 2011.
- [293] Emil J. Bergholtz, Jan Carl Budich, and Flore K. Kunst. Exceptional topology of non-Hermitian systems. *Rev. Mod. Phys.*, 93:015005, Feb 2021.
- [294] Yuto Ashida, Zongping Gong, and Masahito Ueda. Non-hermitian physics. *arXiv preprint arXiv:2006.01837*, 2020.
- [295] Heinz-Peter Breuer, Francesco Petruccione, et al. *The theory of open quantum systems*. Oxford University Press on Demand, 2002.
- [296] Felix Dangel, Marcel Wagner, Holger Cartarius, Jörg Main, and Günter Wunner. Topological invariants in dissipative extensions of the Su-Schrieffer-Heeger model. *Phys. Rev. A*, 98:013628, Jul 2018.
- [297] Fei Song, Shunyu Yao, and Zhong Wang. Non-Hermitian Skin Effect and Chiral Damping in Open Quantum Systems. *Phys. Rev. Lett.*, 123:170401, Oct 2019.
- [298] Haitan Xu, David Mason, Luyao Jiang, and JGE Harris. Topological energy transfer in an optomechanical system with exceptional points. *Nature*, 537(7618):80–83, 2016.
- [299] Lei Xiao, Tianshu Deng, Kunkun Wang, Gaoyan Zhu, Zhong Wang, Wei Yi, and Peng Xue. Non-Hermitian bulk–boundary correspondence in quantum dynamics. *Nature Physics*, pages 1–6, 2020.
- [300] Ananya Ghatak, Martin Brandenbourger, Jasper van Wezel, and Corentin Coulais. Observation of non-Hermitian topology and its bulk-edge correspondence. *arXiv preprint arXiv:1907.11619*, 2019.
- [301] Tobias Hofmann, Tobias Helbig, Frank Schindler, Nora Salgo, Marta Brzezińska, Martin Greiter, Tobias Kiessling, David Wolf, Achim Vollhardt, Anton Kabaši, Ching Hua

- Lee, Ante Bilušić, Ronny Thomale, and Titus Neupert. Reciprocal skin effect and its realization in a topoelectrical circuit. *Phys. Rev. Research*, 2:023265, Jun 2020.
- [302] Carl M Bender and Stefan Boettcher. Real spectra in non-Hermitian Hamiltonians having P T symmetry. *Physical Review Letters*, 80(24):5243, 1998.
- [303] Carl M. Bender, Dorje C. Brody, and Hugh F. Jones. Complex Extension of Quantum Mechanics. *Phys. Rev. Lett.*, 89:270401, Dec 2002.
- [304] Carl M Bender. Introduction to \mathcal{PT} -symmetric quantum theory. *Contemporary Physics*, 46(4):277–292, 2005.
- [305] Shachar Klaiman, Uwe Günther, and Nimrod Moiseyev. Visualization of Branch Points in \mathcal{PT} -Symmetric Waveguides. *Phys. Rev. Lett.*, 101:080402, Aug 2008.
- [306] Ali Mostafazadeh. ExactPT-symmetry is equivalent to Hermiticity. *Journal of Physics A: Mathematical and General*, 36(25):7081–7091, jun 2003.
- [307] Yi-Chan Lee, Min-Hsiu Hsieh, Steven T. Flammia, and Ray-Kuang Lee. Local \mathcal{PT} Symmetry Violates the No-Signaling Principle. *Phys. Rev. Lett.*, 112:130404, Apr 2014.
- [308] Gian-Carlo Ghirardi, Alberto Rimini, and Tullio Weber. A general argument against superluminal transmission through the quantum mechanical measurement process. *Lettere al Nuovo Cimento (1971-1985)*, 27(10):293–298, 1980.
- [309] Gian Carlo Ghirardi, R Grassi, A Rimini, and T Weber. Experiments of the EPR type involving CP-violation do not allow faster-than-light communication between distant observers. *EPL (Europhysics Letters)*, 6(2):95, 1988.
- [310] Dorje C Brody. Biorthogonal quantum mechanics. *Journal of Physics A: Mathematical and Theoretical*, 47(3):035305, 2013.
- [311] Kohei Kawabata, Ken Shiozaki, Masahito Ueda, and Masatoshi Sato. Symmetry and Topology in Non-Hermitian Physics. *Phys. Rev. X*, 9:041015, Oct 2019.
- [312] Nobuyuki Okuma, Kohei Kawabata, Ken Shiozaki, and Masatoshi Sato. Topological Origin of Non-Hermitian Skin Effects. *Phys. Rev. Lett.*, 124:086801, Feb 2020.
- [313] Shunyu Yao and Zhong Wang. Edge States and Topological Invariants of Non-Hermitian Systems. *Phys. Rev. Lett.*, 121:086803, Aug 2018.

-
- [314] Ye Xiong. Why does bulk boundary correspondence fail in some non-hermitian topological models. *Journal of Physics Communications*, 2(3):035043, 2018.
- [315] Zongping Gong, Yuto Ashida, Kohei Kawabata, Kazuaki Takasan, Sho Higashikawa, and Masahito Ueda. Topological Phases of Non-Hermitian Systems. *Phys. Rev. X*, 8:031079, Sep 2018.
- [316] Denis Bernard and André LeClair. A classification of non-Hermitian random matrices. In *Statistical Field Theories*, pages 207–214. Springer, 2002.
- [317] Kohei Kawabata, Takumi Bessho, and Masatoshi Sato. Classification of Exceptional Points and Non-Hermitian Topological Semimetals. *Phys. Rev. Lett.*, 123:066405, Aug 2019.
- [318] A Yu Kitaev. Unpaired Majorana fermions in quantum wires. *Physics-Uspekhi*, 44(10S):131–136, oct 2001.
- [319] Kristian Patrick, Titus Neupert, and Jiannis K. Pachos. Topological Quantum Liquids with Long-Range Couplings. *Phys. Rev. Lett.*, 118:267002, Jun 2017.
- [320] Huitao Shen, Bo Zhen, and Liang Fu. Topological Band Theory for Non-Hermitian Hamiltonians. *Phys. Rev. Lett.*, 120:146402, Apr 2018.
- [321] Andreas Leonhardt, Moritz M Hirschmann, Niclas Heinsdorf, Xianxin Wu, Douglas H Fabini, and Andreas P Schnyder. Symmetry-enforced topological band crossings in orthorhombic crystals: Classification and materials discovery. *arXiv preprint arXiv:2108.05375*, 2021.
- [322] Wan Yee Yau, Moritz M. Hirschmann, Andreas Leonhardt, Niclas Heinsdorf, Xianxin Wu, Douglas H. Fabini, and Andreas P. Schnyder. In preparation.
- [323] Johannes Mitscherling, Moritz M. Hirschmann, and Andreas P. Schnyder. In preparation.
- [324] W. B. Rui, Zhen Zheng, Moritz M. Hirschmann, Song-Bo Zhang, Chenjie Wang, and Z. D. Wang. Intertwined Weyl phases: higher-order topology meets unconventional Weyl fermions via crystalline symmetry. *arXiv preprint arXiv:2105.08443*, 2021.

Deutsche Zusammenfassung

Die vorliegende Dissertation diskutiert topologische Bandkreuzungen in den Energiespektren verschiedener Systeme kondensierter Materie mit diskreter Translationssymmetrie. Topologische Bandkreuzungen können mit Hilfe der Symmetrieeigenwerte der zugehörigen Eigenzustände des Hamiltonoperators untersucht werden. Dabei lassen sich erzwungene Bandkreuzungen, die in jeder Realisierung einer Symmetriegruppen existieren müssen, sowie zufällige Bandkreuzungen charakterisieren. Im Kontext einer topologischen Betrachtung stellen diese Kreuzungen in vielen Fällen den Übergang zwischen verschiedenen topologischen Phasen als Funktion eines Systemparameters dar. Das Feld der Topologie befasst sich mit stetigen Deformationen von mathematischen Objekten und kann benutzt werden um physikalische Systeme mit den sogenannten topologischen Invarianten zu klassifizieren. Mithilfe von kristallinen Symmetrien lässt sich die Notwendigkeit von Bandkreuzungen, Weyl- und Dirac-Punkten, zeigen und damit lassen sich Materialien für mögliche Realisierungen identifizieren. Darüber hinaus studieren wir die Berry-Krümmung und die Oberflächenzustände in Systemen mit topologischen Bandkreuzungen. Diese Arbeit umfasst Bandkreuzungen in Metallen, Magneten und nichthermiteschen Systemen.

Um ein möglichst vollständiges Bild solcher Bandkreuzungen zu erhalten, beginnen wir damit Verallgemeinerungen des Kramers-Theorems zu zeigen. In seiner ursprünglichen Form trifft das Kramers-Theorem Aussagen über die Entartung von Energien des Hamiltonoperators in der Gegenwart der Zeitumkehrsymmetrie. Dies lässt sich erweitern, indem Letztere mit anderen kristallinen Symmetrieeoperationen kombiniert wird, wobei sich zusätzliche Fallunterscheidungen ergeben, bei denen sich die Entartungen nur zwischen Bändern mit bestimmten Symmetrien ergeben. Zusammen mit den Kommutationsrelationen zwischen den Symmetrieeoperationen eines Kristalls lassen sich in vielen Fällen bereits so die Anzahl an Bändern gleicher Energie für sämtliche Punkte in der Brillouin-Zone herleiten. Dieses Vorgehen ermöglicht einen einfachen Zugang zu den bestehenden Charaktertabellen für Raumgruppen und erlaubt gleichzeitig Aussagen zur globalen Bandtopologie. So ergeben sich durch die Betrachtung der Symmetrieeigenschaften der Eigenzustände eines Systems Kompatibilitätsrelationen, die die mögliche Anzahl an Kreuzung entlang von Symmetrieachsen oder auf Spiegelebenen einschränkt. Insbesondere, bei nichtsymmetrischen Symmetrien ist eine nicht verschwindende

Anzahl an Bandkreuzungen notwendig, die auch nicht durch ein Vertauschen der Bänder entfernt werden können. Generische topologische Kreuzungen zwischen zwei nichtentarteten Bändern, also Weyl-Punkte, können nicht allein als einzige Bandkreuzung eines Bandpaars auftreten, sondern müssen mindestens in Paaren auftreten, sodass sich ihre gesamte topologische Ladung kompensiert. Ist zusätzlich eine Zeitumkehrsymmetrie präsent, wird in der Literatur die minimale Anzahl an Weyl-Punkten mit vier angegeben. Wir legen dar, dass die letztere Aussage keine Allgemeingültigkeit besitzt, weil das üblicherweise verwendete Argument nicht zwischen Weyl-Punkten an generischen Positionen und denen an Hochsymmetriepunkten unterscheidet. Mit Zeitumkehrsymmetrie existieren unterschiedliche Systeme, sowohl mit als auch ohne einen Spinfreiheitsgrad, in denen ein, zwei oder drei Weyl-Punkte, also weniger als vier, koexistieren. Dabei kann das Minimum von zwei topologischen Bandkreuzungen ebenfalls umgangen werden, indem zusätzlich neben Weyl-Punkten auch Kreuzungen entlang von Linien oder auf Flächen auftreten. Dies ist der Fall in bestimmten Systemen mit ungeradzahligem Spin, in denen Weyl-Punkte an Hochsymmetriepunkten auftreten aber Bandentartungen auf Linien und Flächen diese mit Ausnahme einzelner Weylpunkte überdecken. Wir greifen solche Fälle in unserer Diskussion zu entarteten Ebenen auf. Für Systeme mit geradzahligem Spin treten dagegen Bandkreuzungen nur im Zusammenspiel mit den kristallinen Symmetrien auf. In einem solchen Fall ist es möglich drei Weyl-Punkte zu erzeugen, wobei einer der drei die Ladungen der anderen beiden kompensiert.

Die Chernzahl definiert die topologische Ladung von Weyl-Punkten und kann aus der Berry-Krümmung bestimmt werden. Letztere unterliegt den Symmetrien des Systems. Dies kann ausgenutzt werden, um allgemeingültige Aussagen bezüglich der Multiplizität von Weyl-Punkten zu treffen. Wir zeigen außerdem, dass die Transformationseigenschaften der Berry-Krümmung nicht für alle kristallinen Symmetrien der Wirkung der Punktgruppe entsprechen. Die Chernzahl beziehungsweise die Berry-Krümmung sind von Interesse, denn sie bestimmen den intrinsischen Anteil des messbaren anomalen Hall-Effekts.

Untersuchung von Raumgruppen und Suche nach topologischen Materialien

Zwar lassen sich mit der Dichtefunktionaltheorie auf numerischen Wege bereits elektronische Bandstrukturen berechnen, aber um die Auswahl der Materialien mit interessanten Bandkreuzungen zu ermöglichen, können die obigen genannten Methoden genutzt werden. Zudem ist es notwendig zu wissen auf welchen Hochsymmetriepfaden in der Brillouin-Zone Bandkreuzungen vor dem Ausbilden einer Bandlücke geschützt sind, um Vorhersagen trotz einer begrenzten Präzision der Numerik treffen zu können. Wir diskutieren die von der Symmetrie erzwungenen topologischen Bandkreuzungen in der Anwesenheit von Spin-Bahn-Kopplung in trigonalen [1]

und tetragonalen [2] Raumgruppen. Unsere Analyse umfasst Weyl- und Dirac-Punkte, ihre Ladungen und Multiplizitäten, Bandkreuzungen entlang von Linien und Flächen, wobei erstere sowohl an Symmetrieachsen fixiert sein können als auch beweglich oder teilweise beweglich sein können. Hierbei sind Punkte oder Linien in dem Sinne beweglich, dass durch eine Änderung der Systemparameter, selbst ohne eine Brechung der Symmetrie, die exakte Position der Bandkreuzungen geändert werden kann. Wir schlagen mehrere Materialien vor, in denen sich die diskutierten Bandkreuzungen finden lassen.

Neben der Existenz von Bandkreuzungen lässt sich aus der Kenntnis der Symmetrieeigenwerte an den zeitumkehrinvarianten Punkten der Brillouin-Zone auf die Existenz topologischer Isolatoren schließen. Während im Allgemeinen die Anordnung dieser Symmetrieeigenwerte von der spezifischen Realisierung abhängig ist, zeigen wir für die tetragonale Raumgruppe 138, dass sich schwache topologische \mathbb{Z}_2 Invarianten aus den Inversionseigenwerten herleiten lassen. Diese \mathbb{Z}_2 Invarianten sind auf zweidimensionalen Teilmengen der Brillouin-Zone definiert und durch Raumgruppensymmetrien auf nichttriviale Werte fixiert. Eine solche Topologie tritt zwar nur in Halbmetallen auf, speziell für Raumgruppe 138 existieren bewegliche Dirac-Punkte, aber dennoch führt die nichttriviale Topologie zu Dirac-Punkten im Oberflächenspektrum. Diese Betrachtung lässt sich auf orthorhombische Raumgruppen verallgemeinern [321]. Außerdem gibt es in den tetragonalen Raumgruppen ebenso die zwei Raumgruppen, 106 und 133, die zu zwei vierfachen Kreuzungen führen, die zwar keine \mathbb{Z}_2 Invariante tragen, aber aus zwei verschiedenen Repräsentationen der vierfachen Rotationssymmetrie aufgebaut sind. Jede der beiden Repräsentationen zeigt für sich genommen Fermi-Bögen. In generischen Modellen zeigt sich, dass diese Oberflächenzustände in den Raumgruppen 106 und 133 auftreten, wobei die Bandtopologie keine Bögen sondern geschlossene Kurven zeigt.

Während wir zuvor, ausgehend von den Raumgruppen und den daraus folgenden Bandkreuzungen, nach geeigneten Materialien gesucht haben, verfolgen wir mit Eu_3PbO einen anderen Ansatz. Eu_3PbO ist in seiner paramagnetischen Phase ein Dirac-Halbmetall, das bei tiefen Temperaturen eine magnetische Ordnung herausbildet. Durch ein angelegtes magnetisches Feld, ergibt sich ein Phasendiagramm mit verschiedenen ferri- und ferromagnetischen Phasen, die mit einer Brechung der Zeitumkehrinvarianz einhergehen. Diese Brechung führt zu einer Aufspaltung der Dirac-Punkte in Paare von Weyl-Punkten sowie weitere Bandkreuzungen. Für die ferromagnetische Phase berechnen wir für mehrere Konfigurationen des externen Feldes die resultierende anomale Hall-Leitfähigkeit mit der Tight-Binding-Methode und setzen diese in Relation zu den auftretenden Weyl-Punkten.

Das Schwerfermionenmetall SmB_6 nimmt unter Druck ebenfalls eine magnetische Ordnung an. Hier analysieren wir nicht nur die Topologie, sondern zeigen, dass sich die tatsächlich realisierte magnetische Ordnung auf die symmetriegeschützten Bandkreuzungen auswirkt.

Während die antiferromagnetische Ordnung des Typs A mit vierfach entarteten Dirac-Linien einhergeht, ist dies nicht der Fall für die Typ G magnetische Ordnung. Dementsprechend ist es prinzipiell möglich experimentell durch die Bestimmung der Bandtopologie auf die realisierte magnetische Ordnung zu schließen.

Bandkreuzungen auf Ebenen

Eine zentrales Resultat dieser Dissertation ist die Zusammenstellung der 254 magnetischen Raumgruppen, die zu Bandkreuzungen für alle Punkten mindestens einer Ebene führen [3]. Mit anderen Worten, diese Kreuzungen ergänzen die Liste der Typen von entarteten Punkten und Linien um Ebenen auf denen alle Bänder jeweils Teil eines Bandpaars mit gleicher Energie sein müssen. Hierzu geben wir die notwendigen und hinreichenden Symmetriekriterien und identifizieren damit aus den 1651 magnetischen Raumgruppen die entsprechenden Symmetriegruppen. Von den 254 verbleibenden Raumgruppen, lassen sich 33 identifizieren, bei denen die Bänder auf den entarteten Ebenen notwendigerweise eine topologische Ladung tragen müssen. Als erste Realisierung solcher topologischer entarteter Ebenen diskutieren wir die ferromagnetische Phase von MnSi. In diesem Material treten den Symmetrien entsprechend zwei sich schneidende entartete Ebenen auf, die mit Hilfe des de-Haas-van-Alphen Effekts, also Oszillationen der Magnetisierung als Funktion der magnetischen Flussdichte, zum ersten mal gemessen werden konnten [3]. Unter den Symmetriegruppen mit notwendigerweise zweidimensionalen topologischen Entartungen befindet sich die bisher nicht beachtete paramagnetische Raumgruppe 94, die Fermi-Bögen zwischen Weylpunkten und der topologisch geladenen Oberfläche notwendig macht.

Die gewonnene Einsicht, dass die Bänder entarteter Ebenen ebenfalls eine Chernzahl tragen und dass sich die Summe solcher topologischen Ladungen zusammen mit allen Weyl-Punkten innerhalb der Brillouin-Zone kompensieren müssen, ermöglicht es uns die bisherigen topologischen Untersuchungen an CoSi zu präzisieren [4]. Insbesondere lassen sich so nun mit der Dichtefunktionaltheorie alle Weyl-Punkte identifizieren.

Topologische Halbmetalle höherer Ordnung

Neben den topologischen Isolatoren und ihren Invarianten, die die Existenz von Oberflächenzuständen innerhalb der Bandlücke des Materials implizieren, gibt es auch eine Topologie höherer Ordnung, bei der die Oberflächen isolierend sind aber Zustände an den Kanten oder Ecken eines Materials die Bandlücke schließen. Während für die Topologie der ersten Ordnung Weyl-Punkte als Übergang zwischen Systemen mit verschiedenen topologischen Invarianten auftreten, liegt die Frage nahe, ob es äquivalente Übergänge auch zwischen Systemen mit

einer Topologie höherer Ordnung gibt. Wir stellen in dieser Arbeit ein Modell eines mit einem elektrischen Feld getriebenen topologischen Supraleiters vor, bei dem sich für bestimmte Parameter des elektrischen Felds Weyl-Punkte bilden. Die Verbindung der Fermi-Bögen ist jedoch abhängig von der gewählten Oberfläche, wobei sich die Randzustände innerhalb der Bandlücke nur für solche Terminierungen herausbilden, die den Kanten des Systems entsprechen [7]. Anders als bisherige Realisierungen zeigt das vorgeschlagene System kein höheres Moment der Polarisierung im Inneren. Dieses Vorgehen lässt sich auf Systeme mit Weylpunkten höherer Ladung verallgemeinern [324].

Topologie in nichthermiteschen Systemen

Ein Axiom der Quantenmechanik fordert die Verwendung hermitescher Hamiltonoperatoren. Wenn diese Bedingung gelockert wird, kann es für bestimmte Systemparameter dazu kommen, dass der Hamiltonoperator nicht mehr diagonalisierbar ist. An einem solchen exzeptionellen Punkt im Parameterraum treffen sich die, nun ebenfalls nicht mehr rein reellen, Energien und berühren sich. Wir untersuchen inwieweit reguläre topologischen Invarianten auf nichthermitesche Systeme anwendbar sind. Dazu ziehen wir die Kitaev-Kette mit nichthermiteschen Potentialen als Modellsystem heran, die näherungsweise den Gewinn und Verlust von Teilchen modellieren [8]. Unter der Annahme der kombinierten Symmetrie aus Inversion und Zeitumkehr lässt sich zeigen, dass die Invariante noch wohldefiniert ist und die Stärke der nichthermiteschen Potentiale äquivalent zum regulären chemischen Potential in die Bestimmungsgleichung für die topologische Phase eingeht.

Im Gegensatz dazu sehen wir für Weyl- und Dirac-Halbleitern, die mit nichthermiteschen Termen modifiziert werden, dass sich die topologische Invariante des hermiteschen Systems nicht direkt übertragen lässt. Stattdessen ist das Auftreten der Oberflächenzustände nicht im Einklang mit der topologischen Invariante. Dies lässt sich beheben, indem direkt das System mitsamt der Oberfläche, anstatt dem System mit periodischen Randbedingungen, untersucht wird. Nach einer Transformation der Basis lässt sich ein effektives System finden, dessen Chernzahl sich in Einklang mit dem Auftreten der Oberflächenzustände befindet [9]. Hierbei unterstützen die nichthermiteschen Terme die Stabilität der nichttrivialen Topologie.

List of publications

Henri Menke and **Moritz M. Hirschmann**.

Topological quantum wires with balanced gain and loss.

Phys. Rev. B, 95:174506, May 2017.

W. B. Rui, **Moritz M. Hirschmann**, and Andreas P. Schnyder.

\mathcal{PT} -symmetric non-Hermitian Dirac semimetals.

Phys. Rev. B, 100:245116, Dec 2019.

Y.-H. Chan, Berkay Kilic, **Moritz M. Hirschmann**, Ching-Kai Chiu, Leslie M. Schoop, Darshan G. Joshi, and Andreas P. Schnyder.

Symmetry-enforced band crossings in trigonal materials: Accordion states and Weyl nodal lines.

Phys. Rev. Materials, 3:124204, Dec 2019.

WB Rui, Song-Bo Zhang, **Moritz M. Hirschmann**, Andreas P Schnyder, Björn Trauzettel, and ZD Wang.

Higher-order Weyl superconductors with anisotropic Weyl-point connectivity.

Phys. Rev. B 103, 184510, May 2021.

Moritz M. Hirschmann, Andreas Leonhardt, Berkay Kilic, Douglas H Fabini, and Andreas P Schnyder.

Symmetry-enforced band crossings in tetragonal materials: Dirac and Weyl degeneracies on points, lines, and planes.

Phys. Rev. Materials 5, 054202, May 2021.

W. B. Rui, Zhen Zheng, **Moritz M. Hirschmann**, Song-Bo Zhang, Chenjie Wang, and Z. D. Wang.

Intertwined Weyl phases: higher-order topology meets unconventional Weyl fermions via crystalline symmetry.

arXiv:2105.08443 (2021).

Marc A. Wilde, Matthias Doderhöft, Arthur Niedermayr, Andreas Bauer, **Moritz M. Hirschmann**, Kirill Alpin, Andreas P. Schnyder, and Christian Pfleiderer.
Symmetry-enforced topological nodal planes at the Fermi surface of a chiral magnet.
Nature 594, 374–37, June 2021.

Nico Huber, Kirill Alpin, Grace Causer, Lukas Worch, Andreas Bauer, Georg Benka, **Moritz M. Hirschmann**, Andreas P. Schnyder, Christian Pfleiderer, and Marc A. Wilde
Network of topological nodal planes, multifold degeneracies, and Weyl points in CoSi.
arXiv:2107.02820 (2021).

Andreas Leonhardt, **Moritz M. Hirschmann**, Niclas Heinsdorf, Xianxin Wu, Douglas H. Fabini, and Andreas P. Schnyder.
Symmetry-enforced topological band crossings in orthorhombic crystals: Classification and materials discovery.
arXiv:2108.05375 (2021).

Huimei Liu, **Moritz M. Hirschmann**, Andreas P. Schnyder, George A. Sawatzky, and Giniyat Khaliullin.
Tunable correlated topological phases in SmB₆.
In preparation.

Moritz M. Hirschmann, Alex S. Gibbs, Fabio Orlandi, Dmitry Khalyavin, Pascal Manuel, Vahideh Abdolazimi, Alexander Yaresko, Jürgen Nuss, Hidenori Takagi, Andreas W. Rost, and Andreas P. Schnyder.
Creating and controlling Dirac fermions, Weyl fermions, and nodal lines in the magnetic antiperovskite Eu₃PbO.
To be submitted.

Acknowledgments

This work would have been neither enjoyable nor possible without the support and company of many to whom I am deeply indebted. I would like to thank Prof. Dr. Walter Metzner for the opportunity to work and to write my doctoral thesis in his department at the Max Planck Institute for Solid State Research. During the various conferences and workshops I gained important insights into the scientific community, learned about topics I would have otherwise missed, and met many interesting people across the field of condensed matter physics. The free-spirited atmosphere of the group has left much room for own ideas and the broad research at the institute is a source of collaborations and new impulses, which I greatly appreciate. My thanks goes also to my other examiners Prof. Dr. Hans Peter Büchler, Prof. Dr. Martin Dressel, and Prof. Dr. Shinsei Ryu, who accepted to review my work. For the help with administrative tasks I want to thank Jeanette Schüller-Knapp.

I want to thank my supervisor Andreas Schnyder for giving me the freedom to try own ideas and for his advice to bring them to fruition. My results would not have been presented half as clear without his contributions. Especially, I want to thank him for involving me in our most recent collaborations, which I believe will prove to be wonderful scientific results.

My office would not have been as gorgeous or homely without my office mate Andreas Leonhardt. He not only joined me during rubber duck debugging my code, but also helped me to answer practically any question, whether it arose or not. The evenings of paper plane folding and aerobatics lightened the mood, when the research progressed slowly. Together with Jáchym Sýkora, Johannes Mitscherling, and Oleksii Maistrenko the office 5C14 became a spot of lively discussions.

Our attempts to read Nakahara's book from cover to cover may have seemed, at the time, in vain, but I do feel it gave us an understanding of topology and differential geometry that we would not have obtained otherwise. Likewise, the journal club as well as our recapitulations of textbook knowledge beyond the scope of our work have been proven to be helpful.

My collaborators not only gave their input but shared their knowledge and approaches with me. I want to thank Wenbin Rui who shared his ideas and tinkered with me on various problems with non-Hermitian systems and model Hamiltonians; Kirill Alpin who patiently dug with me through the band structure of MnSi and CoSi. Huimei Liu, whose advice I would not want to miss, I must give my sincerest thanks for her patience with me; Douglas Fabini for sharing the chemical perspective to solid state research; Henri Menke who got me on board with a great project; as well as Xianxin Wu, Wan Yee Yau, Niclas Heinsdorf, Prof. Dr. Hidenori Takagi, Prof. Dr. Christian Pfleiderer, Alex Gibbs, Andreas Rost, Giniyat Khaliullin, Darshan Joshi, and Berkay Kilic.

I have greatly appreciated the regular coffee-table discussions with all members of the group. Also I want to thank the bouldering group for company, tips, and foremost for introducing me to the sport as well as Desislava Daskalova, who organized and held the Irish dancing class for members of the institute. Playing darts and table tennis with the members of the group was a great exercise in between the desk work.

My special thanks goes to Andreas Schnyder, Andreas Rost, Kirill Alpin, Andreas Leonhardt, Johannes Mitscherling, Josephine Gutekunst, and Carl Bühner, who helped me to proofread this thesis and Regine Noack, who assisted with the printing process.

And finally I want to thank my family for their support throughout my study and PhD.